

NORTHWESTERN UNIVERSITY

Expanding Well-Studied Structural Families of Materials through Exploratory Synthesis

A DISSERTATION

SUBMITTED TO THE GRADUATE SCHOOL
IN PARTIAL FULFILLMENT OF THE REQUIREMENTS

for the degree

DOCTOR OF PHILOSOPHY

Field of Chemistry

By

Steven Flynn

EVANSTON, ILLINOIS

March 2021

ABSTRACT

Expanding Well-Studied Structural Families of Materials through Exploratory Synthesis

Steven Flynn

Continuous and coordinated materials discovery efforts have amassed a wealth of knowledge concerning many general classes of materials. The number of known phases of all structure-types, however, is far less than number of possible materials dictated by the elements on the periodic table. Recently, with improved computational abilities and well-developed theory-based methods, the focus in the materials discovery community has shifted away from exploratory approaches towards targeted synthesis of functional materials predicted by theory. However, several types of materials are ill-suited for a computational approach, such as phases that are metastable, exhibit significant disorder, or have new structure types. This thesis demonstrates that exploratory synthesis complements computational strategies by identifying previously unknown synthetic insights in the well-studied fluorite, rutile, and α - UO_3 structural families.

Anion-deficient fluorite materials exhibit a number of commercially useful properties arising from the specific arrangement of anion vacancies in each structure. Cu, Mn, Fe, Co, and Ni substitutions were performed in a new member of this family, $\text{Zn}_{0.456}\text{In}_{1.084}\text{Ge}_{0.46}\text{O}_3$, to attempt to tune its properties and probe the generalizability of its unique structure. While substitution was found to greatly lower both transparency and conductivity, a surprising flexibility for transition metals and tendency for single site substitution revealed the extent to which order and disorder may coexist in fluorite-related materials.

Rutile-related materials are widely applied and well-studied, with tunnels that are beneficial to ionic transport applications. Single-crystal growth of $\text{LiIn}_2\text{SbO}_6$ revealed an unprecedented variation on the rutile-related structure in which the chains and channels exhibit an alternating-width configuration. Substitution of In with Sc or Fe appears to affect Li ordering, potentially changing the space group with implications for Li mobility and noncentrosymmetric properties. A relationship between alkali metal size and chain structure is suggested which may lead to design principles for targeting phases with alternating-width channels.

Materials in the anion deficient $\alpha\text{-UO}_3$ family are known for their large, complex structures. A new, phase pure member of the family was synthesized by the reaction of HfO_2 and NH_4HF_2 , potentially the Hf analogue to $\text{Zr}_7\text{O}_9\text{F}_{10}$. Another distinct unreported hafnium oxyfluoride phase, which could not be isolated, was obtained by fluorination of HfO_2 with polymer-based fluorinating agents. Comparison to the hydrolysis of $\beta\text{-HfF}_4$ under identical conditions shows that the NH_4HF_2 route produces the oxyfluoride with greater selectivity and at lower temperatures. Potential reaction pathways for the NH_4HF_2 fluorination of HfO_2 are discussed.

These new discoveries are substantive additions to the already expansive body of knowledge about these three structural families and they suggest that there is still more information that can be gained by exploring well-studied systems. Furthermore, as disordered phases and new structures, these additions would also be difficult to predict with a computational approach. Together, these results demonstrate how exploratory synthesis can complement theory-based predictions to generate fundamental insights. As such, both strategies should be employed by future materials discovery initiatives for optimal outcomes.

ACKNOWLEDGMENTS

Undoubtedly, I owe a lot of people a lot of gratitude for their part in helping me reach this point. First and foremost, I have to thank my advisor, Prof. Kenneth Poeppelmeier. Throughout my graduate school career he has provided me with opportunities, guidance, and (most importantly) encouragement on any of the many occasions where the natural ups and down of research had left me disillusioned, if only temporarily.

Next, I am very grateful to the many collaborators without whom much of the work in this thesis would have, at best, been much less interesting, and at worst not at all possible: Dr. Sheel Sanghvi and Prof. Haile assisted me with AC impedance measurements and related sample preparation. AJ Adekoya and Prof. Gabriela Gonzalez Aviles performed extensive refinements and data collection at multiple national lab. Matt Nisbett and Ella Wang were collected all the single crystal diffraction data for me and helped to solve it as well. None of the excellent TEM work and interpretation would have happened without Zachary Mansley, Chi Zhang, and Dr. Roberto dos Reis. Finally, Dr. Kent Griffith collected many solid-state NMR spectra on my samples and taught me how to interpret the results. I also owe special thanks to Jerry Carsello, manager of the J.B. Cohen X-ray facility, as much for his assistance with diffraction experiments and instrumentation as for his always cheerful presence and amusing conversations. Likewise, I'm indebted to Dr. Chris Malliakis, Associate director at IMSERC, who patiently assisted me with various variable temperature and thermogravimetric experiments, even on a few weekends.

I am similarly appreciative of my current and former labmates in the Poeppelmeier group, many of whom I now consider my friends, for the helpful and educational scientific discussions, the often-welcome (and maybe a little too frequent) distractions in lab, the snacks at group meeting,

and fun events outside of work like board game nights, cookie swaps, and mini-golf. Thanks to Justin Hancock, Prof. Michael Tyrone Yeung, Dr. Nenian Charles, Dr. James McCarthy, Anita Chen, Dr. Fenghua Ding, Ian Peczak, Dr. Ryan Paull, Saeed Saeed, Jaye Harada, Dr. Lingyun Li, Dr. Karl Rickert, Dr. Jared Incorvati, Dr. Jacquelyn Cantwell, and Dr. Allison Wustrow.

Last, but certainly not least, I am indebted to my friends and family who supported me and kept me sane over the past five years and change. I cannot adequately express what that has meant to me. Special thanks to those of you who made Chicago a better place to be (Grace Yang, Kevin Shi, Mark Stone, and Jasper Ryckman), and those who were always just a quick phone or video call away (Alexa Yuen, Ming-Ming Tran, Jeffmin Lin, Taylor Brown, and Dan Mossing), especially since I'm not the best at initiating contact. Even though it should go without saying, I am forever grateful to my mom, dad, sisters Jamie and Elizabeth, and the many aunts, uncles, and cousins for all of the love and encouragement that helped me get to where I am now.

The work in this thesis was made possible with support from the Northwestern University Ryan Fellowship and MRSEC program (DMR-1720319). This work also made use of the EPIC, Jerome B. Cohen, Keck-II, and/or SPID facilities of Northwestern University's NUANCE Center and IMSERC PCM facility, which have received support from the Soft and Hybrid Nanotechnology Experimental (SHyNE) Resource (NSF ECCS 2025633); the MRSEC program (NSF DMR-1720319) at the Materials Research Center; the International Institute for Nanotechnology (IIN); the Keck Foundation; and the State of Illinois, through the IIN. Use of the Advanced Photon Source at Argonne National Laboratory was supported by the U. S. Department of Energy, Office of Science, Office of Basic Energy Sciences, under Contract No. DE-AC02-06CH11357.

TABLE OF CONTENTS

| | |
|--|-----------|
| ABSTRACT | 2 |
| ACKNOWLEDGMENTS..... | 4 |
| TABLE OF CONTENTS | 6 |
| LIST OF FIGURES..... | 9 |
| LIST OF TABLES..... | 17 |
| CHAPTER 1: INTRODUCTION..... | 18 |
| 1.1: MATERIALS DISCOVERY | 19 |
| 1.2 SELECTED CHEMICAL COMPOSITIONS FOR EXPLORATORY SYNTHESIS | 22 |
| <i>1.2.1: High Lewis Acid Strength Components in Transparent Conducting Oxides</i> | <i>22</i> |
| <i>1.2.2: Heteroanionic Materials Synthesis.....</i> | <i>26</i> |
| 1.3: NEW PHASE CLASSIFICATION..... | 27 |
| <i>1.3.1: Anion-Deficient Fluorite-related phases</i> | <i>27</i> |
| <i>1.3.2: Rutile-related phases</i> | <i>29</i> |
| <i>1.3.3: Anion-deficient α-UO_3 related phases</i> | <i>31</i> |
| CHAPTER 2: MATERIALS AND METHODS | 33 |
| 2.1: SYNTHESIS | 34 |
| <i>2.1.1: Solid-State Synthesis.....</i> | <i>34</i> |
| <i>2.1.2: Molten Flux Crystal Growth.....</i> | <i>37</i> |
| 2.2: STRUCTURAL CHARACTERIZATION..... | 39 |
| <i>2.2.1: Diffraction</i> | <i>39</i> |
| <i>2.2.2: Rietveld Refinement</i> | <i>42</i> |
| <i>2.2.3: Bond Valence Theory.....</i> | <i>43</i> |
| <i>2.2.4: Solid-State Nuclear Magnetic Resonance.....</i> | <i>44</i> |

| | |
|--|-----------|
| | 7 |
| 2.2.5: Elemental Analysis | 45 |
| 2.3: PROPERTY CHARACTERIZATION | 47 |
| 2.3.1: Diffuse Reflectance | 47 |
| 2.3.2: Conductivity Measurements..... | 48 |
| 2.3.3: Thermal Analysis | 51 |
| CHAPTER 3: NEW ANION-DEFICIENT FLUORITE OXIDES WITH SIGNIFICANT DISORDER..... | 52 |
| 3.1: INTRODUCTION..... | 53 |
| 3.2: MATERIALS AND METHODS | 56 |
| 3.2.1: Synthesis | 56 |
| 3.2.2: X-Ray Diffraction | 58 |
| 3.2.3: Elemental Analysis | 59 |
| 3.3.4: Scanning and Transmission Electron Microscopy..... | 60 |
| 3.3.5: Diffuse Reflectance | 60 |
| 3.3: NEW ZIGO STRUCTURE PHASES VIA ISOVALENT CHEMICAL SUBSTITUTION | 61 |
| 3.3.1: Structural Characterization of CuZIGO..... | 61 |
| 3.3.2: Property Characterization of CuZIGO..... | 74 |
| 3.3.3: Further substitution in the ZIGO structure..... | 76 |
| 3.4: DEFECT FLUORITES IN M-IN-SB-O | 83 |
| 3.5: CONCLUSIONS AND FUTURE DIRECTIONS | 90 |
| CHAPTER 4: NEW ADDITIONS TO THE RUTILE-RELATED FAMILY OF STRUCTURES | 97 |
| 4.1: INTRODUCTION..... | 98 |
| 4.2: MATERIALS AND METHODS | 99 |
| 4.2.1: Synthesis | 99 |
| 4.2.2: Structural Characterization..... | 100 |
| 4.2.3: Solid-state NMR Spectroscopy..... | 102 |
| 4.2.4: Optical Characterization | 104 |

| | |
|---|------------|
| 4.2.5: Impedance Spectroscopy | 104 |
| 4.3: RESULTS AND DISCUSSION:..... | 105 |
| 4.3.1: The Structure of $\text{LiIn}_2\text{SbO}_6$ | 105 |
| 4.3.2: Relationship to Known Structures | 112 |
| 4.3.3: Thermal Behavior:..... | 117 |
| 4.3.4: Property Characterization..... | 119 |
| 4.3.5: (Structural) Effect of Changing 3^+ Chain Cation: LSAO, LFAO | 122 |
| 4.3.6: (Structural) Effect of Changing Tunnel Cation | 131 |
| 4.4: CONCLUSIONS AND FUTURE DIRECTIONS | 134 |
| CHAPTER 5: SOLID-STATE FLUORINATION OF HAFNIUM OXIDE | 137 |
| 5.1: INTRODUCTION..... | 138 |
| 5.2: EXPERIMENTAL METHODS | 140 |
| 5.2.1: Synthesis | 140 |
| 5.2.2: Diffraction | 142 |
| 5.2.3: Characterization..... | 142 |
| 5.3: RESULTS AND DISCUSSION | 144 |
| 5.3.1: Reaction with Fluoropolymers | 144 |
| 5.3.2: Reaction with NH_4HF_2 | 151 |
| 5.3.3: Possible NH_4HF_2 Reaction Pathway | 163 |
| 5.4: CONCLUSIONS AND FUTURE DIRECTIONS | 169 |
| CHAPTER 6: CONCLUSIONS AND FUTURE WORK | 171 |
| APPENDIX 1. SUPPORTING INFORMATION..... | 177 |
| APPENDIX 2. REFERENCES..... | 187 |

LIST OF FIGURES

- Figure 1.1.** Comparison of the number of compounds contained within the ICSD to that in computational databases. Only the relevant information from each database is reflected here. Figure is adapted from Ref. [9]. 21
- Figure 1.2.** Schematic of a device containing a transparent conductor layer. Red (dark blue) elements depict a process emitting (absorbing) a photon typical of a TCO-containing device such as an LED (solar cell). 22
- Figure 1.3.** The typical phase space focused on by inorganic TCO research.¹¹ 23
- Figure 1.4.** Common coordination polyhedral in fluorite-related materials. a) Cubic-coordination with all tetrahedral holes filled. b) Octahedral coordination with 2 out of 8 tetrahedral holes empty, observed on the b-site in bixbyite structures. c) Alternative 6-coordinate site formed by removing a different pair of anions from the cubic environment. Observed on the d-site in bixbyite structures. d) Tetrahedral coordination made by emptying half the tetrahedral holes around the cation. 28
- Figure 1.5.** Several fluorite related crystal structures and representative compounds. a) Fluorite (CaF_2) b) Pyrochlore ($\text{Y}_2\text{Mo}_2\text{O}_7$) c) Bixbyite (In_2O_3) d) Defect fluorite ($\text{CeO}_{1.66}$). Anion sites are enlarged to better depict the random distribution of vacancies in the form of partial occupancy. 29
- Figure 1.6.** The rutile structure. a) Staggered close-packed layers of anions indicated by large, hollow red circles. Blue circles are cation atoms sitting in octahedral holes defined by 3 anions below (solid) and 3 anions above (dotted) with 180° rotation around the cation position. b) The same view as in a), but redrawn to emphasize the octahedral coordination of the cations (blue spheres) by the anions (red spheres). c) View of the rutile structure down the direction indicated by the arrow in b). 30
- Figure 1.7.** Crystal structures of selected rutile-related phases. a) ramsdellite- MnO_2 b) Post-spinel CaFe_2O_4 c) Hollandite $\text{Ba}_2\text{Mn}_8\text{O}_{16}$.⁶¹⁻⁶³ 31
- Figure 1.8.** The crystal structures of anion deficient materials $\alpha\text{-UO}_3$. a) $\alpha\text{-UO}_3$ viewed perpendicular (top) and parallel (bottom) to the pseudo-hexagonal layers. b) $\alpha\text{-U}_3\text{O}_8$ with the unit cell of $\alpha\text{-UO}_3$ indicated by black dashed rectangles. Anion vacancies are marked with a red x. c) $\text{Zr}_7\text{O}_9\text{F}_{10}$. d) $\text{Ta}_{22}\text{W}_4\text{O}_{67}$ 32
- Figure 2.1.** Schematic heating profile depicting typical values employed in this work for each step. Quench cooling refers to instantly removing the sample from the furnace to room, allowing it cool as quickly as possible. 35
- Figure 2.2.** Common reaction vessels used in solid-state synthesis. From left: An opened fused silica tube, a platinum crucible lid, and three alumina crucibles with lids which can be nested. 36

Figure 2.3. A cartoon depiction of a a) polycrystalline and b) single-crystalline sample. The former exhibits multiple crystallites with different orientations such that the lattice planes are not aligned. Material properties measured on a polycrystalline sample will average the theoretical values from all of these orientations and will include an additional contribution from the boundaries and voids between grains..... 37

Figure 2.4. Diffraction in an idealized crystal demonstrating the geometry of Bragg's Law. Incident radiation (arrows) scatter off identical atoms in parallel crystalline planes. The difference in path length for the two rays, $2d \sin\theta$ must be an integer multiple of the radiation wavelength in order for the scattered beams to constructively interfere.^{8,9} 40

Figure 2.5. Stages of a diffuse reflectance experiment for determining the band gap of a material. a) Diffuse reflectance is collected in a UV/Vis spectrophotometer. Incident light (orange arrow) is shone on a sintered pellet (yellow cylinder) and reflected as diffuse (blue arrows) and specular (red arrow) reflectance. b) A schematic plot of reflectance versus wavelength produced by the collection in (a). c) Schematic pseudoabsorbance derived from the Kubelka-Munk transformation with a sample band gap determination via linear extrapolation..... 48

Figure 2.6. An illustrative Nyquist plot and equivalent circuit demonstrating a system with two processes contributing to the total impedance. In a sintered pellet the high frequency (RC) process would typically be bulk conduction whereas the low frequency one (R'C') would be grain boundary conduction.²⁹ 50

Figure 3.1. (Left) The crystal structure of ZIGO. (Right) the four distinct cation sites and their occupancies in ZIGO. Adapted from ref [1]..... 53

Figure 3.2. (Left) Crystal structure of braunite, Mn_7SiO_{12} , depicting its layered nature with conventional labels indicated. Purple octahedra are Mn^{3+} sites, black distorted cubes are Mn^{2+} sites, and blue tetrahedra are Si^{4+} . (Right) Relationship between analogous layers in ZIGO and braunite, as viewed down the c-axis. Site coloration are identical to those in **Figure 3.1** and in the left panel for ZIGO and braunite, respectively. Dashed lines indicate a single unit cell in each structure. Bold lines in the ZIGO layers indicates an $\sqrt{2} \times \sqrt{2}$ supercell..... 54

Figure 3.3. Color of loose powders of $(Cu_xZn_{1-x})_{0.456}In_{1.084}Ge_{0.46}O_3$ as a function of x. 61

Figure 3.4. Rietveld Refinement of synchrotron XRD data of CuZIGO samples with peak markers indicating the ZIGO structure phase (red) and two secondary phases where present..... 62

Figure 3.5. Dependence of Secondary Phases on Nominal Composition of CIGO. Laboratory PXRD patterns of $Cu_{0.456}In_{1.084}Ge_{0.46}O_3$ (black), $Cu_{0.46}In_{1.08}Ge_{0.46}O_3$ (blue) and $Cu_{0.5}InGe_{0.5}O_3$ (red). Black arrows indicate secondary phase peaks that are already present in the black pattern (primarily belonging to $In_2Ge_2O_7$). Blue arrows indicate extra secondary phase peaks only observed in the rounded (red and blue) stoichiometries. Both sets of secondary phase peaks become more intense as the composition increasingly deviates from that of the black pattern... 62

Figure 3.6. Relationship of the Coordination Polyhedra for the 8e and 16f Sites of CuZIGO to the 24d and 8b Sites of In_2O_3 as a Function of Composition. O atom labels on $x = 0$ are consistent for all x values. $x = 0$ data from ICSD-238681. 67

Figure 3.7. Laboratory PXRD comparing $x = 0.25$ CuZIGO samples after synthesis at $1250\text{ }^\circ\text{C}$ (black) and after an additional, subsequent $700\text{ }^\circ\text{C}$ anneal (red). Black arrows indicate minor $\text{In}_2\text{Ge}_2\text{O}_7$ secondary phase. 70

Figure 3.8. Lattice parameters refined from X-ray data for CuZIGO phases as a function of Cu content (x). $x = 0$ values reproduced from Rickert et al.⁶ 71

Figure 3.9. (a) HRTEM and SAED of $x = 0.25$ sample at $[111]$ zone. Some lattice planes and their corresponding distances are marked in (a). Reflection indices are based on the refined structures. (b) HAADF-HRSTEM image and SAED of $x = 0.25$ sample at $[001]$ zone, average unit cell calculated from the HAADF image (upper), structure schematic and simulated image (lower) overlaid. All reflections can be indexed with the refined structure. Darker dots (see insert) in the HAADF image are columns of 16f sites. No contrast is apparent between different 16f sites. 72

Figure 3.10. Simulated SAED patterns of $[111]$ (a) and $[001]$ (b) zone axes of the $x = 0.25$ sample. Several SAED patterns, including $[041]$ (c) and $[223]$ (d) zone axes of the $x = 0.25$ sample with simulated (inset). 72

Figure 3.11. SAED images of the $[221]$ zone axes for $x = 0.25$ (a), $x = 0.5$ (b), and $x = 0.75$ (c) respectively. All of them can match with the simulated diffraction pattern (d). 73

Figure 3.12. Bright-field STEM image and corresponding chemical maps of Cu, Ge, In, Zn and O respectively for $x = 0.25$ sample, which confirm the homogeneous distribution of those elements. 73

Figure 3.13. (a) Kubelka-Munk transformed diffuse reflectance spectra for CuZIGO samples, $x = 0$ data from Rickert et al.⁶, and (b) extrapolated band gap estimates for CuZIGO. 76

Figure 3.14. PXRD patterns of substituted ZIGO materials with the pristine ZIGO pattern for comparison. Symbols mark the apparent presence of the secondary phases In_2O_3 (diamond) and ZnFe_2O_4 (star). 77

Figure 3.15. Partial solubility of (a) Fe^{3+} and (b) Ni^{2+} in the ZIGO structure. PXRD patterns as a function of nominal replacement percentage for each cation. Vertical lines represent calculated reflections for secondary phases. In (a): ZnFe_2O_4 (black) or $\text{Zn}_5\text{Fe}_{10}\text{Ge}_8\text{O}_{36}$ (red). In (b): In_2O_3 (black), Ni_2GeO_4 (blue), or $\text{In}_2\text{Ge}_2\text{O}_7$ (red). 78

Figure 3.16. PXRD patterns of Mn-containing ZIGO samples. Vertical lines indicate calculated reflections for a ZIGO structure phase (black) and In_2O_3 (blue). 80

Figure 3.17. PXRD pattern of the nominal composition $(\text{Cu}_{0.25}\text{Co}_{0.25}\text{Ni}_{0.25}\text{Zn}_{0.25})_{0.456}\text{In}_{1.084}\text{Ge}_{0.46}\text{O}_3$. Vertical lines indicate ZIGO reflection positions. .. 82

Figure 3.18. Experimental and simulated SAED pattern of the $[\bar{2}61]$ zone axis in CuCoNiZIGO. Simulated spots assume $I4_1/amd$ symmetry, with disorder on the 16f sites. Closed red circles indicate main reflections, open circles denote expected systematic absences..... 83

Figure 3.19. (a) PXRD patterns of three new possible defect-fluorite phases with nominal compositions normalized to a total of four cations. Vertical lines indicate the (111), (200), and (220) reflections of a hypothetical defect fluorite phase with a lattice parameter $a = 5.07 \text{ \AA}$. (b) Close-up of the highlighted region in (a) with 20x intensity. 84

Figure 3.20. PXRD patterns of mixtures of Ga and In_3SbO_7 with systematically varied Ga content. Peaks marked by an “x” arise from an Al sample holder. Phase pure composition is shown in normalized form as well. The peaks marked with an asterisk indicates an unknown secondary phase present only at the highest Ga^{3+} concentration..... 85

Figure 3.21. TEM EDX performed on two grains of nominally $\text{Cr}_{0.4}\text{In}_3\text{SbO}_{7.6}$ 87

Figure 3.22. SAED (a, b, c) and corresponding HRTEM (d, e, f) performed on $\text{Cr}_{0.4}\text{In}_3\text{SbO}_{7.6}$ from grain 2 (a, d) and grain 1 (b, e and c, f). Red spots are simulated diffraction patterns for a defect fluorite structure. Inset regions in (a, b) are free of the simulated overlay to clearly show main reflections. Dashed blue lines in (d, e) are guides for the eye to emphasize the observed contrast striations. 89

Figure 4.1: Body-centered crystal structure solutions of $\text{LiIn}_2\text{SbO}_6$ and their predicted PXRD patterns compared with the experimentally observed one. Only one predicted pattern is shown for simplicity, as the two are visibly identical. Peaks marked with an asterisk are unaccounted for by the body-centered structures. The left ($Immm$) structure demonstrates that each layer of half-filled O positions consists of two individual orientations of a close-packed layer super imposed on top of each other. The right structure ($I222$) shows the unrealistically flat or non-positive definite (cylinders) ellipsoids apparent in some 100 K body-centered solutions. 106

Figure 4.2. Structural Refinement of $\text{LiIn}_2\text{SbO}_6$. a) The single crystal solution as viewed down the $[281]$ direction. b) The portion of an isolated edge-sharing chain of InO_6 and SbO_6 octahedra contained within a single unit cell, viewed down the a-axis. c,d) Structural solutions for LIAO at 323 and 500 K respectively with the same orientation. Purple, orange, and green polyhedra are respectively centered on the 4f (In^{3+}), 2a (Sb^{5+}), and 4g (Li^+) crystallographic sites. Red spheres/ellipsoids are O^{2-} ions..... 107

Figure 4.3. Rietveld refinement of powder LIAO samples. (Blue) Observed powder pattern. (Green) Predicted pattern. (Red) background. (Light Blue) Difference pattern. (Blue ticks) Predicted reflections from $\text{LiIn}_2\text{SbO}_6$ 108

Figure 4.4. ^6Li solid-state 5 kHz MAS NMR spectroscopy. a) ^6Li central resonance and b) ^7Li spectra showing the spinning sidebands and fits to the experimental lineshapes. Fit parameters are given in **Table 4**. 112

Figure 4.5. Relationship between the close-packed layers of LiSbO_3 and $\text{LiIn}_2\text{SbO}_6$. Open circles are O^{2-} ions. Cation positions for all framework ions of LIAO are present in LiSbO_3 , and Li positions are slightly offset between tetrahedral and octahedral sites. 113

Figure 4.6. a) Several-unit-cells long segment of an isolated chain from selected rutile-like phases viewed perpendicular to the chain direction.^{3-6,48,49} Regions of LIAO chains are labeled with the structure they most closely resemble. b) 1:1 intergrowth structure of rutile and ramsdellite as observed in Li-intercalated ramsdellite $\text{Li}_{0.9}\text{Ti}_{2.94}\text{O}_6$ viewed parallel to the chain direction, with rutile and ramsdellite slabs indicated.⁶ 114

Figure 4.7. Geometrical relationship between occupied octahedral holes in a single, ideal close-packed layer (dashed circles) in the LIAO (triangles) and rutile (circles) structures. (a) Rutile octahedral sites lie parallel to the rows of close-packed O^{2-} ions, whereas LIAO chains are rotated by 30° . (b) Close-up of the boxed region in (a). The observed chain direction lattice parameters in LIAO (5.33 Å) arises from the characteristic value of ~ 3 Å in rutile-related oxides. 115

Figure 4.8. Unit cell lattice parameters a , b , and c (a , b , c) and volume (d) as a function of temperature determined by refinement of high-temperature PXRD data. 118

Figure 4.9. Differential thermal analysis of LIAO samples from 300 to 673 K. 118

Figure 4.10. Temperature-dependent PXRD pattern of LIAO from 300 to 1200 K. 119

Figure 4.11. Comparison of $F(R)^{1/2}$ and $F(R)^2$ extracted from diffuse reflectance measurements of LIAO. Extrapolation of the linear portion of $F(R)^2$ suggests a direct band gap of 3.9 eV. 120

Figure 4.12. Impedance spectra of LIAO at (a) room temperature, (b) 373 K, (c) 623 K, and (d) 773 K, and (e) bulk conductivity. Room temperature spectra are measured under ambient conditions (blue), immediately under synthetic air (red) and after drying in synthetic air for 2 hours (blue). High temperature spectra are measured under synthetic air. Select frequencies are indicated by a star. Bulk conductivity values are those corresponding to the high frequency arcs spectra such as in (c) and (d). 122

Figure 4.13. Potential high energy sites in the channels of LIAO: (blue) octahedral sites with Wyckoff position 2d between SbO_6 chain units and (gray) 3-coordinate sites between Li tetrahedra and the 2d sites. 123

Figure 4.14. Crystal structures of LSAO at 100 K viewed down the $[3\ 4\ 12]$ direction. Red spheres are O atoms and indigo, orange, and green polyhedra are centered on Sc, Sb, and Li, respectively. 124

Figure 4.15. ^7Li solid-state 5 kHz MAS NMR spectroscopy central resonance of LSAO compared with that of LIAO and LiSbO_3 125

Figure 4.16. The oppositely polarized twin to the LSAO structure, generated by 180° rotation around the b -axis, is simply translated relative to that which would be obtained if Li were to hop into adjacent vacancies..... 126

Figure 4.17. Differential thermal analysis of LSAO (top) and LFAO (bottom) polycrystalline samples from 300 to 673 K. 128

Figure 4.18. High temperature crystal structures of LMAO, $M = (\text{Sc}, \text{Fe})$. (a) LSAO at 500 K down the $[8\bar{2}1]$ direction. (b) LFAO at 400 K viewed down the $[281]$ direction. Red spheres are O atoms and indigo, brown, orange, and green polyhedra are centered on Sc, Fe, Sb, and Li, respectively. 129

Figure 4.19. LeBail fit of powder KIAO sample with nominal composition $\text{KIn}_{1.5}\text{SbO}_{5.25}$. (Blue) Observed powder pattern. (Green) Predicted pattern. (Red) background. (Light Blue) Difference pattern. (Blue ticks) Predicted reflections from $\text{K}_2\text{In}_5\text{Sb}_3\text{O}_{16}$ (Red ticks) Predicted reflections from In_2O_3 , present as a minor secondary phase. (Inset) Crystal structure of hypothetical KIAO phase. Purple and red spheres are K^+ and O^{2-} ions, respectively. Pink polyhedral are centered on framework sites containing a statistical mix of In^{3+} and Sb^{5+} 132

Figure 5.1. PXRD patterns of reaction products of HfO_2 and PVDF in (a) air and (b) an evacuated sealed tube (350°C). Vertical lines are the reflections for known or reported phases: HfO_2 in the baddelyite structure (black), HfSiO_4 (red), Zr_2OF_6 (blue), and tetragonal Hf_2OF_6 (magenta). Dashed lines indicate phases reported as a list of reflections without further structural information..... 146

Figure 5.2. PXRD patterns of reaction products of HfO_2 and PTFE. Vertical lines are the predicted reflections for HfO_2 (black), $\alpha\text{-HfF}_4$ (red), and Zr_2OF_6 (blue). Dashed lines indicate phases reported as a list of reflections without further structural information..... 148

Figure 5.3. PXRD patterns of the reaction products of HfO_2 and NH_4HF_2 at three different weight ratios. Vertical lines indicate theoretical peak positions for $\beta\text{-HfF}_4$ (red) and $\text{Zr}_7\text{O}_9\text{F}_{10}$ (black). The shaded region indicates one easily-distinguished high intensity peak from each phase. The relative intensities of these peaks reverses as the reactant ratio is increased from 1:1 to 2:1 ($\text{HfO}_2:\text{NH}_4\text{HF}_2$)..... 152

Figure 5.4. PXRD pattern of the reaction of HfO_2 with NH_4HF_2 in a 2:1 weight ratio after one and two heating steps at 420°C . Vertical lines indicate theoretical peak positions for $\beta\text{-HfF}_4$ (red), $\text{Zr}_7\text{O}_9\text{F}_{10}$ (black), and HfO_2 (blue). Asterisks indicate the HfO_2 peaks in the top pattern for clarity. 153

Figure 5.5. Rietveld refinement of synchrotron diffraction data of the new hafnium oxyfluoride phase, $w\text{R} = 26.409\%$. (Inset) Zoom-in views of areas of disagreement between refined model and experimental data..... 155

Figure 5.6. ^{19}F solid-state NMR spectroscopy of $\beta\text{-HfF}_4$ and the unknown Hf-O-F phase. (a) Isotropic resonances and (b) full spectrum of $\beta\text{-HfF}_4$. (c) Spectral fitting revealed that seven signals (bottom) were required to reproduce the experimental lineshape (top). The sum of the individual signals is shown just below the experimental spectrum. Details of the fitting parameters are given in **Table A.4**. Spectra were recorded at 40 kHz MAS; spinning sidebands are denoted with asterisks..... 156

Figure 5.7. TEM of Hf-O-F compared with simulations based on hypothetical $\text{Hf}_7\text{O}_9\text{F}_{10}$ model with refined lattice parameters. SAED down the [017] (a), [027] (b), [012] (c) and [215] (d) zone axes. Simultaneously acquired HAADF-HRSTEM (e) and ABF-HRSTEM (f) images with SAED at the [010] zone (upper), structure schematic (middle) and simulated image (lower) overlaid. The structure schematic inserted in (e) only shows the positions of Hf. Some lattice planes and their corresponding distances are marked. 159

Figure 5.8. Defective regions in Hf-O-F particles. SAED patterns along [010] from the same particle without (a) and with (b) extra diffused spots. Convergent beam electron diffraction patterns along [210] without (c) and with (d) diffuse intensity. The patterns in (b) and (d) were colored to enhance the contrast. (e) HAADF-HRSTEM from a region of interest where some planar defects can be observed as marked with dashed boxes. (f) High-magnification image of the yellow-outlined region in (e) showing additional sets of atomic planes. 161

Figure 5.9. Improved Rietveld refinement using of synchrotron diffraction data of the new hafnium oxyfluoride phase using TEM results, $wR = 18.258\%$. (Insets) Zoom-in views of areas of disagreement between refined model and experimental data. (Blue) Observed powder pattern. (Green) Calculated powder pattern. (Light blue) Difference. 162

Figure 5.10. TGA in flowing He of the phase pure hafnium oxyfluoride obtained via reaction of HfO_2 and NH_4HF_2 163

Figure 5.11. Calculated Gibbs reaction energy (ΔG) for the hydrolysis of $\beta\text{-HfF}_4$ as a function of temperature. (inset) Close-up on the temperatures at which ΔG becomes negative. 167

Figure A.1. Temperature-dependent impedance spectra of LIAO from: (a) 298 to 473 K, (b) 448 to 573 K, (c) 573 to 673 K, (d) 673 to 773 K, and (e) 773 to 848 K. Spectra are measured under synthetic air. Select frequencies are indicated by a star. 178

Figure A.2. Crystal structure of LFAO at 400 K with 4e off-center channel sites marked as black spheres, as viewed down the (a) b-axis and (b) c-axis. Overlap with Li thermal ellipsoid suggests there may be some transient Li content on the 4e site, which lies along the diffusion path between the adjacent Li sites. 180

Figure A.3. Color changes upon reaction of HfO_2 with PVDF. Fluoropolymer was added only to the initial reaction mixture..... 180

Figure A.4. PXRD patterns of reaction products of HfO_2 and PVDF in an evacuated sealed tube (350 °C). Blue vertical lines are the reflections for $\text{Zr}_3(\text{OH})_2\text{F}_{10}$, which is reported as a list of reflections without further structural information. 181

Figure A.5. Comparison of the products of heating a small amount of PTFE at 450 °C in a sealed fused silica tube with (black) and without (blue) the presence of HfO_2 . The most intense peaks of the latter matches the position of the only unknown peak in the former (**Figure 2**, main text). 181

Figure A.6. PXRD patterns of the reaction products of HfO_2 and NH_4HF_2 after 1-3 additional heating cycles in different seasons (and therefore different ambient humidities). Asterisks mark prominent $\beta\text{-HfF}_4$ peaks. 182

Figure A.7. Comparison of ^{19}F NMR of the unknown Hf-O-F phase at 40 (black) and 36 (red) kHz MAS. Peaks that do not shift represent isotropic resonances. Spinning sidebands are denoted with asterisks. 183

Figure A.8. Simulated SAED patterns of [010] (a), [017] (b), [027] (c), [210] (d), [012] (e) and [215] (f) zone axes of the Hf-O-F sample based on hypothetical model with lattice parameters from Rietveld refinement. 184

Figure A.9. PXRD of bulk hafnium oxyfluoride produced by reaction of HfO_2 with NH_4HF_2 after thermal analysis (TGA). Sample was heated at 10 °C/min to 800 °C in He atmosphere, held there for 30 minutes and cooled at the same rate. Red vertical lines indicate theoretical reflections for HfO_2 . Low sample quantity (~30 mg) resulted in an incompletely covered glass PXRD slide, producing the observed amorphous background. 185

Figure A.10. PXRD of the product of a mixture of HfO_2 and NH_4HF_2 in 1:0.9486 weight (1:4 molar) ratio. After reaction at 250 °C in air for 12 hours. Vertical lines indicate the predicted peak positions for $(\text{NH}_4)_2\text{HfF}_6$ (black) and $(\text{NH}_4)_3\text{HfF}_7$ (red). 185

Figure A.11. PXRD of well-ground, commercial HfF_4 after heating in a covered Al_2O_3 crucible air. (left) successive cycles of heating to 420 °C and dwelling for 12 hours. (right) High temperature heating cycles. Asterisks indicated positions of minor secondary phases. Vertical lines indicate predicted reflections for $\beta\text{-HfF}_4$ (red), HfO_2 (blue), and $\text{Zr}_7\text{O}_9\text{F}_{10}$ (black). 186

LIST OF TABLES

| | |
|--|-----|
| Table 3.1. ICP-OES data for $(\text{Cu}_x\text{Zn}_{1-x})_{0.456}\text{In}_{1.084}\text{Ge}_{0.46}\text{O}_3$ phases | 63 |
| Table 3.2. Rietveld Refinement of Synchrotron X-ray Diffraction Data of CuZIGO | 63 |
| Table 3.3. Atomic Positions from Synchrotron XRD Refinement..... | 65 |
| Table 3.4. Refinement results with Cu in non-16f sites | 66 |
| Table 3.5. Bond Valence Analysis for X-ray Models of CuZIGO ¹⁹ | 68 |
| Table 3.6 M-O bond distances for the 16f and 8e sites from X-ray Data. $x = 0$ data from ICSD-238681..... | 69 |
| Table 3.7. Successful isovalent cation substitutions performed in the ZIGO structure. | 76 |
| Table 3.8. Average experimental and nominal composition of two $\text{Cr}_{0.4}\text{In}_3\text{SbO}_{7.6}$ grains as determined by TEM EDX..... | 86 |
| Table 4.1: Crystallographic Data For $\text{LiIn}_2\text{SbO}_6$ | 102 |
| Table 4.2. Atomic coordinates and isotropic thermal parameters in LIAO at 100, 323, and 500 K. | 107 |
| Table 4.3. Rietveld refinement parameters..... | 108 |
| Table 4.4 Selected M-O bond-lengths, O-M-O bond angles, and multiplicities in LIAO. | 110 |
| Table 4.5. Bond Valence Analysis in LIAO at 100 K..... | 111 |
| Table 4.6. Calculated and experimental NMR parameters of LIAO and LiSbO_3 | 111 |
| Table 4.7. Bond Valence Sums of Li^+ sites in LMAO phases with $Pn\bar{m}$ symmetry..... | 130 |
| Table 4.8. Parameters of the LeBail fit of hypothetical KIAO to $\text{KIn}_{1.5}\text{SbO}_{5.25}$ PXRD pattern.. | 133 |
| Table A.1. Crystallographic and collection parameters for LMAO ($M = \text{Sc}, \text{Fe}$). | 179 |
| Table A.2. Atomic coordinates and isotropic thermal parameters in LSAO at 100 and 500 K. | 179 |
| Table A.3. Atomic coordinates and isotropic thermal parameters in LFAO at 400 K..... | 180 |
| Table A.4. Spectral parameters used to fit the ¹⁹ F NMR spectrum of the hafnium oxyfluoride sample in Figure 3 in the main text. ^a | 183 |
| Table A.5. Rietveld refinement parameters for the hypothetical “ $\text{Hf}_7\text{O}_9\text{F}_{10}$ ” structure. | 184 |

CHAPTER 1: INTRODUCTION

1.1: Materials Discovery

Technological innovation is driven by the discovery and characterization of materials. In particular, crystalline inorganic compounds, materials with an infinitely repeating atomic structure that do not contain C-H molecules, have played an irreplaceable part in the technological leaps of the past century.^{1,2} LiCoO_2 paved the way for the Li-ion batteries that are now essential to ubiquitous portable electronics such as laptops and cell phones. Superconductors such as NbTi are critical components in magnetic resonance technologies of great use to both research and medicine.³ Advances in semiconductors such as Si and GaAs have led to transistors, LEDs, and lasers which have revolutionized industries ranging from computing to telecommunications. These make up only a small portion of all the examples of this phenomenon; there are too many to list them all here. While some of these materials inspired innovations immediately after their discovery, others had been known for a long time before a use was identified. As such every new material discovered may be of value for future research, even when no appropriate application is immediately obvious. Currently, the Inorganic Crystal Structure Database (ICSD), a repository for published crystal structures in the literature, contains $\sim 10^5$ experimental structures.⁴ However, despite thousands of years of history and a more concerted effort materials discovery effort for at least a century, this number still pales in comparison to the amount of possible combinations of elements on the periodic table – considering only unique compositions containing four elements or fewer (no polymorphism), the amount already exceeds 10^6 .^{5,6} It is no surprise, therefore, that materials discovery remains a critical and extremely active field of research.

These efforts are generally characterized as embodying one of two approaches: 1) exploratory or 2) targeted or application-based. In the former, the goal is to identify any new single

phase compositions produced through reactions and characterize their structure and properties. Simple precursors are mixed together in different proportions in order to probe different regions of the “potential energy landscape”.⁷ Products generally represent significant thermodynamic minima in the phase space accessed by the composition of the reactants and the conditions under which the reaction was carried out. Often, many different combinations and reaction conditions must be tried before a new material is observed, and then further work is required to isolate and characterize the phase. “Chemical intuition” and a variety of empirically-based theories provide frameworks that are often used to guide expectations for outcomes of these experiments. However, the fact that the product may be structurally (and in open systems, compositionally) very distinct from the reactant mixture commonly inhibits prediction, giving this approach its “exploratory” nature.

For the second approach, a product with a specific structure and composition is targeted based on the expectation that it will exhibit a desired property. For much of human history materials discovery pursuits were dominated by the former strategy.^{1,2,4-9} However, the trend has shifted strongly towards targeted efforts in the past few decades.^{6,8} Relatively recent advancements in theory and modelling, such as improvements in density functional theory (DFT), have made it possible to accurately predict the stability, structure, and properties of a material without having to spend the time or resources making and isolating it in a lab.¹⁰ **Figure 1** demonstrates that the total number of predicted phases in computational databases exceeds the amount of experimentally verified ones in the ICSD by nearly an order of magnitude.⁹ In theory, these advancements present the opportunity to drastically enhance the efficiency of synthetic operations, allowing experimentalists to focus their efforts only on phases that have been predicted to be stable and

exhibit exceptional properties instead of wasting time chasing compositions which may, at best, have no useful application and, at worst, not form a new phase under any achievable conditions. However, there are a few key shortcomings to this approach: 1) ab initio structure prediction for complex

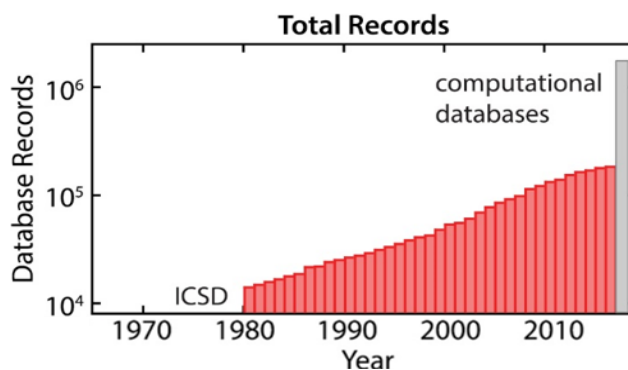


Figure 1.1. Comparison of the number of compounds contained within the ICSD to that in computational databases. Only the relevant information from each database is reflected here. Figure is adapted from Ref. [9].

(ternary and higher) remains computationally difficult, 2) modelling disorder is computationally expensive, especially in large unit cells and 3) stability calculations do not guarantee synthesizability - materials calculated to be stable may not be synthesizable for a variety of reasons, whereas metastable phases may be achievable through specific low energy routes. Furthermore, high-throughput studies rely on a library of known structures and compositions to which a new composition in question can be fit, computationally relaxed, and then compared energetically to all known competing phases. If the library is incomplete because a stable structure has not been discovered yet, then many theory-based approaches will fail for any compositions that are stable in the missing structure. Likewise, they will likely be inaccurate when dealing with composition spaces in which the missing compounds could serve as competing phases. Exploratory synthesis permits the pursuit and discovery of materials that may be overlooked by computational materials design approaches for the reasons above.

The work in this thesis demonstrates that exploratory solid-state synthesis may provide new fundamental knowledge even when not, and possibly complementary to, the focus of property prediction studies. Broadly, it addresses the question “What phases remain undiscovered in

previously studied materials systems that might be outside the purview of theory-based approaches, and what new synthetic and chemical knowledge, if any, can they provide?”

1.2 Selected Chemical Compositions for Exploratory Synthesis

The work in this thesis describes exploratory synthesis experiments targeting three general composition spaces: 1) M-In-Ge-O (M = Mn, Fe, Co, Ni, Cu, Zn, or a mixture of these elements), 2) M'-In-Sb-O (M' = Li, K, Cr, Fe, Ga), and 3) Hf-O-F. The initial selection of these targets was motivated by one of two goals. (Cu, Zn)-In-Ge-O (1), Ga-In-Sb-O (2), and Li-In-Sb-O (2) were looked at for potential new transparent conducting oxide (TCO) materials. Hf-O-F was explored to identify new heteroanionic materials and develop the science behind their syntheses. As identification of new phases was the overall objective in either case, these phase spaces were expanded based on what new phases were observed, resulting in some investigations diverging from their original purposes. Nevertheless, an introduction to these concepts and the rationalization for the selection of the relevant systems follows.

1.2.1: High Lewis Acid Strength Components in Transparent Conducting Oxides

Transparent conductors are materials which simultaneously exhibit electrical conductivity and optical transparency. As depicted in **Figure 1.2**, they are a critical component to technologies which require light to pass through a conducting layer, such as flat-panel displays (FPDs), touch screens, and photovoltaics (PVs). Efficient performance of these devices is dependent on sufficiently large band gaps

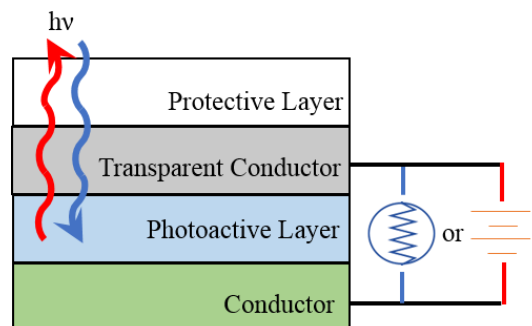


Figure 1.2. Schematic of a device containing a transparent conductor layer. Red (dark blue) elements depict a process emitting (absorbing) a photon typical of a TCO-containing device such as an LED (solar cell).

(greater than 3 eV), leading to over 80% transmittance of visible light and conductivities above 1000 S/cm.¹¹⁻¹⁵ The most commercially important subset of transparent conductors consists of those based on oxides, the TCOs. Tin-doped indium oxide (ITO) and indium zinc oxide (IZO) exhibit especially high conductivity, which has made them the most commonly used TCOs in high end electronics applications by far.^{11,15-17} Unfortunately, both of these materials have In as a major component. Indium is estimated to be 1/6th as abundant as gold, mostly located in China, and can only be found naturally as an impurity in other metal ores.¹⁵⁻¹⁷ These factors raise the materials costs for indium-based TCO products. Coupled with increasing demand due to the growth of the PV and FPD industries over the past few decades, these concerns have inspired a substantial research effort targeted at finding alternative TCOs with comparable performance but lower In contents.^{11-15,17-19}

The classic approach to this endeavor is a two-part process involving the identification of new insulating compound which shows desirable transparency, known as the host phase, and subsequently of effective dopants for that material.²⁰ Successful dopants are highly dependent on the host phase and have been identified from many areas of the periodic table including transition metals, rare earths, and main group elements.¹¹⁻²⁴ In contrast, the composition space explored for new host phases by the majority of these investigations is quite limited. Depicted in **Figure 1.3**, it is defined by a set of five binary post-transition metal oxides (vertices) and their combinations (edges and faces). Each of the fully oxidized post-transition metal cations has an $(n-1)d^{10} ns^0 np^0$ electron configuration in its outermost subshells. Transparency occurs

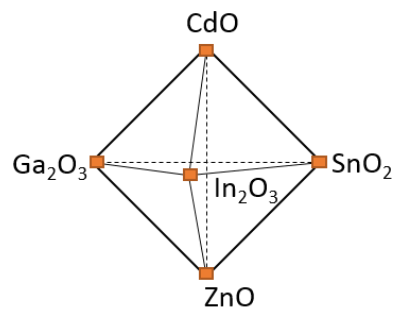


Figure 1.3. The typical phase space focused on by inorganic TCO research.¹¹

because the filled d-orbitals negate the possibility of any d-d electronic transitions which typically absorb visible light, and do not participate in bonding, resulting in wide band gaps (~ 3 eV) between the O-2p states which primarily compose the valence band maximum and metal s states in the conduction band minimum. The electron configuration similarly favors conductivity (σ), which is given by equation 1.1.

$$\sigma = ne\mu \quad (1.1)$$

where n is the carrier density, e is the carrier charge constant, and μ is the carrier mobility. The diffuse, empty s-orbitals offer an efficient conduction path for electrons, benefitting μ . Furthermore, the post-transition metal oxides are particularly susceptible to carrier-producing defects, which increase n , such as O vacancies in In_2O_3 or cation interstitials in ZnO. These effects result in relatively high values of σ without loss of transparency in both the pure and processed materials.²³ These characteristics make the post-transition metal oxides particularly attractive as TCO host phases. Thorough investigation of these oxides over the past several decades has produced a number of alternative TCOs, none of which have supplanted ITO in industrial use, and many of the possible phases within this system have already been explored.

Other post-transition metal oxides such as Al_2O_3 , SiO_2 , GeO_2 , and Sb_2O_5 are not included in the phase space depicted in **Figure 1.3**, despite having the same beneficial electron configuration. A key factor cited for this is the Lewis Acid Strength (L) of the associated cations, which is directly related to the charge and electronegativity of the ion, and inversely dependent on its size. Owing to higher charges and smaller radii, the neglected cations, such as Ge^{4+} , have much higher L values than typical TCO cations such as In^{3+} , Sn^{4+} , Ga^{3+} , or Zn^{2+} .^{14, 25} Ions with higher L values are thought to bind O more strongly, suppressing O vacancies and producing O interstitials.

This may harm conductivity, decreasing n by the eliminating carrier-producing defects or introducing electron-accepting ones, and impacting μ through introduction of new scattering centers.^{13,26,27} However, studies in which ITO was doped with SiO_2 and GeO_2 , have found that at low concentrations of either dopant σ is enhanced overall due to an increase in μ . This result has also been attributed to the high L of the dopants, which is thought to reduce scattering by screening charge away from the O 2p valence band, reducing its ability to act as a scattering center, or by suppressing scattering from oxygen vacancies.^{13,27-29} The effect of high L components on TCO properties therefore remains unclear, particularly as part of the host phase and not just dopants.

Some potential TCO host phases with Ge^{4+} components are known, demonstrating the ability of GeO_2 to expand the phase space used to design new TCOs. Notably, $\text{Zn}_{0.456}\text{In}_{1.084}\text{Ge}_{0.46}\text{O}_3$ (ZIGO) was reported as a previously unknown phase with a new, tetragonal fluorite-related structure.³⁰ This may be considered a structural transition caused by the replacement of Sn^{4+} with the stronger Lewis acid Ge^{4+} in the cubic, bixbyite TCO $\text{Zn}_{0.4}\text{In}_{1.2}\text{Sn}_{0.4}\text{O}_3$ (ZITO).³¹ Despite the complete substitution, ZIGO maintains transparency and σ comparable to In_2O_3 , the host compound of ITO. These results suggest that high L components may facilitate the formation of previously undiscovered phases without compromising transparency and conductivity. However, currently no effective dopants for ZIGO have been reported.

Two exploratory efforts were spawned from these observations. First, investigation of the M-In-Ge-O system began as an investigation of effective dopants in ZIGO. Second, new phases were sought out in the M-In-Sb-O to further to probe the capabilities of Sb_2O_5 to reveal previously unknown materials that could be investigated as new TCO hosts. Although neither resulted in the

discovery of new TCOs, they did result in the identification of new phases and insights detailed later in this work.

1.2.2: Heteroanionic Materials Synthesis

There is a large discrepancy between the ability of solid state chemists and materials scientists to manipulate the cations of a system versus its anions. This is reflected in a much larger prevalence of known heterocationic materials over heteroanionic ones.^{4,32} As the name suggests, heteroanionic phases are defined by the presence of two or more anions in their composition, each with distinct properties such as polarizability, electronegativity, ionic radius, and charge, which leads to a greater variety of possible bonding characteristics and local environments.³² These, in turn, may produce enhanced or even novel functionality compared to their single-anion precursors or analogues. This phenomenon has been observed in a wide variety of applications including water-splitting catalysts, phosphors, thermoelectrics, and battery cathodes among others.³²⁻⁴⁰ Oxyfluorides, or compounds containing both oxide and fluoride anions, are one set of these materials in which improved functionality has already been demonstrated. The layered molybdenum fluoro-bronze $\text{MoO}_{2.8}\text{F}_{0.2}$ exhibits an improvement in Mg capacity of nearly 80 mAh/g compared to the isostructural binary oxide $\alpha\text{-MoO}_3$.^{33,34} The introduction of fluorine is concurrent with reduction of the redox-active late transition metal in disordered rocksalt lithium-ion battery cathodes, leading to higher reversible capacities and lower oxygen loss.^{41,42} Fluoride doping in insulating WO_3 and Sr_2CuO_3 gives rise to superconductivity.^{35,36} Furthermore, metal oxyfluoride coordination complexes have been observed to play an important role in the non-centrosymmetry of some materials, which gives rise to the useful property of second-harmonic

generation.³⁷ There is a clear motivation for the identification of new oxyfluoride materials as well as safe and efficient methodologies for their production.

1.3: New Phase Classification

The newly discovered materials in this thesis can generally be grouped into three established crystalline structural materials families: 1) fluorite-related, 2) rutile-related, and 3) α - UO_3 related, each of which is the subject of a chapter. As such, a general introduction to each of these structure-types is presented here.

1.3.1: Anion-Deficient Fluorite-related phases

The anion-deficient fluorite (ADF) family of materials has been the subject of sustained research interest for decades. Fluorite, the aristotype of these phases, has one of the simplest structures of any inorganic ionic material. Its cation positions are arranged in a close-packed lattice with anion sites in every tetrahedral hole, resulting in the cubic cation coordination environment shown in **Figure 1.4a**. In ADF phases a fraction of these anions are missing, while the cation lattice remains at most slightly distorted. If these vacancies are ordered, the symmetry of the structure is reduced and at least some of the 8-coordinate cation sites of fluorite are transformed to lower coordination environments. **Figure 1.4(b,c,d)** depicts some examples of these commonly observed in ADF phases.

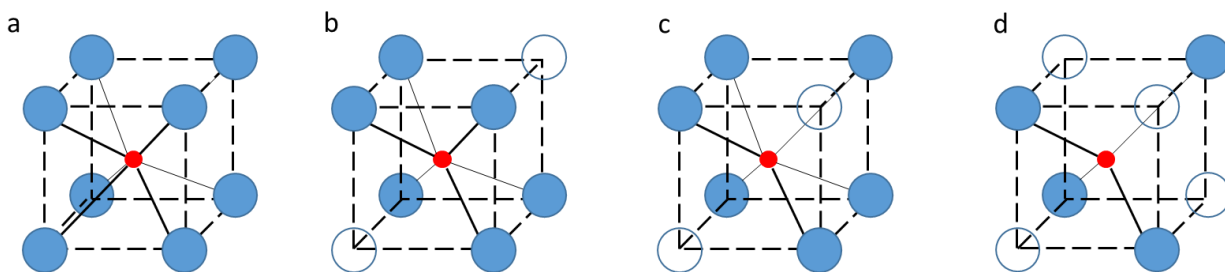


Figure 1.4. Common coordination polyhedra in fluorite-related materials. a) Cubic-coordination with all tetrahedral holes filled. b) Octahedral coordination with 2 out of 8 tetrahedral holes empty, observed on the b-site in bixbyite structures. c) Alternative 6-coordinate site formed by removing a different pair of anions from the cubic environment. Observed on the d-site in bixbyite structures. d) Tetrahedral coordination made by emptying half the tetrahedral holes around the cation.

In combination with possible cation disorder and lattice relaxation, this variety of coordination environments gives rise to the large number of derived structures and interesting properties that belong to the ADF family.⁴³ In the pyrochlore structure, 1/8 of the anion positions are vacant and ordered in such a way that 2/8 anions are missing from every other cation polyhedron. This produces an equal number of 8-coordinate (**Figure 1.4a**) and 6-coordinate (**Figure 1.4(b,c)**) sites. The resulting cation network geometrically frustrates long-range magnetic ordering, prompting many investigations into interesting forms of magnetism such as spin glasses and spin ices.^{44,45} With 1/4 of anion positions vacant, fluorite may become the bixbyite structure which exhibits two independent 6-coordinate cation sites. Tin-doped indium oxide, which has the bixbyite structure, is one of the most commercially important transparent conducting oxides.⁴⁶ ADF phases may also retain the symmetry and average coordination environments of fluorite if their missing anions are disordered among all anion sites. Yttria-stabilized zirconia ($Y_xZr_{1-x}O_{2-x/2}$) and oxygen-deficient ceria (CeO_{2-x}), which exhibit this defect fluorite structure, have been rigorously investigated and employed as solid-electrolytes in solid-oxide fuel cells for their oxygen mobility.^{47,48} The structure of these ADF materials are shown in **Figure 1.5**, along with that of the parent phase fluorite for comparison. Given the complexity possible in ADF phases, many more

permutations exist, and several already discovered ones remain to be investigated in detail.

Chapter 3 describes the discovery of several new ADF phases.

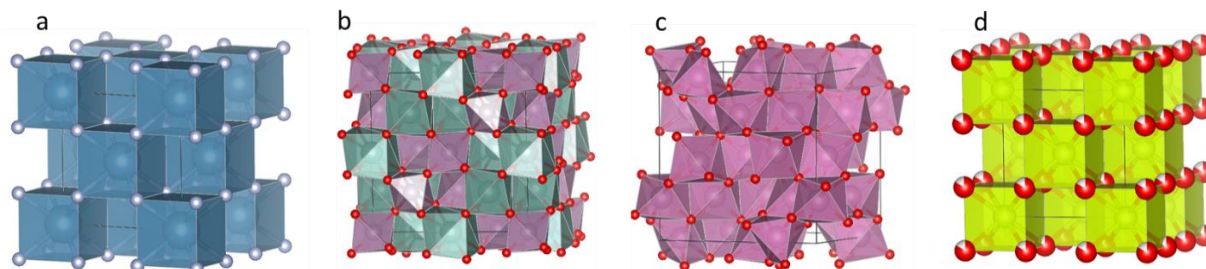


Figure 1.5. Several fluorite related crystal structures and representative compounds. a) Fluorite (CaF_2) b) Pyrochlore ($\text{Y}_2\text{Mo}_2\text{O}_7$) c) Bixbyite (In_2O_3) d) Defect fluorite ($\text{CeO}_{1.66}$). Anion sites are enlarged to better depict the random distribution of vacancies in the form of partial occupancy.

1.3.2: Rutile-related phases

Like fluorite, the rutile structure is a classic, simple ionic structure and one of the first identified by crystallographers.⁴⁹ In it, anions are arranged in staggered, close-packed layers as depicted in **Figure 1.6a**. Between each pair of layers, the cations sit in parallel rows of octahedral sites that alternate with empty rows, resulting in a total filling of half of the octahedral holes and an overall MX_2 stoichiometry. Depicting this structure with a focus on cation-centered polyhedral (**Figure 1.6b**) transforms these rows into chains of edge-sharing octahedra. These chains are not only staggered within the plane defined by adjacent anion layers, but also in the orthogonal direction of layer stacking, giving each one corner-sharing connectivity with the four others diagonally above and below it. This creates a 3-dimensional checkerboard pattern in the plane perpendicular to the chain direction, as shown in **Figure 1.6c**.

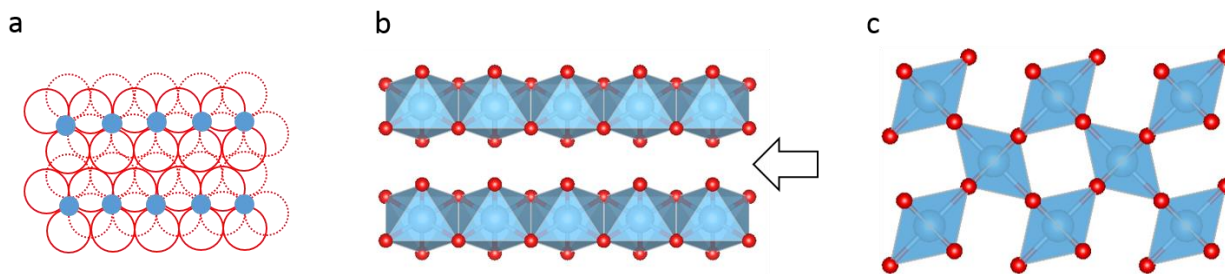


Figure 1.6. The rutile structure. a) Staggered close-packed layers of anions indicated by large, hollow red circles. Blue circles are cation atoms sitting in octahedral holes defined by 3 anions below (solid) and 3 anions above (dotted) with 180° rotation around the cation position. b) The same view as in a), but redrawn to emphasize the octahedral coordination of the cations (blue spheres) by the anions (red spheres). c) View of the rutile structure down the direction indicated by the arrow in b).

The rutile-related family of materials is a diverse set of phases with structures that is broadly defined by the presence of the three key structural motifs identified above: 1) chains composed of edge-sharing octahedra, 2) connections between independent chains occurring exclusively via corner-sharing, and 3) an MX_2 framework stoichiometry. They differ, however, in the arrangement or width of their chains and the presence or lack of ions in the channels between chains, as well as their chemical composition.^{43,49} The variety that such factors produce in these phases has long made them of great interest to researchers as catalysts, photoanodes, battery materials, ion conductors, and for capture of contaminants such as radioactive isotopes.^{43, 49-60} The structures of ramsdellite, CaFe_2O_4 , and hollandite are presented in **Figure 1.7** as several examples of the wide-ranging structures which are encompassed in this family beyond rutile.^{43,49-52} The first is directly analogous to rutile but with wider chains, and the other two demonstrate different possible arrangements of ramsdellite-like chains to accommodate ions in the tunnels. In this work, a newly-discovered rutile-related structure and material are discussed in **Chapter 4**.

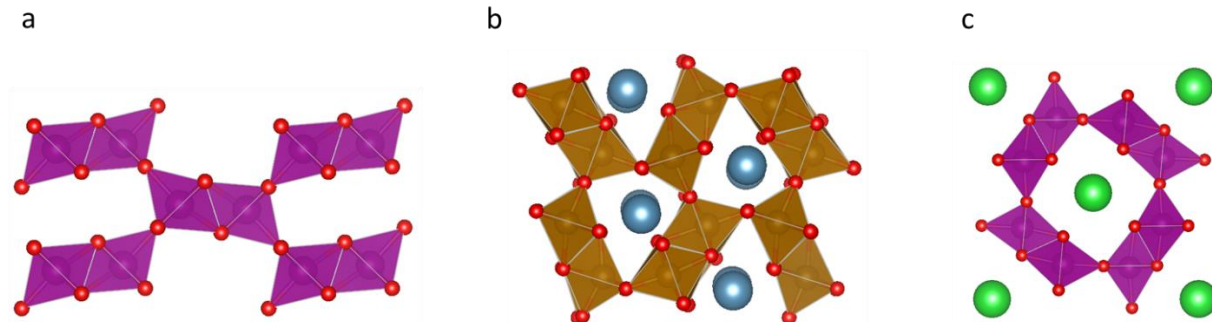


Figure 1.7. Crystal structures of selected rutile-related phases. a) ramsdellite- MnO_2 b) Post-spinel CaFe_2O_4 c) Hollandite $\text{Ba}_2\text{Mn}_8\text{O}_{16}$.⁶¹⁻⁶³

1.3.3: Anion-deficient $\alpha\text{-UO}_3$ related phases

Anion-deficient $\alpha\text{-UO}_3$ (ADU) phases are similar to ADF ones in that they are derived by removing anions in a specific manner from the parent structure. However, despite also being a binary compound, the structure of $\alpha\text{-UO}_3$, depicted in **Figure 1.8**, is more complicated than fluorite. It consists of U^{6+} ions arranged in layered pseudo-hexagonal nets making up that are stacked in an eclipsed alignment. Each cation is at the center of a hexagonal bipyramid with O^{2-} ions on the vertices. Equatorial O^{2-} ions lie in the hexagonal plane with trigonal planar coordination, whereas apical O^{2-} lie halfway between adjacent hexagonal layers in linear coordination. Since anion vacancies occur almost exclusively on the equatorial sites, vacancy ordering can only occur within the pseudo-hexagonal layers. Thus, the structural motifs common to all ADU phases are the pseudo-hexagonal layers of cations and the linearly coordinated anions between them, guaranteeing some sort of bipyramidal cation coordination. **Figure 1.8b** depicts the structure of $\alpha\text{-U}_3\text{O}_8$ and demonstrates that it is a supercell of the parent structure, indicated by the black dotted lines, where one axis is tripled. This arises from the stoichiometry difference between the two compositions. Since one O is lost for every three U atoms, and there are two U atoms per unit cell of $\alpha\text{-UO}_3$, two vacancies occur per every three unit cells. The larger supercells of $\text{Zr}_7\text{O}_9\text{F}_{10}$ (7x) and $\text{Ta}_{22}\text{W}_4\text{O}_6$ (13x), depicted in **Figures 1.8c,d** are formed in a very similar process, except

with a different distribution of vacancies.⁶⁴⁻⁶⁶ Notably, despite different anion to cation ratios all three phases exhibit primarily 7-coordinate pentagonal bipyramids, with the latter two also presenting a few 6-coordinate sites through relaxation of the equatorial O atoms. Thus, unlike the ADF phases in **Figure 1.5**, variety in the ADU family does not come from a multitude of cation coordination environments, but rather through modulation within the hexagonal layers. In fact, because modulation may be incommensurate with the underlying structure and flexibility in the planar anion sites may be high, solving the structures of ADU phases is challenging and sometimes cannot be done exactly.^{64,66} A newly discovered ADU material is discussed in **Chapter 5**.

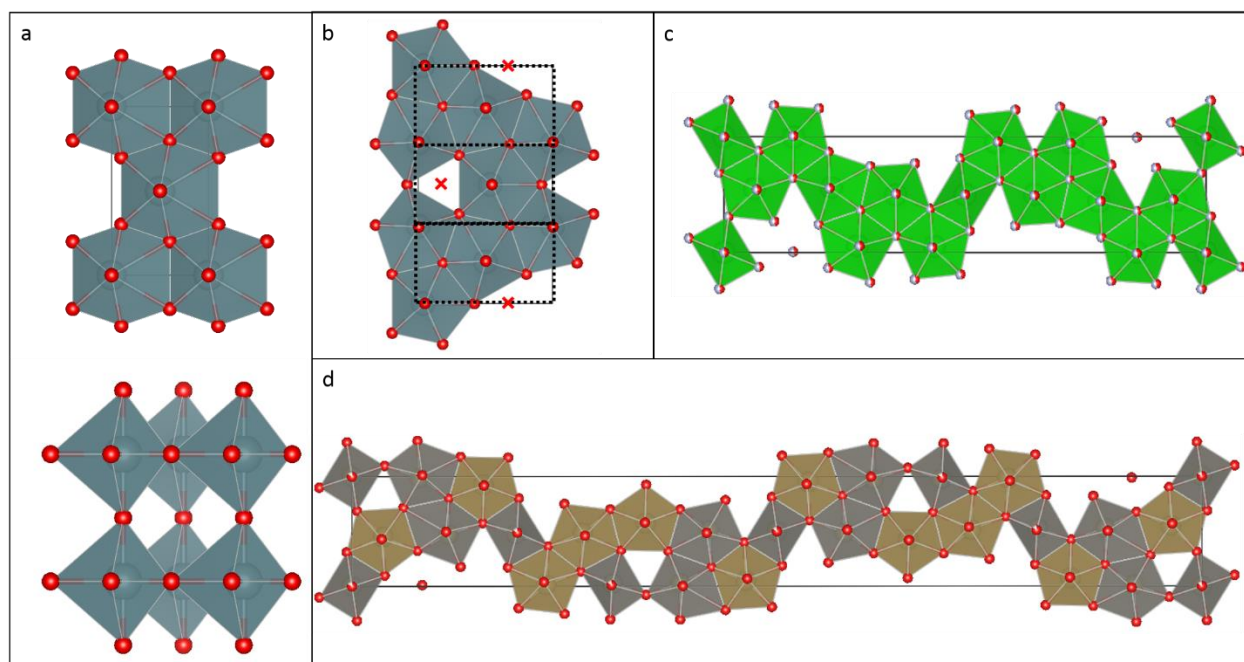


Figure 1.8. The crystal structures of anion deficient materials $\alpha\text{-UO}_3$. a) $\alpha\text{-UO}_3$ viewed perpendicular (top) and parallel (bottom) to the pseudo-hexagonal layers. b) $\alpha\text{-U}_3\text{O}_8$ with the unit cell of $\alpha\text{-UO}_3$ indicated by black dashed rectangles. Anion vacancies are marked with a red x. c) $\text{Zr}_7\text{O}_9\text{F}_{10}$. d) $\text{Ta}_{22}\text{W}_4\text{O}_{67}$.

This thesis describes experiments led and primarily performed by Steven Flynn. Where appropriate, data collected and/or analyzed by Gabriela Gonzalez-Aviles, Sheel Sanghvi, Matt Nisbett, Ella Wang, Chi Zhang, Jiahong Shen, or Kent Griffiths are included.

CHAPTER 2: MATERIALS AND METHODS

The content in this chapter serves as a basic introduction to the techniques and instrumentation employed in the body of this work. A brief description of the purpose, mechanism, advantages, and challenges of each method will be provided with references. The specific protocols by which each of these methods were employed during the course of the work reported in this thesis can be found in the experimental section of each respective chapter.

2.1: Synthesis

2.1.1: Solid-State Synthesis

Solid-state synthesis broadly refers to chemical reactions in which one or more solid reagents are used to create a different solid product. Typically, both the reactants and product are polycrystalline or amorphous powders. This type of chemistry is far removed from the more conventional liquid-phase reactions and has its own set of inherent challenges and protocols. Central to this distinction is that, in solids, the constituent components of the material are trapped within a lattice or rigid matrix. As such, the atoms, ions, or molecules of each reactant are unable to move and react freely except at very small scales by hopping to local unoccupied sites. In consequence, solid-state reactions can only occur at the interface of two reagents where components of one are directly in contact with the other, and are rate-limited by the speed of solid-state diffusion which is prohibitively slow at room temperature, on the order of $10^{-12} \text{ cm}^2\text{s}^{-1}$.¹ To resolve this issue, solid-state chemists traditionally employ a four-part strategy involving grinding, mixing, pressing, and heating.

Grinding reagents into as fine a powder as possible increases the surface area of reactant particles whereas thorough mixing ensures contact between particles of different reagents and increases the homogeneity of the mixture. Together, this minimizes the distance that any given

component needs to travel in order to react, decreasing the reaction time. These steps are commonly performed simultaneously by hand with a mortar and pestle, but can also be performed mechanically by a ball mill. The latter approach rapidly rotates small spheres of hard material such as ZrO_2 or WC, referred to as media, in a sealed cup to grind and mix the powder.^{2,3} Ball milling typically achieves smaller particle sizes and greater homogenization than an equivalent amount of hand grinding, but runs the risk of contamination by the media material and requires more material owing to losses from powder coating the balls and cup. Both hand grinding and ball mills are employed in this work. In the former case, acetone is commonly added to the mixture to form a paste which assists in homogenizing and helps prevent ejection of material from the mortar. As a volatile solvent, the acetone evaporates from the mixture during grinding and therefore has no unintended effect on the reaction. Once thoroughly ground and homogenized, reactant mixtures are commonly compressed into a cylindrical pellet using uniaxial pressure. This increases the amount of reactant particles in direct contact with their neighbors by increasing packing density.

Finally, the pellet is heated to initiate the reaction. A schematic heating profile is depicted in **Figure 2.1** The heating and cooling rates, dwell temperature, length of reaction, and even

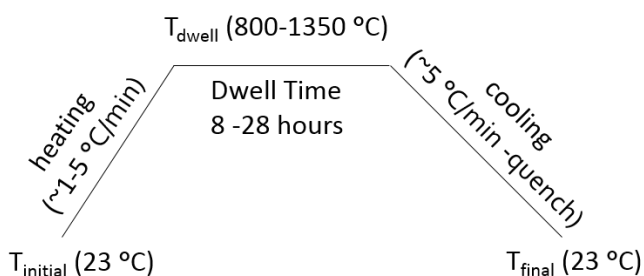


Figure 2.1. Schematic heating profile depicting typical values employed in this work for each step. Quench cooling refers to instantly removing the sample from the furnace to room, allowing it cool as quickly as possible.

number of cycles all affect the outcome of the reaction and often must be optimized through repeated syntheses in order to obtain a desired result. Sufficiently high temperatures must be used such that solid-state diffusion occurs on reasonably

fast time scales, hours to days. As indicated in **Figure 2.1** for the metal oxide precursors used in

this work, reaction temperatures can exceed 1300 °C. As such, these reactions mainly fall into the regime of thermodynamic control, meaning the products obtained represent the lowest energy combination of all possible compositions and structures. Thus the potential output of traditional solid-state synthesis is limited relative to liquid-phase organic chemistry, which can regularly obtain metastable products through the use of selective reactions.^{1,4}

The high temperatures of solid-state synthesis limit the possible choices for reaction vessels, as the container material must remain structurally sound and chemically inert with respect to the reagents as the reaction occurs. Common choices include silica, alumina, boron nitride, graphite, platinum, and other metals depending on the reaction temperature, atmosphere, and reagents. In this work, silica, alumina, and platinum vessels like those shown in **Figure 2.2** are used. Silica tubes can be shaped through heating with a torch, making them a convenient option when an air-tight seal is needed, possibly because a reaction needs to occur in vacuum or one of

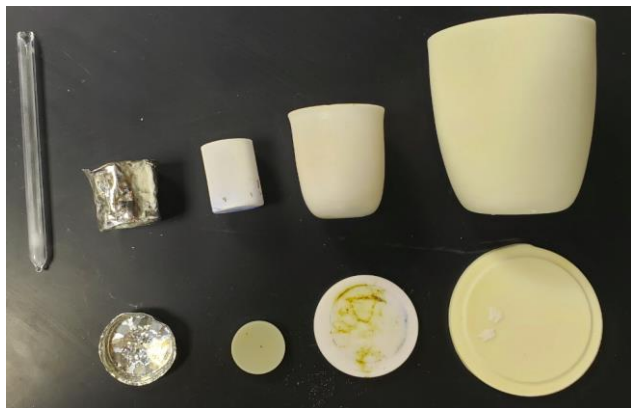


Figure 2.2. Common reaction vessels used in solid-state synthesis. From left: An opened fused silica tube, a platinum crucible lid, and three alumina crucibles with lids which can be nested.

the precursors is very volatile. However, its plasticity at high-temperatures make silica a poor option above 1100 °C, and it is reactive to a number of reagents employed here including alkali and fluoride salts. Alumina crucibles are stable to very high temperatures, and the relative abundance of Al_2O_3 means they are

readily available in multiple sizes allowing for nesting to combat precursor volatilization. In cases where the reagent oxides are reactive with alumina at reaction temperatures, platinum crucibles provide an effective, inert alternative.

2.1.2: Molten Flux Crystal Growth

High-temperature, direct-combination synthesis is a reliable and effective strategy for getting around the inherent obstacles to solid-state diffusion, but it does so, as described above, by effectively promoting the occurrence of many independent, local reactions in parallel to speed up the overall interaction of reagents. As a result, the product is frequently polycrystalline, i.e. consisting of large number of crystallites that vary in orientation of their crystalline lattices. For example, in a material made up of planes stacked on top of each other, the absolute direction of layer stacking of one grain may be perpendicular to that of another, as depicted in **Figure 2.3a**. However, for analytical techniques such as single crystal X-ray diffraction (SCXRD), or in order to measure the dependence of a property on crystallographic orientation, the desired form of the material is a single crystal in which there are no grain boundaries, as in **Figure 2.3b**. Generally, special techniques must be used for single crystal growth in order to keep the genesis of new

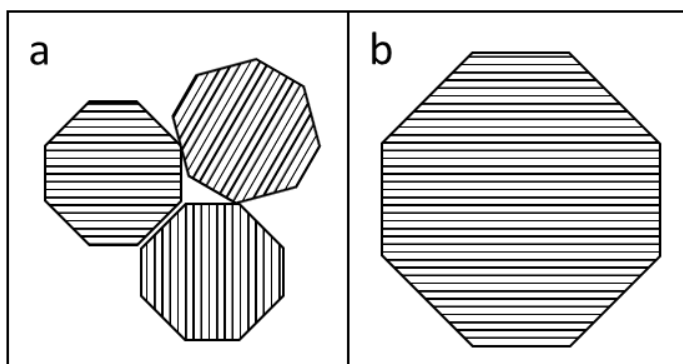


Figure 2.3. A cartoon depiction of a) polycrystalline and b) single-crystalline sample. The former exhibits multiple crystallites with different orientations such that the lattice planes are not aligned. Material properties measured on a polycrystalline sample will average the theoretical values from all of these orientations and will include an additional contribution from the boundaries and voids between grains.

crystallites of the target material, known as nucleation, to a minimum while favoring growth of existing crystallites. In this work, the molten flux crystal growth method is employed. It involves dissolving the target phase or its components in a relatively low-melting solid, termed the “flux agent”, and then

very gradually cooling the solution to decrease the solubility of the target phase leading to controlled precipitation.^{5,6} Slowing down crystallization gives the precipitating particles sufficient

time to adopt their lowest energy configuration on the surface of an already nucleated crystal rather than becoming kinetically trapped in a new crystallite. Subsequently, the flux and crystals can be separated by centrifuging the former away while it is still molten. Alternatively, after the flux has cooled, the crystals can be removed manually if they are large enough, or they can be washed with a carefully selected solvent that preferentially dissolves the flux agent. The stages of this process are depicted below in **Figure 2.4**.

Several requirements must be met when selecting an appropriate flux agent: 1) the target material must dissolve in the flux, and 2) the flux must not react with the target material or its components. Additionally, if the target phase is being synthesized in-situ during the crystal growth, the flux agent must be molten at the temperature at which its formation is thermodynamically favored. Typically, the first condition can be met by choosing flux agents that exhibit a similar degree of covalency in bonding as the target material. The second can be satisfied by selecting a flux agent made up of components which differ from those in the target phase with respect to size or valence.⁵ Both criteria are benefitted when there is a common cation or anion in both the target and the flux agent. For these reasons metal salts with large halide or polyatomic anions are popular flux materials for oxides which are commonly ionic in character and exhibit relatively small coordination environments that are not suitable for larger anions.

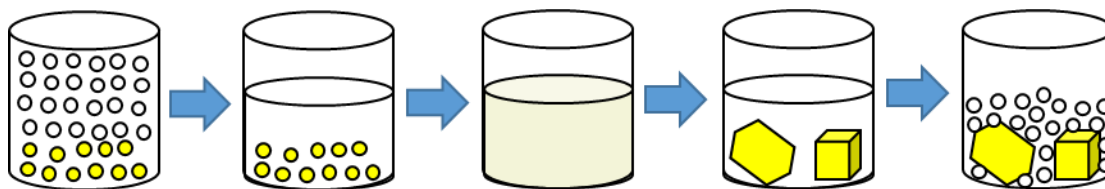


Figure 2.4. The stages of a flux crystal growth. (From left) i) Solid powder of target material or precursor mixture are mixed with an excess of solid flux agent. ii) At a relatively low temperature, the flux material melts. iii) At the dwell temperature, target material dissolves into liquid flux. iv) Upon slow cooling, the solubility of the target material in the flux gradually decreases, and controlled precipitation occurs. v) After most of the target material has crystallized, the mixture is rapidly cooled and the flux solidifies, allowing it to be separated from the crystals.

2.2: Structural Characterization

A crystalline phase is uniquely defined as a specific composition arranged in a specific structure. As such, determination of these qualities is a crucial step in the process of materials synthesis and discovery. In this section, the various techniques and strategies employed in order to determine structure and composition in this work are briefly reviewed.

2.2.1: Diffraction

Diffraction is one of the most powerful tools available to solid state chemists and crystallographers for the structural determination of crystalline materials.⁷⁻⁹ Crystals are defined by a regular arrangement of atoms, ions, or molecules repeating semi-indefinitely in three dimensions. This periodic structure acts as a diffraction grating when interacting with radiation with a wavelength comparable to the distance between crystallographic planes, $\sim 1 \text{ \AA}$. In the electromagnetic spectrum, this corresponds to X-rays.⁸ **Figure 2.5** depicts a simple example of this, in which X-ray beams are scattered off a simple crystal consisting of rows of atoms. As shown in the figure, two beams which scatter off adjacent, parallel layers will exhibit a total path length difference that is a function of both the interplanar spacing and the angle of incidence.⁷⁻⁹ Assuming the two beams are emitted from the source in-phase, if the difference in path length is equal to an integer multiple of the wavelength, the scattered beams will also be in-phase. This condition at which the scattered beams will constructively interfere, known as *Bragg's Law*, is given by the equation:

$$n \lambda = 2 d \sin(\theta)$$

where n is an integer, λ is the wavelength of the incident radiation, d is the interplanar spacing, and θ is the incident angle.^{8,9} Thus, with monochromated light every given set of planes

in the crystal will produce a bright spot of reflected intensity at the specific set of angles which satisfy Bragg's law. By rotating the crystal through a large range of θ values in many different orientations, a three-dimensional pattern of spots is obtained which can be used to solve the structure. When the sample is a polycrystalline powder instead of a single crystal, the presence of many crystallites produces a statistical representation of all orientations at once, except in cases where a few orientations are preferred over others. As a result, the spots from the diffraction pattern become spread out into rings of intensity, which are often integrated to produce a one-dimensional pattern of intensity as a function of the diffraction angle, 2θ . These powder patterns are characteristic of each phase and can be used as a fingerprint to identify any known products of solid-state reactions by comparison with a database of reported materials. Solving the crystal structure from scratch using a powder pattern is also possible, but very high quality data is required to account for complicating effects arising from a distribution of crystallite sizes, strains, and possibly even composition.

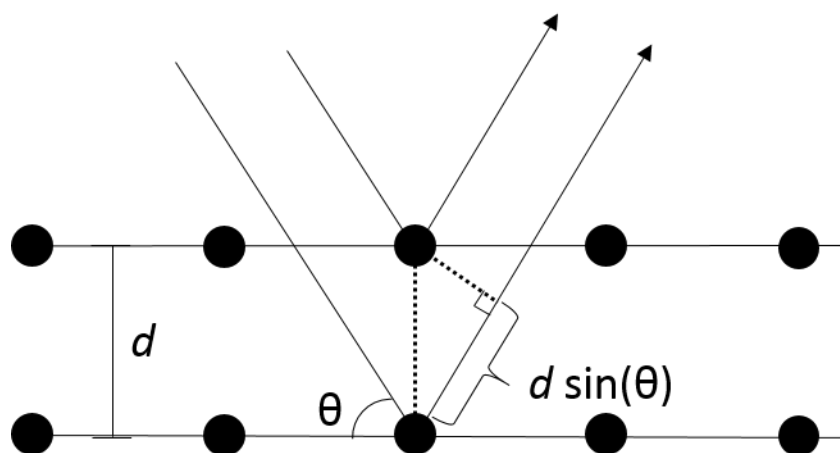


Figure 2.4. Diffraction in an idealized crystal demonstrating the geometry of Bragg's Law. Incident radiation (arrows) scatter off identical atoms in parallel crystalline planes. The difference in path length for the two rays, $2d \sin\theta$ must be an integer multiple of the radiation wavelength in order for the scattered beams to constructively interfere.^{8,9}

The quality of X-ray diffraction (XRD) data is dependent on a variety of factors, including the θ range used and the speed of collection, but one of the most important ones is the radiation

source. Typical lab diffractometers use the characteristic X-rays of metal targets produced by core electron transitions as sources. Common examples are Cu ($\lambda = 1.54 \text{ \AA}$) or Mo ($\lambda = 0.709 \text{ \AA}$) sources, although other metals such as Co ($\lambda = 1.79 \text{ \AA}$) and Ag ($\lambda = 0.56 \text{ \AA}$) are also used under special circumstances.¹⁰ While shorter wavelengths offer higher resolution scans, they also scatter less effectively so a higher X-ray flux is needed to maintain a good signal-to-noise ratio. This is not a problem for a synchrotron source, which uses the acceleration of electrons in a particle accelerator to generate extremely high X-ray fluxes with tunable wavelengths. However, even though synchrotrons offer the highest quality XRD data, they can only be used at specialized facilities and are often in high demand, making it relatively difficult to use them in an experiment.

Furthermore, X-rays are not suitable for all diffraction needs, so even synchrotron data is not necessarily sufficient in some cases. X-rays interact with the electron cloud of an atom or ion, and therefore scatter most effectively off heavier atoms. As a result structures refined by X-rays may have difficulty assigning light elements like H.⁷ Likewise, it is difficult for X-rays to differentiate between ions with that are adjacent on the periodic table, such as Cu^{2+} and Zn^{2+} . Fortunately, diffraction in crystals is not only limited to electromagnetic radiation. According to quantum mechanics, subatomic particles exhibit wave-like properties with a wavelength given by $\lambda = h(mv)^{-1}$. As such, with sufficiently high kinetic energy both neutrons and electrons exhibit wavelengths suitable for diffraction.^{7,11} Neutrons are not charged and therefore do not interact appreciably with the electron cloud of an atom or ion. They are primarily scattered by nuclei, and as a result do not share the same dependence on atomic number of X-rays and can be used to determine H atom positions and to differentiate chemically adjacent species. Furthermore the spin of neutrons allows them to probe long range magnetic ordering in addition to the crystal structure

of a material.⁷ Electrons are readily accelerated to high speeds in an electron microscope (EM), achieving much smaller wavelengths than X-rays or neutrons. Additionally, they are more strongly scattered than either neutrons or X-rays. Together, these factors make electrons a better probe of subtle structural features like modulation or defects.¹¹

2.2.2: Rietveld Refinement

As mentioned above, in powder diffraction the data from many different crystallites is compiled together at any given diffraction angle. However, this information is not lost, it is simply more difficult to process. Rietveld refinement is a least squares fitting technique used to maximize the crystallographic information obtained from a powder diffraction pattern.^{12,13} It takes a known crystal structure model as input and uses it along with provided instrumental parameters to calculate a theoretical powder pattern. The result is then compared to the experimental data in question. The refinement then iteratively and systematically alters aspects of the model selected by the user in order to minimize the difference between the two patterns. The set of refineable variables encompass all aspects of the crystal structure, including unit cell parameters, atomic position, atomic occupancy factors, thermal parameters, crystallite size and strain, as well as non-crystallographic parameters including the background and instrumental parameters.¹²⁻¹⁴ Crystal structures are most often determined using single-crystal diffraction, but a single crystal generally represents only a very small portion of the reactant mixture used in the crystal growth attempt. Grinding the rest of the product into a powder and then performing a refining the single crystal solution against the powder pattern is a common and convenient method to show that the analyzed crystal selected is representative of the bulk product. Additionally, some phases are prohibitively difficult to crystallize for a variety of reasons including incongruent melting points, volatile

components, poor solubility in available fluxes and more. In these cases, it is sometimes possible to identify a similar powder pattern in a phase that is compositionally or stoichiometrically related to the unknown one. If so, Rietveld refinement starting with a modified version of the analogous model offers an alternative method to obtain structure information for the unknown phase.

2.2.3: Bond Valence Theory

Bond valence (BV) theory relates the length of a given bond to the amount of charge “shared” between the bonding species.¹⁵ It postulates that for a species to be stable in a given coordination environment, its nominal valence should be equal to the amount of charge contributed to it by all of its bonding interactions. The formula for the sum of all bond valences (BVS) supplied to a species is:

$$BVS = \sum_i e^{\frac{R_o - R_i}{B}}$$

In this equation R_i is the length of i^{th} bond to the reference species and R_o and B are empirically determined constants, the latter determined by the identity and oxidation states of the two species of the bond.¹⁵ The B parameter typically takes a fixed value of 0.37, however it has been claimed that this may be an overly simplistic of a treatment of the parameter.^{15,16} Although it is an empirical theory, it has been successfully applied for decades in describing the site preference and stability of atoms and ions in a crystal structure. In this work, BV theory is used to validate the proposed cation site preferences. The BV sums for all potential occupants are calculated and those with sufficiently close values to their oxidation state are considered candidates for occupancy on the site in question. In cases where the occupying species for a site is already known, BV theory can evaluate the stability of a given site by analyzing how under or over-bonded a species is in it.

2.2.4: Solid-State Nuclear Magnetic Resonance

Nuclear magnetic resonance (NMR) is a spectroscopic technique that uses radio waves to probe the local environments of isotopes of a wide variety of elements. In an external magnetic field, the nuclear spin states of isotopes with a nonzero spin will undergo Zeeman splitting into high and low energy states depending on whether they are aligned parallel or anti-parallel with the field. For an isolated nuclei, the energy difference between these alignments is given by:

$$\Delta E = \left| \frac{h\gamma B_o}{2\pi} \right|$$

Where h is Planck's constant, B_o is the applied field strength, and γ is the gyromagnetic ratio specific to each type of nuclei.¹⁷ At the field strengths used in modern devices, these energies correspond with those of radio waves, which can therefore be used to excite nuclei. However, interactions between these nuclei, and the electron, and nuclei of neighboring species cause perturbations in the splitting energy. This effect, measured relative to a standard nuclei of the desired isotope, is known as the chemical shift.¹⁷ Thus, the chemical shift of a given nucleus is a very sensitive indicator of local environment which can be directly probed by an NMR experiment.

Solid-state NMR (SSNMR) refers to the special case of this technique concerned with its application to crystalline and amorphous solid phases, which creates additional obstacles to measurements. For example, for nuclei fixed in a lattice or matrix, a given local environment may exhibit a large range in chemical shifts depending on the orientation of the solid relative the magnetic field. When many orientations are present, as in a polycrystalline powder, a very broad, low signal-to-noise spectrum may be produced that is difficult to interpret. Fortunately, NMR specialists have determined that rapidly spinning a sample around an axis at an angle 54.74° relative to the magnetic field direction can average out this effect and produce meaningful

spectra.^{17,18} Discussion of further challenges of SSNMR and the strategies to resolve them their is beyond the scope of this text. Nevertheless, when properly executed, SSNMR is a powerful structural tool that provides detailed information about the symmetry and bonding environments for specific elements and isotopes of interest.

2.2.5: Elemental Analysis

Often it is desirable to independently verify the elemental composition of a solid material, particularly if it is a new phase. Deviations from the intended or nominal stoichiometry are possible owing to measurement errors, poor homogenization, selective volatility losses during reaction and more. Furthermore, even minor deviations from a perfectly stoichiometric composition can have major effects on materials properties such as conductivity or optical properties.¹⁹⁻²¹ A variety of techniques exist for elemental analysis such as inductively-coupled plasma optical emission spectroscopy (ICP-OES), energy dispersive X-ray spectroscopy (EDX), X-ray Photoelectron Spectroscopy, X-ray fluorescence, and more. The first two are used in this work.

ICP-OES is a common technique for measuring the concentrations of typically cationic species in a material with very high sensitivity. It takes advantage of the fact that the energy levels available to electrons are unique to each element, resulting in characteristic atomic emission spectra during relaxation from an excited state.²² ICP-OES samples are first dissolved, typically in acid, and then sprayed into a plasma where their atomic components are ionized and excited. Monochromators are used to carefully measure the intensity of the light emitted at frequencies characteristic of the expected species. This is then converted into a concentration value using a calibration curve interpolated from a carefully prepared set of standards spanning the expected concentration. While ICP-OES is a powerful technique, it has several important downsides. It is

destructive and cannot be used for a sample that cannot be dissolved or atomized. It also cannot be used to directly measure atmosphere or solvent abundant species like H, O, and N.²² Finally, it must be used on phase pure samples, as dissolved secondary phases skew the results.

EDX is an alternative method of elemental analysis that may be performed in an electron microscope. Like ICP-OES, EDX makes use of the characteristic emissions caused by electron relaxation from an excited state. However, in the former case these transitions occur in the outermost electron energy levels of an atom or ion, resulting in visible light or UV light emissions. In contrast, EDX uses a high energy electron beam to excite core electrons, and the subsequent relaxation releases characteristic X-rays.²³ This technique is non-destructive and, because the signal comes from a highly focused electron beam, the X-rays of different components can be spatially resolved. This allows for identification of inhomogeneity or secondary phases, eliminating the need for a phase pure sample. In a transmission electron microscope, EDX can be carried out alongside diffraction to ensure that the particle being measured is the intended phase. It should be noted that the detection limits for EDX are much higher (~ 1%) than ICP-OES and measured compositions have very large uncertainties unless calibrated with well-characterized standards. Furthermore, it cannot detect very light elements (up to Na, depending on the detector used).²³ For these reasons, EDX is typically used more as a qualitative probe of composition, rather than a quantitative one, although carefully obtained quantitative EDX compositions are still common as approximations when other methods cannot be used. In this work it is employed to confirm the successful incorporation of dopants or substitutes that were present in very low quantities in the initial reaction mixture, analyze the homogeneity of samples, and provide an approximate composition in materials that were unable to be dissolved for ICP.

2.3: Property Characterization

The newly discovered phase always brings with it the potential to expand basic knowledge or be used in an application. As such, characterizing the most likely properties of interest for a new phase is a key part of materials discovery, whether targeted or exploratory. Many specialized techniques and instruments have been developed to probe specific electronic, optical, thermal, or physical properties. In this section, the techniques employed in this work and the properties they measure are briefly overviewed.

2.3.1: Diffuse Reflectance

Diffuse reflectance is a technique used to investigate the optical and electronic properties of an opaque material. As shown in **Figure 2.5a**, this type of experiment involves shining light of a fixed wavelength and known intensity on a well-sintered pellet at one end of a sphere of highly reflective material which preserves the reflected signal until it is captured by a photodetector. All the reflected light is collected to determine what percentage of the initial signal was reflected as a function of wavelength, as shown in **Figure 2.5b**. For particularly smooth samples there may be a component of specular reflectance, a physical process, which must be removed from the total signal. The fraction of light that becomes diffuse reflectance value is related to the intrinsic absorbance of the material by the Kubelka-Munk transformation.²⁴ It is given by the equation:

$$F(R_{\infty}) = \frac{K}{S} = \frac{(1 - R_{\infty})^2}{2R_{\infty}}$$

where R_{∞} is the reflectance of a sample of infinite thickness, K is the absorption coefficient, and S is the scattering coefficient.²⁴ Since S depends on the factors such as the grain packing and morphology, it is sample dependent and therefore time consuming and exacting to determine precisely.²⁵ As such, the absolute absorbance indicated by K is also difficult to know exactly.

However, because S is relatively constant as a function of wavelength in a solid, $F(R_\infty)$ should be approximately proportional to K , making it a relative measure of absorbance, referred to as pseudoabsorbance. **Figure 2.5c** depicts a spectrum produced by this equation. The most important use of this data is determining the band gap of a material and whether it is direct or indirect. The band gap is a central feature of the electronic structure of a material, and it is intimately related to conductivity, transparency, dopability, and more. A plot of $F(R_\infty)^n$ is expected to be linear at the band edge for $n = 2$ for the former case, and $n = 1/2$ for the latter.²⁶ Linear extrapolation to a baseline or the x-axis gives the band gap.

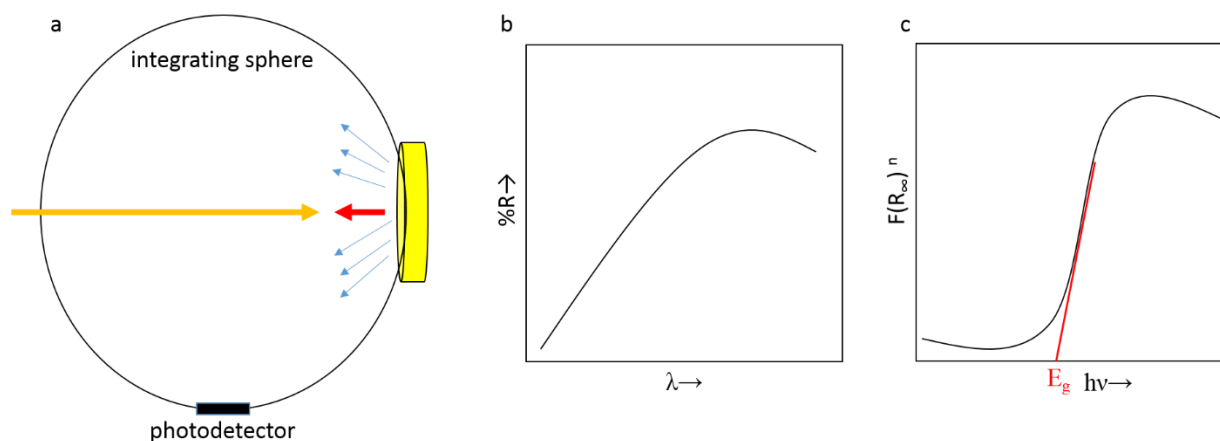


Figure 2.5. Stages of a diffuse reflectance experiment for determining the band gap of a material. a) Diffuse reflectance is collected in a UV/Vis spectrophotometer. Incident light (orange arrow) is shone on a sintered pellet (yellow cylinder) and reflected as diffuse (blue arrows) and specular (red arrow) reflectance. b) A schematic plot of reflectance versus wavelength produced by the collection in (a). c) Schematic pseudoabsorbance derived from the Kubelka-Munk transformation with a sample band gap determination via linear extrapolation.

2.3.2: Conductivity Measurements

Electronic conductivity is a key property for many important classes of materials including superconductors, TCOs, thermoelectrics, solid electrolytes and more. In this work, two methods are used to investigate the electrical conductivity of new materials. In the first method, DC four-point probe, four electrodes arranged in an evenly-spaced line are pressed against the surface of a sample, typically a sintered pellet. A known current (I) is applied across the outer two probes and

the resulting potential (V) is detected by the inner two probes.²⁷ Ohm's law is then used calculate the sheet resistance:

$$R_s = \frac{V}{I}$$

Various corrections depending on the sample geometry and form (thin film or sintered pellet) may then be applied to convert the extrinsic sheet resistance measurement into an intrinsic resistivity value. In the simplest case, where the sample is effectively infinitely long and thin relative to the probe spacing, this only involves multiplication of R_s by the thickness, but if the sample dimensions are not significantly larger than the probe spacing, more complicated corrections are necessary.^{27,28}

The second conductivity-probing method used in this work is AC impedance spectroscopy. A key disadvantage of four-point probe is that the value measured is a composite of all contributions to the bulk conductivity, including electronic and ionic carriers and scattering from grain boundary, pore, and secondary phases. In AC impedance spectroscopy, an alternating current is applied across the body of sintered pellet or single crystal, and the response current is measured as the frequency of the voltage is varied over several orders of magnitude.²⁹ The impedance (Z), which is the AC analogue to resistance which also accounts for reactive effects like inductance, is given by an expression analogous to Ohm's Law:

$$Z(t) = \frac{V(t)}{I(t)}$$

Since the voltage and current are sinusoidal and vary with time, the response signal has both an amplitude and phase which is related to the lag between the input and output signals. Plotting the in-phase (Z_{real}) and out-of-phase (Z_{im}) components of impedance against each other

gives a characteristic plot, known as a Nyquist plot. Its features can be modeled as equivalent circuit elements which may then be related to physical aspects of the sample. For example, the plot in **Figure 2.6** corresponds to two RC circuits in series. Each semicircle is characterized by a time-constant, RC , which is the reciprocal of the frequency at the top of the semicircle, ω_{max} . Extracting the value of R from the diameter of the semicircle allows calculation of its characteristic capacitance of the curve. This type of plot is common for a sintered pellet which exhibits both bulk ($C \sim 10^{-12}$ F) and grain boundary ($C \sim 10^{-8}$ - 10^{-11} F) conduction. Different contributions to the total electrical conductivity typically have distinct capacitance ranges, so AC impedance spectroscopy readily decouples their contributions into separate responses. This allows for more accurate determination of the intrinsic conductivity (i.e. of a single crystal) when only polycrystalline samples are available. Likewise, decoupling ionic and electronic conductivity is important for candidate solid-state electrolytes, which must have high ionic conductivity with negligible electronic conductivity.

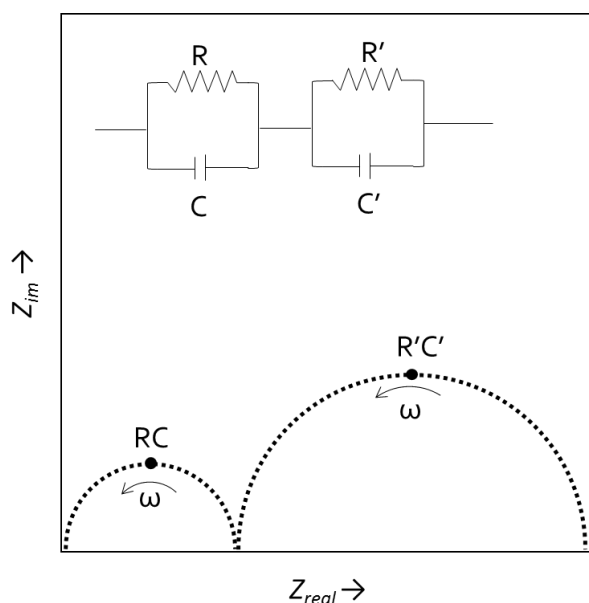


Figure 2.6. An illustrative Nyquist plot and equivalent circuit demonstrating a system with two processes contributing to the total impedance. In a sintered pellet the high frequency (RC) process would typically be bulk conduction whereas the low frequency one ($R'C'$) would be grain boundary conduction.²⁹

2.3.3: Thermal Analysis

Thermogravimetric analysis (TGA) and differential thermal analysis (DTA) are two techniques that are often run simultaneously to characterize the behavior of a material upon heating.³⁰ For the former, a precisely weighed sample is placed on a sensitive balance (typically with an accuracy on the order of 1 μg) in an atmosphere-controlled furnace to detect any changes in mass upon heating or cooling.³⁰ Usually, a TGA experiment also includes a background collection run under identical conditions (heating rate, max temperature, atmosphere, etc.) without the sample to correct for extra mass changes that arise from non-sample effects such as buoyancy and convection.³⁰ This technique can provide precise, easily obtainable information on the stability of a material, its interaction with various atmospheres, and even the mechanism and kinetics of reactions it may undergo. Complementary to TGA, DTA uses multiple thermocouples to measure and compare the temperatures of the furnace chamber, a sample, and a reference. This allows for detection of changes in “heat content” of the sample, which occur with chemical and physical processes such as phase changes and reactions. This is particularly useful in cases where the process does not involve a change in mass, such as melting or shifts in the crystalline or electronic structure of a material. While some of these can also be detected more directly using variable-temperature X-ray diffraction, DTA is a simpler and faster technique that can optimize subsequent powder diffraction experiments. Furthermore, DTA detects whether or not a thermal event is endo- or exothermic, providing insight on the thermodynamics of new materials such as whether or not they are metastable.

CHAPTER 3: NEW ANION-DEFICIENT FLUORITE OXIDES WITH SIGNIFICANT DISORDER

Sections of this work are reprinted with permission from

Flynn, S.; Adekoya, A. J.; Saeed, S.; Zhang, C.; Dravid, V. P.; Gonzalez, G. B.; Poepelmeier, K. R. $(\text{Cu}_x\text{Zn}_{1-x})_{0.456}\text{In}_{1.084}\text{Ge}_{0.46}\text{O}_3$ ($0 \leq x \leq 1$): A Complex, Ordered, Anion-Deficient Fluorite with Unusual Site-Specific Cation Mixing. *Inorg. Chem.* **2019**, 58 (22), 15610–15617.

3.1: Introduction

The structure of $\text{Zn}_{0.456}\text{In}_{1.084}\text{Ge}_{0.46}\text{O}_3$ (ZIGO), first reported in 2015 and until now only observed in that phase, is an ADF-phase of particular interest. Depicted in **Figure 3.1**, it is a fluorite-related structure in which approximately 25% of the anions are absent, resulting in a reduction in the average cation coordination from eight (in fluorite) to six as in bixbyite, but differing in that it is split between one 8-, one 4-, and two 6-coordinate sites. These sites segregate into two types of layers that alternate in the c-direction, one that solely consists of 6-coordinate sites and another that is mixed between 4-, 6-, and 8-coordinate sites in a 1:2:1 ratio.

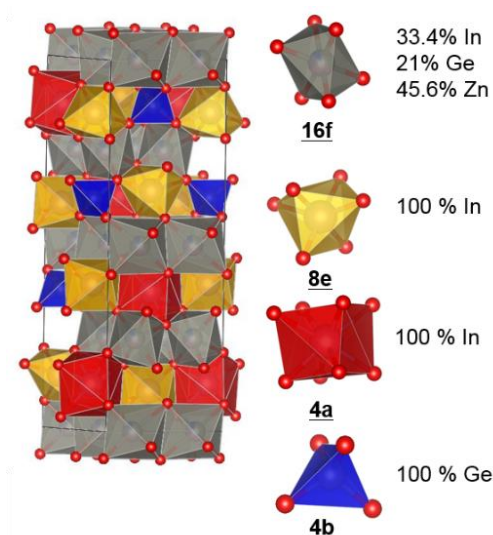


Figure 3.1. (Left) The crystal structure of ZIGO. (Right) the four distinct cation sites and their occupancies in ZIGO. Adapted from ref [1].

Although not indicated in the initial report of ZIGO, the layered structure and proportion of sites are strongly reminiscent of another complex ADF phase, braunite ($\text{Mn}_7\text{SiO}_{12}$).² **Figure 3.2** shows the structure of braunite, and compares structure of its two layers, conventionally referred to as “A” and “B”, to the analogous ones in ZIGO. It should be noted that the unit cell of ZIGO ($I4_1/amd$) is smaller than that of braunite ($I4_1/acd$), containing only half the atoms, owing to the slight difference in symmetry between the two phases. Both the standard unit cell and a $\sqrt{2} \times \sqrt{2}$

supercell of ZIGO are outlined for ease of comparison with the braunite structure. It is clear from **Figure 3.2** that the cation sublattices of the two phases are nearly identical. The cation positions in both layers form a slightly distorted centered square lattice or checkerboard arrangement. Likewise, in both materials the “B” type layers are further divided into individual rows of 6-coordinate and alternating 4- and 8-coordinate sites. The layers are staggered such that all cations are sandwiched between the holes of adjacent layers, characteristic of the fluorite aristotype. While in both compounds the coordination number for analogous cations is identical, the orientation and degree of distortion for comparable coordination polyhedra is often visibly different. In particular, all cations in the “A” layers in ZIGO are symmetrically equivalent, whereas in braunite they are split into two crystallographic sites arranged in a checkerboard pattern. This indicates that there are significant, but correlated differences in the anion sublattices of the two compounds.

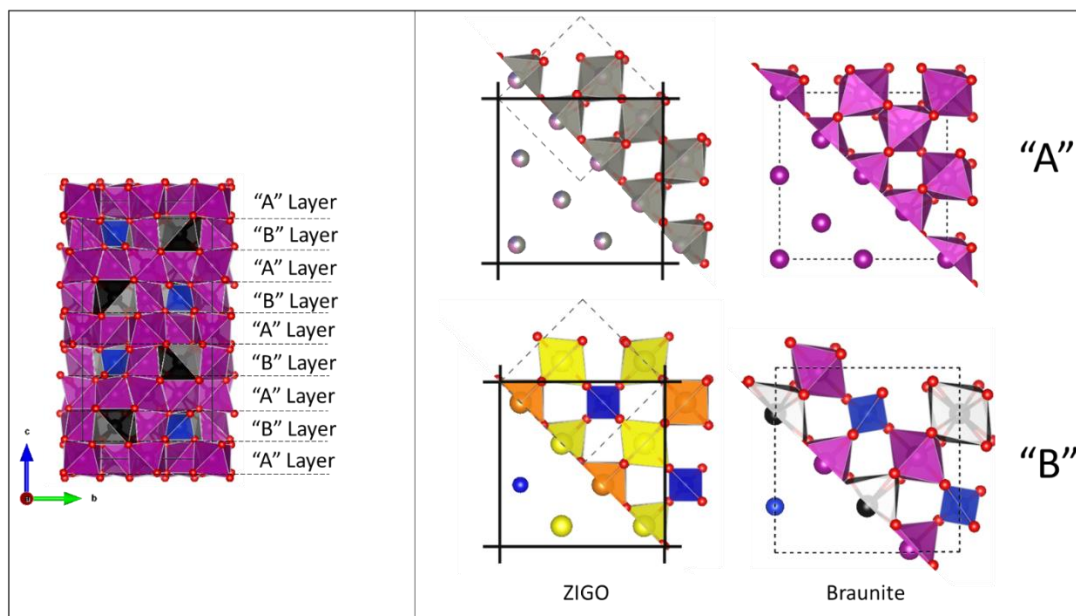


Figure 3.2. (Left) Crystal structure of braunite, Mn_7SiO_{12} , depicting its layered nature with conventional labels indicated. Purple octahedra are Mn^{3+} sites, black distorted cubes are Mn^{2+} sites, and blue tetrahedra are Si^{4+} . (Right) Relationship between analogous layers in ZIGO and braunite, as viewed down the c-axis. Site coloration are identical to those in **Figure 3.1** and in the left panel for ZIGO and braunite, respectively. Dashed lines indicate a single unit cell in each structure. Bold lines in the ZIGO layers indicates an $\sqrt{2} \times \sqrt{2}$ supercell.

The most interesting discrepancy between the two structures, however, is not found in their anion arrangements. The 16f site in ZIGO, which makes up its “A” layers, is occupied by a statistical distribution of three different cations, whereas in braunite all sites are fully ordered.² The coexistence of random mixing of all cations in a material on only a single crystallographic site in an otherwise highly ordered cation sublattice with three other distinguishable, singly-occupied sites is very rare among ADF-related phases. As mentioned in **Chapter 1**, disordered systems are difficult to model and predict with theory owing to the need to simulate them with computationally expensive supercells. Additionally, the large unit cell of the ZIGO structure (80 atoms) makes it particularly ill-suited for theory-based, high-throughput investigations. The contrast with the closely-related braunite suggests that the disorder could be inherent to the ZIGO structure and will be preserved in isostructural compositions. Therefore this set of materials, some of which may have useful properties akin to other ADF phases, will likely remain neglected unless investigated with an exploratory synthesis approach. Expanding the phase space will reveal whether this system is an effective avenue for pursuing computational blindspots.

The defect fluorite structure depicted in **Figure 1.5d** is another ADF phase with significant disorder. In contrast with the ZIGO structure, its disorder is only inherent to the anion sublattice, and its higher symmetry results in a much smaller unit cell with only one cation site. These features make it more tractable to computational approaches, which have been used extensively to model defect configurations in oxygen ion-conductors.³ However, the occurrence of defect fluorite phases with multiple cations is not uncommon.⁴ Since the cations must be disordered on the one available crystallographic site, the cost required to model and investigate these phases computationally increases with their number. Thus, multi-cation defect fluorites may also be considered a blindspot

for materials design, and those encountered in exploratory experiments are worth isolating and characterizing as they may reveal new materials which could exhibit useful properties.

This chapter discusses several new compositions in two ADF structures, ZIGO and defect fluorite, which exhibit significant disorder arising from multi- and partial occupancy on atomic sites. Isovalent chemical substitution, a typical exploratory approach for identifying new phases in a target structure, was successfully performed on ZIGO with a variety of transition metal ions. As a case study, a full structural characterization and property investigation is performed on the complete solid solution between the new phase $\text{Cu}_{0.456}\text{In}_{1.084}\text{Ge}_{0.46}\text{O}_3$ (CIGO) and ZIGO. Reported powder diffraction results for $\text{Mn}^{2/3+}$, Fe^{3+} , Co^{2+} , and Ni^{2+} substitutions further expand the known ZIGO-structure phase space. Three previously unknown multi-cation defect fluorite phases with nominal compositions $\text{M}_{0.4}\text{In}_3\text{SbO}_{7.6}$ ($\text{M} = \text{Cr}^{3+}$, Fe^{3+} , Ga^{3+}) are identified. The degree of disorder on the cation site is probed with transmission electron microscopy (TEM). Next steps for each of these systems and their potential connection to the high-interest research area concerning high-entropy oxide phases and their potential applications is discussed.

3.2: Materials and Methods

3.2.1: Synthesis

All samples were synthesized using high temperature solid-state reactions. To search for new phases isostructural to ZIGO, stoichiometric amounts of MnO (Alfa Aesar, 99%), NiO (Alfa Aesar, 99%), Co_3O_4 (Fisher Scientific, 99.9%), Cu_2O (Alfa Aesar, 99.9%), In_2O_3 (Alfa Aesar, 99.994%), Fe_2O_3 (Alfa Aesar, 99.8%), GeO_2 (Sigma Aldrich, 99.998%), and/or ZnO (Alfa Aesar, 99.9%) were ball milled with agate media for four, 15-minute cycles at 450 rpm. Co_3O_4 and Cu_2O were used as Co^{2+} and Cu^{2+} sources respectively, under the assumption of rapid

reduction/oxidation during the heating step.⁵ Four compositions corresponding to the direct substitution of Cu for Zn in ZIGO, $(\text{Cu}_x\text{Zn}_{1-x})_{0.456}\text{In}_{1.084}\text{Ge}_{0.46}\text{O}_3$ ($x = 0.25, 0.5, 0.75, \text{ and } 1$), henceforth referred to as CuZIGO, were investigated. The nominal compositions of other targeted samples were either $(\text{M}_x\text{Zn}_{1-x})_{0.456}\text{In}_{1.084}\text{Ge}_{0.46}\text{O}_3$ ($x = 0.25, 0.5, 0.75, \text{ or } 1$) for 2+ cations or $\text{Zn}_{0.456}(\text{In}_{1-x}\text{M}_x)_{1.084}\text{Ge}_{0.46}\text{O}_3$ ($x = 0.1, 0.5, 1$) for 3+ cations. For simplicity, these will be referred to as MZIGO or ZIMGO with M replaced with the appropriate elemental symbol. Precursor mixtures were pressed into 13 mm diameter cylindrical pellets and individually buried in sacrificial powder in triply nested-alumina crucibles to suppress preferential loss of volatile components such as Zn and Cu owing to volatilization.^{6,7} Samples containing Mn^{2+} were placed in a Pt boat covered with alumina, and immersed in a flowing Ar atmosphere during reaction to limit oxidation of Mn^{2+} . Samples were heated to 1250 °C (1150 °C for $x = 1$ CuZIGO) at 5 °C per min, held there for 16 hours, and then cooled to room temperature at 10 °C per min. Lower reaction temperatures were used for the highest Cu-content mixtures to prevent excessive loss during the reaction.

Synthesis of the defect fluorite phases proceeded through an alternative heating profile. Stoichiometric amounts of Ga_2O_3 (Sigma Aldrich, 99.99%), Cr_2O_3 (Aldrich, 98 %), or Fe_2O_3 (Alfa Aesar, 99.8%,) were ground with In_2O_3 (Alfa Aesar, 99.994%), and Sb_2O_3 (Aldrich, 99%) with acetone in a mortar and pestle until homogenous. Sb_2O_3 was used as an Sb^{5+} source owing to the tendency for Sb_2O_5 to exist as a hydrate with a variable amount of H_2O , complicating accurate measurement of the desired amount of Sb. The mixtures were first heated in air in a platinum crucible with an alumina lid to 900 °C at 5 °C/min and held for 8 hours to ensure oxidation of Sb^{3+} to Sb^{5+} .⁸ After cooling to room temperature at 5 °C/min, the samples were re-homogenized in a mortar and pestle and then pressed into 13 mm diameter cylindrical pellets. The pellets were

returned to their crucibles and reacted at 1200 °C for 20 hours with the same heating and cooling rates as in the pre-reaction.

3.2.2: X-Ray Diffraction

Phase purity and reaction completeness was checked with laboratory powder X-ray diffraction patterns (PXRD) collected over a 2θ range of 10–60° on a Rigaku IV (Ultima) X-ray diffractometer with Cu K α radiation under ambient conditions. Synchrotron X-ray diffraction patterns were collected at 11-BM at the Advanced Photon Source at Argonne National Laboratory with a wavelength of 0.41267 Å at 300 K. To minimize absorption of the X-ray beam by In, a small Kapton capillary (outer diameter ~1mm) was lightly covered with grease (Dow), gently rolled in sample powder to generate a thin, uniform coating, and inserted in a larger Kapton capillary (inner diameter 1.5 mm) which had both ends sealed with Q compound (Apiezone).

Lattice parameters and atomic coordinates were obtained for CuZIGO samples from XRD data using Rietveld refinement performed with the General Structure Analysis System II (GSAS II) package on all four samples.⁹ Ionic x-ray scattering factors for Cu⁺², Zn⁺², Ge⁺⁴, In⁺³, and O⁻² were used. Occupations for the 4a, 4b, 8e, 16f and 16h sites were fixed to 100% as in ZIGO. Initial refinements included only indium at the 8e and 4a sites, and only germanium at the 4b site. The fractions of Cu, Zn, Ge, and In at the 16f site were fixed to values calculated assuming that Cu replaced for Zn at this site only. The atomic positions and isotropic thermal parameters were refined but constrained to be the same for all cations at the 16f site. Other refinement scenarios allowed the presence of Cu at the 4a, 4b, and 8e sites while keeping the same calculated occupations for 16f as before. Likewise, the atomic positions and isotropic thermal parameters

were refined but constrained to be the same for all cations in each site. For each sample, lattice parameters, the sample X displacement perpendicular to the beam, and a 7th order chebyshev polynomial to fit the background were refined.

3.2.3: Elemental Analysis

Quantification of In, Cu and Zn in CuZIGO was accomplished using ICP-OES of acid digested samples. Specifically, solid samples were digested in concentrated hydrochloric acid (> 34%, Thermo Fisher Scientific, Waltham, MA, USA) at room temperature for 48 hours until completely dissolved. Ultra pure H₂O (18.2 MΩ·cm), concentrated trace nitric acid (> 69%, Thermo Fisher Scientific, Waltham, MA, USA), and concentrated hydrochloric acid was added to produce a final solution of 2.0% nitric acid (v/v) and 2.0% hydrochloric acid (v/v) in a total sample volume of 10 mL. Dilutions of these samples were prepared by diluting 1 mL of stock sample solution with 9 mL of 2.0% nitric acid (v/v) and 2.0% hydrochloric acid (v/v). Quantitative standards consisting of 15/5/5, 7.5/2.5/2.5, 3.75/1.25/1.25, 1.875/0.625/0.625, 0.9375/0.3125/0.3125, and 0.46875/0.15625/0.15625 ng/g In/Cu/Zn were made using a 1000 µg/mL In standard and a 100 ug/mL mixed element standard including Cu and Zn (Inorganic Ventures, Christiansburg, VA, USA) in 2.0% nitric acid (v/v) and 2.0% hydrochloric acid (v/v) in a total sample volume of 5 mL.

ICP-OES was performed on a computer-controlled (QTEGRA software) Thermo iCap7600 ICP-OES (Thermo Fisher Scientific, Waltham, MA, USA) operating in axial view and equipped with a CETAC 520 autosampler (Omaha, NE, USA). Each sample was acquired using 5 second visible exposure time and 15 second UV exposure time, running 3 replicates. The spectral

lines selected for analysis were: Zn (213.856, 202.548 nm), Cu (327.396, 224.700 nm), and In (325.609, 303.936 nm).

3.3.4: Scanning and Transmission Electron Microscopy

Polycrystalline products were crushed to powders and dropped on ultrathin C-coated Mo grids. High-resolution transmission electron microscopy (HRTEM) images, selected area electron diffraction (SAED) patterns, bright field scanning transmission electron microscopy imaging and energy dispersive X-ray spectroscopy (EDS) were obtained using a JEOL Grand ARM operated at 300 kV, and atomic resolution high angle annular dark-field (HAADF) (90 – 200 mrad of collection angle) scanning transmission electron microscopy (STEM) were acquired using a Cs-corrected JEOL ARM 200CF operated at 200 kV. The multislice simulation was conducted with software Dr. Probe under 200 kV, the thickness of 31.53 nm, convergence angle of 24 mrad and defocus of 0 nm, using Frozen-lattice configurations and the number of variants per slice is 10.¹⁰

3.3.5: Diffuse Reflectance

Diffuse reflectance measurements were collected on the sample pellets using a Lambda 1050 UV-Vis spectrophotometer with integrating sphere attachment (Perkin Elmer). Background spectra were collected on compacted polystyrene. Collected spectra were converted to pseudoabsorbance using the Kubelka-Munk transformation.¹¹ Optical band gaps for each sample were approximated as the intersection of two linear extrapolations, one of the band edge and the other of the region immediately preceding the band edge (see **Section 2.3.1**). The average value of four pellets at each nominal Cu content was taken to be the optical band gap at the composition.

3.3: New ZIGO Structure Phases via Isovalent Chemical Substitution

3.3.1: Structural Characterization of CuZIGO

The polycrystalline CuZIGO products ranged in color from light green at 25% to dark olive with complete substitution of Zn with Cu (See **Figure 3.3**). The $x = 0$ (Zn only) endpoint has been reported as pale yellow, so the apparent color change is indicative of significant Cu-content remaining in the product, despite the synthesis temperatures being above or around the melting point of Cu_2O , where slight Cu volatility and reactivity with the crucible are possible.^{5,7,12}

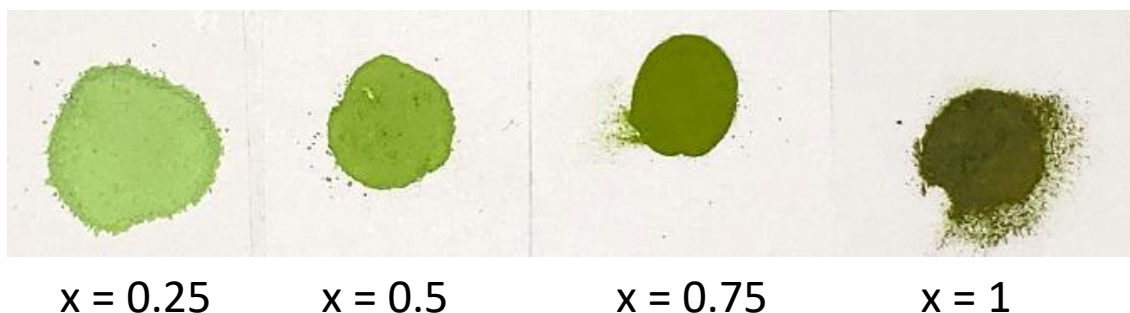


Figure 3.3. Color of loose powders of $(\text{Cu}_x\text{Zn}_{1-x})_{0.456}\text{In}_{1.084}\text{Ge}_{0.46}\text{O}_3$ as a function of x .

Rietveld refinements of the synchrotron XRD data are presented in **Figure 3.4**. Cation ratios were treated as following the off-stoichiometry observed in ZIGO, as experiments in which the nominal cation ratios were rounded resulted in increased intensity of secondary phase peaks (See **Figure 3.5**). Minor (< 2 wt % for $x = 0.25$ and < 7 wt % for $x = 1$) amounts of the secondary phases In_2O_3 and $\text{In}_2\text{Ge}_2\text{O}_7$ are observed for some compositions. This is likely caused by Cu volatilization, consistent with the fact that significantly higher amount of secondary phases are observed when $x = 1$.

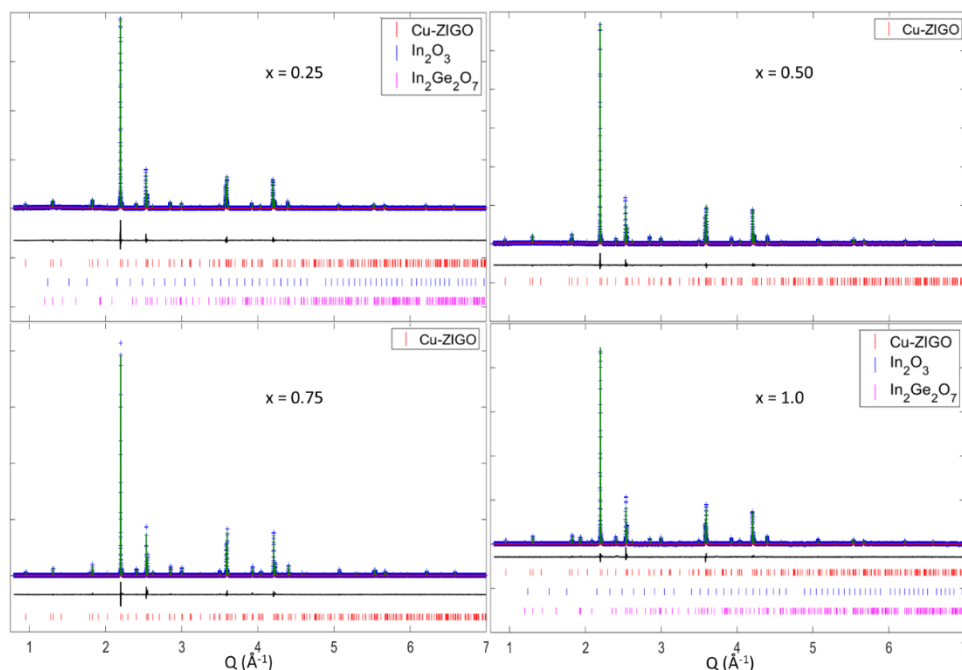


Figure 3.4. Rietveld Refinement of synchrotron XRD data of CuZIGO samples with peak markers indicating the ZIGO structure phase (red) and two secondary phases where present.

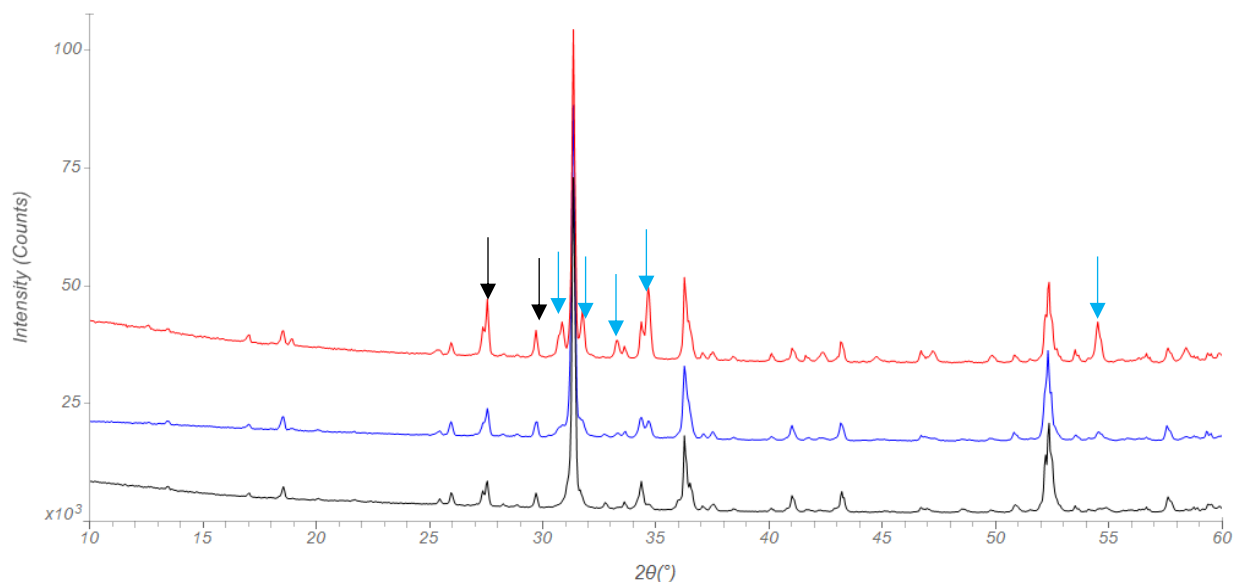


Figure 3.5. Dependence of Secondary Phases on Nominal Composition of CIGO. Laboratory PXRD patterns of $\text{Cu}_{0.456}\text{In}_{1.084}\text{Ge}_{0.46}\text{O}_3$ (black), $\text{Cu}_{0.46}\text{In}_{1.08}\text{Ge}_{0.46}\text{O}_3$ (blue) and $\text{Cu}_{0.5}\text{InGe}_{0.5}\text{O}_3$ (red). Black arrows indicate secondary phase peaks that are already present in the black pattern (primarily belonging to $\text{In}_2\text{Ge}_2\text{O}_7$). Blue arrows indicate extra secondary phase peaks only observed in the rounded (red and blue) stoichiometries. Both sets of secondary phase peaks become more intense as the composition increasingly deviates from that of the black pattern.

Product stoichiometries determined by ICP-OES (**Table 3.1**) show the Cu+Zn to In ratios are slightly lower than expected from the nominal formula, consistent with this explanation.

Furthermore, the Cu to Zn ratios match very closely to the expected values, suggesting similar amounts of Zn volatilization which is not unreasonable given the high synthesis temperature.¹³ At $x = 0.25$ these are the only observed secondary phases, so all remaining Cu content must be incorporated in the ZIGO-structure phase. The higher Cu contents ($x = 0.75, 1$) exhibit an additional set of peaks which could not be attributed to any reported phases, possibly including some of the precursor Cu content. However, these peaks are very small at $x = 0.75$, and the presence of the ZIGO phase at $x = 1$ means the structure must be stable with no Zn content, supporting the conclusion that these secondary phases are a result of volatilization and not an inherent solubility limit. The refinement parameters given in **Table 3.2**, support the accuracy of these models. The atomic and thermal parameters from these refinements may be found in **Table 3.3**.

Table 3.1. ICP-OES data for $(\text{Cu}_x\text{Zn}_{1-x})_{0.456}\text{In}_{1.084}\text{Ge}_{0.46}\text{O}_3$ phases

| | Cu : Zn (molar %) | | (Zn+Cu) : In (molar) | |
|-----------------|-------------------|----------|----------------------|---------------|
| | Observed | Expected | Observed | Expected |
| x = 0.25 | 25.308 : 74.692 | 25:75 | 0.43056 : 1.084 | 0.456 : 1.084 |
| x = 0.5 | 50.338 : 49.662 | 50:50 | 0.43203 : 1.084 | 0.456 : 1.084 |
| x = 0.75 | 74.394 : 25.606 | 75:25 | 0.42719 : 1.084 | 0.456 : 1.084 |
| x = 1.0 | 99.421 : 0.579* | 100:0 | 0.40321 : 1.084 | 0.456 : 1.084 |

*Minor Zn content in $x = 1.0$ arises from known interference by Cu in Zn detection.

Table 3.2. Rietveld Refinement of Synchrotron X-ray Diffraction Data of CuZIGO

| Source | Synchrotron | | | |
|---------------------------------|--------------------------------|--------------|-------------|--------------|
| Chemical Formula | $x = 0.25$ | $x = 0.5$ | $x = 0.75$ | $x = 1.0$ |
| Formula Weight | 235.49 | 235.28 | 235.07 | 234.87 |
| Temperature (K) | 295 | | | |
| Wavelength (Å) | 0.412670 | | | |
| Crystal System | Tetragonal | | | |
| Space group (No.) | I 4 ₁ / a m d (141) | | | |
| $a = b$ (Å) | 7.02293(2) | 7.015155(15) | 7.009175(9) | 7.012091(19) |
| c (Å) | 19.71426(8) | 19.69666(5) | 19.68660(3) | 19.72457(6) |
| $\alpha = \beta = \gamma$ (deg) | 90 | 90 | 90 | 90 |
| V (Å ³) | 972.338(9) | 969.320(6) | 967.174(3) | 969.846(7) |
| Z | 16 | | | |
| Profile range | $0.5 \leq 2\theta \leq 50$ | | | |

| | | | | |
|---------------------|-------|-------|-------|-------|
| GOF | 1.52 | 1.48 | 1.64 | 2.44 |
| R _p (%) | 8.47 | 7.70 | 10.15 | 9.60 |
| R _{wp} (%) | 10.58 | 10.12 | 13.07 | 13.96 |

Initial refinements were performed with Cu²⁺ directly replacing Zn on the 16f site, analogous to the x = 0 composition. The Cu²⁺ content on the 16f site could not be directly refined as Cu and Zn have 29 and 30 electrons respectively, so their X-ray scattering power is indistinguishable at most wavelengths, and that a single dataset is insufficient to refine more than two occupancies on a single site. In order to refine the occupations of all four cations at the 16f site, three independent diffraction data sets are needed for each sample. As such, alternative site preference of Cu²⁺ in the ZIGO structure was investigated by refinement of Cu-content on the singly occupied sites (4a, 4b, and 8e), with the global composition constrained to match the nominal composition. As shown in **Table 3.4**, these refinements changed the wR values only slightly and resulted in inconsistent, non-physical results such as occupancy values that were often either negative (4a, 4b, and 8e) or greater than one (16f). It is possible that the complex structure and similar electron account of Ge and Cu make X-ray data insensitive to these occupancies. As such, the complex structure and chemistry of CuZIGO limits the utility of Rietveld refinement in directly determining site occupancies with only synchrotron data.

However, even without definitive refinement results the hypothesis that the 16f site is favored over the 4a, 4b, and 8e sites for Cu occupancy remains strongly supported by bond valence (BV) analysis and the literature on related phases. The former, performed using the refined lattice parameters and atomic positions is summarized in **Table 3.5**. The data strongly suggest that Cu²⁺ does not incorporate on either the 4a or 4b sites. The fact that the best match for the 4a site, In³⁺, is somewhat under-bonded strongly suggests that smaller species, including Cu²⁺, will not be stable

on this 8-fold site. Although Cu^{2+} incorporation in braunite has been reported to prefer the 8-fold site, the difference in the long and short bonds of this site makes it more accommodating to Jahn-Teller (JT) active Cu^{2+} than the less distorted 4a site in ZIGO ($\Delta_{\text{M-O}}$ of 0.349 Å vs. 0.259 Å).^{7,8} Furthermore, increasing Cu incorporation in braunite is accompanied by further distortion in the bond lengths on that site.^{14,15} The decreased initial distortion and minor effect of increasing Cu-content on the bond lengths (**Table 3.6**) of the 4a site in CuZIGO makes Cu incorporation there doubtful. Likewise, although Cu^{2+} frequently adopts tetrahedral coordination, **Table 3.5** shows that in CuZIGO the 4b is too small and would result in significant over-bonding, strongly suggesting this site is not suitable for it. This is consistent with, and likely the cause of, Zn only being found on the 16f site in ZIGO despite commonly occupying tetrahedral sites in other oxides.

Table 3.3. Atomic Positions from Synchrotron XRD Refinement

| Atom | Site | X | y | z | Fraction (nominal) | U_{iso} (Å ²) |
|-----------------|------|-------------|-----------|--------------|------------------------|------------------------------------|
| x = 0.25 | | | | | | |
| In | 4a | 0 | -0.25 | 0.125 | 1 | 0.0197(3) |
| Ge | 4b | 0.5 | 0.25 | 0.125 | 1 | 0.0147(4) |
| In | 8e | 0.5 | 0.25 | -0.10499(3) | 1 | 0.01279(19) |
| Zn/Cu/Ge/In | 16f | 0.22717(10) | 0 | 0 | 0.342/0.114/0.21/0.334 | 0.0217(2) |
| O1 | 16h | 0 | 0.0288(7) | 0.0723(2) | 1 | 0.0315(13) |
| O2 | 16h | 0.5 | 0.0486(7) | 0.0759(2) | 1 | 0.0333(15) |
| O3 | 16h | 0.2547(7) | 0.25 | -0.0378(2) | 1 | 0.0347 |
| x = 0.5 | | | | | | |
| In | 4a | 0 | -0.25 | 0.125 | 1 | 0.0217(2) |
| Ge | 4b | 0.5 | 0.25 | 0.125 | 1 | 0.0148(3) |
| In | 8e | 0.5 | 0.25 | -0.10495(3) | 1 | 0.01407(15) |
| Zn/Cu/Ge/In | 16f | 0.22730(8) | 0 | 0 | 0.228/0.228/0.21/0.334 | 0.02229(16) |
| O1 | 16h | 0 | 0.0284(6) | 0.07147(18) | 1 | 0.0260(10) |
| O2 | 16h | 0.5 | 0.0499(6) | 0.07549(18) | 1 | 0.0376(13) |
| O3 | 16h | 0.2535(6) | 0.25 | -0.03663(18) | 1 | 0.0464(14) |
| x = 0.75 | | | | | | |
| In | 4a | 0 | -0.25 | 0.125 | 1 | 0.0239(2) |
| Ge | 4b | 0.5 | 0.25 | 0.125 | 1 | 0.0170(3) |
| In | 8e | 0.5 | 0.25 | -0.10483(3) | 1 | 0.01521(13) |

| | | | | | | |
|----------------|-----|-------------|-----------|--------------|------------------------|-------------|
| Zn/Cu/Ge/In | 16f | 0.22716(7) | 0 | 0 | 0.114/0.342/0.21/0.334 | 0.02320(14) |
| O1 | 16h | 0 | 0.0285(5) | 0.07022(17) | 1 | 0.0231(9) |
| O2 | 16h | 0.5 | 0.0503(5) | 0.07402(18) | 1 | 0.0411(12) |
| O3 | 16h | 0.2544(6) | 0.25 | -0.03586(17) | 1 | 0.0467(13) |
| x = 1.0 | | | | | | |
| In | 4a | 0 | -0.25 | 0.125 | 1 | 0.0226(3) |
| Ge | 4b | 0.5 | 0.25 | 0.125 | 1 | 0.0171(4) |
| In | 8e | 0.5 | 0.25 | -0.10523(4) | 1 | 0.0162(2) |
| Cu/Ge/In | 16f | 0.22781(10) | 0 | 0 | 0.456/0.21/0.334 | 0.0207(2) |
| O1 | 16h | 0 | 0.0291(7) | 0.0706(2) | 1 | 0.0264(13) |
| O2 | 16h | 0.5 | 0.0487(7) | 0.0734(2) | 1 | 0.0398(17) |
| O3 | 16h | 0.2568(8) | 0.25 | -0.0358(3) | 1 | 0.064(2) |

Table 3.4. Refinement results with Cu in non-16f sites

| | R_{wp} (%) | | Cu Occupancy (non 16f) | | | Total 16f Occupancy (1.000 expected) |
|-----------------|---------------------------|-----------------|-------------------------------|-----------|-----------|--|
| | new | <i>Original</i> | 4a | 4b | 8e | |
| x = 0.25 | 10.78 | <i>10.61</i> | -0.075(5) | -0.039(3) | -0.059(9) | 1.058 |
| x = 0.5 | 10.16 | <i>10.09</i> | 0.073(12) | -0.29(4) | 0.021(10) | 1.043 |
| x = 0.75 | 13.07 | <i>13.08</i> | 0.021(11) | -0.18(4) | 0.019(8) | 1.030 |
| x = 1.0 | 13.88 | <i>13.96</i> | -0.022(10) | -0.20(3) | 0.002(3) | 1.058 |

Regarding the 8e and 16f sites, the BV data is less clear. For the former, while In³⁺ shows the best match between expected and calculated valence, the Cu²⁺ and Zn²⁺ values are too close to be overlooked. In contrast, on the 16f site In³⁺ and Ge⁴⁺ are poor matches despite being known to occupy that site in this structure. The values in **Table 3.5** are calculated using average bond lengths for each site determined by the refinement.⁶ On multi-occupancy sites in which the species vary significantly in size, the averages will match best to intermediate-sized species, with larger and smaller atoms appearing over and under-bonded respectively. This is exactly what is seen with the 16f site. Thus, BV analysis is likely insufficient to probe the distribution of Cu²⁺ between these two sites.

The relative likelihood of Cu in 16f versus 8e may be elucidated by examining site preferences in Cu-containing bixbyite phases, which have been examined in past investigations. In ZIGO, as was described previously by Rickert *et al.*, the 16f and 8e sites are structurally

analogous to the 8b and 24d sites, respectively, of bixbyite In_2O_3 . The refined atomic positions for $x = 0.25-1$ samples here show that this relationship is maintained throughout the Cu-Zn solid solution (**Figure 3.6**). As such, the occupancy behavior in CuZIGO in the two systems is expected to be related.

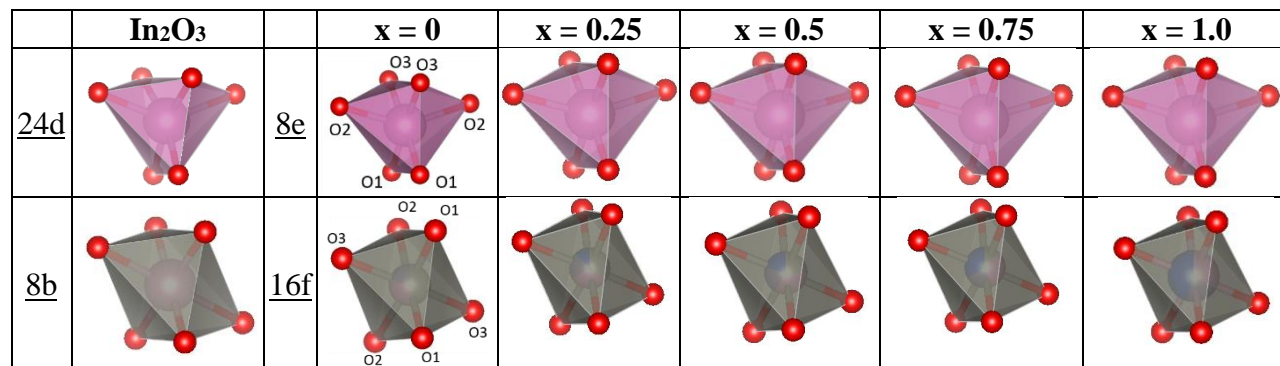


Figure 3.6. Relationship of the Coordination Polyhedra for the 8e and 16f Sites of CuZIGO to the 24d and 8b Sites of In_2O_3 as a Function of Composition. O atom labels on $x = 0$ are consistent for all x values. $x = 0$ data from ICSD-238681.

Previous reports of Cu^{2+} incorporation in In_2O_3 through co-doping have observed distribution across both types of sites with either no preference ($\text{Cu/Sn:In}_2\text{O}_3$) or an only slight preference for the 8b site ($\text{Cu/Sb:In}_2\text{O}_3$).^{16,17} However, in non-In containing bixbyite phases such as $\text{Cu}_{2/3}\text{Ti}_{2/3}\text{Fe}_{2/3}\text{O}_3$ and $\text{Cu}_3\text{TiFeSbO}_9$, Cu^{2+} was found to exclusively incorporate on the 24d site (8e analogue). The driving force for this selectivity was identified as the JT effect of Cu^{2+} favoring more distorted coordination environments. In the Ti and Fe based materials the 24d site is highly distorted, whereas it shows relatively little distortion in the In-based bixbyite phases, allowing for distribution on both sites.^{12,16-18} Applying the same metric for distortion as in these studies, the differences between the longest and shortest M-O bond lengths, to the ZIGO structure shows that the 16f site is significantly more distorted than both the 8e at all synthesized compositions (**Table 3.6**) as well as the 24d sites in $\text{Cu}_{2/3}\text{Ti}_{2/3}\text{Fe}_{2/3}\text{O}_3$ and $\text{Cu}_3\text{TiFeSbO}_9$.^{17,18} Therefore, the previously

observed JT-driven selectivity is expected to significantly favor the 16f site over the 8e site, making it highly likely that is where the majority of the Cu-content in CuZIGO phases is located.

Table 3.5. Bond Valence Analysis for X-ray Models of CuZIGO¹⁹

| Site | | x = 0.25 | x = 0.50 | x = 0.75 | x = 1.0 |
|------|----|-------------|-------------|-------------|-------------|
| 4a | In | 2.55 | 2.52 | 2.48 | 2.40 |
| | Cu | 1.39 | 1.38 | 1.35 | 1.31 |
| | Zn | 1.49 | 1.48 | 1.45 | ----- |
| | Ge | 1.68 | 1.66 | 1.63 | 1.58 |
| 16f | In | 3.41 | 3.51 | 3.62 | 3.60 |
| | Cu | 1.86 | 1.92 | 1.98 | 1.96 |
| | Zn | 1.99 | 2.05 | 2.12 | ----- |
| | Ge | 2.24 | 2.31 | 2.38 | 2.36 |
| 8e | In | 3.06 | 2.95 | 2.89 | 2.94 |
| | Cu | 1.67 | 1.61 | 1.58 | 1.60 |
| | Zn | 1.78 | 1.73 | 1.69 | ----- |
| | Ge | 2.01 | 1.94 | 1.90 | 1.93 |
| 4b | In | 6.67 | 6.76 | 6.51 | 6.21 |
| | Cu | 3.64 | 3.69 | 3.55 | 3.39 |
| | Zn | 3.89 | 3.95 | 3.80 | ----- |
| | Ge | 4.38 | 4.44 | 4.28 | 4.09 |

*Bold values indicate best match to expected oxidation state

As a result of the likely Cu²⁺ site preference, the 16f site in the investigated solid solution has either three, at endpoint compositions, or four cations distributed on it. Such a high degree of mixing is reminiscent of entropy stabilized oxides (ESOs) such as Mg_{0.2}Co_{0.2}Ni_{0.2}Zn_{0.2}Cu_{0.2}O in which the configurational entropy plays a critical role in stabilizing the structure.²⁰⁻²² Several factors suggest that the contribution of entropy in stabilizing the ZIGO structure is significant. First, Zn²⁺ exhibits a similar discrepancy in site selectivity to Cu²⁺ between ZIGO and co-doped In₂O₃ phases, despite it not being JT active. Second, the cations on the 16f site range significantly in size from 53 pm (Ge⁴⁺) to 80 pm (In³⁺) resulting in severe underbonding for Ge⁴⁺ as indicated

by bond valence analysis which the energetic benefit of multi-occupancy evidently outweighs.²³ However, low-temperature sintering experiments with the $x = 0.25$ and $x = 0.5$ compositions show that the formation of CuZIGO from the binary oxides is not a reversible reaction (**Figure 3.7**). No major decomposition into constituent binary or ternary compounds is observed as would be expected for a true entropy-stabilized material. Although a small amount of $\text{In}_2\text{Ge}_2\text{O}_7$ appears to form, this is likely due to very slight Cu^{2+} volatilization. Thus, entropy is not the controlling thermodynamic factor in the reaction, unlike in true ESOs.²⁰ The range in size and fractional occupancy of the cations on the disordered site, as well as the existence of multiple singly-occupied cation sites in the structure, further distinguishes ZIGO-structure phases from ESOs.²⁰⁻²³ As such, they may represent a related, but distinct direction functional materials discovery that, like ESOs, current computational and high-throughput techniques are unsuitable to explore.

Table 3.6 M-O bond distances for the 16f and 8e sites from X-ray Data. $x = 0$ data from ICSD-238681

| | | x = 0 | | x = 0.25 | | x = 0.5 | | x = 0.75 | | x = 1.0 | |
|---------------|----|-------|-------|----------|------------|---------|------------|----------|------------|---------|----------|
| | | # | d (Å) | # | d (Å) | # | d (Å) | # | d (Å) | # | d (Å) |
| 16f | O3 | 2 | 1.903 | 2 | 1.9171(17) | 2 | 1.9050(14) | 2 | 1.8989(13) | 2 | 1.901(2) |
| | O1 | 2 | 2.117 | 2 | 2.148(3) | 2 | 2.136(2) | 2 | 2.118(2) | 2 | 2.138(3) |
| | O2 | 2 | 2.426 | 2 | 2.454(3) | 2 | 2.448(2) | 2 | 2.430(2) | 2 | 2.419(3) |
| 8e | O1 | 2 | 2.155 | 2 | 2.114(3) | 2 | 2.125(2) | 2 | 2.142(2) | 2 | 2.131(3) |
| | O2 | 2 | 2.191 | 2 | 2.174(5) | 2 | 2.182(4) | 2 | 2.189(4) | 2 | 2.187(5) |
| | O3 | 2 | 2.215 | 2 | 2.173(5) | 2 | 2.192(4) | 2 | 2.193(4) | 2 | 2.187(5) |
| 4a | O1 | 2 | 2.244 | 4 | 2.217(5) | 4 | 2.219(4) | 4 | 2.223(4) | 4 | 2.232(5) |
| | O3 | 2 | 2.503 | 4 | 2.480(5) | 4 | 2.488(4) | 4 | 2.501(4) | 4 | 2.517(5) |
| Delta M-O 16f | | | 0.523 | | 0.537(3) | | 0.543(2) | | 0.531(2) | | 0.518(3) |
| Delta M-O 8e | | | 0.060 | | 0.059(6) | | 0.067(4) | | 0.051(3) | | 0.056(6) |

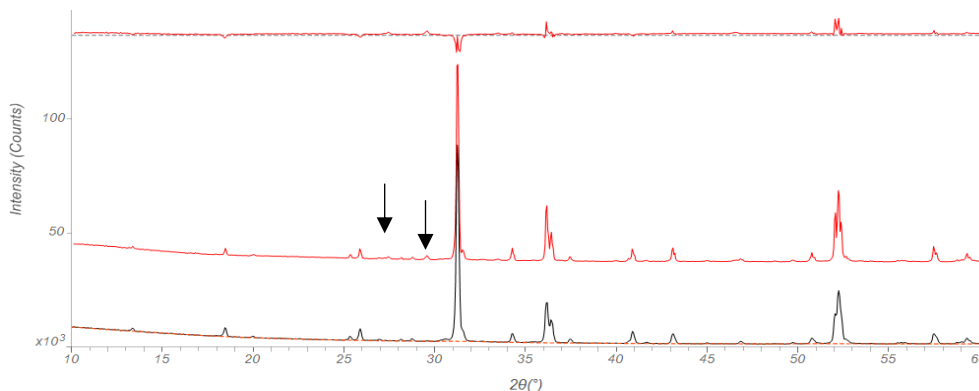


Figure 3.7. Laboratory PXRD comparing $x = 0.25$ CuZIGO samples after synthesis at 1250 °C (black) and after an additional, subsequent 700 °C anneal (red). Black arrows indicate minor $\text{In}_2\text{Ge}_2\text{O}_7$ secondary phase.

Figure 3.8 displays the lattice parameters refined from the synchrotron X-ray data for all four compositions, as well as those parameters for the fully Zn endpoint ($x = 0$) for comparison. Both independent lattice parameters (a and c) exhibit a gradual decrease from $x = 0$ to 0.75, consistent with the slightly smaller radius of Cu^{2+} compared to Zn^{2+} .²³ However, an increase is observed in both a and c between $x = 0.75$ and complete substitution, with the change in the latter being significantly larger. Overall, the observed trends deviate significantly from the expected Vegard's law behavior for solid solutions: monotonic, linear changes.²⁵ Previous reports of non-Vegard's law behavior in oxides and intermetallics have attributed the cause to potential ordering, clustering, and magnetic effects of the introduced species.²⁸ Since Cu^{2+} , a strong JT active ion, is replacing Zn^{2+} which exhibits no JT effect owing to its filled d-subshell, it is possible that ordering of the Cu^{2+} at low x values allows the system to minimize the energy penalty of this conflict. Their likely position on the 16f site is consistent with this explanation, as it is the only site which forms a continuous network in the crystal structure allowing for the greatest degree of interaction between nearby Cu^{2+} polyhedra. As shown in **Figure 3.1**, these networks present as complete layers solely made up of 16f sites perpendicular to the c -axis. As such, any distortion-minimizing interactions would be expected to be enhanced in the a and b directions relative to c in which 16f sites are not

directly connected, possibly explaining why the expansion in c is significantly larger than the other two directions.

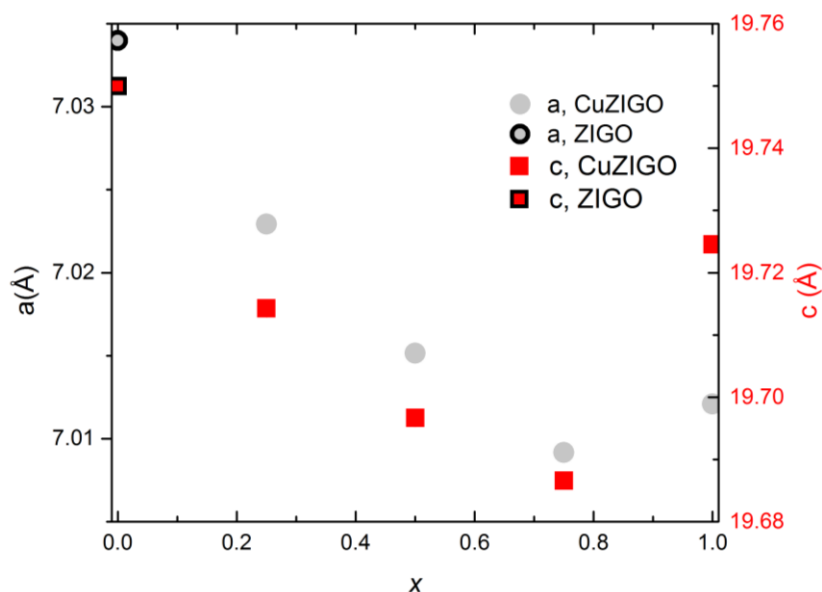


Figure 3.8. Lattice parameters refined from X-ray data for CuZIGO phases as a function of Cu content (x). $x = 0$ values reproduced from Rickert et al.⁶

In order to investigate this possibility and further analyze the atomic structure, a TEM and STEM investigation was performed. **Figure 3.9a** displays an HRTEM image of the $x = 0.25$ composition along the $[111]$ zone axis. The measured interplanar d-spacings of the $(10\bar{1})$, $(0\bar{1}1)$, and $(1\bar{1}0)$ planes in HRTEM are 6.56 \AA , 6.59 \AA , and 4.96 \AA , respectively, which are in good agreement with the refinement results. SAED of the $[111]$ zone axis inserted in **Figure 3.9a** matches very well with the reflections predicted by the CIF produced from its Rietveld refinement (**Figure 3.10a**). No extra spots, spot splitting, or streaking were observed. This is true for all the examined zone axes of the $x = 0.25$ sample (**Figure 3.10c-d**), and was not observed to change with increasing Cu-content (**Figure 3.11**). As such, there is no evidence of superstructure or symmetry lowering which would accompany long range ordering on the $16f$ site at any Cu-content. Furthermore, a typical HAADF-HRSTEM image (**Figure 3.9b**) taken down the $[001]$ zone axis

allows for direct observation of atomic columns exclusively made up of 16f sites (dark gray dots). The SAED pattern of the [001] zone axis inserted in **Figure 3.9b** also matches very well with the simulated diffraction pattern (**Figure 3.10b**).

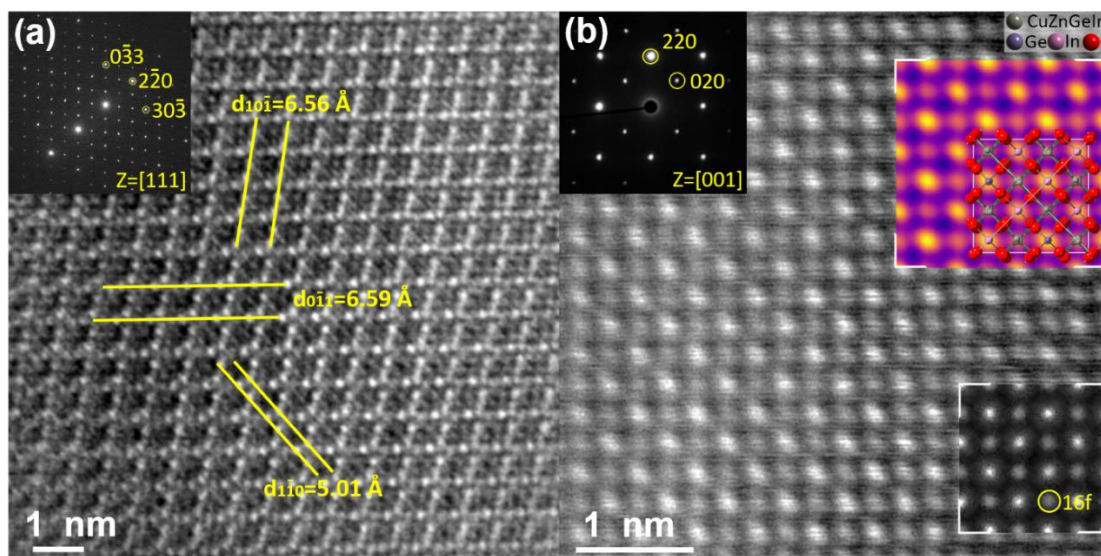


Figure 3.9. (a) HRTEM and SAED of $x = 0.25$ sample at [111] zone. Some lattice planes and their corresponding distances are marked in (a). Reflection indices are based on the refined structures. (b) HAADF-HRSTEM image and SAED of $x = 0.25$ sample at [001] zone, average unit cell calculated from the HAADF image (upper), structure schematic and simulated image (lower) overlaid. All reflections can be indexed with the refined structure. Darker dots (see insert) in the HAADF image are columns of 16f sites. No contrast is apparent between different 16f sites.

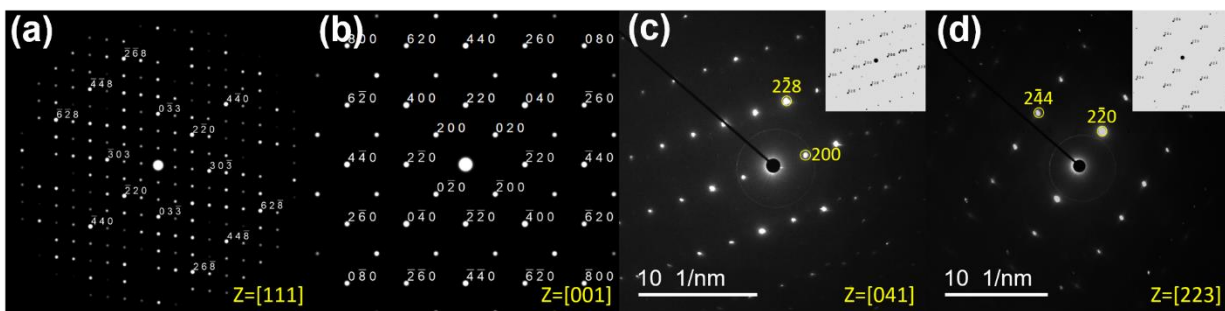


Figure 3.10. Simulated SAED patterns of [111] (a) and [001] (b) zone axes of the $x = 0.25$ sample. Several SAED patterns, including [041] (c) and [223] (d) zone axes of the $x = 0.25$ sample with simulated (inset).

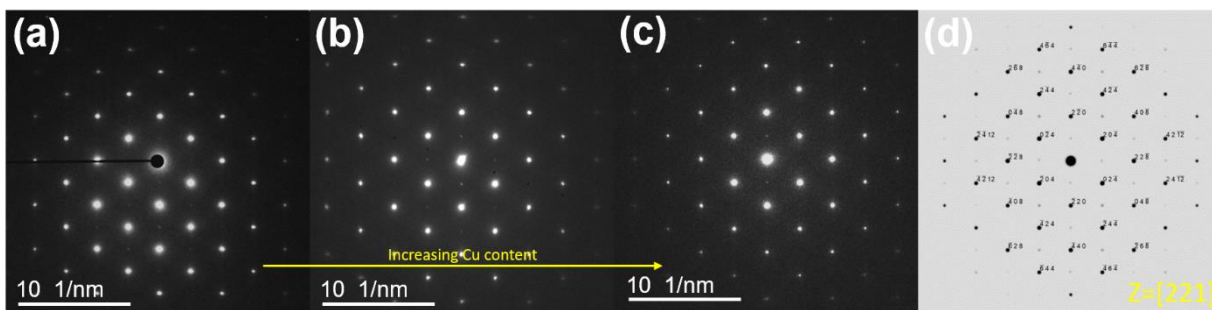


Figure 3.11. SAED images of the [221] zone axes for $x = 0.25$ (a), $x = 0.5$ (b), and $x = 0.75$ (c) respectively. All of them can match with the simulated diffraction pattern (d).

Since contrast in HAADF depends on the atomic number, the atomic column of 16f sites is darker than the columns of 4a, 4b, and 8e sites, which have a higher proportion of In. If the cations in the 16f site ordered within the ab plane and stacked in such a way that these columns had distinct average compositions, they would exhibit different contrasts in the image. The lack of obvious contrast between individual columns offers more evidence against ordering of Cu and In on the 16f site. The insets of Figure 4b project both the theoretical crystal structure along the [001] direction and the HAADF simulation based on the Rietveld results onto the experimental image. The atomic resolution images thereby confirm the expected crystal structure. In addition, chemical maps using STEM-EDS confirm the homogeneous distribution of Cu, Ge, In, Zn and O (**Figure 3.12**).

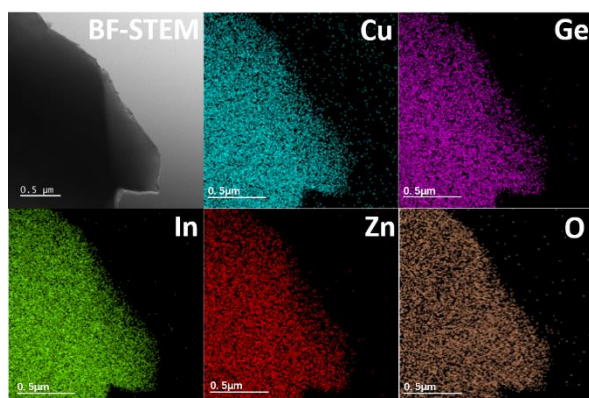


Figure 3.12. Bright-field STEM image and corresponding chemical maps of Cu, Ge, In, Zn and O respectively for $x = 0.25$ sample, which confirm the homogeneous distribution of those elements.

3.3.2: Property Characterization of CuZIGO

Conductivity and diffuse reflectance measurements were performed on the solid solution investigated in this study as the $x = 0$ endpoint had been previously described as a potential transparent conducting oxide.⁶ Four-point probe measurements on sintered pellets revealed no detectable conductivity at any of the synthesized contents ($x = 0.25 - 1$), indicating that Cu^{2+} incorporation inhibits conductivity in the ZIGO structure, which has been reported to have conductivity comparable to In_2O_3 at $x = 0$. In contrast, comparison of literature studies on the co-doping of In_2O_3 with either Zn^{2+} and Sn^{4+} or Cu^{2+} and Sn^{4+} shows that with either pair of dopants, the conductivity remains fairly high, and at the same order of magnitude, over a wide range of %In replacements.^{16, 27} This demonstrates that simple chemical substitution is unlikely to account for the sharp decrease in conductivity with Cu-content in the CuZIGO system on its own, but that some structure-specific component contributes as well. The multi-occupancy 16f site is most directly affected by changes in the Cu^{2+} concentration, and is likely related to the transport behavior in CuZIGO. Similar relationships have been observed in some high entropy oxides, materials closely related to ESOs, in which colossal dielectric constants were attributed to the highly disordered nature of the cation site.²⁸ In particular, the JT effect of Cu^{2+} has also been suggested to be a tunable parameter for manipulating the dielectric constant resistivity in high entropy oxides.²⁹ As such, although the lack of conductivity makes CuZIGO unsuitable for TCO applications, further investigation should be performed to explore these alternative possibilities.

The pseudoabsorbance spectra extracted from total reflectance data for the $x = 0.25, 0.5, 0.75$, and 1 samples are depicted in **Figure 3.13a**, along with the spectra for $x = 0$ (ZIGO) from Rickert *et al.*⁶ for comparison. All four compositions show a peak centered around 1.6-1.7 eV,

which corresponds closely to the observed absorbance features attributed to characteristic d-d transitions of octahedral Cu^{2+} in previously studied Cu-containing oxides.³⁰⁻³⁵ This explanation is consistent with the facts that the peak is absent in the $x = 0$ spectrum, becoming more intense relative to the maximum absorbance with increasing Cu^{2+} content, and that it shifts minimally in energy between $x = 0.25$ and $x = 1$. It also adds further support to the assignment of Cu^{2+} to the 16f site over non-octahedral sites like the 4a or 4b sites, and supports that the conclusion that Cu-occupancy behavior is constant at all Cu contents.

All four spectra in **Figure 3.13a** also exhibit an absorbance edge between 2 and 3 eV, shifting to lower energies with increasing Cu^{2+} content. The band gap values associated with these edges were extracted and depicted in **Figure 3.13b** as a function of Cu^{2+} content with the reported E_g value for ZIGO for comparison. Substitution of Zn with Cu causes continuous band gap narrowing, possibly through mixing of the Cu 3d orbitals with the valence band of ZIGO as has been reported for other Cu-Zn solid solutions.^{31,34,35} The decrease in estimated band gap occurs sharply from $x = 0$ to 0.5, and subsequently vary gradually until $x = 1$. Although this behavior is often indicative of a solubility limit, as discussed previously, diffraction data strongly suggests that the solid solution is complete. Alternatively, like the observed lattice parameter trends in **Figure 3.8**, the band gap may exhibit deviation from that of an ideal (linear) solid solution. However, given that the departure from linear behavior occurs at a different composition than the lattice parameters, this is probably not the case. Most likely, the observed plateau in band gap is an artifact of the band edge crossing into the energy range of the Cu d-d transitions, resulting in a fixed, false minimum treated as the pre-edge background in the employed method of estimation.

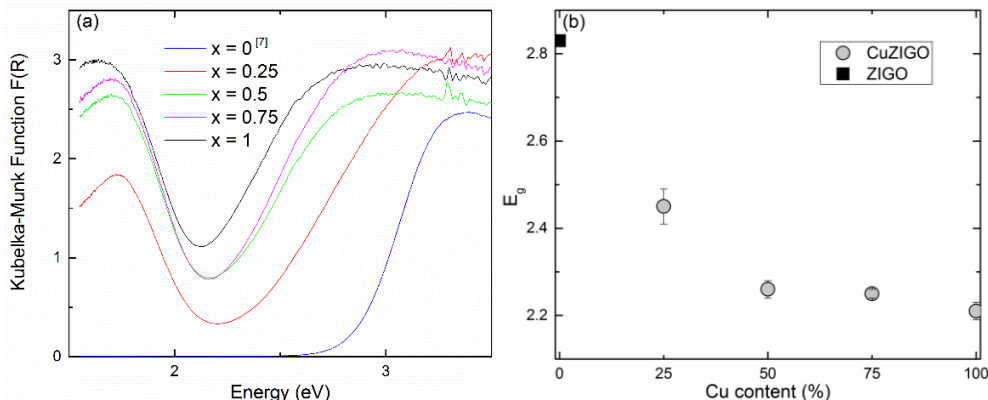


Figure 3.13. (a) Kubelka-Munk transformed diffuse reflectance spectra for CuZIGO samples, $x = 0$ data from Rickert *et al.*⁶, and (b) extrapolated band gap estimates for CuZIGO

3.3.3: Further substitution in the ZIGO structure

In addition to Cu^{2+} , other first row transition metal cations commonly occurring with either a 2+ or 3+ oxidation state were substituted into ZIGO to probe the extent of its compositional space. A summary of these experiments and their results is provided in **Table 3.7**. Estimated solubility limits were determined for each substitute-target pair by the highest nominal replacement percentage in the precursor mixture which produced either a phase pure product, or one in which secondary phases were present in such minor amounts that they could be reasonably attributed to causes such as precursor volatilization rather than inherent solubility limits. The PXRD patterns for these (nearly) phase pure compositions are presented in **Figure 3.14**.

Table 3.7. Successful isovalent cation substitutions performed in the ZIGO structure.

| Substitute | Target | Estimated Solubility Limit (%) |
|------------|--------|--------------------------------|
| Mn | Zn | 100 |
| Mn | In | 12.5 |
| Fe | In | 50 |
| Co | Zn | 100 |
| Ni | Zn | 50 |

In their original report of ZIGO, the authors found no evidence of solid solution and concluded that the material was a distinct phase with a very narrowly defined composition. The results presented here augment this description by showing that while the stoichiometry of the

structure is seemingly constrained, the composition is less so. However, that does not mean that the specific substitution behavior for any given cation is as straightforward as that of Cu^{2+} . While characterization comparable in detail to that for CuZIGO has yet to be performed for each of these new ZIGO structure phases, all of the patterns in **Figure 3.14** exhibit features that may provide insight into their substitution behavior, such as partial solubility or unexpected changes in the unit cell size.

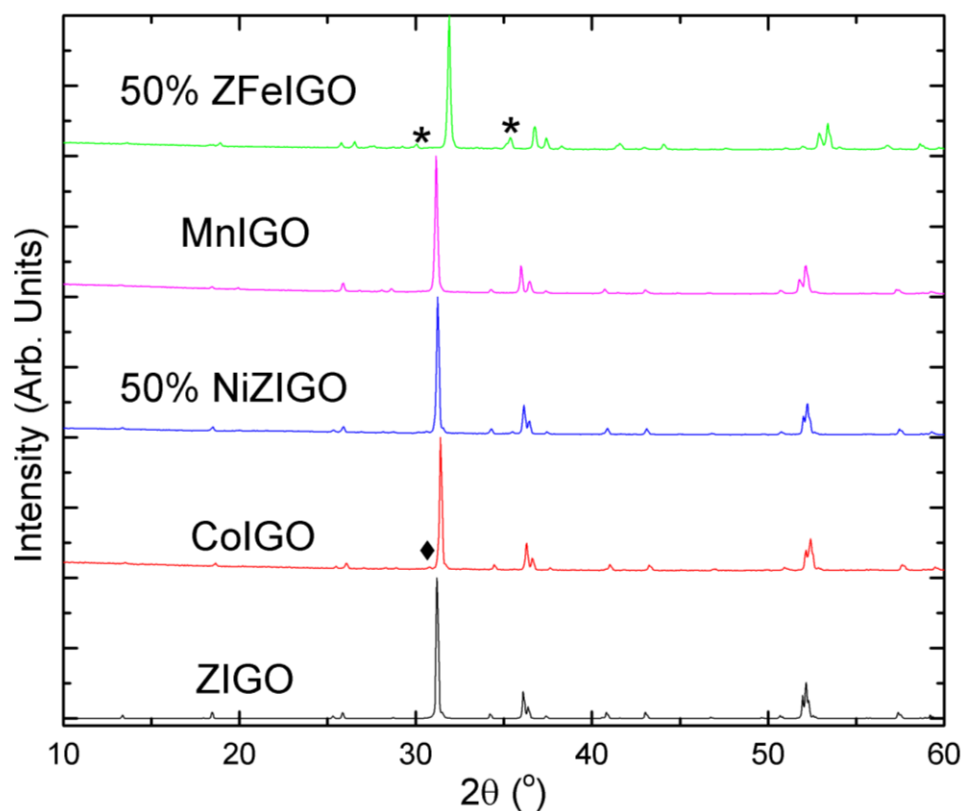


Figure 3.14. PXRD patterns of substituted ZIGO materials with the pristine ZIGO pattern for comparison. Symbols mark the apparent presence of the secondary phases In_2O_3 (diamond) and ZnFe_2O_4 (star).

The apparent solubility limits for Fe and Ni are an obvious deviation from the observed behavior in CuZIGO. As shown in the series of powder patterns in **Figure 3.15** complete replacement of either In^{3+} with Fe^{3+} or Zn^{2+} with Ni^{2+} , results in a pattern entirely consisting of secondary phases and no trace of the ZIGO structure remaining. In both cases, decreasing the

(nominal) amount of replacement increases the amount of ZIGO-structure phase observed. For Fe^{3+} , a small amount of ZnFe_2O_4 is observed at $x = 0.5$, suggesting the solubility limit lies just below that. Interestingly, this corresponds quite closely with the proportion of In occupying the 8e site (~46 %) and therefore may suggest preferential Fe^{3+} occupancy on that site. It is also worth noting, however, In substitution with Fe significantly contracts the unit cell, as evidenced in **Figures 3.15** by a large shift of peak positions to high angles. Thus it is possible, that beyond ~50 % Fe substitution the structure becomes too strained to be stable, regardless of which site is occupies. For Ni, however, strain is unlikely to be the issue as its size is comparable to that of Zn^{2+} and Cu^{2+} . An alternative explanation is its d^8 configuration, which switches from JT inactive in octahedral environments to JT active when tetrahedral. This makes Ni^{2+} highly sensitive to local coordination, and gives it a preference for undistorted octahedral sites like those in Ni_2GeO_4 , the observed secondary phase at high Ni-concentrations.³⁶ Since the partial solubility of Ni^{2+} demonstrates its limited stability in the structure, it is more consistent with substitution on the strongly distorted 16f site than on the much more regular 8e site (see **Table 3.6**).

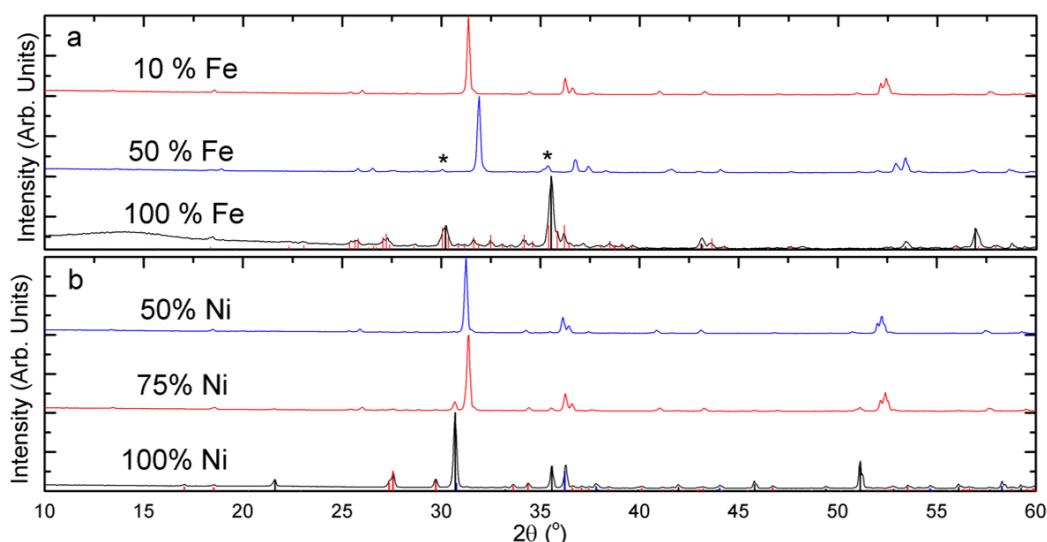


Figure 3.15. Partial solubility of (a) Fe^{3+} and (b) Ni^{2+} in the ZIGO structure. PXRD patterns as a function of nominal replacement percentage for each cation. Vertical lines represent calculated reflections for secondary phases. In (a): ZnFe_2O_4 (black) or $\text{Zn}_5\text{Fe}_{10}\text{Ge}_8\text{O}_{36}$ (red). In (b): In_2O_3 (black), Ni_2GeO_4 (blue), or $\text{In}_2\text{Ge}_2\text{O}_7$ (red).

The most interesting aspect of the CoIGO pattern in **Figure 3.14** is that it appears to be contracted relative to ZIGO. Since Co^{2+} in an octahedral environment is the same size as, or even slightly larger than Zn^{2+} , complete replacement would be expected to result in either little change to the lattice parameters or even a slight increase, contrary to what is observed. Since Co^{2+} has a d^7 electron configuration, it should exhibit a weak JT effect in a high spin environment, typical of oxides under ambient pressure. As such, this unexpected contraction may be a related effect to the expansion observed in CuZIGO at high Cu^{2+} contents. However, without more detailed characterization of CoIGO, the relationship between these effects and the JT effect remains inconclusive.

Mn substitution presented the most complex behavior of any of the cations incorporated into the ZIGO structure. **Figure 3.16** depicts the powder patterns from a several different MnZIGO samples. At $x = 0.25$, the product is clearly a mixture of a ZIGO-structure phase and In_2O_3 , suggesting that somehow In was being replaced instead of Zn. As this should produce a deficit in $2+$ cations, it also implied the loss of Ge^{4+} to maintain the ZIGO stoichiometry although this was not observed in a secondary phase likely because of GeO_2 volatility at high temperatures in inert atmosphere.³⁷ The same products, in a different ratio, are observed at $x = 1$, so Mn must present in both the $2+$ and $3+$ oxidation states in order to maintain the ZIGO stoichiometry. Systematically decreasing the In_2O_3 present in the precursor mixture directly reduced the amount of In_2O_3 in the product mixture without affecting the ZIGO-phase product (MnIGO). Phase-purity was achieved after elimination of 35% of In from the precursor mixture. This corresponds to a nominal composition of $\text{Mn}_{0.456}\text{In}_{0.705}\text{Ge}_{0.46}\text{O}_{2.43}$. Constraining this to a 1:2:1 ratio for $2+, 3+,$ and $4+$ cations (rounded ZIGO stoichiometry) gives $\text{Mn}_{0.4}(\text{Mn}_{0.1}\text{In}_{0.7})\text{Ge}_{0.4}\text{O}_{2.4}$, or about 1/8 of the In sites

containing Mn^{3+} . This would require a loss of about 20% of the original GeO_2 content, or 21 mg, which would account for part of the observed mass change after reaction (-52 mg). GeO_2 volatilization is expected to proceed through decomposition into $\text{GeO}_{(g)}$ and $\text{O}_{2(g)}$, which likely explains how Mn^{2+} was oxidized even in a flowing Ar atmosphere. The ratio of $\text{Mn}^{2+}:\text{Mn}^{3+}$ is therefore $\sim 4:1$ in MnIGO, in contrast to the 1:6 ratio in braunite, likely explaining the stability of the ZIGO structure at this composition.

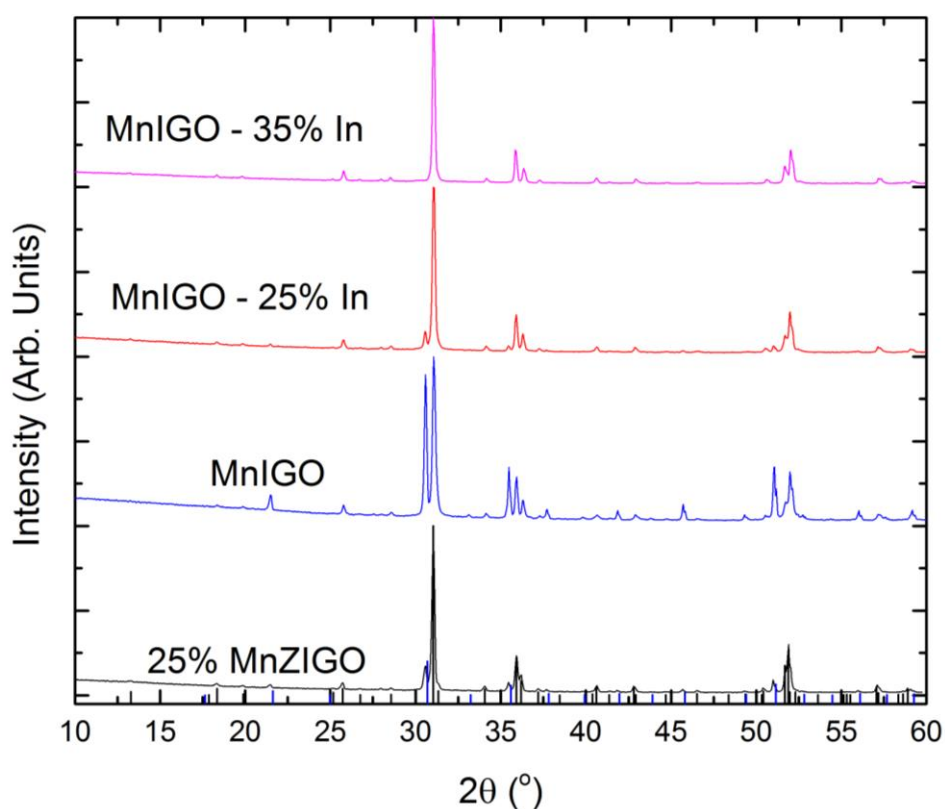


Figure 3.16. PXRD patterns of Mn-containing ZIGO samples. Vertical lines indicate calculated reflections for a ZIGO structure phase (black) and In_2O_3 (blue).

The peak positions of the MnIGO pattern show very little change from those of ZIGO, despite the fact that in 6-coordinate sites Mn^{2+} ($r = 83, 90$ pm) is substantially larger than the Zn^{2+} ($r = 0.74$ pm) it is replacing.²⁴ It may be that this substitution is stabilized by the simultaneous replacement of Mn^{3+} ($r = 64.5$ pm) for In^{3+} ($r = 80, 92$ pm), which should lead to a contraction,

which would explain why it appears both substitutions occur together despite conditions which should favor only Mn^{2+} being present. Additionally, the comparable sizes of In^{3+} and Mn^{2+} in 8-coordinate sites ($r = 92, 90$ pm respectively) may predispose the latter to substitution in the 4a site, analogous to its site preference in braunite.^{15,16,24} Furthermore, $d^4 \text{Mn}^{3+}$ has a strong JT effect like Cu^{2+} which may predispose it to occupy the 16f site. Together, this would change the charge distribution of the structure significantly, as well as confine the magnetically interesting Mn^{3+} ions to the “A” layers of the ZIGO structure. More detailed structural characterization may be carried out to determine if this is the case.

As discussed above, the existence of these single-phase compositions demonstrates significant compositional robustness in the ZIGO structure which, at least in the case of the Cu-Zn solid solution, gives rise to notable occupational disorder. If all of these phases are freely soluble in each other, in particular those that appear to prefer the 16f site (NiZIGO, CoIGO, and CuIGO), it is possible that several truly high-entropy or entropy-stabilized compositions may be obtained. As such, a precursor mixture containing equimolar amounts of Cu^{2+} , Co^{2+} , Ni^{2+} , and Zn^{2+} was prepared (CuCoNiZIGO). The powder pattern of this mixture post-reaction is depicted in **Figure 3.17** compared with the calculated reflections of ZIGO. There are no unaccounted for or unmatched peaks (except the main peak Cu $K\beta$ satellite at $2\theta = 27^\circ$), indicating that the product is phase pure. Lack of any In or Ge-containing secondary phases suggests that none of the 2+ cations were lost to volatilization, maintaining the stoichiometry. The increasing offset between the experimental predicted peak positions with increasing angle shows a contraction in the CuCoNiZIGO product relative to the pure Zn phase, like in CoIGO. Overall, the pattern appears to suggest the successful synthesis of ZIGO phase with six cations.

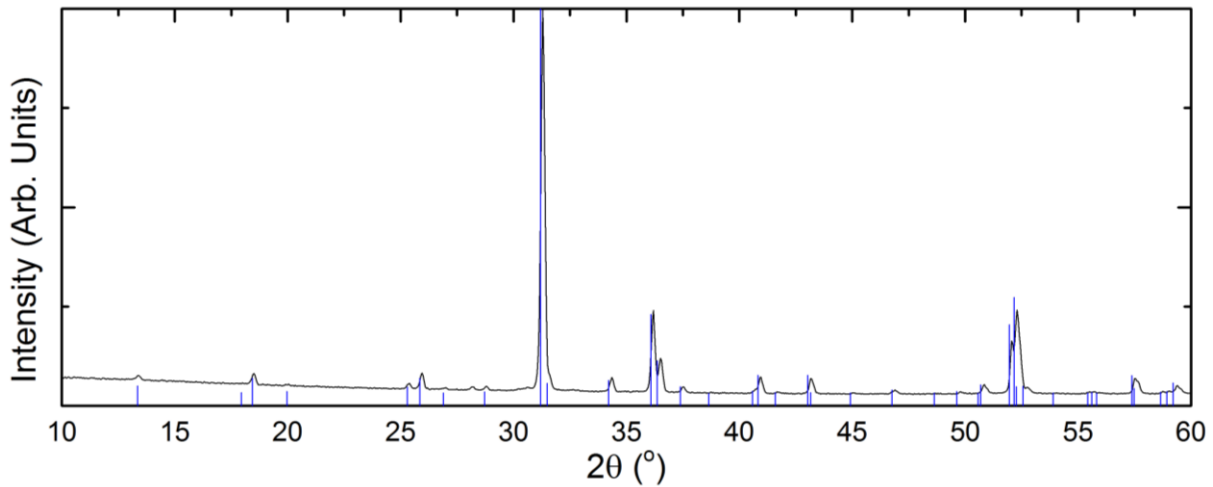


Figure 3.17. PXRD pattern of the nominal composition $(\text{Cu}_{0.25}\text{Co}_{0.25}\text{Ni}_{0.25}\text{Zn}_{0.25})_{0.456}\text{In}_{1.084}\text{Ge}_{0.46}\text{O}_3$. Vertical lines indicate ZIGO reflection positions.

Given the tendency towards disorder on the 16f site in the ZIGO structure demonstrated by the CuZIGO solid solution and the large number of cations in this product, there is a significant probability that it qualifies as a high entropy oxide. The conventional threshold for high entropy has been established as a configurational entropy greater than $1.5 \cdot R$.^{21,38,39} The molar configurational entropy (S) in an ideal solution with N -components is given by the equation:

$$S = -R \sum_i^N x_i \ln(x_i) \quad (3.1)$$

where R is the molar gas constant and x_i is the mole fraction of the i th component. Applying equation 3.1 to the nominal cation stoichiometry of CuCoNiZIGO results in an ideal $S = 1.68 \cdot R$, qualifying as a high entropy phase. However, this assumes that all the cations substitute preferentially on the 16f site without ordering. **Figure 3.18** compares the experimental and simulated, assuming the ZIGO structure, SAED patterns of the $[\bar{2}61]$ zone axis in CuCoNiZIGO. This clearly show the emergence of extra spots between the main expected reflections. A subset of these correspond well with reflections from the $(1\bar{1}4)$ family of planes which should be systematically absent in the $I4_1/amd$ space group, implying the presence of super structure ordering

which reduces the symmetry of the phase. The additional extra spots that lie halfway between the $1\bar{1}4$ and $2\bar{2}8$ reflections may be a result of modulation in the material. Further characterization is necessary to determine how ordering occurs and whether or not the phase still exhibits significant configurational entropy.

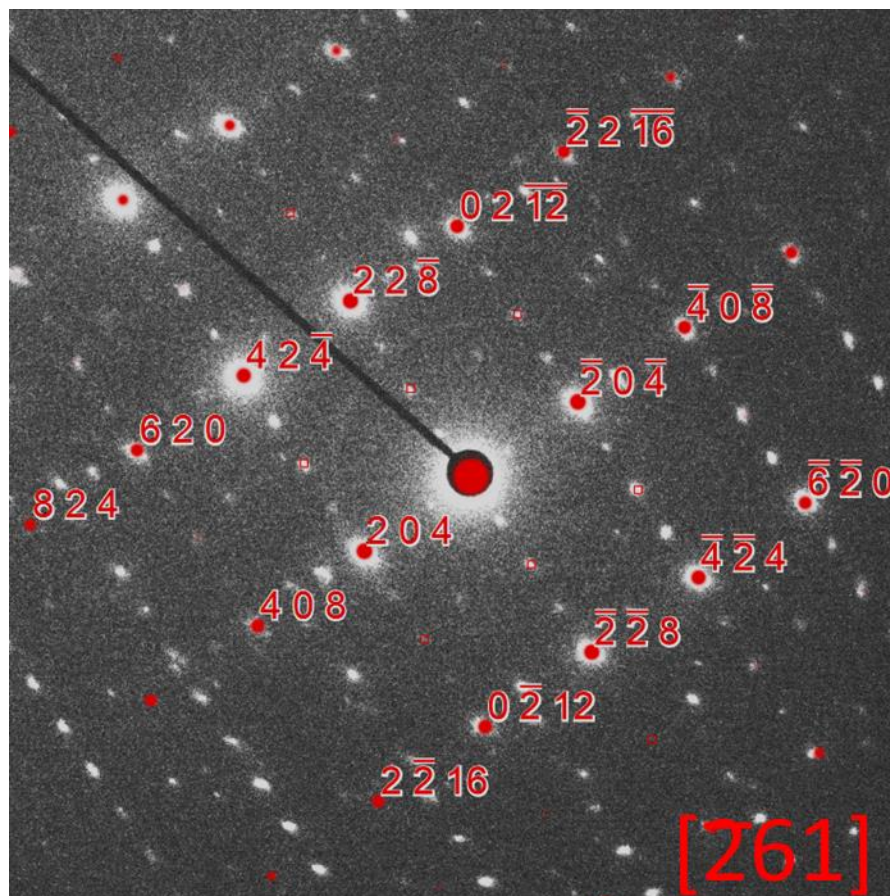


Figure 3.18. Experimental and simulated SAED pattern of the $[261]$ zone axis in CuCoNiZiGO. Simulated spots assume $I4_1/amd$ symmetry, with disorder on the 16f sites. Closed red circles indicate main reflections, open circles denote expected systematic absences.

3.4: Defect Fluorites in M-In-Sb-O

Simple powder patterns for three different metal indium antimony oxides are shown below in **Figure 3.19a**. As depicted, the principle peaks in these patterns are an excellent match for a hypothetical defect-fluorite phase with a lattice parameter of about 5.07 \AA . This is notable because ordered ADF structures are common in chemically related materials such as In_2O_3 and

$\text{In}_{5.5}\text{Sb}_{1.5}\text{O}_{12}$, whereas only one In- or Sb-based disordered defect fluorite oxide has been reported in the ICSD.^{8,40} However, in all three patterns there are minor, broad peaks that should not appear in a pure fluorite pattern. A close-up of the region from $36^\circ < 2\theta < 50^\circ$ shows that these minor peaks are remarkably consistent between all three patterns. Furthermore, they do not match any known phases in the In-Sb-O system. As such, they are unlikely to represent the presence of a secondary phase common to all three compositions. Instead they probably indicate subtle structural features such as modulation or superstructure which modify the basic fluorite unit cell.

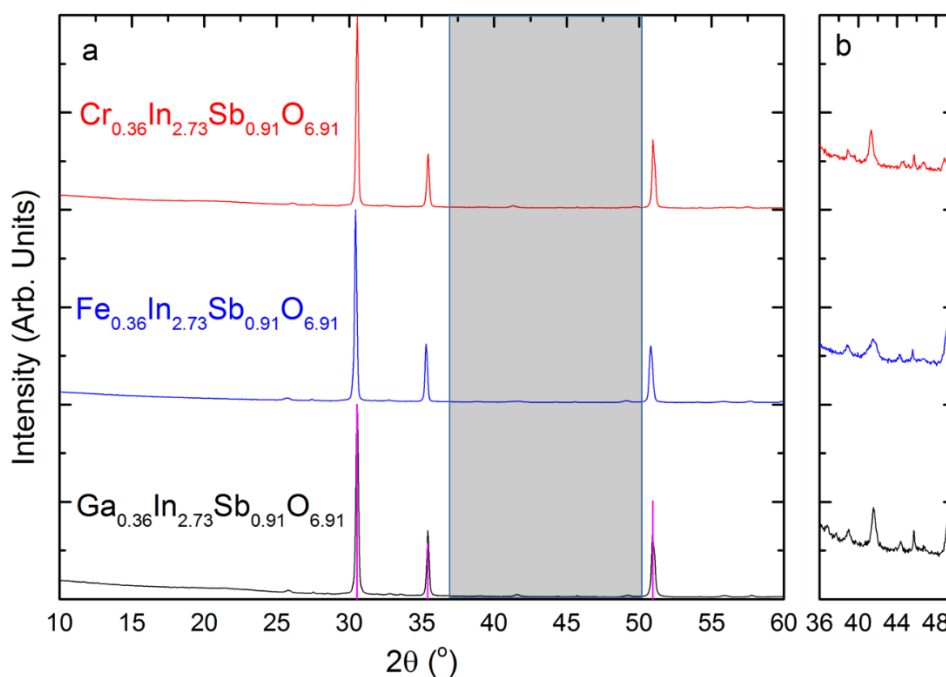


Figure 3.19. (a) PXRD patterns of three new possible defect-fluorite phases with nominal compositions normalized to a total of four cations. Vertical lines indicate the (111), (200), and (220) reflections of a hypothetical defect fluorite phase with a lattice parameter $a = 5.07$ Å. (b) Close-up of the highlighted region in (a) with 20x intensity.

It should be noted that the nominal compositions of these phases comprises primarily In and Sb with only minor amounts of a third metal ($M = \text{Cr}, \text{Fe}, \text{or Ga}$) added. Specifically, the cation ratio is 0.4:3:1 ($M:\text{In}:\text{Sb}$). Curiously, these phases appear very sensitive to this amount of M in the precursor mixture, despite that it accounts for only a $1/11^{\text{th}}$ of the total cation content and lacks any quantitative relationship to the symmetry of the defect fluorite structure. **Figure 3.20** depicts

the changes observed in the PXRD patterns of products as the amount of Ga, as representative example, is varied systematically. When increased, slight secondary phase peaks appear, indicating that a solubility limit has been exceeded. Upon decrease, the (111) and (220) peaks begin to broaden and split, suggesting decomposition into a lower symmetry phase, likely an ordered ADF structure.

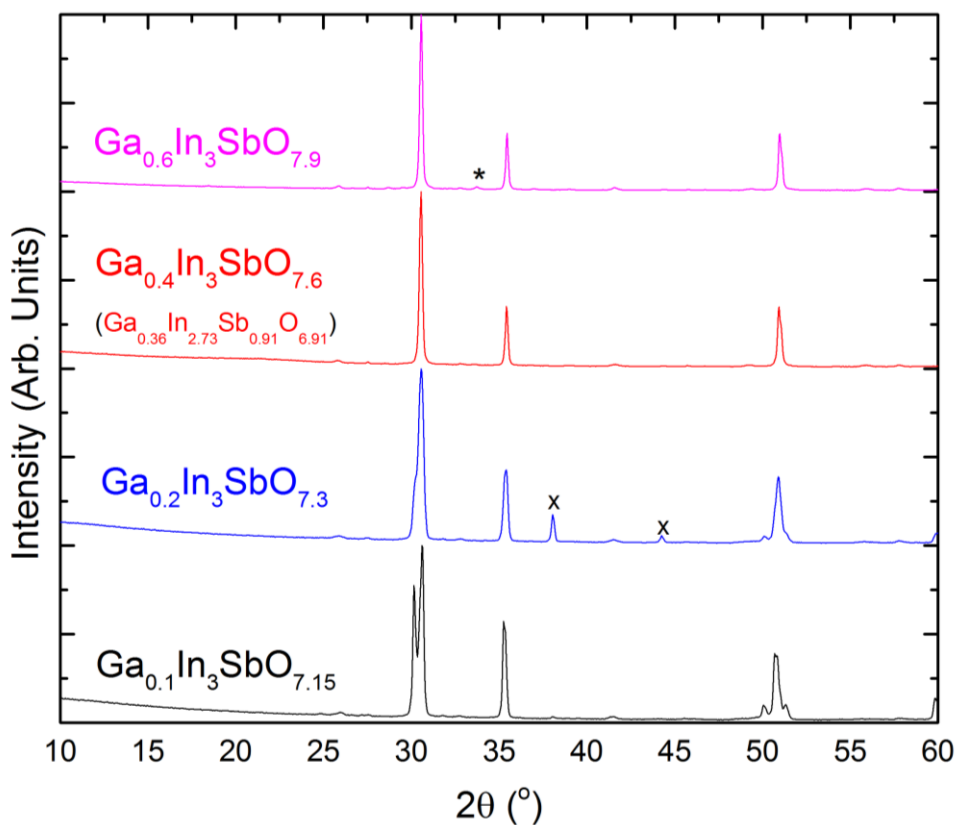


Figure 3.20. PXRD patterns of mixtures of Ga and In_3SbO_7 with systematically varied Ga content. Peaks marked by an “x” arise from an Al sample holder. Phase pure composition is shown in normalized form as well. The peaks marked with an asterisk indicates an unknown secondary phase present only at the highest Ga^{3+} concentration.

Such transitions are common in the rare earth fluorite related phases, where the stable structure commonly changes from defect fluorite to pyrochlore with increasing cation size.^{41,42} Similarly, the transition indicated in **Figure 3.21** is correlated with average cation size, as all of the M^{3+} metals are smaller than In^{3+} and removing them increases the average cation size on the multi-occupancy site. However, previously studied disorder-order ADF transitions show that the

superstructure reflections are distinct from the main fluorite peaks, simply growing in intensity as the cation size increases.⁴¹ In contrast, the new peaks in **Figure 3.21** change in both intensity and position, appearing to gradually split from the main peaks as the concentration of Ga decreases. This continuous behavior is more reminiscent of a solid solution than a sudden structural transition or two-phase equilibrium. If that is the case, it would appear that the Ga (as well as Cr and Fe) content is a parameter which can be manipulated to continuously tune the degree of ordering in the structure. The reason for this is unclear, although it may be tied to an entropic driving force in combination with a more favorable ability to mix with the small Sb^{5+} cation sites. If applicable to other systems, this phenomenon could be leveraged to target new, disordered phases outside of theory-based prediction methods by starting with ordered superstructures.

Verification of the accuracy of the nominal stoichiometry was attempted using both ICP-OES and TEM EDX. Unfortunately, the samples proved insufficiently soluble in HNO_3 , HCl , HF , or mixtures thereof to be investigated with the former technique. The latter was performed on two grains of $\text{Cr}_{0.4}\text{In}_3\text{SbO}_{7.6}$, with two spectra collected on each grain representing the bulk and edge respectively. The area of each EDX scan as well as general elemental maps for both particles are shown below in **Figure 3.21**, and the calculated compositions for each spectrum are presented in **Table 3.8**. In both cases, the only variation apparent in the elemental distribution is the expected gradient towards the edge of the particle where the thickness is lower, resulting in lower counts. As this is consistent for all observed elements, the grains appear to be highly homogenous.

Table 3.8. Average experimental and nominal composition of two $\text{Cr}_{0.4}\text{In}_3\text{SbO}_{7.6}$ grains as determined by TEM EDX.

| Element | Nominal (%) | Spectrum 1 (%) | Spectrum 2 (%) | Spectrum 3 (%) | Spectrum 4 (%) |
|---------|-------------|----------------|----------------|----------------|----------------|
| O | 63.33 | 60 | 60 | 60 | 60 |
| Cr | 3.33 | 5.23 | 5.24 | 5.52 | 5.89 |
| In | 25.00 | 27.54 | 27.54 | 27.65 | 27.47 |
| Sb | 8.33 | 7.23 | 7.22 | 6.83 | 6.64 |

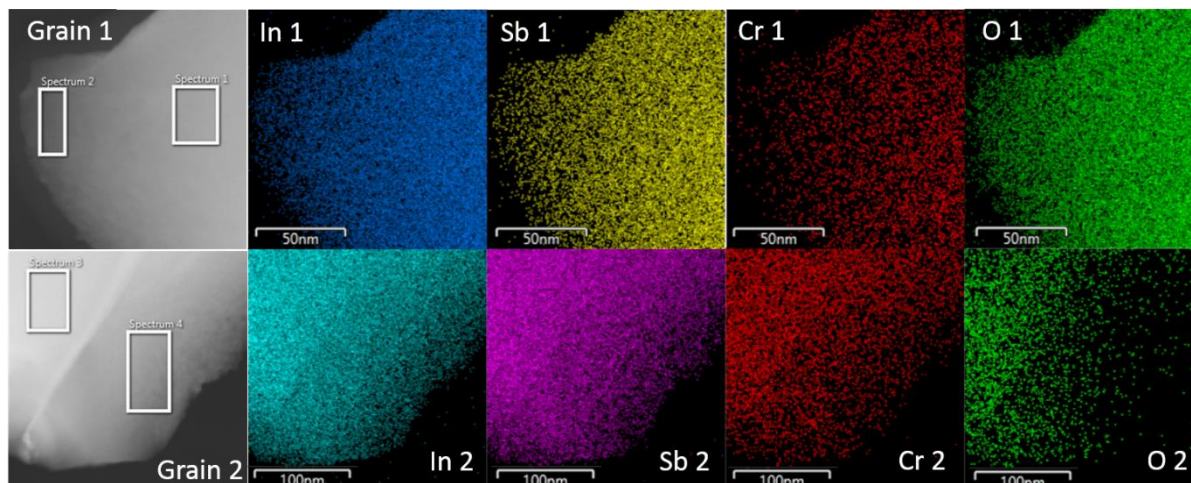


Figure 3.21. TEM EDX performed on two grains of nominally $\text{Cr}_{0.4}\text{In}_3\text{SbO}_{7.6}$.

The values in **Table 3.8** clearly suggest that the actual composition differs from the nominal one. The samples are enriched in In and Cr while being deficient in Sb. However, assuming an uncertainty of $\pm 5\%$ all four spectra are the same within error. The average composition of the four spectra is $\text{Cr}_{0.55}\text{In}_{2.75}\text{Sb}_{0.7}\text{O}_6$. However, this is not charge-balanced, with an excess charge of +1.4 per formula unit. Since O is a very light atom, a higher error in the uncertainty of its composition is expected. Thus, it is not unreasonable to adjust the O amount slightly for charge compensation, especially since this only requires $\sim 10\%$ deviation from the experimental value. The experimental composition, normalized to four cations, is therefore $\text{Cr}_{0.55}\text{In}_{2.75}\text{Sb}_{0.7}\text{O}_{6.7}$. Notably, the experimental anion to cation ratio, 1.675, is within the typical range for a defect fluorite structure. Assuming no loss of Cr during reaction, the shift from the nominal stoichiometry to the experimental one requires a loss of about 34% In and 50% Sb. Given their original 3:1 ratio, that is a 2:1 ratio of In:Sb in the lost material. There is no known In-Sb-O phase with this cation stoichiometry, so it is not clear how exactly these losses would arise consistently. However, the enriched Cr amount is about $1/8^{\text{th}}$ of the total cation content. Since the cation site in the defect fluorite structure has a multiplicity of four, this corresponds to about one

Cr atom in every other unit cell, which could be related to the superstructure/modulation peaks hinted at in the PXRD patterns.⁴¹ If so, this relationship may explain why phase purity is so specific to a particular precursor composition.

Given the homogeneity of the particles and the consistency between all four spectra this should reflect the bulk composition of these grains, if not the entire material. However, an important consideration in TEM is that only a small fraction of the sample is actually measured, and it is possible that two grains of a minor secondary phase that are not representative of the bulk were coincidentally selected. This is especially important to consider given the discrepancy between the nominal and experimental compositions without an obvious explanation about what happened to the excess In and Sb. SAED and HRTEM were performed to check whether this was the case.

Figure 3.22 shows the results of this analysis on the Cr-In-Sb-O particles. The SAED patterns for the [112] and [110] zone axes (**Figure 3.22a,b**) reveal that their main spots clearly match those of the simulated defect fluorite diffraction pattern. This indicates that the basic, bulk structure of these particles is defect fluorite, despite their deviations from the nominal stoichiometry. However, both zone axes also show distinct satellite reflections between the main spots consistent with additional long range symmetry such as superstructure or modulation. Interestingly, the corresponding high resolution micrographs (**Figure 3.22d,e**) depict distinct, periodic stripes of contrast. Similar features have previously been attributed to superstructure arising from periodic distortion in the basic crystal structure, or interference arising from superimposed, slightly-mismatched lattices.^{43,44} The latter is unlikely here as it would also result in two slightly-offset but superimposed sets of diffraction spots, whereas the SAED patterns

clearly show only one set with well-defined spots.. Here, **Figure 3.22e** shows that these stripes are either not present or not as well resolved the very edge of the particle. Collecting SAED on this part (**Figure 3.22c,f**) reveals only the main fluorite reflections without any extra spots. This further suggests that the stripes arise from the same source as the satellite spots, long-range ordering, rather than interference. The apparent thickness dependence of these effects may indicate that at the edge, the particle is thinner than the characteristic length scale of the ordering. However, it is also possible that they are weaker and need a longer exposure time to be observed at the thinner edge. EDX spectrum 2 (**Figure 3.21**) shows that the edge composition does not deviate from the rest of the particle, ruling it out as an explanation for the lack of long-range ordering at the edge.

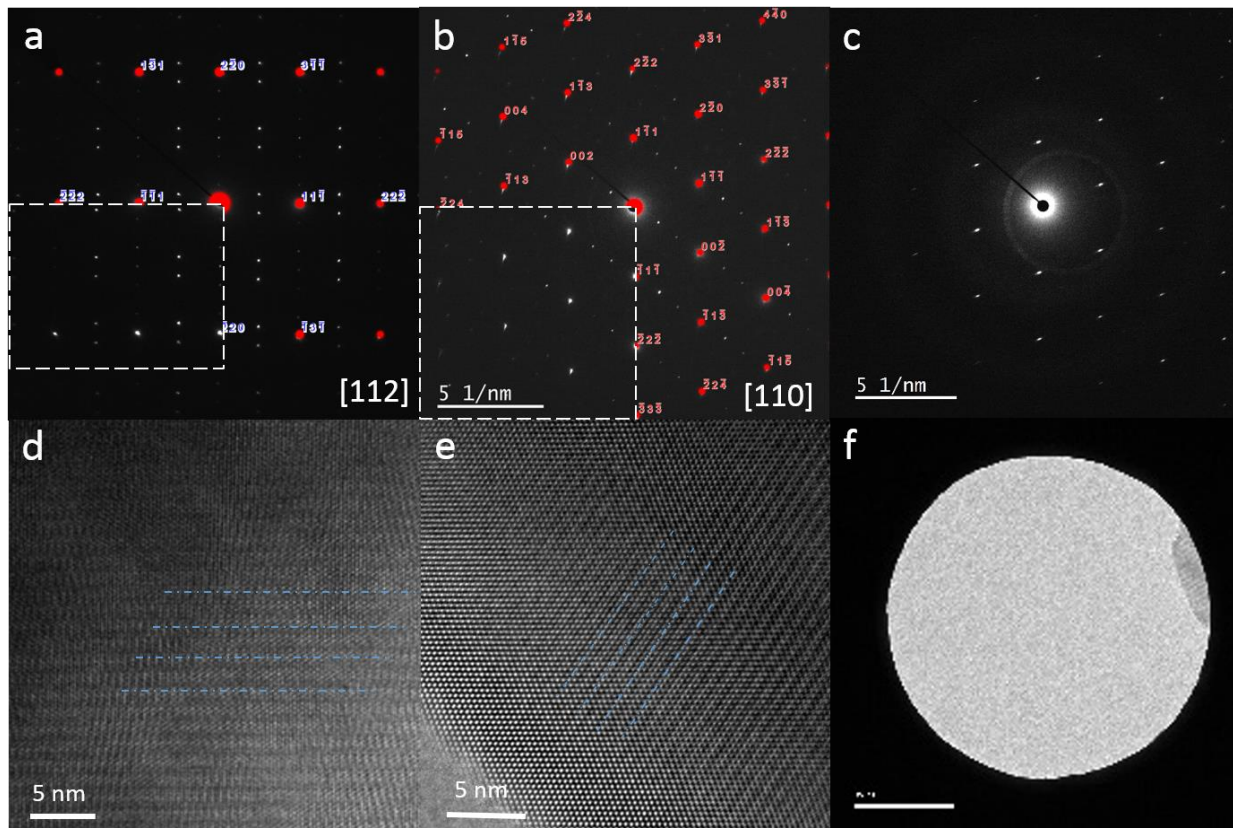


Figure 3.22. SAED (a, b, c) and corresponding HRTEM (d, e, f) performed on $\text{Cr}_{0.4}\text{In}_3\text{SbO}_{7.6}$ from grain 2 (a, d) and grain 1 (b, e and c, f). Red spots are simulated diffraction patterns for a defect fluorite structure. Inset regions in (a, b) are free of the simulated overlay to clearly show main reflections. Dashed blue lines in (d, e) are guides for the eye to emphasize the observed contrast striations.

Satellite peaks like those in **Figure 3.22** were also observed in $\text{Y}_2\text{Sn}_{2-x}\text{Zr}_x\text{O}_7$, which undergoes transition from defect pyrochlore to defect fluorite at $x = 1.4$. In that case, the authors ascribed them to compositional and/or displacive modulation, owing to local (10-30 Å) retention of pyrochlore ordering.⁴² Given the gradual nature of the order-disorder transition depicted in **Figure 3.20**, it is possible that it entails a continuous confinement of anion ordered domains to progressively smaller scales. When the structure is disordered on average, the sparse distribution of ordered regions may appear as long range modulation. As mentioned above, ordering in the ADF family of phases reflects the arrangement of the anion sublattice, but with three cations of varying radius in all of these phases, cation ordering is likely as well. Further characterization, with local and long-range techniques, is critical to elucidate the subtle structural aspects of these phases which are expected to have strong implications for potential properties of interest in these materials such as their configurational entropy or oxygen-ion mobility.⁴¹

3.5: Conclusions and Future Directions

In summary, several new phases have been identified in two ADF structure types with significant disorder, putting them outside the practical scope of theory-based materials design. Single phase ZIGO-structure materials have been obtained for Cu^{2+} , Co^{2+} , and $\text{Mn}^{2+}/\text{Mn}^{3+}$ analogues of ZIGO, as well as with ~50% Zn-replacement by Ni^{2+} or ~50% In replacement by Fe^{3+} . Furthermore, a complete solid solution between the Cu and Zn analogues has been demonstrated. Additionally, three previously unknown defect fluorite phases have been identified in the M-In-Sb-O ($\text{M} = \text{Cr}^{3+}, \text{Fe}^{3+}, \text{Ga}^{3+}$) phase space. A systematic synthetic investigation revealed that the phase purity of these products, as determined by PXRD, exhibits a strong dependence on

the nominal composition, with single phase patterns for all M appearing only with a 0.4:3:1 M:In:Sb ratio in the precursor. These discoveries represent both a radical expansion of the known phase space of the ZIGO structure, until now containing only the eponymous material which exhibits little compositional flexibility, and the first examples of defect fluorite in any indium antimonates.

One set of samples from each was selected for more detailed characterization, serving as a case study of these structure types. In ZIGO, structural investigations of the Cu/Zn solid solution as a case study suggest that Cu^{2+} sits only on the 16f site, resulting in quadruple occupancy of that site in compositions intermediate to the solid solution. Variation in the lattice parameters with Cu^{2+} reveal negative deviations from Vegard's law and an abnormal increase at the CIGO endpoint. Pseudoabsorbance data derived from diffuse reflectance measurements similarly show deviations from linear behavior, as well as demonstrates tunability of the band gap with Cu^{2+} content. In defect fluorite, the stoichiometry for M = Cr samples determined by EDX, $\text{Cr}_{0.55}\text{In}_{2.75}\text{Sb}_{0.7}\text{O}_{6.7}$, indicates an excess of Cr relative to the nominal composition, but the mechanism of In and Sb loss during reaction remains unclear. However, the experimental anion:cation ratio (1.675) remains within the range previously observed for defect fluorite. SAED and HAADF performed on these samples confirmed the fundamental defect fluorite structure but also revealed strong evidence for additional long-range order in the form of satellite spots between the fundamental fluorite reflections and contrast stripes in high-resolution images of the lattice. As the search for new materials continues, quaternary and quinary phases are likely to become increasingly relevant owing to the already thorough exploration of binary and ternary compounds becoming increasingly complete. As such, not only does the discovery of these new phases complement theory-based

materials design approaches, it also demonstrates some of the challenges and opportunities that will become more common as new phases become increasingly complex.

The most relevant opportunity to the phases found here is probably the potential to identify new high entropy oxides (HEOs). The study of these materials is a recent field of materials science which developed from investigations into the more broadly defined high entropy alloys (HEAs). HEAs are typically mixtures of five or more metals, often equiatomic, that crystalize in simple atomic arrangements such as FCC, BCC, or HCP lattices, and as a result have high configurational entropy. This has been shown to result in remarkable improvements in strength, thermal stability, fatigue and fracture resistance, and other physical properties over their low-entropy alternatives.^{45,46} Inspired by these results, Rost et al. applied the same approach to equiatomic mixtures of binary oxides, and found that they could make a single-phase rocksalt structure with a high-entropy cation sublattice, demonstrating that it could arise from more complex precursors than pure elements.²¹ Further research has discovered high entropy in other ceramic structures like fluorite, perovskite, and spinel, the latter two being especially notable as they indicate that HEOs can form in host structures with multiple cation sites.^{22-24,47,48} Importantly, all reported HEOs follow the same approach of combining precursor oxides in which the cations are similar in size, typically being either all transition or rare-earth metals. In perovskite HEOs, these two sets of cations can be used to produce high entropy exclusively on B or A sites respectively, or both when transition and rare-earth metals are incorporated together.⁴⁸ Owing to the nascent nature of the field, the properties of HEOs have not been as well-explored as those of HEAs. However they have already demonstrated colossal dielectric constants, superionic conductivity, and enhanced

catalytic and thermal properties tied to their high configurational entropy.^{28,29,48} As such, the discovery of new HEOs is a valuable pursuit to the materials research community.

The inherent disorder in both the ZIGO structure (on the 16f site) and the defect fluorite structure makes them good candidates for HEO research. However, as referenced in the discussion of CuZIGO, the specific examples here also offer an additional advantage to this endeavor: the (apparent) inclusion of In^{3+} and either Ge^{4+} or Sb^{5+} on the high entropy site. As neither transition metals nor rare-earth elements, these species represent an important addition to the design principles for targeting HEOs. Furthermore, the large difference in size between these species would also set a new precedent for what can be tolerated in HEOs. It should also be noted that the defect fluorite structure provides an opportunity to use disorder on the anion sublattice to increase the total configurational entropy, which has generally been ignored in HEO research up to now and might be an orthogonal strategy for creating these phases.³⁹ Finally, a ZIGO-structure HEO would be the first example with more than two cation Wyckoff positions. Thus, confirming high-entropy in these phases would be an important step forward for the field of HEOs.

The compositional robustness and phase space of the ZIGO-structure established in this work is theoretically sufficient to reach a high-entropy regime, as indicated by the six-cation single phase composition, in CuCoNiZIGO. Determining whether or not this composition is actually an HEO requires elucidation of the structural causes of the extra reflections observed in SAED and their effect on the total configurational entropy. For example, should these spots indicate a displacive modulation on the disordered site rather than a compositional one, the ideal S value of $1.68 \cdot R$ may still be accurate. X-ray absorbance techniques such as XANES and EXAFS will reveal whether the cation coordination environments are the same, as they can reflect n^{th} -nearest

neighbor interactions to fairly high values of n . HAADF-HRSTEM or STEM-EDX techniques can also be used to resolve ordering by detecting compositional variation with atomic resolution. More rigorous structure solution may be obtained directly from a single crystal using X-ray and neutron diffraction. If the material melts congruently, crystals may be grown from a melt using a floating zone method to achieve the high temperatures required. Otherwise, lower temperature methods such as vapor transport or flux may be attempted. In either case, however, the complexity of the composition is likely to cause problems, either by favoring decomposition before melting or by making it very difficult to find a solvent or vapor transport agent that will be suitable to interact with all the components under the same conditions. If a single crystal cannot be obtained, precession electron diffraction may be used to get similar information from the polycrystalline material, although this technique is time and labor intensive.⁴⁹ In the event that present ordering does mitigate the entropy of the phase, systematic high temperature annealings will be performed to encourage cation mixing on one site. If it is revealed that one particular species, such as Co or Ni, is preferentially substituting on a site other than 16f, substitution with other transition metals (like Fe^{3+} or Mn^{2+}) is another possible route to achieving high entropy. Once an HEO sample has been obtained, characterization of properties of interest such as the dielectric constant or ionic mobility in Li^+ doped samples can proceed.

The complex substitution behavior of Mn requires more investigation if it is to be considered as a component for a high entropy ZIGO phase. Several aspects of this behavior must be elucidated, such as the preferred substitution site for each oxidation state. Only a species that substitutes on the 16f site will be useful from a high entropy perspective. Analysis analogous to that performed on CuZIGO in this work should be sufficient to determine this given that Mn-In-

Ge-O does not contain indistinguishable species, especially if augmented with neutron diffraction. Additionally, further study is needed to determine whether the 4:1 Mn^{2+} : Mn^{3+} ratio observed in MnIGO is a fixed, stable ratio or whether a range is possible. If GeO_2 is serving as the oxidizer, then theoretically up to two Mn^{2+} may be oxidized for every Ge reduced, whereas the current formula appears to reflect a 1:1 ratio. Decoupling of the substitution of Mn^{2+} and Mn^{3+} will facilitate the targeting of high entropy compositions. Deliberate incorporation of Mn^{3+} , independent of Mn^{2+} , in the precursor mixture will allow for exploration of this phase space, which could possibly lead to interesting magnetic properties. Finally, given that $\text{Mn}_7\text{GeO}_{12}$ adopts the braunite structure, there should be some critical level of In replacement by Mn in MnIGO which will stabilize braunite over ZIGO. Since one of the key differences between these two structures is ordering on the “A” layer, which is solely composed of 16f sites in the latter, its absence that structure appears to be important to multi-occupancy in ZIGO. A synthetic investigation of this transition will therefore provide insight on possible driving forces for and robustness of high entropy in this system.

Regarding the defect fluorite phases, further investigation must begin with confirmation of the stoichiometry and structure of the M = Fe and Ga phases with SAED and EDX, to ensure that they are analogous to the M = Cr phase as PXRD suggests. If possible bulk compositional analysis methods, such as ICP, should be employed to assess the compositional range of these phases – since the nominal and experimental stoichiometries do not match, it is possible that the formula of the defect fluorite phase is more robust than suggested by the synthetic experiments. Elucidation of the true nature of ordering in these phases will provide insight on whether or not these phases can reveal a new strategy for high entropy materials, and can be performed with many of the same

techniques described for use with high entropy ZIGO phases. Additionally, since disorder in the defect fluorite structure is reflected in the anion sublattice as well, vibrational spectroscopy and ^{17}O solid state NMR could inform whether the anion coordination environments vary from what would be expected. With a complete understanding of their structure, a synthetic investigation of potential solid solutions between these three phases can be carried out to maximize their HEO potential. Simultaneously, it may be worth characterizing their properties of interest. With an anion:cation ratio of 1.675, significantly less than the ideal value of 2, there should be significant concentration of O-vacancies on the anion sublattice in $M = \text{Cr}$. If $M = \text{Fe}$, Ga are analogous, all three might exhibit O-ion conductivity favorable for fuel cell applications, which can be measured with impedance spectroscopy. The $M = \text{Ga}$ sample has a composition entirely composed of p-block metals and O, making it a potential n-type TCO candidate. Its transparency can be investigated with diffuse reflectance, while its conductivity can be measured with a 4-point probe or Hall effect measurement as part of a systematic doping study. Finally, an effort to understand the reasons that the same drastic increase in symmetry is caused by minor incorporation of either Fe, Cr, or Ga, despite difference in their size and electronic configurations, is needed in order to determine whether the effect can be generalized to make new HEOs in other anion ordered systems.

CHAPTER 4: NEW ADDITIONS TO THE RUTILE-RELATED FAMILY OF STRUCTURES

Sections of this work are reprinted with permission from

Flynn, S.; Sanghvi, S.; Nisbet, M. L.; Griffith, K. J.; Zhang, W.; Halasyamani, P. S.; Haile, S. M.; Poeppelmeier, K. R. $\text{LiIn}_2\text{SbO}_6$: A New Rutile-Related Structure-Type with Unique Ion Channels. *Chem. Mater.* **2020**.

4.1: Introduction

The wide variety of applications for rutile-related materials described in **Section 1.3.2** has made them the subject of sustained interest in the materials community for decades. One important subset of rutile-related materials that has been the target of a dedicated research focus is the Li-containing group. The characteristic channels of these compounds are theoretically conducive to high Li capacities (335 mAh/g in ramsdellite-type TiO_2) and relatively high Li-mobilities owing to an unobstructed diffusion path.^{1,2} In electrolytic manganese dioxide, a disordered intergrowth of pyrolusite (rutile-type) and ramsdellite, these properties have led to very successful application as a cathode in lithium and alkaline batteries.^{3,4} Numerous theory-based and experimental studies have utilized the diversity of structures in the rutile-related family to probe the dependency on channel size and structure type of parameters central to their possible performance as battery components, including the preferred sites of Li-occupancy in tetrahedral vs. octahedral vs. in framework sites and stability with respect to structural transitions and hydrolysis.^{1, 3-8,9-15} As such, the discovery of an entirely new Li-containing channel structure is valuable to this community by offering additional insight to previous studies and opportunities for designing solid-state Li-battery components.

This work presents the crystal structure of $\text{LiIn}_2\text{SbO}_6$ (lithium indium antimony oxide, or LIAO), which adopts a previously unreported rutile-related structure with $Pnmm$ symmetry. This conflicts with earlier reports of LIAO that describe it as cation-ordered LiSbO_3 in the $Pnn2$ space group without providing a full structural solution.¹⁶⁻¹⁸ The source of this discrepancy is identified as an unrecognized shift of Li^+ into tetrahedral coordination, which also results in a structure consistent with the Li-filled rutile-related framework motif. The chains in LIAO are comprised of

edge-sharing octahedra, with a chain width that alternates between one and two octahedral groups. That this is the first example of a rutile-related phase with this chain structure is remarkable given the chemical and structural diversity within the rutile-related family. A search of the inorganic crystal structure database reveals more than 60 phases with the FeTa_2O_6 (trirutile) structure type alone, a subfamily of rutile which has a 2:1 cation ordering in its chains, just like the framework in LIAO, but formed of simpler chains of fixed width.^{19,20,21} As such, LIAO expands the well-studied rutile-related materials family in a profound and unprecedented way which, while unlikely to have been anticipated by theory-based materials design, can now augment it as a template for new materials.

With further study, the frequency and variation of width-changes in edge-sharing chains may function as new design parameters with which to tune the properties of target materials in both theoretical and experimental studies. Here, several properties of LIAO are characterized, providing some insights on LIAO and the effect of its unique tunnel structure on ionic mobility. Subsequently, isovalent chemical substitution experiments were carried out to probe the underlying chemical factors which lead to this structure, and expand its known phase space to identify plausible routes for tuning any desirable properties it may exhibit.

4.2: Materials and Methods

4.2.1: Synthesis

Powder samples of $\text{LiIn}_2\text{SbO}_6$ (LIAO) were synthesized using standard solid state techniques. Stoichiometric amounts of Li_2CO_3 (Aldrich, 99.999%), In_2O_3 (Alfa Aesar, 99.994%), and Sb_2O_3 (Aldrich, 99%) were ground together with acetone in a mortar and pestle until

homogenous. The mixtures were then heated in air in a platinum crucible with an alumina lid to 1173 K at 5 K/min and held for 8 hours to allow for the decomposition of Li_2CO_3 and ensure oxidation of Sb^{3+} to Sb^{5+} .²² After cooling to room temperature at 5 K/min, the samples were re-homogenized in a mortar and pestle and then pressed into 13 mm diameter cylindrical pellets. The pellets were returned to their crucibles and reacted at 1473 K for 20 hours with the same heating and cooling rates as in the pre-reaction. White sintered pellets were obtained. The same procedure was used for substituted samples, but with replacement of either Li_2CO_3 with K_2CO_3 (Sigma Aldrich, 99%) or In_2O_3 with Sc_2O_3 (Alfa Aesar, 99.9%) or Fe_2O_3 (Alfa Aesar, 99.8%). Single crystals of LIAO and substituted compositions were grown using a Li_2MoO_4 flux. Polycrystalline samples were combined with Li_2MoO_4 in a 1:10 ratio by weight. The mixture was heated in a capped platinum crucible in air to 1523 K at 5 K/min. After 16 hours the furnace was first cooled to 1223 K at 3 K/hour, then to room temperature at 5 K/min. The solid product was sonicated in 200 mL of water and then vacuum filtered. A mixture of yellow, rod-like crystals of $\text{Li}_3\text{InMo}_3\text{O}_{12}$ and clear, well-faceted crystals without a well-defined shape, identified as LIAO, was obtained.

4.2.2: Structural Characterization

Phase identity and purity were investigated with laboratory PXRD patterns collected over a 2θ range of $10\text{--}60^\circ$ on a Rigaku IV (Ultima) X-ray diffractometer with Cu $K\alpha$ ($\lambda = 1.54 \text{ \AA}$) radiation under ambient conditions. SCXRD diffraction was used to determine the structure of LiM_2SbO_6 . To ensure reproducibility of the structure, a new crystal was used for each collection. CIFs are available for download in the Supporting Information and using CSD codes 1976009-1976011. Single crystal diffraction data for $\text{LiIn}_2\text{SbO}_6$ were collected at 100 K, 323K, 400 K and

500K using a Bruker Apex II CCD diffractometer with monochromated Mo K α ($\lambda = 0.71073 \text{ \AA}$) radiation. The crystal-to-detector distance was 40 mm. SAINT V8.38A was used for data integration and a multi-scan absorption correction was applied using SADABS.^{23,24} Single crystal data of LiM₂SbO₆ (M = Sc, Fe) were collected at 100 K (Sc), 400 K (Fe), and 500 K (Sc) on XtaLAB Synergy diffractometer equipped with a (micro-focus sealed X-ray tube PhotonJet (Mo) X-ray source and a Hybrid Pixel Array Detector(HyPix) detector. Temperature of the crystal was controlled with an Oxford Cryosystems low-temperature device. Data reduction was performed with the CrysAlisPro software using a numerical absorption correction. The structures was solved using SHELXS and refined using SHELXL.^{25,26} No additional symmetry was found when checking for higher symmetry using PLATON.²⁷ Crystallographic data for LiM₂SbO₆ are reported in **Tables 4.1** (M = In) and **A.1** (M = Sc, Fe). High temperature PXRD data were collected at 50 K intervals between 300 and 1200 K on a STOE-STADI-MP powder diffractometer equipped with an asymmetric curved Germanium monochromator (MoK α 1 radiation, $\lambda = 0.70930 \text{ \AA}$) and one-dimensional silicon strip detector (MYTHEN2 1K from DECTRIS). The line focused Mo X-ray tube was operated at 50 kV and 40 mA. The powder was packed in a 0.3 mm quartz capillary and placed into the furnace. Temperature stability is typically 0.1 K. Intensity data from 0 to 45 degrees two theta were collected over a period of 45 mins. Instrumental shifts and peak shape were calibrated against a NIST Silicon standard (640d) prior to the measurement. Powder diffraction data were analyzed by Rietveld refinement using the GSAS II package.²⁸

Table 4.1: Crystallographic Data For $\text{LiIn}_2\text{SbO}_6$

| Compound | $\text{LiIn}_2\text{SbO}_6$ | | |
|---|-----------------------------|-----------------------|-----------------------|
| | 1976009 | 1976010 | 1976011 |
| ICSD code | 1976009 | 1976010 | 1976011 |
| Temperature, K | 99.96 | 323.0 | 500.01 |
| λ , Å | 0.71073 | 0.71073 | 0.71073 |
| space group (No.) | <i>Pnmm</i> (58) | <i>Pnmm</i> (58) | <i>Pnmm</i> (58) |
| unit cell | | | |
| a, Å | 5.0902(4) | 5.0991(2) | 5.1170(3) |
| b, Å | 5.3328(4) | 5.3298(2) | 5.3335(3) |
| c, Å | 8.8813(6) | 8.8729(3) | 8.8794(6) |
| V, Å ³ | 241.08(3) | 241.140(15) | 242.33(3) |
| Z | 2 | 2 | 2 |
| crystal color | Colorless | Colorless | Colorless |
| crystal size, mm | 0.055 x 0.055 x 0.09 | 0.041 x 0.052 x 0.058 | 0.037 x 0.047 x 0.092 |
| ρ_{calc} , g cm ⁻³ | 6.259 | 6.257 | 6.226 |
| μ , mm ⁻¹ | 14.997 | 14.993 | 14.919 |
| Θ_{max} , deg | 72.67 | 72.644 | 73.222 |
| reflections collected | 3367 | 3815 | 4015 |
| R_{int} | 0.0513 | 0.0497 | 0.0895 |
| unique reflections | 615 | 619 | 633 |
| parameters refined | 32 | 32 | 32 |
| R_1 , wR_2 [$F_o > 4\text{sig}(F_o)$] | 0.0206, 0.0547 | 0.0194, 0.0508 | 0.0314, 0.0756 |
| goodness-of-fit | 1.134 | 1.055 | 0.961 |
| diff. peak and hole, e Å ⁻³ | 1.88,-2.59 | 0.9, -1.96 | 2.23,-1.81 |

4.2.3: Solid-state NMR Spectroscopy

^6Li ($I = 1$) and ^7Li ($I = 3/2$) solid-state nuclear magnetic resonance (NMR) spectra were recorded in a static magnetic field of 9.4 T with a Bruker Advance III spectrometer. The samples, LIAO and LiSbO_3 (the latter used as a reference), were separately packed into 4.0 mm diameter zirconia rotors and spectra were recorded under static and 5 kHz and 12.5 kHz magic-angle spinning (MAS) conditions in a Bruker narrow-bore 4.0 mm HX probe. T_1 (spin–lattice) relaxation was measured with a saturation recovery pulse. Quantitative ^6Li spectra were measured with a single 90° RF pulse of 1.6 μs ; the recycle delay was fixed at 200 s for LIAO and at 100 s for LiSbO_3 , which were approximately $5 \times T_1$. ^6Li enrichment was unnecessary owing to the relatively large sample volume. ^7Li spectra were measured with a single $<90^\circ$ RF pulse to ensure sufficient quadrupolar excitation; a liquid 90° pulse of 4.0 μs was calibrated on 1.0 M $\text{LiCl}_{(\text{aq})}$ and a 2.5 μs pulse was applied to the solids. For each measurement, 8 or 16 scans were co-added. A recycle

delay of 10 s was used for the ^7Li spectra. All $^{6/7}\text{Li}$ spectra were referenced to the primary standard 1.0 M $\text{LiCl}_{(\text{aq})}$ at 0 ppm. Density functional theory (DFT) was used to compute the chemical shift tensor and quadrupolar tensor of LIAO and LiSbO_3 . The calculations were performed in the plane wave code CASTEP v19.11 with “on-the-fly” ultrasoft pseudopotentials and the general-gradient-approximation Perdew–Burke–Ernzerhof (PBE) exchange–correlation functional.^{29–31} The plane-wave basis set was truncated at an energy cutoff of 700 eV, and integration over reciprocal space was performed using a $7 \times 7 \times 4$ and $7 \times 4 \times 7$ Monkhorst–Pack grid for LIAO and LiSbO_3 , respectively.³² Structures were geometry optimized prior to NMR calculations.^{33–35} Spectral simulations of the calculated tensors were performed with the Solid Lineshape Analysis (SOLA) tool in TopSpin v3.6.1. Euler angles relating the orientation of the magnetic shielding to the electric field gradient (EFG) tensors were generated in Magres View v1.6.2.³⁶ The isotropic shift δ_{iso} is defined in the Haeberlen convention $\delta_{\text{iso}} = \frac{\delta_{\text{XX}} + \delta_{\text{YY}} + \delta_{\text{ZZ}}}{3}$ with the chemical shift anisotropy (CSA) defined as $\text{CSA} = \delta_{\text{ZZ}} - \delta_{\text{iso}}$ and the shift asymmetry η_{CSA} defined as $\eta_{\text{CSA}} = \frac{\delta_{\text{YY}} - \delta_{\text{XX}}}{\delta_{\text{ZZ}} - \delta_{\text{iso}}}$. With these definitions, the principal components of the shift tensor are ordered such that $|\delta_{\text{ZZ}} - \delta_{\text{iso}}| \geq |\delta_{\text{XX}} - \delta_{\text{iso}}| \geq |\delta_{\text{YY}} - \delta_{\text{iso}}|$. The above definition of CSA is sometimes referred to as the reduced anisotropy, which is equal to 2/3 of the ‘full’ anisotropy $\delta_{\text{ZZ}} - \frac{\delta_{\text{XX}} + \delta_{\text{YY}}}{2}$ used by some authors and programs. The quadrupolar coupling constant C_Q is defined by the nuclear quadrupole moment (Q) and the largest principal component V_{ZZ} of the EFG at the nucleus according to $C_Q = \frac{eQV_{\text{ZZ}}}{h}$, where e is the electric charge and h is Planck’s constant. The quadrupolar asymmetry parameter η_Q is defined by the EFG tensor components as $\eta_Q = \frac{V_{\text{XX}} - V_{\text{YY}}}{V_{\text{ZZ}}}$, with components similarly ordered such that $|V_{\text{ZZ}}| \geq |V_{\text{YY}}| \geq |V_{\text{XX}}|$.

4.2.4: Optical Characterization

Diffuse reflectance measurements were performed on a sintered pellet sample of LIAO using a Lambda 1050 UV-Vis spectrophotometer with integrating sphere attachment (Perkin Elmer). Background spectra were collected on compacted polystyrene. The Kubelka-Munk transformation was used to transform the collected spectra into pseudoabsorbance as a function of energy.³⁷ Linear extrapolations were performed on both the band edge and the background immediately preceding it, and the intersection was taken as an estimate for the optical band gap for each sample. Powder Second Harmonic Generation (SHG) measurements were performed using a pulse Nd:YAG laser (Quantel Laser, Ultra 50) with a wavelength of 1064 nm. The sample, was loaded into a fused silica tube and placed on the sample holder. The generated SHG signal was separated from the fundamental light by a 1064 nm filter, detected by a photomultiplier tube (PMT) and shown on an oscilloscope (Tektronix, TDS3032). For comparison, α -SiO₂ (polycrystalline powder) was measured under the same condition.

4.2.5: Impedance Spectroscopy

Polycrystalline compacts of LIAO were prepared from powders synthesized using the solid state reaction methods described above. The resulting powders were ground further with agate media in a Fritsch pulverisette 7 ball mill for 12 cycles of 5 min at 500 rpm. The ball milled powders were then mixed in ethanol with 2% polyvinyl butyral (PVB) by weight and a small amount of dibutyl phthalate as binding and plasticizer agents. Then, the sample was pressed into a thin, dense pellet first in a uniaxial press and then in an isostatic press at 250 MPa for 20 mins. The pellet was subsequently heated at 3 K/min to 573 K, 773 K, and 1373 K and held for 3 hours

at each temperature to burnout organics and sinter to 68% of theoretical density. The pellet was phase pure as confirmed by XRD. Pt electrodes were applied as a paste and fired at 1173 K for 1 hr. (Au electrodes on a second sample produced nearly identical results.) Impedance spectroscopy measurements were performed on the prepared pellet in a custom test station using a Faraday-cage incased sample holder and a Modulab XM(Solartron Analytical) analyzer equipped with a XM Femto Ampere card.³⁸ Under flowing (40 sccm) synthetic air, the sample was heated from room temperature to 873 K in 25 K increments and held for 30 minutes before each impedance measurement from 1 MHz to 1 Hz at a perturbation voltage of 20 – 50 mV.

4.3: Results and Discussion:

4.3.1: *The Structure of $LiIn_2SbO_6$*

Initial structural solutions were carried out with body-centering as recommended by XPREP, the space group determination program of the ShelXTL package. Although the obtained structures result in low refinement parameters ($R_1 = 1.50-1.66\%$, $wR_2 = 3.69-4.04\%$), they also exhibit several unrealistic features, including half-filled O positions and non-positive definite atoms (See **Figure 4.1**). Repeating the measurement at higher temperature (323 K) eliminates the non-positive definite atoms but otherwise gives the same structural solution, suggesting that the unrealistic solution was not caused by freezing of disorder at low temperatures. Comparison of the predicted powder pattern for this structure with experimental patterns on the material revealed several unaccounted for peaks corresponding to the (120), (113), and (212) reflections for the given lattice parameters, all of which should be absent with a body-centered space group.

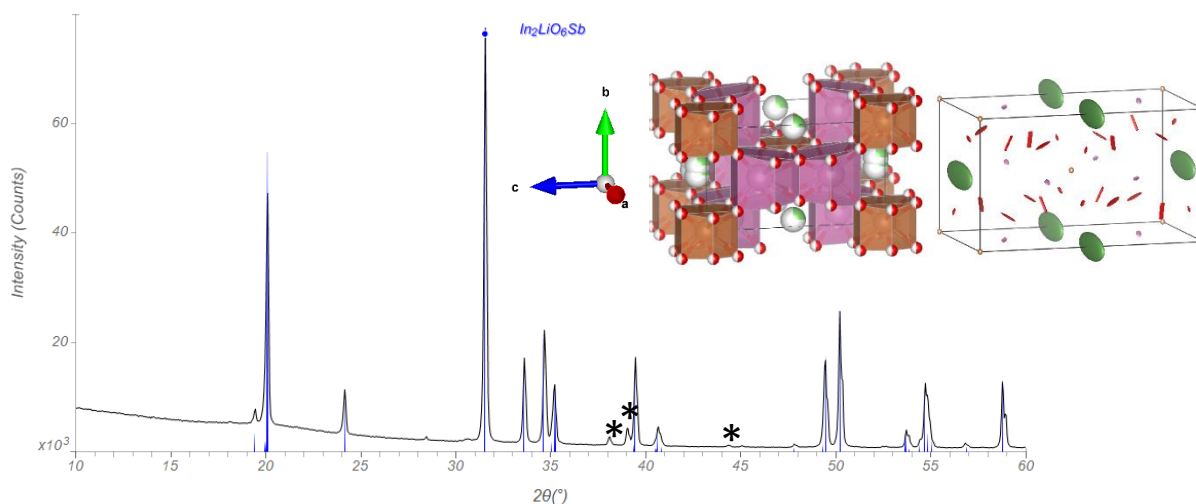


Figure 4.1: Body-centered crystal structure solutions of $\text{LiIn}_2\text{SbO}_6$ and their predicted PXRD patterns compared with the experimentally observed one. Only one predicted pattern is shown for simplicity, as the two are visibly identical. Peaks marked with an asterisk are unaccounted for by the body-centered structures. The left (*Immm*) structure demonstrates that each layer of half-filled O positions consists of two individual orientations of a close-packed layer super imposed on top of each other. The right structure (*I222*) shows the unrealistically flat or non-positive definite (cylinders) ellipsoids apparent in some 100 K body-centered solutions.

As such, the crystal structure was re-solved with primitive centering. The resulting solution, summarized in **Tables 4.1** and **4.2** with atomic arrangement depicted in **Figures 4.2**, retains the same metric unit cell as the body centered structure, but displays several improvements; it has no non-positive definite atoms and only half the number of O positions, all of which are fully occupied. As depicted, this structural solution is valid at all three measured temperatures, with only expected increases in thermal parameters observed. Notably, the predicted powder pattern for the primitive solution accounts for all the peaks in the experimental one. A Rietveld refinement performed with this structure is shown below in **Figure 4.3** with relevant parameters summarized in **Table 4.3**.

Table 4.2. Atomic coordinates and isotropic thermal parameters in LIAO at 100, 323, and 500 K.

| Atom | Wyckoff Position | x | y | z | U_{eq} |
|-------|------------------|-----------|-----------|-------------|----------|
| 100 K | | | | | |
| In | 4f | 0.5 | 0 | 0.30098(2) | 2.32(9) |
| Sb | 2a | 0.5 | 0.5 | 0.5 | 2.03(9) |
| Li | 4g | 0.051(2) | 0.107(3) | 0.5 | 10(2) |
| O1 | 8h | 0.2785(3) | 0.3368(3) | 0.34348(15) | 8.5(3) |
| O2 | 4g | 0.6984(4) | 0.1837(4) | 0.5 | 3.9(3) |
| 323 K | | | | | |
| In | 4f | 0.5 | 0 | 0.30041(2) | 6.05(9) |
| Sb | 2a | 0.5 | 0.5 | 0.5 | 5.23(9) |
| Li | 4g | 0.046(3) | 0.101(3) | 0.5 | 24(3) |
| O1 | 8h | 0.2787(3) | 0.3364(3) | 0.34378(13) | 11.7(3) |
| O2 | 4g | 0.6980(4) | 0.1842(3) | 0.5 | 7.2(3) |
| 500 K | | | | | |
| In | 4f | 0.5 | 0 | 0.29965(4) | 9.4(2) |
| Sb | 2a | 0.5 | 0.5 | 0.5 | 7.4(2) |
| Li | 4g | 0.049(4) | 0.086(5) | 0.5 | 29(6) |
| O1 | 8h | 0.2801(5) | 0.3362(6) | 0.3432(3) | 15.5(6) |
| O2 | 4g | 0.6979(6) | 0.1843(7) | 0.5 | 12.6(7) |

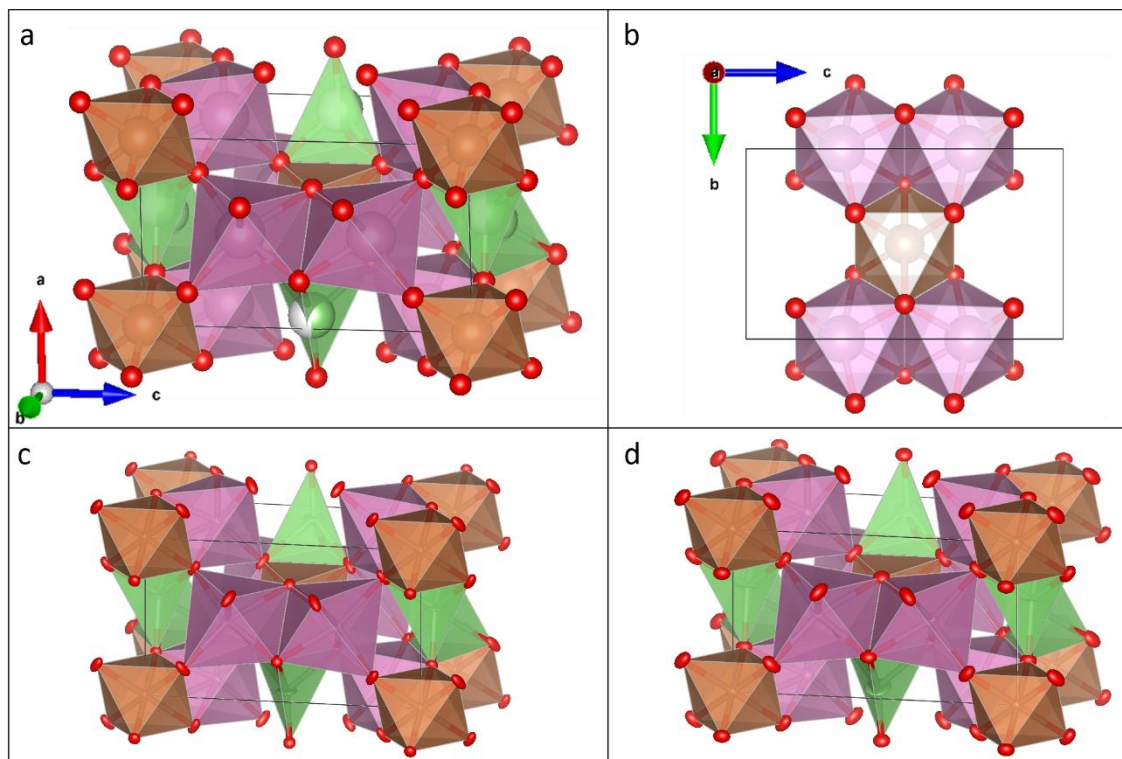


Figure 4.2. Structural Refinement of $\text{LiIn}_2\text{SbO}_6$. a) The single crystal solution as viewed down the $[281]$ direction. b) The portion of an isolated edge-sharing chain of InO_6 and SbO_6 octahedra contained within a single unit cell, viewed down the a -axis. c,d) Structural solutions for LIAO at 323 and 500 K respectively with the same orientation. Purple, orange, and green polyhedra are respectively centered on the 4f (In^{3+}), 2a (Sb^{5+}), and 4g (Li^+) crystallographic sites. Red spheres/ellipsoids are O^{2-} ions.

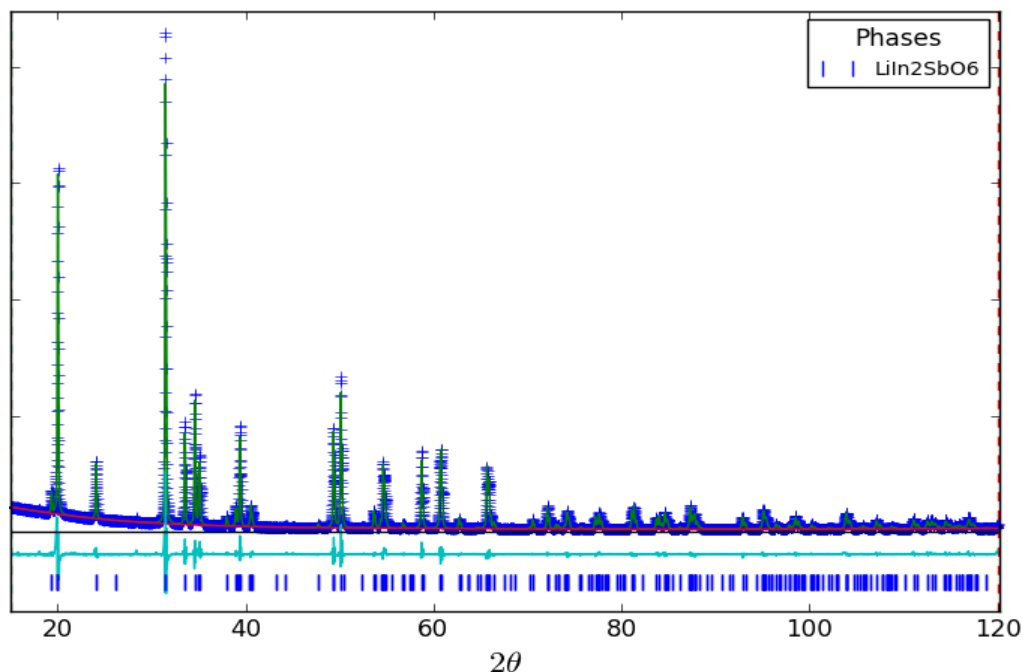


Figure 4.3. Rietveld refinement of powder LIAO samples. (Blue) Observed powder pattern. (Green) Predicted pattern. (Red) background. (Light Blue) Difference pattern. (Blue ticks) Predicted reflections from $\text{LiIn}_2\text{SbO}_6$.

The crystal structure of $\text{LiIn}_2\text{SbO}_6$ may be described as a distorted hexagonal close-packed array of O^{2-} ions with half the octahedral holes filled by In^{3+} and Sb^{5+} and one sixth of the tetrahedral holes containing Li^+ . The InO_6 and SbO_6 octahedra make up a framework of edge-sharing chains along the b axis connected to each other via corner-sharing, with Li^+ distributed within channels between them. Along the length of the chains, dimers of InO_6 octahedra alternate with single SbO_6 octahedra, and thus the width of the chain along the c direction varies between one and two octahedra for each step in the b direction, as shown in **Figure 4.2b**. This motif is known as a “diamond chain” in magnetic materials with analogous dimer-monomer-dimer

Table 4.3. Rietveld refinement parameters.

| Source | Laboratory X-ray |
|---------------------------------|-----------------------------|
| Chemical Formula | $\text{LiIn}_2\text{SbO}_6$ |
| Formula Weight | 454.33 |
| Temperature (K) | 298 |
| Wavelength (\AA) | 1.54 (CuK α) |
| Crystal System | Orthorhombic |
| Space group (No.) | Pnmm (58) |
| a (\AA) | 5.10174(4) |
| b (\AA) | 5.33510(4) |
| c (\AA) | 8.88091(6) |
| $\alpha = \beta = \gamma$ (deg) | 90 |
| V (\AA^3) | 241.723(3) |
| Z | 2 |
| Profile range | $10 \leq 2\theta \leq 120$ |
| GOF | 2.65 |
| R_p (%) | 6.22 |
| R_{wp} (%) | 8.88 |

arrangements of unpaired spins.^{39,40} **Table 4.4** presents selected bond lengths and angles for LIAO at 100, 323, and 500 K. Whereas the Sb-O bond lengths are very close in value, producing only a slight axial elongation in SbO₆ octahedra, the In-O bond length variation indicates a much more significant distortion. The differences in distortion are also evident in the O-M-O octahedral angles, which are very close in value in SbO₆, but vary significantly in InO₆. The In³⁺ in these InO₆ octahedra are shifted away from the center of the dimer, towards the opposite edge, likely owing to electrostatic repulsion between the two cation arising from the asymmetric edge-sharing surrounding the dimers. This effect is well-known in other rutile-related phases with doubled octahedral chains, and is distinct from displacements along the chain in rutile-related NbO₂ and VO₂, in which metal-metal bond formation causes the cations in adjacent dimers to move away from each other.^{3,41} In³⁺ does not have the d¹ configuration which makes the latter favorable, plus the In³⁺ centers which “approach” each other remain separated by over 5 Å owing to the intervening channel and therefore cannot be participating in metallic bonding. Complete ordering of In and Sb within these chains is supported by bond valence calculations, as shown in **Table 4.5**. The chains are arranged in a checker-board fashion when viewed down the b-axis with each being diagonally connected to four others. Connected chains are staggered along *b* such that Sb-centered octahedra exclusively share corners with InO₆ dimers and vice versa. The spaces between chains formed by this arrangement are the channels in which the Li⁺ tetrahedra are located. These channels have the same alternating structure as the chains.

Table 4.4 Selected M-O bond-lengths, O-M-O bond angles, and multiplicities in LIAO.

| bond lengths (Å) | | angles (°) | |
|------------------|------------|-------------|------------|
| 100 K | | | |
| 2x In-O1 | 2.1537(17) | 1x O1-In-O1 | 104.72(6) |
| 2x In-O1 | 2.1009(15) | 2x O1-In-O1 | 96.59(6) |
| 2x In-O2 | 2.2592(13) | 2x O1-In-O1 | 95.70(6) |
| | | 2x O1-In-O2 | 89.80(4) |
| | | 2x O1-In-O2 | 89.46(4) |
| | | 1x O2-In-O2 | 77.04(1) |
| | | 2x O1-In-O2 | 74.65(4) |
| 4x Sb-O1 | 1.9903(15) | 4x O2-Sb-O1 | 94.83(5) |
| 2x Sb-O2 | 1.966(2) | 2x O1-Sb-O1 | 91.39(6) |
| | | 2x O1-Sb-O1 | 88.61(6) |
| | | 4x O2-Sb-O1 | 85.17(5) |
| 2x Li-O1 | 2.185(11) | 1x O2-Li-O2 | 142.3 (6) |
| 1x Li-O2 | 1.841(11) | 2x O2-Li-O1 | 113.08 (4) |
| 1x Li-O2 | 2.008(14) | 2x O2-Li-O1 | 95.53(4) |
| | | 1x O1-Li-O1 | 79.01(6) |
| 323 K | | | |
| 2x In-O1 | 2.1533(16) | 1x O1-In-O1 | 105.00(6) |
| 2x In-O1 | 2.1012(14) | 2x O1-In-O1 | 96.59(6) |
| 2x In-O2 | 2.2628(12) | 2x O1-In-O1 | 95.76(6) |
| | | 2x O1-In-O2 | 89.70(4) |
| | | 2x O1-In-O2 | 89.29(3) |
| | | 1x O2-In-O2 | 76.98(1) |
| | | 2x O1-In-O2 | 74.49(3) |
| 4x Sb-O1 | 1.9888(14) | 4x O2-Sb-O1 | 94.83(5) |
| 2x Sb-O2 | 1.9627(17) | 2x O1-Sb-O1 | 91.63(5) |
| | | 2x O1-Sb-O1 | 88.37(5) |
| | | 4x O2-Sb-O1 | 85.18(5) |
| 2x Li-O1 | 2.214(12) | 1x O2-Li-O2 | 142.7(9) |
| 1x Li-O2 | 1.829(16) | 2x O2-Li-O1 | 112.49(4) |
| 1x Li-O2 | 2.004(16) | 2x O2-Li-O1 | 94.63(4) |
| | | 1x O1-Li-O1 | 77.51(5) |
| 500 K | | | |
| 2x In-O1 | 2.152(2) | 1x O1-In-O1 | 105.85(10) |
| 2x In-O1 | 2.104(3) | 2x O1-In-O1 | 96.81(11) |
| 2x In-O2 | 2.271(2) | 2x O1-In-O1 | 95.63(11) |
| | | 2x O1-In-O2 | 89.36(7) |
| | | 2x O1-In-O2 | 89.24(7) |
| | | 1x O2-In-O2 | 76.85(1) |
| | | 2x O1-In-O2 | 74.44(8) |
| 4x Sb-O1 | 1.992(3) | 4x O2-Sb-O1 | 94.86(9) |
| 2x Sb-O2 | 1.965(4) | 2x O1-Sb-O1 | 91.31(11) |
| | | 2x O1-Sb-O1 | 88.69(11) |
| | | 4x O2-Sb-O1 | 85.14(9) |
| 2x Li-O1 | 2.262(19) | 1x O2-Li-O2 | 148.2(12) |
| 1x Li-O2 | 1.87(2) | 2x O2-Li-O1 | 109.67(7) |
| 1x Li-O2 | 1.93(2) | 2x O2-Li-O1 | 95.13(7) |
| | | 1x O1-Li-O1 | 77.97(10) |

The Li⁺ ions reside, at 50% occupancy levels, in tetrahedral sites sandwiched between InO₆ dimers. The coordination polyhedra defined by these sites are somewhat distorted, as indicated by the bond lengths in **Table 4.4**, but these distances remain within 1.8-2.2 Å, the normal range for LiO₄ tetrahedra. Solid-state NMR spectroscopy provides confirmation of the Li coordination. The ⁶Li central resonances and ⁷Li full spinning sideband manifolds of LIAO and LiSbO₃ at 5 kHz MAS are shown in **Figure 4.4**. The spectra show the Li resonance in LIAO to occur at 0.65(1) ppm, whereas that in octahedral LiO₆ in LiSO₃ to occur at -0.05(2) ppm. These shifts are typical for LiO₄ and LiO₆, respectively.⁴⁵ As Li has a small

chemical shift range, the coordination was also probed by examining the simulated and

experimental quadrupolar parameters, which are very sensitive to local coordination symmetry and

Table 4.5. Bond Valence Analysis in LIAO at 100 K

| Site | In ³⁺ | Sb ⁵⁺ | Li ⁺ |
|------|------------------|------------------|-----------------|
| 2a | 4.83 | 5.00 | 1.49 |
| 4f | 2.94 | 3.26 | 0.91 |
| 4g | 2.86 | 2.98 | 0.88 |

distortions. Simulations of the spectra were performed using the

X-ray single crystal structure solution described in this work for

LIAO and the known *Pncn* structure of LiSbO₃ (ICSD39574),

whereas experimental parameters were obtained by fitting the

quadrupolar lineshapes of the ⁷Li MAS NMR spectra. As depicted in **Figure 4.4b** and quantified

in **Table 4.6**, the experimental data for LIAO are in good agreement with the tetrahedral lithium

site calculated in the *Pnnm* structure. Thus, the occupancy of Li in tetrahedral sites is fully

established. Notably, the distance between Li sites in LIAO is significantly smaller than the typical

separation of tetrahedrally coordinated Li (3 Å), suggesting there may be a low barrier to migration

between them.¹⁴ Moreover, the arrangement is reminiscent of that of Li in the paraelectric phases

of known ferroelectrics LiNbO₃ and LiTaO₃.^{43,44} However, no change to a lower symmetry space

group is observed in the single crystal solution LIAO between 500K and 100 K, in contrast to the

observed Li ordering which accompanies the ferroelectric transition in LiNbO₃ and LiTaO₃.

Table 4.6. Calculated and experimental NMR parameters of LIAO and LiSbO₃.

| Parameter | LiIn ₂ SbO ₆ | | LiSbO ₃ | |
|---|------------------------------------|------------------|--------------------|------------------|
| | Calculated | Experimental Fit | Calculated | Experimental Fit |
| Isotropic Shift (δ_{iso} ; ppm) | 0.65 ^a | 0.65(1) | -0.55 ^a | -0.05(0.02) |
| Chemical Shift Anisotropy (CSA; ppm) | -7.3 | n/a ^b | -2.8 | n/a ^b |
| Shift Asymmetry (η_{CS}) | 0.13 | n/a ^b | 0.18 | n/a ^b |
| Quadrupolar Coupling (C_Q ; kHz) | 141 | 150(10) | 103 | 108(5) |
| Quadrupolar Asymmetry (η_Q) | 0.57 | 0.6(1) | 0.42 | 0.2(1) |
| Euler angles (α, β, γ ; °) | -90, 10.4, 90 | n/a ^b | 0, 168.3, 90 | n/a ^b |

^aCalculated shielding values must be referenced. Here, the shielding of LIAO was arbitrarily converted to the experimental shift value, which allows for relative comparison of the LIAO and LiSbO₃ shifts. ^bToo small to significantly affect the fit. Calculated values used directly without refinement.

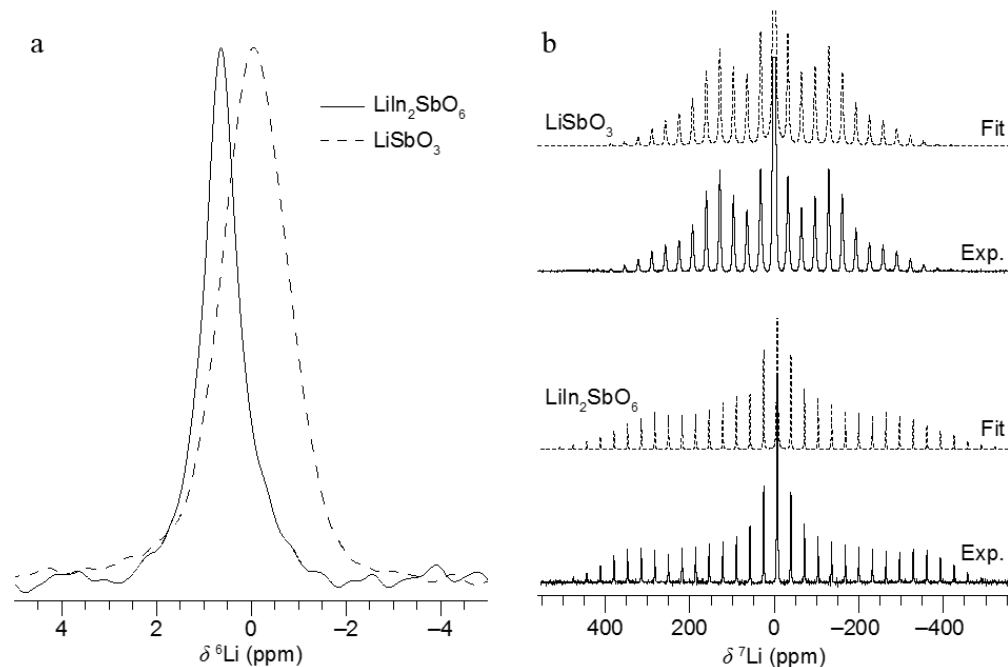


Figure 4.4. ^{67}Li solid-state 5 kHz MAS NMR spectroscopy. a) ^6Li central resonance and b) ^7Li spectra showing the spinning sidebands and fits to the experimental lineshapes. Fit parameters are given in **Table 4**.

4.3.2: Relationship to Known Structures

The original report of LIAO by Tarte et al. noted clear relationships between $\text{LiIn}_2\text{SbO}_6$ and LiSbO_3 .¹⁶ The compounds have the same cation-anion ratio and share three out of four elemental components. The reported PXRD patterns are analogous except for the (110) reflection, which is forbidden in LiSbO_3 and observed for LIAO. From these similarities the authors hypothesized that the LIAO structure was identical to that of LiSbO_3 with cation ordering that reduced the symmetry from $Pnna$ to $Pnn2$. However, the true structural relationship between the phases, as determined here, is more complex. The relationship is most easily understood by looking at a single set of AB layers in the hexagonal close-packed anion array for each phase, with cations positions indicated.⁴⁵ **Figure 4.5** shows how LiSbO_3 can be transformed to LIAO in two steps: 1. Replacing every other adjacent set of octahedrally placed $\text{Li}^+/\text{Sb}^{5+}$ ions with a pair of In^{3+} ions, and 2. Splitting the remaining Li^+ content between the two nearest, equidistant tetrahedral

positions. It should be noted that the hypothetical structure produced after step 1 exhibits the $Pnn2$ symmetry expected by Tarte and colleagues. The second step produces mirror plane symmetry between the chains, resulting in our observed $Pnmm$ space group.

Checking for SHG, which can only be observed from space groups lacking inversion symmetry such as $Pnn2$, in LIAO detected an intense, transient response that quickly decayed to nothing. While this initially suggested that LIAO may not have $Pnmm$ symmetry, further investigation of this result revealed that the signal originated in a brief emission of white light from the sample rather than the green light that should arise from frequency doubling the incident beam. This is a known phenomenon in wide bandgap inorganic materials arising from bulk optical breakdown caused by irradiation with a 1064 nm laser, identical to the one used in this work.⁴⁶ The white color of LIAO is consistent with a wide band gap, so the signal detected here was also attributed solely to this alternative effect. No SHG was observed in LIAO.

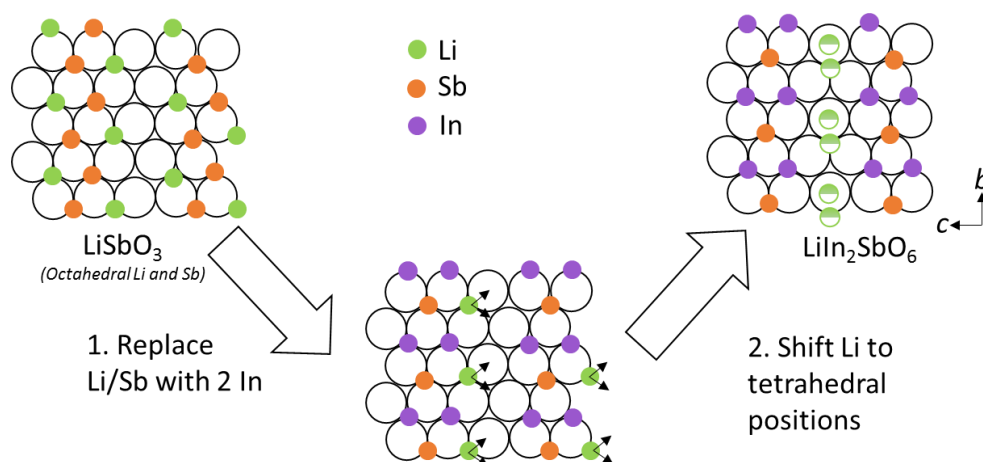


Figure 4.5. Relationship between the close-packed layers of LiSbO_3 and $\text{LiIn}_2\text{SbO}_6$. Open circles are O^{2-} ions. Cation positions for all framework ions of LIAO are present in LiSbO_3 , and Li positions are slightly offset between tetrahedral and octahedral sites.

The adoption of tetrahedral coordination by Li^+ transforms the 3D edge-sharing octahedral network of LiSbO_3 into the filled framework arrangement, described above, with the connectivity

of an Li-filled rutile-related phase. However, the framework of LIAO is distinguished from other members of the rutile-related family by the alternating width along its chains and the ordering of cations within them. Isolated chains from several representative rutile-like structure materials are compared in **Figure 4.6a**. The prototype rutile has chains that are 1x1, meaning that each octahedral unit shares edges only with the octahedra ahead and behind it in the direction of the chain. The related ramsdellite structure has 2x1 chains. The diamond pattern of LIAO chains can be thought of as a one-to-one alternation of these two chain structures along the chain direction. In fact, intergrowths of rutile and ramsdellite containing both types of chains have been reported previously, such as in $\gamma\text{-MnO}_2$ or $\text{Li}_{0.9}\text{Ti}_{2.94}\text{O}_6$.^{3,4,10,47} The TiO_6 framework of the latter material, shown in **Figure 4.6b**, even has a one-to-one ratio of rutile and ramsdellite, as found in the LIAO framework. However, the slabs of rutile and ramsdellite alternate in a direction perpendicular to the chains rather than parallel to them (as in LIAO), thereby preserving the fixed width of any individual chain. This appears to be true for all reported intergrowths of these two structures. Thus, the chains of LIAO appear unique in this aspect.

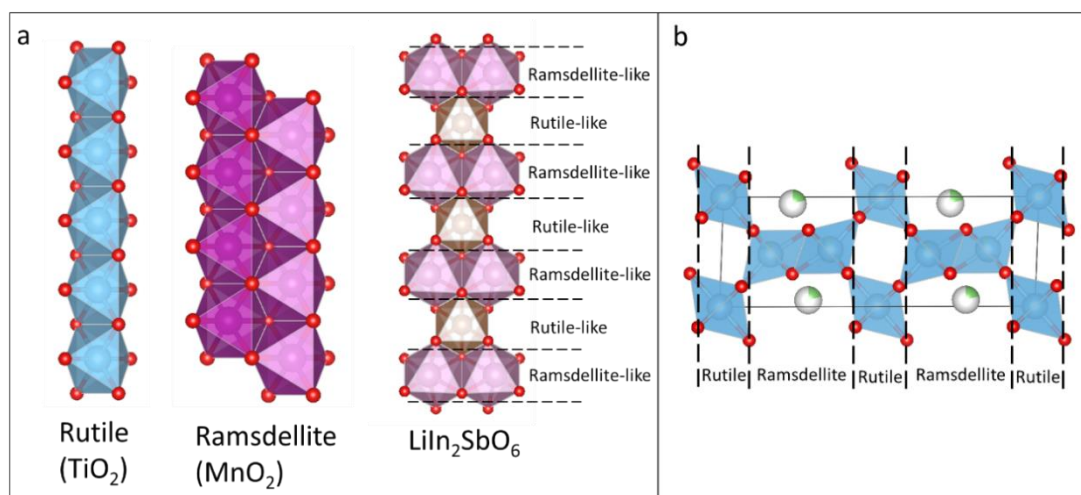


Figure 4.6. a) Several-unit-cells long segment of an isolated chain from selected rutile-like phases viewed perpendicular to the chain direction.^{3-6,48,49} Regions of LIAO chains are labeled with the structure they most closely resemble. b) 1:1 intergrowth structure of rutile and ramsdellite as observed in Li-intercalated ramsdellite $\text{Li}_{0.9}\text{Ti}_{2.94}\text{O}_6$ viewed parallel to the chain direction, with rutile and ramsdellite slabs indicated.⁶

As a consequence of the unique pattern of LIAO chains, their orientation with respect to the rows of O in the close-packed layer is rotated by 30° as compared to similar structures (**Figure 4.7**). According to Baur, members of the rutile-related family are sometimes referred to as “ 3\AA structures” because, in oxides and fluorides, the lattice parameter parallel to the chain direction is either $\sim 3\text{\AA}$ or a multiple of that in ordered variants such as trirutile.¹⁹ The corresponding value in LIAO (5.33\AA) deviates but still bears a close geometrical relationship to the characteristic length as shown in **Figure 4.7**.

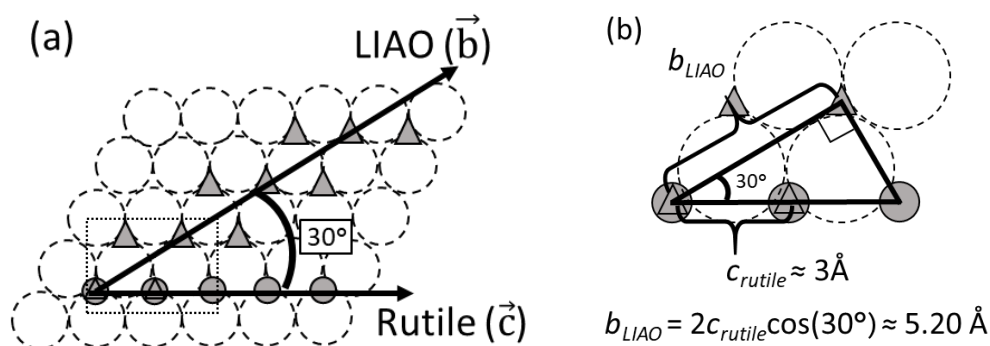


Figure 4.7. Geometrical relationship between occupied octahedral holes in a single, ideal close-packed layer (dashed circles) in the LIAO (triangles) and rutile (circles) structures. (a) Rutile octahedral sites lie parallel to the rows of close-packed O^{2-} ions, whereas LIAO chains are rotated by 30° . (b) Close-up of the boxed region in (a). The observed chain direction lattice parameters in LIAO (5.33\AA) arises from the characteristic value of $\sim 3\text{\AA}$ in rutile-related oxides.

An explanation for the formation of alternating-width chains instead of either rutile or ramsdellite ones deserves some consideration. The characteristics of the framework in LIAO alone are unlikely to account for the formation of its unique chain-structure. Neither its cation chemistry nor its stoichiometry is unique among the rutile-related phases. For example, InSbO_4 crystallizes with a random rutile structure rather than an ordered variant, indicating In^{3+} and Sb^{5+} are similar enough that they do not necessarily favor ordering in related materials.^{50,51} Likewise, many compounds with the trirutile structure, such as ZnSb_2O_6 , have the $M'M''_2\text{O}_6$ stoichiometry of the In_2SbO_6 framework in LIAO. These phases demonstrate that the 1×1 chains of rutile can readily

accommodate ordering commensurate with the 1:2:6 stoichiometry.¹ Most importantly, unlike other rutile-related phases with Li in the channels, attaining charge neutrality in the structure requires incorporation of Li⁺ into the framework of LIAO as In³⁺ and Sb⁵⁺ cannot be further oxidized to compensate for empty channel sites. Thus, the presence of the Li appears critical to the formation of alternating-width chains.

Li⁺ behavior in Li-filled TiO₂ provides insight on how this hypothesis could be true. In the 2x1 channels of the ramsdellite-type TiO₂, electrochemical insertion of up to 0.5 Li per framework cation site is found to favor tetrahedral sites owing to space and charge screening considerations.^{12,14,15} With 0.33 Li per framework site, tetrahedral Li-coordination in LIAO is likely a result of the same considerations. Furthermore, the intergrowth phase shown in **Figure 4.6b**, formed by high-temperature solid state methods, suggests that under certain conditions, such as high temperatures or reducing environments, Li⁺ coordinated by 2x1 chains in tetrahedral sites is found in the thermodynamic ground state.¹³ Likewise, density functional theory and potential modeling studies have found a reversal in the relative stability of the rutile and ramsdellite-type polymorphs of Li_xTiO₂ with increasing *x*, such that 2x1 chains are favored over 1x1 at higher Li⁺ content.^{9,14} Thus, the presence of Li provides a thermodynamic driving force for the formation of 2x1 units in the chain. The alternating chain structure of LIAO appears to be another mechanism to provide Li⁺ with this favorable coordination environment without a fully 2x1 chain. It is possible that ramsdellite-type chains are destabilized for LIAO relative to the alternating-width chains by increased repulsion from highly charged Sb⁵⁺ centers being in closer proximity to each other or Li⁺. This is consistent with the fact that In³⁺ and Sb⁵⁺ are fully ordered in LIAO such that the distance between Li⁺ and Sb⁵⁺ is maximized, despite the same two cations showing full disorder

in rutile-type InSbO_4 (no Li present).⁵⁰ As such, the other stoichiometrically analogous phases identified by Tarte et al. as having cation ordered LiSbO_3 structures (LiM_2SbO_6 , $M = \text{Sc, Mn, Fe}$) may also exhibit these alternating-width chains.¹⁶

4.3.3: Thermal Behavior:

The refined unit cell volume and lattice parameters for LIAO up to 1200 K are depicted below in **Figure 4.8**. The overall volume expands nearly linearly over the entire temperature range, with a slight anomaly at 450 K (**Figure 4.8d**). Examination of the individual lattice parameter behaviors shows that this expansion is dominated by the behavior in the a direction, which shows only a very slight change at 450 K. Expansion along b and c is more than an order of magnitude smaller than that along a at ambient temperature, and increases substantially on heating through 450 K. These distinct changes suggest the possibility of a phase transition. Differential thermal analysis (DTA) (**Figure 4.9**) performed over this temperature range for two LIAO samples showed two small endothermic peaks at about 390 K. However, the evolution of the PXRD pattern over the measured temperature range (**Figure 4.10**) shows no apparent changes in the peaks other than shifts in their positions, suggesting the absence of structural changes involving symmetry changes or a decomposition reaction. Furthermore, SCXRD performed at 500 K (**Figure 4.2**) gives an identical solution to those at 100 K and 323 K, accounting for thermal expansion and larger atomic displacement parameters expected at higher temperatures.

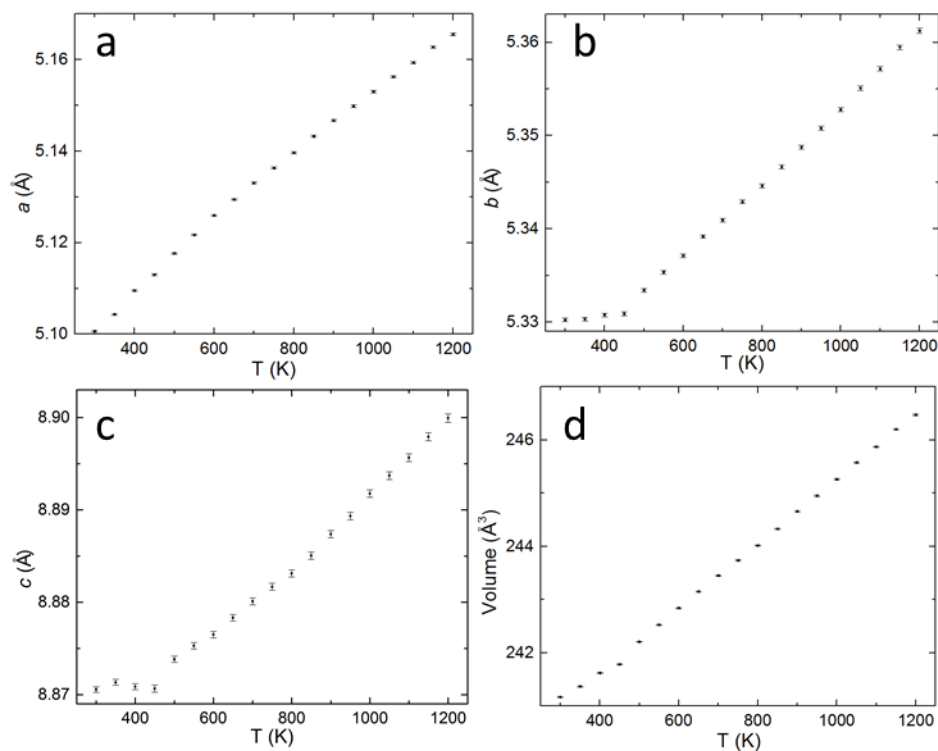


Figure 4.8. Unit cell lattice parameters a , b , and c (a , b , c) and volume (d) as a function of temperature determined by refinement of high-temperature PXRD data.

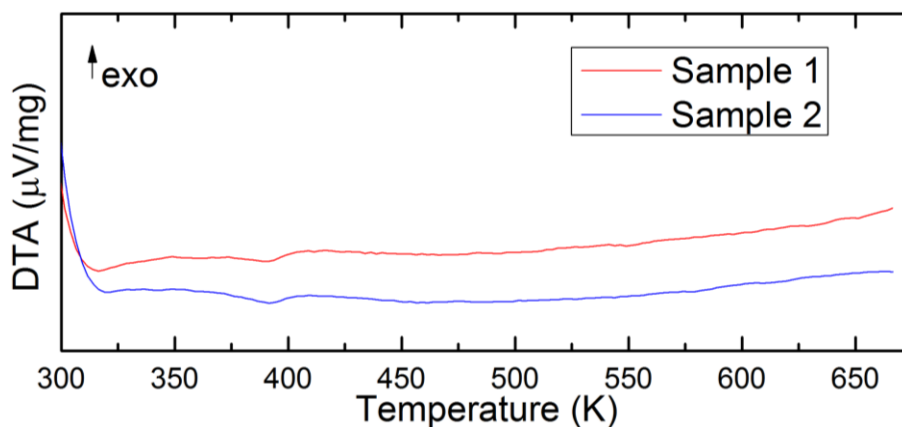


Figure 4.9. Differential thermal analysis of LIAO samples from 300 to 673 K.

These observations may indicate a transition from static to dynamic disorder of Li at the transition temperature. A similar process accompanies the ferroelectric ordering in LiNbO_3 and LiTaO_3 mentioned earlier. However, without second-order JT active ions in LIAO, it seems that no distortion in the framework occurs to break the degeneracy of the tetrahedral sites. Thus, even

if Li lacked sufficient energy to actively hop between adjacent sites, a statistical distribution would still be expected and the average structure would remain disordered on either side of the transition, as observed. DTA on other order to disorder transitions, like that in $\text{Li}_2\text{TiO}_3\text{-MgO}$ have been observed to exhibit broad, weak endotherms that are even unobservable at some compositions, consistent with what is depicted in **Figure 4.10**.⁵⁴ Regardless of whether this is the true origin of the slope change in the refined b and c parameters, LIAO appears to be stable up to 1200 K, consistent with previous reports of significant thermal stability in related materials.¹⁸

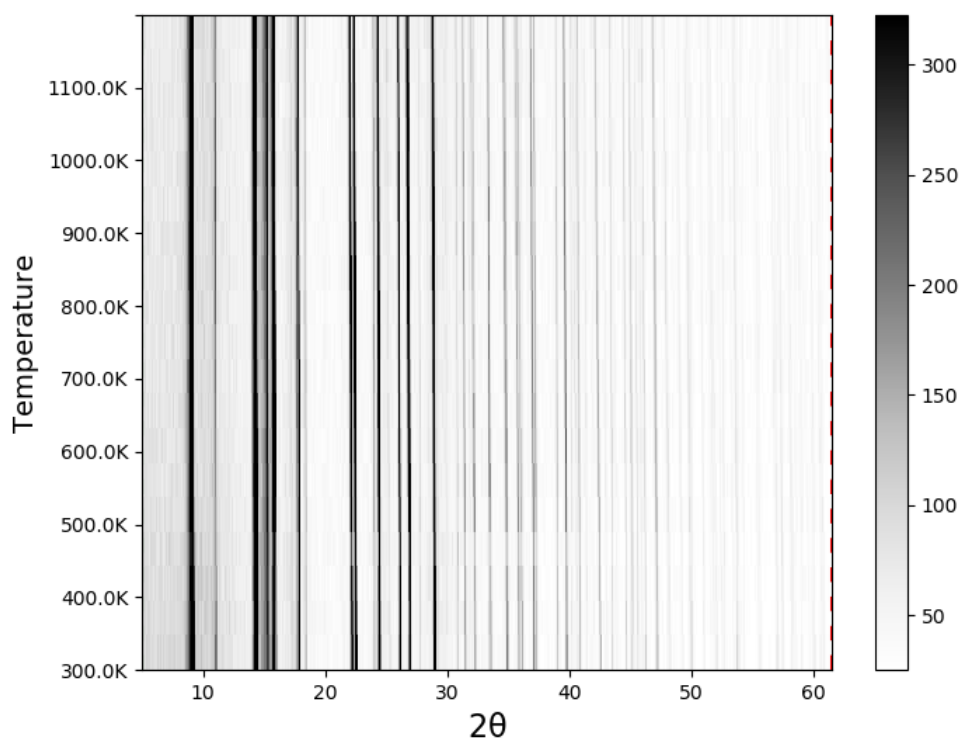


Figure 4.10. Temperature-dependent PXRD pattern of LIAO from 300 to 1200 K.

4.3.4: Property Characterization

The pseudoabsorbance ($F(R)$) spectra of LIAO was extracted from diffuse reflectance data. Plots of the data for LIAO to the powers of $\frac{1}{2}$ and 2, depicted in **Figure 4.11**, show that the energy dependence appears linear only in the latter case, as is expected for a direct gap material.³⁷

Extrapolation of this curve to the x-axis gives an estimated band gap of 3.9 eV, consistent with the band gaps of chemically related phases such as LiInO_2 .⁵² This confirms LIAO as a wide bandgap material as suggested by the results of the SHG experiments described above.

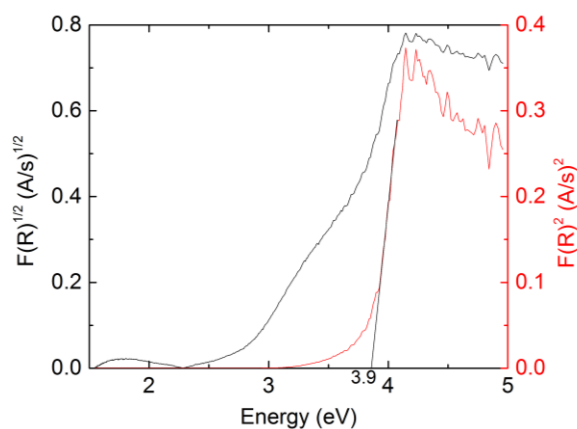


Figure 4.11. Comparison of $F(R)^{1/2}$ and $F(R)^2$ extracted from diffuse reflectance measurements of LIAO. Extrapolation of the linear portion of $F(R)^2$ suggests a direct band gap of 3.9 eV.

The large band gap of LIAO likely precludes significant electronic conductivity in the pure phase. As expected, measurements with a four-point probe indicated an immeasurably large sheet resistance. However, the channels in the LIAO structure as well as the split occupancy and tetrahedral coordination of Li^+ are conditions which have been considered favorable to ionic conductivity in related materials.^{2,7,11-14} Li^+ conductors that are electronically insulating are of interest as solid state electrolytes, motivating the AC impedance measurements.⁵³ Room temperature impedance spectra, **Figure 4.12a**, indicate that LIAO is not a good Li^+ conductor, despite the favorable structural features. In ambient conditions LIAO has a moderate resistance that rapidly increases as dry gas is introduced. The behavior suggests that in ambient humidity conditions transport in LIAO is dominated by $\text{H}^+/\text{H}_3\text{O}^+$ migration along grain boundaries or internal pore surfaces and changes to bulk sluggish Li^+ conduction in dry conditions. On heating (select spectra in **Figure 4.12(b,c,d)** and a complete dataset in **Figure A.1**), the overall resistance

of the sample decreases as reflected in the decreasing magnitude of the impedance arcs. At temperatures of 623 K and above, the spectra are characterized by two arcs, typical of polycrystalline in which the high frequency arc reflects bulk transport and the low frequency arc reflects transport across resistive grain boundaries. The bulk conductivity obtained by such an interpretation and associated impedance fitting, **Figure 4.12(e)**, reveals a conductivity, σ , of 1.3×10^{-7} S/cm at 623 K and an activation energy for transport, E_{σ} , of 1.1 eV (taking the conductivity to be of the form $\sigma = \frac{A}{T} \exp\left(\frac{-E_{\sigma}}{k_b T}\right)$, where A is a constant, T is temperature and k_b is Boltzmann's constant). The relative dielectric constant obtained from the analysis is ~ 70 , a reasonable value for an oxide material far from any phase transitions.⁵⁴ While the large bandgap suggests the transport is ionic, it is not possible to rule out a possible electronic contribution to the conductivity on the basis of the features of the impedance spectra.

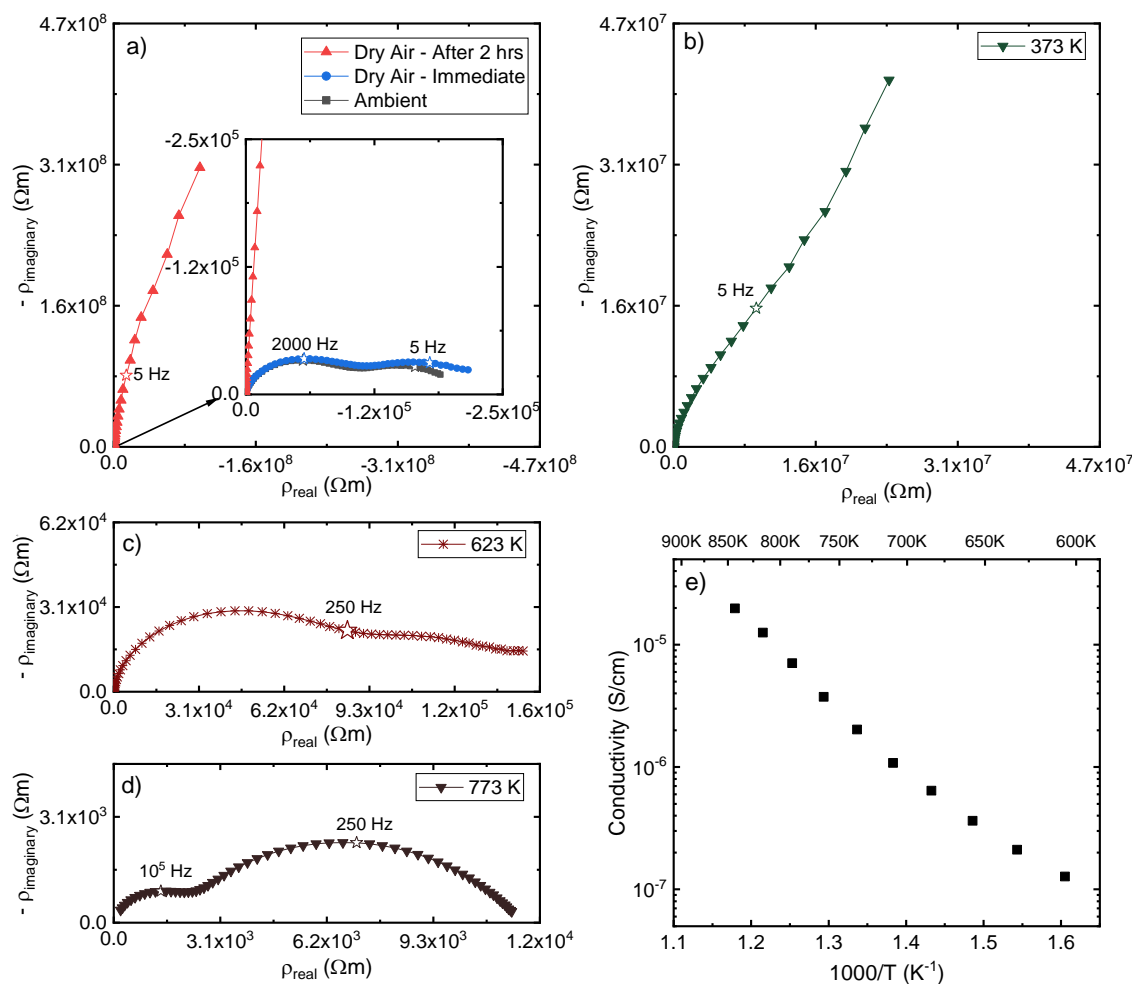


Figure 4.12. Impedance spectra of LIAO at (a) room temperature, (b) 373 K, (c) 623 K, and (d) 773 K, and (e) bulk conductivity. Room temperature spectra are measured under ambient conditions (blue), immediately under synthetic air (red) and after drying in synthetic air for 2 hours (blue). High temperature spectra are measured under synthetic air. Select frequencies are indicated by a star. Bulk conductivity values are those corresponding to the high frequency arcs spectra such as in (c) and (d).

4.3.5: (Structural) Effect of Changing 3^+ Chain Cation: LSAO, LFAO

The large activation barrier to ionic transport measured in LIAO suggest that a significant difference in site energies at different points along the tunnel diffusion pathway are an obstacle to fast ion-conduction in this phase. The energies for these sites are intimately tied to the framework composition via the size of the site, inductive effects, and second nearest neighbor interactions. As

such, substitution of the framework ions is a potential strategy for tuning the ionic conductivity in this structure. Both destabilizing the minimum energy site and/or stabilizing the maximum energy one should theoretically lower the activation energy. Given the observed Li site preference, the former should be the tetrahedral sites, while the latter has not been determined. **Figure 4.13** shows two possible high energy channel sites that on the line between successive tetrahedral sites: the 2d octahedral site sandwiched between two Sb^{5+} octahedra and the 3-coordinate 4g site between the 2d site and the low energy tetrahedral site. Since it is unclear which site serves as the maximum along the diffusion path, targeting the known minimum is a more effective initial strategy. These sites are located between In dimers, and should be significantly affected by substitution of In^{3+} .

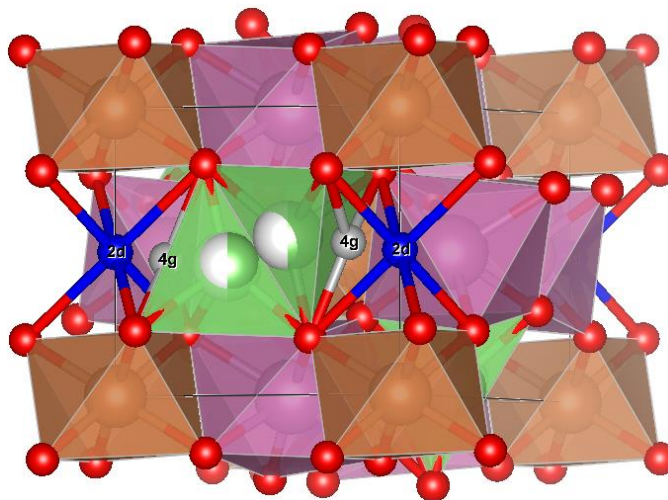


Figure 4.13. Potential high energy sites in the channels of LIAO: (blue) octahedral sites with Wyckoff position 2d between SbO_6 chain units and (gray) 3-coordinate sites between Li tetrahedra and the 2d sites.

The first step of this process is determining what 3+ ions can replace In^{3+} while maintaining this unique structure. Fortunately, as mentioned previously, the original report of LIAO identified the Fe and Sc analogous of LIAO as having the same powder pattern. Single crystals of both were grown with the same process as LIAO in order to investigate whether these compositions were isostructural to LIAO or exhibited the ordered LiSbO_3 structure predicted by Tarte and Gabelica-

Robert (see **Table A.1**).¹⁶ **Figure 4.14** shows the obtained single crystal structure solution for $\text{LiSc}_2\text{SbO}_6$ (LSAO) at 100 K. Analogous data collected on $\text{LiFe}_2\text{SbO}_6$ (LFAO) crystals could not be solved into a satisfactory structure, i.e. one without any non-positive definite atoms. The atomic coordinates and isotropic thermal parameters for the refined structures can be found in **Tables A.2**. Notably, the structure for deviates from the $Pnmm$ symmetry of LIAO.

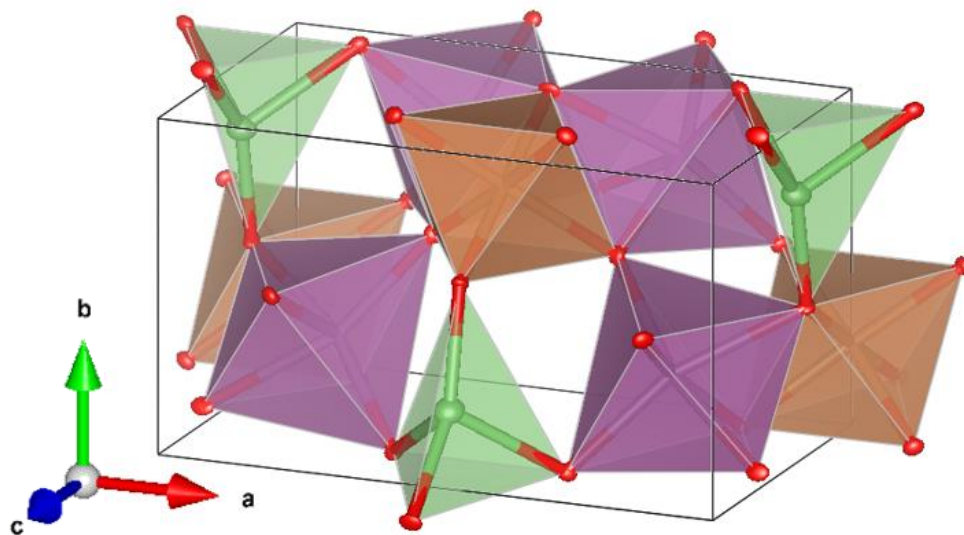


Figure 4.14. Crystal structures of LSAO at 100 K viewed down the $[3\ 4\ 12]$ direction. Red spheres are O atoms and indigo, orange, and green polyhedra are centered on Sc, Sb, and Li, respectively.

Surprisingly, the LSAO solution also does not exhibit the $Pnn2$ symmetry predicted for ordered LiSbO_3 , but rather $Pmn2_1$ symmetry, which is a noncentrosymmetric maximal subgroup of $Pnmm$. The framework remains unchanged in LSAO showing that alternating-width chains are stable with Sc replacing In. The lowering of symmetry arises from apparent ordering of Li on the tetrahedral sites in LSAO resulting in polarization along the c-axis. As in the case of LIAO, solid state NMR was used to independently probe the Li environments, since X-rays can only weakly interact with light elements such as Li. **Figure 4.15** shows that the Li environments closely resemble those in LIAO, confirming tetrahedral coordination. It should be noted that the wider peaks relative to those in **Figure 4.4a** arise from the larger dipolar and quadrupolar broadening of

^7Li versus ^6Li . Furthermore, the greater degree of broadening observed in LiSbO_3 than LIAO is consistent with face-sharing octahedral coordination in the former and isolated tetrahedral coordination in the latter.^{45,55} Unfortunately, since Li is tetrahedral in both the ordered and disordered structures, NMR cannot distinguish them.

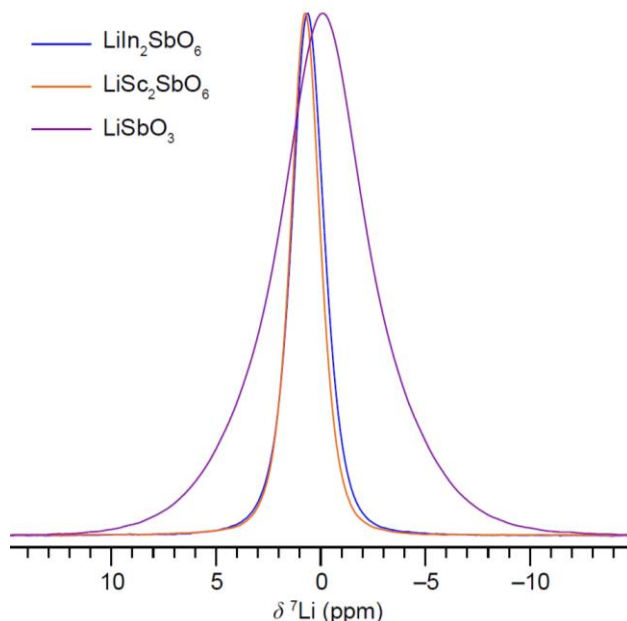


Figure 4.15. ^7Li solid-state 5 kHz MAS NMR spectroscopy central resonance of LSAO compared with that of LIAO and LiSbO_3 .

As such careful consideration of the 100 K structural solution of LSAO is warranted. Notably, it exhibits a Flack parameter value of 0.5. This parameter reflects the absolute configuration of the crystal and a structural solution and ranges from 0, if the solution is correct, to 1 if it is inverted relative to the sample structure. A value of 0.5 indicates the presence of both configurations in equal amounts, but is also commonly observed when a truly centrosymmetric structure is solved in a noncentrosymmetric space group.⁵⁶ Attempts to solve the LSAO structure in $Pn\bar{m}$ resulted in a statistically significant worsening of the refinement parameters (R_1/wR_2 from 1.76/4.91% to 4.79/10.87%) as indicated by Hamilton's R-Ratio test, and the introduction of non-positive definite atoms as well as an increase in systematic absence violations from 0 to 53. This

suggests that the former explanation for the Flack value applies here. As indicated in **Table A.1**, modelling this as twinning indicates that the opposite configurations are related via 180° rotation around the b-axis. No obvious domains were observed in the crystal when observed under polarized light, suggesting that they are homogeneously distributed throughout it. It should also be noted that the same net transformation can be achieved if all Li in a given configuration are moved into their adjacent, vacant tetrahedral sites, and the origin is shifted as shown in **Figure 4.16**. Thus, inverse configurations are related to local Li-exchange through a simple translation. Since static disorder may appear as Li being shifted onto the vacant site in some unit cells, it is unclear how physically meaningful the twinned, ordered model is, as the presence of randomly distributed twinned domains of an ordered $Pmn2_1$ structure should be indistinguishable from a statically disordered $Pnmm$ structure on the atomic scale.

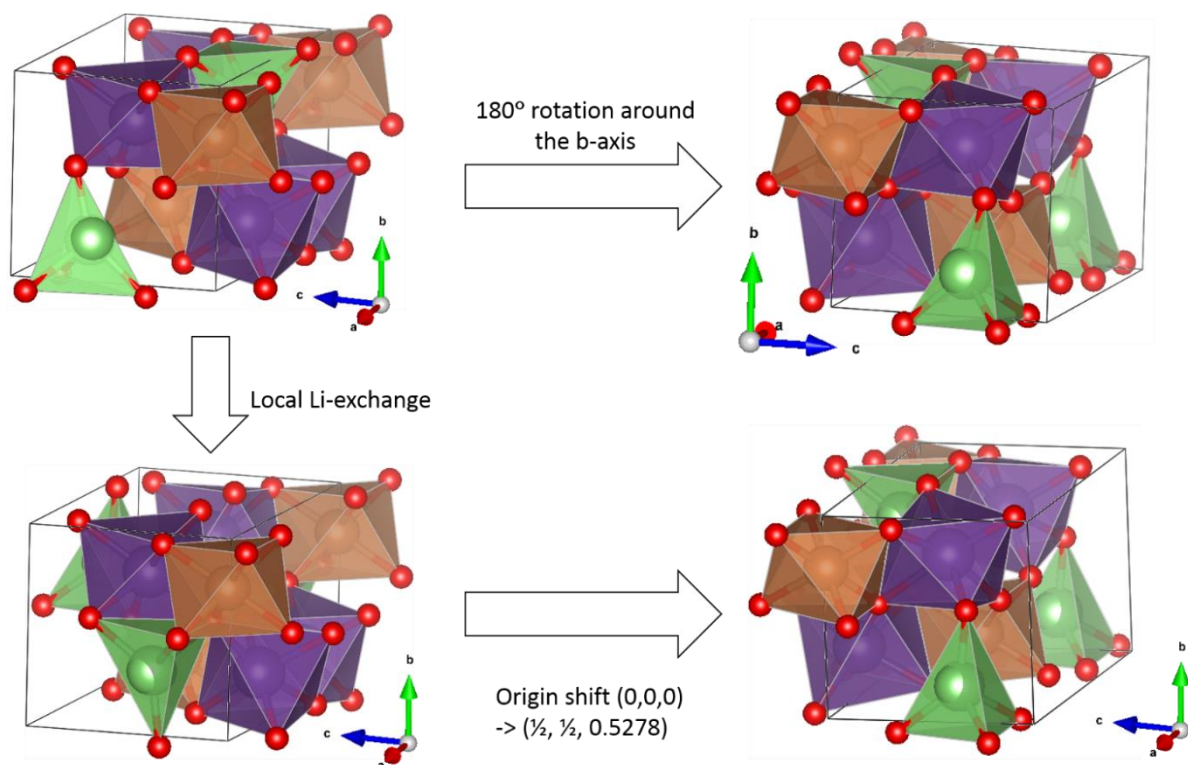


Figure 4.16. The oppositely polarized twin to the LSAO structure, generated by 180° rotation around the b-axis, is simply translated relative to that which would be obtained if Li were to hop into adjacent vacancies.

In either case, the octahedral framework is identical, so their differences should disappear if the Li become dynamically disordered. Thus, diffraction at temperatures high enough to allow for Li-hopping between adjacent occupied and vacant sites should always result in the LIAO structure, *Pnmm* solution. DTA was performed for LSAO and LFAO in order to probe whether a clear signal that may indicate this transition could be observed. The former was included despite the failure to refine a low temperature structure, because the powder pattern contains an analogous set of peaks to LSAO and LIAO, indicating that they have either the same or closely related structures.¹⁶ The data are shown below in **Figure 4.17**. LSAO shows a small, but distinct peak between 425 and 450 K that is endothermic on heating and exothermic on cooling with a slight hysteresis. This behavior is similar to that observed for LIAO and consistent with a phase change from static to dynamic Li-ions.⁵⁴ That the peak occurs at slightly higher temperatures than in LIAO suggests that there is a greater barrier to Li movement in LSAO and potentially lower bulk Li conductivity. For LFAO, a discontinuous slope change is observed in both the heating and cooling curves between 350 and 375 K. Previous work in the Li_2TiO_3 rock-salt phase has demonstrated that increasing MgO-doping causes the order-disorder transition to both shift to a lower temperature and become increasingly broad in DTA data, until it could no longer be observed.⁵⁴ Thus, it is possible that the features in the LFAO data are indicative of a more gradual version of the transition in LIAO and LSAO. The fact that it occurs at a lower temperature is both consistent with observations in the rock-salt phase and indicative that LFAO has a lower barrier to local Li diffusion than the other phases. While this could mean that LFAO will be a better Li conductor, it should be noted that the observed transition most likely corresponds only to local Li-motion,

between adjacent tetrahedral sites, and that the energies of the intermediate channel sites in **Figure 4.13**, the most likely barriers to bulk diffusion, may show different trends with composition.

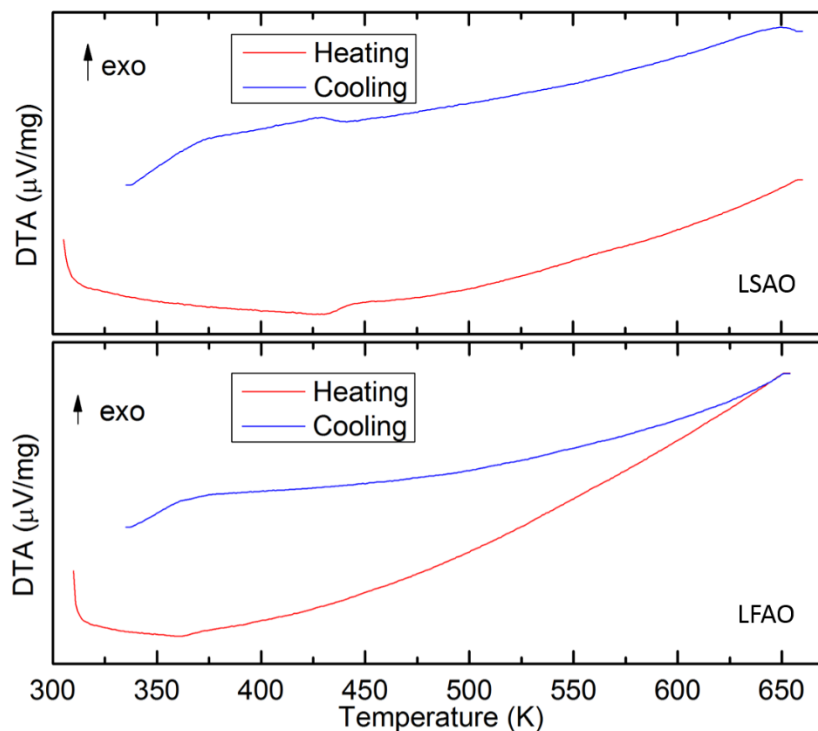


Figure 4.17. Differential thermal analysis of LSAO (top) and LFAO (bottom) polycrystalline samples from 300 to 673 K.

Given the DTA results, single crystal diffraction data were collected on LSAO and LFAO at 500 K and 400 K, respectively, above the apparent transition temperatures. The observed solutions are depicted in **Figure 4.18** with atomic positions and isotropic thermal parameters in **Tables A.2,3**. As expected, both structures are analogous to LIAO with a framework of alternating-width chains and disordered Li-centered tetrahedra giving rise to $Pnmm$ symmetry. This supports the conclusion that the peaks in the DTA are caused by a reversible activation of local Li-hopping. Notably, the thermal ellipsoids for Li in the LFAO solution are significantly larger than those in both high-temperature LIAO and LSAO, despite the fact that the structure was collected 100 K lower. Furthermore, **Figure 4.18b** shows that the major axis of the Li thermal

ellipsoid in LFAO is in the c-direction, orthogonal to the channels. These ellipsoids overlap with the distorted octahedral (4e) site depicted in **Figure A.2**, the main intermediate position along the diffusion path with the lowest bond-valence mismatch between adjacent Li tetrahedra. This suggests that the 4e sites are more favorable in LFAO than in LIAO or LSAO. As such, it is possible that below the disordering temperature, some of the Li becomes trapped in the off-center sites creating local domains of LiSbO_3 -like ordering while others remain in the central tetrahedral sites as in LSAO. Static disorder of these dissimilar domains would not be easily modeled with twinning or a 0.5 Flack parameter as they are not symmetrically related, which may be the reason that the low temperature crystal structure could not be satisfactorily solved. Additionally, as a transition state for local Li diffusion, the 4e site being stabilized can also explain why the disordering temperature, and therefore activation energy, is lowered.

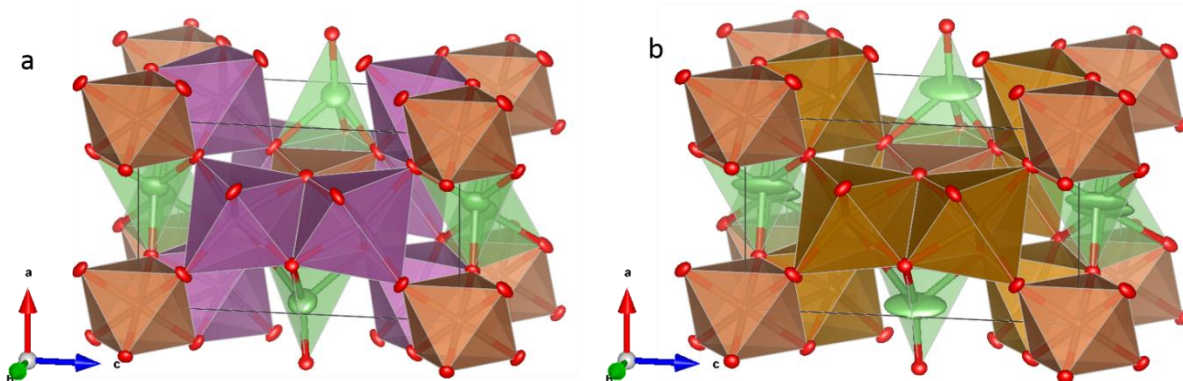


Figure 4.18. High temperature crystal structures of LMAO, $M = (\text{Sc}, \text{Fe})$. (a) LSAO at 500 K down the $[82\bar{1}]$ direction. (b) LFAO at 400 K viewed down the $[281]$ direction. Red spheres are O atoms and indigo, brown, orange, and green polyhedra are centered on Sc, Fe, Sb, and Li, respectively.

Bond valence analysis of the LMAO phases supports these conclusions. The BVS values for both the occupied tetrahedral (4g) and 4e sites are reported in **Table 4.7** along with the values for the high energy 2d site (see **Figure 4.13**) which lies directly between two Sb^{5+} octahedra. Evidently, in LIAO and LSAO both the 4g and 4e are underbonded, with the latter significantly

Table 4.7. Bond Valence Sums of Li⁺ sites in LMAO phases with *Pnmm* symmetry

| Site | LIAO | | LSAO | LFAO |
|------|-------|-------|-------|-------|
| | 100 K | 500 K | 500 K | 400 K |
| 4g | 0.88 | 0.93 | 0.85 | 1.07 |
| 4e | 0.73 | 0.81 | 0.72 | 0.94 |
| 2d | 0.82 | 0.84 | 0.80 | 0.92 |

more so. However, substitution of small Fe³⁺ (65 pm) for the significantly larger Sc³⁺ (75 pm) or In³⁺ (80 pm) contracts both sites significantly, even compared to the 100 K LIAO structure. As a result the 4g site becomes slightly overbonded while the 4e site remains underbonded but to a lesser extent than even the occupied 4e site in the other two phases.⁵⁷ This suggests that the 4g and 4e sites are closer in energy in LFAO, which should lead to a lower barrier to local Li hopping. However, it is worth noting that the opposite trend is observed between LIAO and LSAO: even though Sc is also smaller than In, which also slightly improves the underbondedness of both sites relative to LIAO, the disorder temperature increases slightly. This is likely because Sc is also less electronegative which may increase the covalent character and directionality of Li-O bonds, hindering Li mobility.

The BVS results suggest that the employed substitutions for In³⁺ had the opposite effect of what was desired. Instead of destabilizing the Li tetrahedra, the lowest energy site in the diffusion pathway, lattice contraction appears to have further stabilized it. However, the BVS data in **Table 4.7** for the 2d site indicates that high energy sites along the diffusion pathway felt a similar effect, meaning the overall activation energy to Li diffusion can still have decreased. This preserves the possibility of higher ionic conductivity in LFAO relative to LIAO. Additionally, since replacing In³⁺ with Fe³⁺ pushes the 4g site from underbonded to overbonded, slightly smaller 3+ ions should destabilize it, achieving the original intent of raising the minimum energy in the channel to benefit conductivity. Unfortunately, unit cell contraction also shrinks the Li-Sb⁵⁺ bond distance on the 2d site significantly from 2.55 (LIAO, 100 K) to 2.46 (LFAO, 400 K), increasing the cation-cation repulsion on that site. Furthermore, BVS analysis suggests the 2d site should actually be more

favorable than the 4e off channel site in LIAO given that is slightly less underbonded. However, since the impedance and DTA data together indicate that local Li-hopping occurs before bulk Li transport is significant, it is possible that cation-cation repulsion is the largest factor in the ionic conduction activation energy in these phases. Future measurement of the activation energy for Li conduction in LFAO using impedance spectroscopy will provide insight into this tradeoff and reveal whether lattice contraction is beneficial or not.

4.3.6: (Structural) Effect of Changing Tunnel Cation

Expansion of the phase space of the LIAO structure beyond the limited set of chemically analogous materials already identified will require a thorough understanding of the fundamental driving force behind alternating-width chains. As stated above, it is believed that in LIAO the presence of Li is a critical factor in stabilizing the chain shape. To probe this possibility, K_2CO_3 was substituted for Li_2CO_3 in mixtures with In_2O_3 and Sb_2O_3 with the goal of synthesizing a K-containing analogue of LIAO. PXRD of the products of these reactions, however, indicated the presence of In_2O_3 and a set of unidentified peaks. A search for similar patterns in a database of known K-containing oxides found a remarkably good match between the unidentified peaks and a 1% expanded hollandite-structure phase $\text{K}_2\text{MgSn}_7\text{O}_{16}$. Subsequent literature review revealed previous reports of $\text{K}_2\text{In}_2\text{Sn}_6\text{O}_{16}$, a tetragonal ($I4/m$) hollandite-structure material that has been investigated as a possible anode for Li-batteries.⁵⁸ Since it has been previously demonstrated that In^{3+} and Sb^{5+} can form a complete solid solution with Sn^{4+} in oxides via cosubstitution, the unidentified PXRD peaks were taken to belong to previously unreported $\text{K}_2\text{In}_5\text{Sb}_3\text{O}_{16}$ (KIAO) in the hollandite structure.⁵¹ Since there is no published cif for the In-Sn hollandite, a hypothetical

model of KIAO was built based on $\text{K}_2\text{Fe}_2\text{Sn}_6\text{O}_{16}$, another hollandite phase with $I4/m$ symmetry, via substitution of one In for each Fe and 0.5 In + 0.5 Sb for each Sn.⁵⁹ A whole profile fit using the LeBail method was performed on the most phase sample with this model are depicted in **Figure 4.19** and summarized in **Table 4.8**.

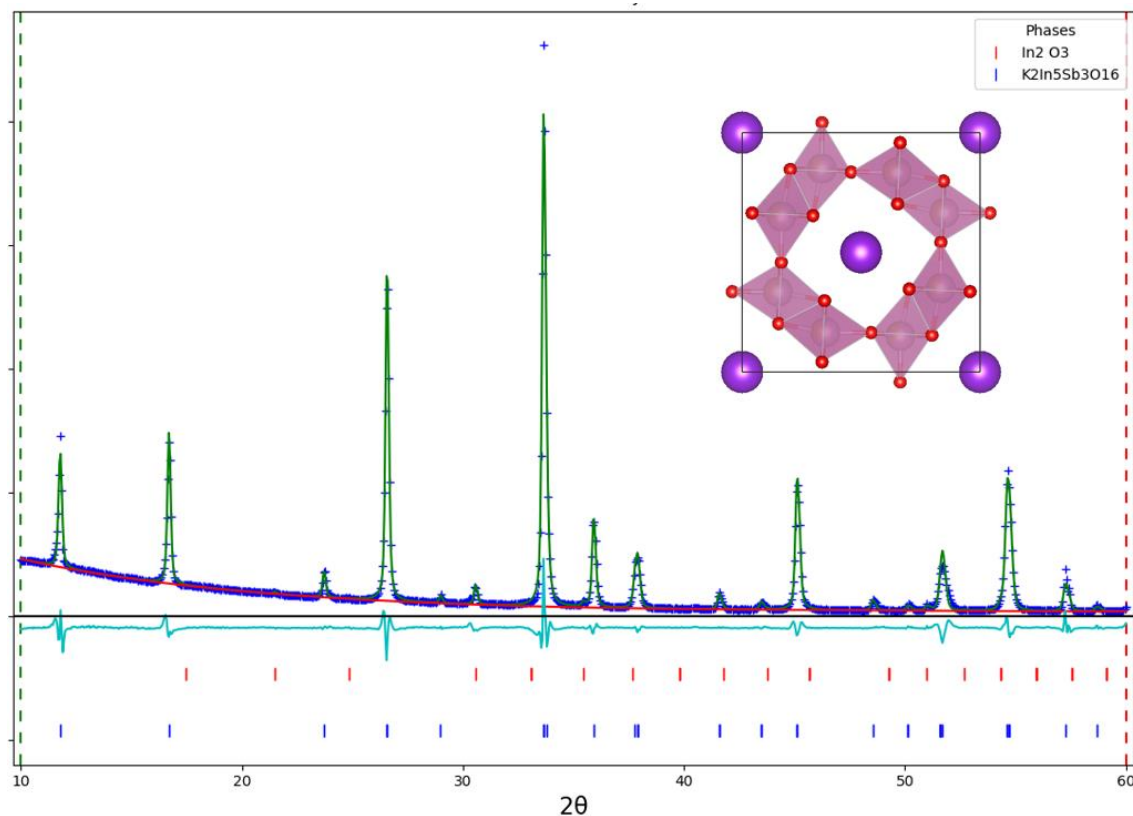


Figure 4.19. LeBail fit of powder KIAO sample with nominal composition $\text{KIn}_{1.5}\text{Sb}_{0.5}\text{O}_{5.25}$. (Blue) Observed powder pattern. (Green) Predicted pattern. (Red) background. (Light Blue) Difference pattern. (Blue ticks) Predicted reflections from $\text{K}_2\text{In}_5\text{Sb}_3\text{O}_{16}$ (Red ticks) Predicted reflections from In_2O_3 , present as a minor secondary phase. (Inset) Crystal structure of hypothetical KIAO phase. Purple and red spheres are K^+ and O^{2-} ions, respectively. Pink polyhedral are centered on framework sites containing a statistical mix of In^{3+} and Sb^{5+} .

The whole profile fit strongly supports the presence of a hollandite-structure as the major phase of the product. As another member of the rutile-related family, hollandite provides an interesting point of contrast with LIAO. The former exhibits typical 2x1, ramsdellite-type chains instead of the alternating-width ones. As previously discussed, the driving force for chain structure in LIAO is thought to be cation-cation repulsion minimization by maximizing distances between

Sb⁵⁺ and other ions. However, the nearest cation-cation distances within the 2x1 chains in KIAO are about the same as those in the framework of LIAO, ~3.2 Å, casting doubt on this explanation. In contrast, the distance between the Li⁺/K⁺ and the framework cations increases significantly from 2.96/3.14 Å (In/Sb) in LIAO to 3.90 Å in KIAO. While, this is unsurprising given that the large, 2x2 channels in hollandite are needed to accommodate K⁺ (138 pm) which is much

Table 4.8. Parameters of the LeBail fit of hypothetical KIAO to KIn_{1.5}SbO_{5.25} PXRD pattern.

| | |
|---------------------|--|
| Source | Lab X-ray |
| Formula | K ₂ In ₅ Sb ₃ O ₁₆ |
| Temperature (K) | 298 |
| Wavelength (Å) | 1.54 (CuKα) |
| Profile range | 10 ≤ 2θ ≤ 60 |
| Crystal System | Tetragonal |
| Space group (No.) | I4/m (87) |
| a = b (Å) | 10.5942(9) |
| c (Å) | 3.21348(14) |
| α = β = γ (deg) | 90 |
| V (Å ³) | 360.67(7) |
| Weight fraction (%) | 98.1 |
| GOF | 4.91 |
| wR (%) | 7.641 |

larger than Li⁺ (76 pm), it may also represent a tendency to reduce repulsion between the framework and any tunnel cations.⁵⁷ Likewise, in the hollandite structure there is a lower ratio of channel ions to framework anions (1:4) than in LIAO (1:3). Furthermore, the refined composition of ~2 % In₂O₃ by weight and 98% KIAO is K and Sb-poor relative to the nominal stoichiometry. Since K₂CO₃ is expected to be very volatile at reaction temperatures (1200 °C), the actual composition of the hollandite phase may be K-poor and Sb-rich relative to the one used in the refinement, suggesting the possibility of K⁺ vacancies in the channels. Thus, comparison with the theoretical KIAO structure suggests that repulsion between the channel and framework cations is another possible determining factor in stabilizing the alternating-width chains over 2x1 ones in LIAO. Elucidating the ordering and composition of KIAO will be necessary in order to verify this hypothesis. Flux growths of single crystals for this purpose were unfortunately unsuccessful using K₂MoO₄ and K₂O-MoO₃-BO₃, which have successfully been used to grow K-containing hollandite phases previously.⁶⁰

4.4: Conclusions and Future Directions

The previously unknown structure of LIAO has been solved and features a unique Li-filled rutile-related framework structure. The framework is built from chains of edge-linked polyhedra, with widths that alternate along the chain length between one (rutile-like) and two (ramsdellite-like) polyhedra. Each Li^+ is disordered over two neighboring tetrahedral sites sandwiched between the centers two ramsdellite-like sections of the framework. This Li-coordination has three important implications for this structure: 1) it differs from previous reports of an ordered- LiSbO_3 configuration for LiM_2SbO_6 ($M = \text{Sc, Fe, In}$) phases, which continue to be cited in recent literature 2) it is the first example of a rutile-related compounds in which the width of any given chain or tunnel is not constant, and 3) the combination of Li-disorder with an obvious conduction pathway makes it a reasonable candidate Li-conductor. Combined DTA and thermal expansion experiments with high temperature PXRD suggests thermal stability in LIAO up to 1200 K with a transition from static to dynamically disordered Li around 400 K. However, AC impedance reveals a moderate to poor conductivity, with an activation energy for charge transport of 1.1 eV.

The stability of the LIAO crystal structure appears more robust to substitution within the octahedral framework than on the channel sites. DTA performed here on the Sc and Fe analogues reveals a thermal event near 450 and 360 K, respectively, which is believed to indicate activation of local Li-hopping. High temperature single crystal XRD reveals that they are identical to LIAO above this transition. BV analysis of all three phases suggests that all of the channel sites in LFAO are the least underbonded, suggesting it may have the best Li-mobility. Below the transition, LSAO retains the same alternating-width framework with Li-ordering that leads to a NCS structure, albeit with both polar orientations present in equal amounts in every crystal examined.

Although the low-temperature structure of LFAO could not be solved, large Li thermal ellipsoids orthogonal to the channels in LFAO at high-temperatures are suggestive of off-center Li-occupancy at low temperatures, which may be consistent with original reports of an ordered LiSbO_3 structure. Finally, a new hollandite-structure phase has been identified in the K-In-Sb-O phase space, potentially $\text{K}_2\text{In}_5\text{Sb}_3\text{O}_{12}$, which suggests that the larger tunnel dimensions needed for K^+ ion remove the driving force for the alternating-width chains of LIAO.

There are several avenues for continued investigation of these results. Impedance measurements on LFAO will confirm whether or not its Li conductivity is sufficient for application or further investigation. Additionally, comparison of the results with those of LIAO will provide an opportunity to decouple the effects of the alternating-width chains from that of the framework chemistry, which is not readily oxidized or reduced in the latter, on the observed ionic conduction behavior and potentially make chain width oscillation a new design parameter for inorganic framework oxides. Since SHG can only occur in NCS materials, SHG measurements should be performed on LSAO as an attempt to verify whether the ordered structure truly consists of polar domains or is simply statically disordered. Further characterization of the new KIAO phase is critical to understanding the factors which control when and how In and Sb order in rutile and ramsdellite-like chains. Elemental analysis of a pure sample or single crystal combined with SCXRD or neutron diffraction would be the most definitive way to achieve this. However, if single crystals cannot be obtained, simultaneous refinement of X-ray and neutron powder diffraction should be attempted.

The unprecedented structures of the LMAO phases identified here provide a strong demonstration of the value of purely exploratory synthesis to materials discovery initiatives.

Computational approaches require the use of first-principles crystal structure prediction methods to identify stable atomic arrangements that have not yet been observed. However, these methods become prohibitively costly with increasing complexity of the stoichiometry and often require constraints based on experimental knowledge to be feasible.⁶¹ Thus, the probability of the LMAO structures being found with these methods is low. However, with only 20 atoms and minimal partial occupancy, these structures are well-suited to serve as templates for high-throughput approaches which constrain potential new materials to known structures. For example, they could be used to determine the stability of Al or Ga analogue to LIAO. As suggested above, these ions that are smaller than Fe may enhance ionic conductivity through contracting the structure. Likewise, when included in the generic set of known structures in future computational studies, it may also reveal unexpected stable phases in very different compositions. Either way the discovery of new structures in complex compositional space via exploratory synthesis clearly plays an important role in computational investigations, and should not be overlooked.

CHAPTER 5: SOLID-STATE FLUORINATION OF HAFNIUM OXIDE

Sections of this work are reprinted with permission from

Steven Flynn, Kent J. Griffith, Chi Zhang, Jiahong Shen, Chris Wolverton, Vinayak P. Dravid, Kenneth R. Poeppelmeier. "Solid State Fluorination of HfO₂." *Submitted*.

5.1: Introduction

As mentioned in **Chapter 1**, the synthesis of new heteroanionic compounds has recently been the subject of research interest in the materials and solid-state communities. The Zr-O-F phase space is one rich, well-explored system that has yielded several oxyfluoride phases to previous investigations. Kolditz and Feltz reported the existence of $\text{ZrO}_{0.25}\text{F}_{3.5}$, $\text{Zr}_3\text{O}_2\text{F}_8$, $\text{Zr}_2\text{OF}_6 \cdot 2\text{H}_2\text{O}$ and ZrOF_2 via thermal decomposition of zirconium fluoride hydrates and hydroxides in inert atmosphere.¹ An in-depth study by Joubert and Gaudreau identified six distinct crystalline phases in three distinct structural groups: fluorite-related ($\text{ZrO}_{1.917}\text{F}_{0.167}$), $\alpha\text{-U}_3\text{O}_8$ -related ($\text{Zr}_{10}\text{O}_{13}\text{F}_{14}$, $\text{Zr}_4\text{O}_5\text{F}_6$, and $\text{Zr}_7\text{O}_9\text{F}_{10}$) and ReO_3 -related ($\text{ZrO}_{0.67}\text{F}_{2.66}$ and $\text{ZrO}_{0.45}\text{F}_{3.1}$).^{2,3} Meyer reported the formation of $\text{Zr}_3\text{OF}_{10}$ via the reaction of NH_4F with Zr in the presence of trace water in a sealed Cu-Ni alloy tube.⁴ Other studies have focused on some of these materials in more depth. Paperniek and Frik reported that $\text{ZrO}_{0.67}\text{F}_{2.66}$ is a disordered ReO_3 -related material in which excess anions occupy interstitial sites and Holmburg provided an in-depth structural characterization of $\text{Zr}_7\text{O}_9\text{F}_{10}$ (see **Figure 1.8c**).^{5,6} Curiously, despite the generally similar chemical behaviors of Zr and Hf, the Hf-O-F system does not appear to have received much attention yet. This is particularly noteworthy since fluorination of HfO_2 has commonly been studied as a method to improve its performance as a high- k dielectric in field-effect transistors and flash memory.⁷⁻¹⁰ Although the films employed are often amorphous, knowledge of competing crystalline Hf-O-F phases and associated Hf-O-F local structural motifs should be valuable to these studies.

To our knowledge, only three ternary hafnium oxyfluorides have been identified in the literature, $\text{HfO}_{0.25}\text{F}_{3.5}$, Hf_2OF_6 (several polymorphs), and $\text{Hf}_3\text{O}_2\text{F}_8$, all of which were made via the thermal degradation of hafnium fluoride hydrates.^{11,12} The presence of a fourth Hf-O-F phase,

HfOF₂, has been suggested in a thermogravimetric study of fluorination of HfO₂ with F₂, but could not be confirmed via X-ray diffraction.¹³ Notably, all of these compounds have a stoichiometric analogue in the Zr-O-F system, although they are not necessarily isostructural. HfF₄ · 3H₂O, HfF₄ · H₂O, and the hydrated form of Hf₂OF₆ are all reported to have different structures than their Zr equivalents, although later studies on the former have suggested that an isostructural Zr form may exist.^{11,14} As such, there is a large probability that undiscovered hafnium oxyfluoride phases exist, possibly with different structures that exhibit properties of interest.

The limited set of synthetic approaches used in previous studies may have unintentionally constrained the set of observed Hf-O-F phases. A variety of synthetic approaches for oxyfluorides have been explored in the literature. The traditional solid state approach is to combine precursor oxides and fluorides together and heat them until a reaction occurs. The high reactivity of all but the most stable fluoride materials with SiO₂ and/or water means that this often entails costly setups such as sealed metal tubes.²⁻⁵ Alternative methods include exposing the precursor oxide to a reactive fluoride source such as F₂ or HF gas, or aqueous hydrofluoric acid, although these must be handled carefully as they are highly toxic.^{13,15} Safer options include controlled decomposition of stable fluorides and fluoride hydrates or reaction of oxides with solid fluorination agents like XeF₂, CuF₂, ZnF₂, NH₄F (or NH₄HF₂), polytetrafluoroethylene [PTFE; -(CF₂)_n-], or polyvinylidene difluoride [PVDF; -(CH₂-CF₂)_n-] all of which decompose upon heating into more reactive agents.^{16,17,18-22} Of these, the last three are both stable under ambient conditions, therefore easy to work with, and conveniently produce volatile products at high temperatures lowering the risk of secondary phase contamination. Among the hafnium oxyfluoride studies in the literature, it appears that primarily thermal decomposition of fluorides and reaction of HfO₂ with F₂ or HF

have been attempted, whereas a wider variety of synthetic approaches have been used for Zr.^{2-6,11-15} Thus, employing a different fluorination method for HfO₂ may reveal previously unreported Hf-O-F phases.

In this study, we report the attempted fluorination of HfO₂ with NH₄HF₂, PTFE, and PVDF. The two fluoropolymer reagents show similar reaction behavior: fluorinated products are only observed when in a sealed tube and comprise a similar set of phases, including the tetragonal, metastable α -HfF₄ and a new Hf oxyfluoride phase analogous to a reported polymorph of Zr₂OF₆ (PDF 00-040-1095). However, PVDF appears to have greater reactivity with the glass producing side products like HfSiO₄ that are not observed in the PTFE reactions. In contrast, the formation of a new, single phase hafnium oxyfluoride is readily observed after a multi-step reaction with NH₄HF₂ involving the formation and subsequent decomposition of (NH₄)₃HfF₇. The main reflections observed in X-ray and electron diffraction of this phases exhibit a clear relationship to the α -UO₃ structure, whereas ¹⁹F NMR exhibits several environments indicative of anion-deficiency. As such, this phase appears to belong to the same anion deficient α -UO₃ structure family as the previously reported Zr₇O₉F₁₀. The reaction mechanism between HfO₂ and NH₄HF₂, and the implications of the purity and quality of its products for the search for new heteroanionic materials is discussed.

5.2: Experimental Methods

5.2.1: Synthesis

Caution! *The fluorinating agents used in this study release hazardous gasses at elevated temperatures and should only be used in open systems with appropriate isolation and ventilation.*

Fluorination of HfO₂ (98%, Sigma Aldrich) was attempted via solid state reaction with NH₄HF₂ (98%, Sigma Aldrich), PTFE (Aldrich, 1 μm powder), and PVDF (Aldrich). Precursor powders were thoroughly ground together with acetone as a mixing aid in either (i) one of several fixed **weight** ratios of HfO₂ to NH₄HF₂ (1:1, 2:1, and 3:2), (ii) stoichiometric amounts with respect to a target product of (NH₄)₃HfF₇ (1:3.5 **molar** ratio of HfO₂: NH₄HF₂), or (iii) a fixed O to F molar ratio between 1:1 and 1:2 (PTFE and PVDF). Weight ratios were used for ease of measurement in initial, exploratory experiments (case i), whereas molar ratios were used for precision when specific targets had been ascertained (case ii). An initial, pre-reaction step for HfO₂ + NH₄HF₂ samples (case ii) was performed at 250 °C for 12 hours to promote conversion into the desired (NH₄)₃HfF₇ precursor. The main reaction heating profile for all mixture compositions consisted of one to three cycles of heating at 5 °C/min to 350 °C (PVDF), 420 °C (NH₄HF₂), or 450 °C (PTFE) for 12 hours and cooling at the same rate with intermittent grinding. Reaction temperatures were selected that were high enough such that the fluorinating agent would undergo appreciably fast decomposition and low enough that hydrolysis of fluoride-containing products might be suppressed.¹⁸⁻²⁵ All open reactions were carried out in furnaces contained within closed, well-ventilated fume hoods to remove any toxic and/or corrosive volatile products, such as HF gas, released at elevated temperatures. Powder diffraction was carried out between cycles to determine whether the reaction had reached completion. All reactions with NH₄HF₂ were carried out in air in capped Al₂O₃ crucibles. Reactions with PTFE or PVDF were carried out in both capped Al₂O₃ crucibles (20 mL) in air as well as in evacuated and sealed fused silica tubes. Reaction vessels were selected for cheap, widely available materials that have been previously used for related oxide fluorination reactions.^{17,18,26}

5.2.2: Diffraction

Phase purity and reaction completeness was checked with laboratory PXRD collected over a 2θ range of $10\text{--}60^\circ$ (Cu $K\alpha$) on a Rigaku IV (Ultima) X-ray diffractometer under ambient conditions. Synchrotron X-ray diffraction patterns were collected at 11-BM at the Advanced Photon Source at Argonne National Laboratory with a wavelength of 0.41267 \AA at 300 K. The sample was packed into a small Kapton capillary (outer diameter $\sim 1 \text{ mm}$) with both ends sealed with Q compound (Apiezone). Powder diffraction data were analyzed by Rietveld refinement using the General Structure Analysis System II (GSAS II) package.²⁷

5.2.3: Characterization

Elemental analysis was carried out by Galbraith Laboratories. The weight % of Hf was determined via Inductively Coupled Plasma Atomic Emission Spectroscopy (ICP–AES) and while that of F was measured with pyrohydrolysis and an ion selective electrode.

Thermogravimetric analyses were performed in a Netzsch STA 449 F3 Jupiter Simultaneous Thermal Analysis (STA) instrument. 39.049 mg of phase pure Hf-O-F was placed in a gold crucible with weight of 170.977 mg. The sample was measured under ultra-high purity Helium gas (50 ml/min). The buoyancy effect for Helium was corrected by measuring the empty crucible under the same measurement conditions used for the samples. Temperature was increased at a rate of $10 \text{ }^\circ\text{C}/\text{min}$. Performance of the thermobalance of the STA was verified by using a certified sample of calcium oxalate monohydrate (European Pharmacopoeia Reference Standard) up to $1000 \text{ }^\circ\text{C}$.

^{19}F solid-state nuclear magnetic resonance (NMR) spectra were measured under magic angle spinning (MAS) in a static magnetic field of 9.4 T with a Bruker Avance III spectrometer.

The samples were packed into 1.6 mm diameter zirconia rotors and spectra were recorded in a Phoenix narrow-bore 1.6 mm HFX probe. T_1 (spin-lattice) relaxation was measured with a saturation recovery pulse. ^{19}F spectra were measured with a rotor-synchronized Hahn-echo ($\pi/2$ – τ – π – τ –acquire) pulse sequence using a 90° RF pulse of 1.75 μs . Recycle delays were $\geq 5T_1$. The chemical shifts were externally referenced to the center of the doublet in NaPF_6 (at 39 kHz) at –82.5 ppm. Frictional heating at 40 kHz MAS leads to an internal sample temperature of 44 $^\circ\text{C}$, as calibrated via the temperature-dependent ^{207}Pb shift of lead nitrate.^{28,29}

Scanning/transmission electron microscopy (S/TEM) was carried out to investigate the structure. Polycrystalline products were crushed to powder and dropped on ultrathin C-coated Cu grids. Selected-area electron diffraction (SAED) patterns, convergent beam electron diffraction (CBED) (6.9 mrad of convergence angle) patterns atomic-resolution high-angle annular dark-field (HAADF) (90–200 mrad of collection angle) and annular bright-field (ABF) (11–24 mrad of collection angle) scanning transmission electron microscopy (STEM) were acquired using a Cs-corrected JEOL ARM 200CF operated at 200 kV. The multislice simulation was conducted with software Dr. Probe under 200 kV, a thickness of 33.49 nm, a convergence angle of 20.6 mrad, and a defocus of 0 nm, using frozen lattice configurations and the number of variants per slice set to 10.³⁰

Thermodynamic analyses were performed with density functional theory (DFT) calculations using the Vienna ab initio simulation package (VASP) along with the projector augmented wave (PAW) method.^{31–35} The Perdew-Burke-Ernzerhof (PBE) generalized gradient approximation (GGA) was used as the exchange-correlation functional. 520 eV was chosen as cutoff energy of the plane wave basis set, and the structures were fully relaxed until the total energy

converged to 10^{-8} eV and the force on each atom is less than 0.001 eV/Å.^{36,37} Γ -centered k-point meshes were constructed with at least 8000 k-points per reciprocal atom (KPPRA). The Gibbs reaction energies were calculated by subtracting the total energies of the reactants from those of the products, and the experimental enthalpy and entropy data from NIST-JANAF thermochemical tables were considered for gaseous phases (H_2O and HF).³⁸

5.3: Results and Discussion

5.3.1: Reaction with Fluoropolymers

Reactions of HfO_2 with PVDF in air produced an obvious color change from bright white precursor mixture to light brown product (**Figure A.3**). Previously reported reactions with fluoropolymers have also observed color changes from light to dark.^{17,21} Since C in the fluoropolymer can act as a reducing agent by abstracting oxygen to form CO or CO_2 , this is usually attributed to the reduction of a transition metal to a lower oxidation state compensated by substitution of F^- for O^{2-} , introducing d-electrons which readily absorb visible light.²⁹ However, Hf^{4+} has no other stable oxidation states in air, so this is not a valid mechanism in HfO_2 . Furthermore, the representative PXRD patterns shown below in **Figure 5.1a** appear to only contain HfO_2 , without shifting that would be expected from introduction of oxygen vacancies or the substitution of O^{2-} with 2F^- . As such the color change does not represent any significant structural deviation from the initial material. More likely, the PVDF is breaking down into an amorphous carbon residue which is providing color to the mixture without being observed in the PXRD.^{18,21} This is consistent with the more prominent amorphous hump in the PXRD pattern of the sealed tube sample compared to the one exposed to air since a larger percentage of residue is expected

because loss of C as CO₂ is prevented in the former case. Heating the brown product in air at 450 °C for 12 hours returned the powder to its bright white color, indicating that this is a high enough temperature to burn off the carbon residues.

Evacuated, sealed tube reactions between HfO₂ and PVDF show distinctly different behavior compared to reactions in air. Superficially, they result in an even more drastic color change than the in-air reactions, from white to black. Given that the reaction vessel is a closed system and there is no O₂ present to allow the carbon in the polymer to burn off as CO₂, most of it should remain in the product in some form. Thus, a darker color is consistent with the C-residue explanation of the in-air reactions. Of greater consequence is that the powder patterns of sealed samples, such as the representative one shown in **Figure 5.1b**, are significantly more complex than those of the in-air reactions, indicating reaction successfully occurs when contained. In addition to unreacted HfO₂, which still appears to make up a majority of the product, a set of peaks matching HfSiO₄ is clearly present, suggesting that some reaction with the tube took place. The remaining peaks were compared to reported patterns for known fluorides and oxyfluorides of Hf and Zr. The latter phase space was included because it has been more thoroughly investigated and the similar chemistries of Hf and Zr makes analogous compounds between the two quite likely. One set of peaks appears to be a close match for tetragonal Hf₂OF₆, except the (112) peak at ~22.5° which is slightly shifted from the predicted position. Rickard and Waters reported that the primary effect of hydration on the structure of this phase was to expand the *c*-axis, suggesting that water content may be responsible for this mismatch.¹¹ Alternatively, **Figure A.4** shows that the same set of peaks can be matched to the reported pattern for Zr₃(OH)₂F₁₀ (PDF 00-020-1466). While no structural model has been reported for this phase, it is possible that an Hf analogue has been formed. Finally,

the remaining unmatched peaks in the product pattern appear to correspond well to a reported pattern for Zr_2OF_6 (PDF-00-040-1095), suggesting that this may be an unreported polymorph of the isostructural Hf analogue, Hf_2OF_6 . Although a discrepancy between the predicted and actual positions is clearly apparent, it is consistent with other isostructural Hf and Zr compounds such as HfO_2 and ZrO_2 , where the former is slightly contracted relative to the latter. Unfortunately, no crystallographic model has been reported in association with this powder pattern for Zr_2OF_6 , so the relationship with known Hf_2OF_6 structures remains unclear. Attempts to isolate this potentially new heteroanionic Hf compound via adjustment of the fluorinating agent ratio, tube size, and reaction time were unsuccessful. It should be noted that HfO_2 , $HfSiO_4$, and HfF_4 are white powders (the first two are used as a high- k dielectrics).⁷ It follows that chemically related Hf-O-F ceramics should exhibit the same large band gap, making them white as well, and that the dark color of the mixture is better attributed to C-residue than any of the crystalline phases observed.

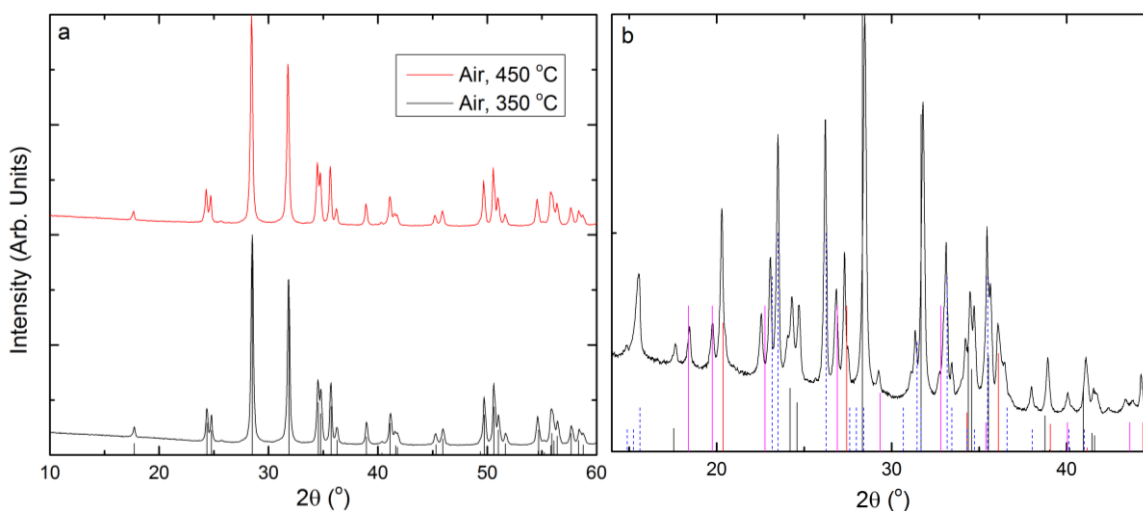


Figure 5.1. PXRD patterns of reaction products of HfO_2 and PVDF in (a) air and (b) an evacuated sealed tube (350 °C). Vertical lines are the reflections for known or reported phases: HfO_2 in the baddelyite structure (black), $HfSiO_4$ (red), Zr_2OF_6 (blue), and tetragonal Hf_2OF_6 (magenta). Dashed lines indicate phases reported as a list of reflections without further structural information.

For the reaction of HfO_2 with PTFE, no color change is observed when carried out in air whereas the reaction mixture shifts from white to black after heating in an evacuated, sealed tube. **Figure 5.2** shows a representative PXRD pattern from each of these reaction conditions. Although PTFE decomposition occurs as low as 260 °C, appreciable rates are only observed above 400 °C, unlike PVDF.^{16,22,23} As such, these reactions were carried out at 450 °C. Given the results of the PVDF reactions, this temperature appears to be sufficient to volatilize any carbonaceous byproducts, which is likely what happened for the in-air reaction. The PXRD pattern for the open reaction is consistent with this explanation as it shows only phase pure HfO_2 .

Inversely, the complex second pattern shows that when volatilization is prevented through use of a sealed reaction vessel the products are much more varied. Like with the PVDF reactions, the most prominent peaks most likely indicate the presence of HfO_2 and an unreported Hf analogue of Zr_2OF_6 . Furthermore, the remaining minor peaks are best matched by $\alpha\text{-HfF}_4$, a fully fluorinated product. Finally, in some cases, an additional peak was observed at $\sim 18^\circ$ with no obvious match to any known Zr or Hf oxide, fluoride, or oxyfluoride phases. However, previous studies of fluorination with fluoropolymers have indicated the presence of extra peaks arising from carbonaceous byproducts such as graphite fluoride.¹⁸ As such, a control was performed under the same conditions as the reaction but without the addition of any HfO_2 , only PTFE. As shown **Figure A.5**, the main peak of this reaction exactly matches the unknown peak. Thus, this product appears solely attributable to the breakdown of PTFE in vacuum, and possibly with its reactions with the fused silica tube.¹⁵ As with PVDF, all of the identifiable products are either known or most likely to be white and cannot explain the observed color change.²³ Likewise, efforts to isolate the product phases of the PTFE reactions were unsuccessful.

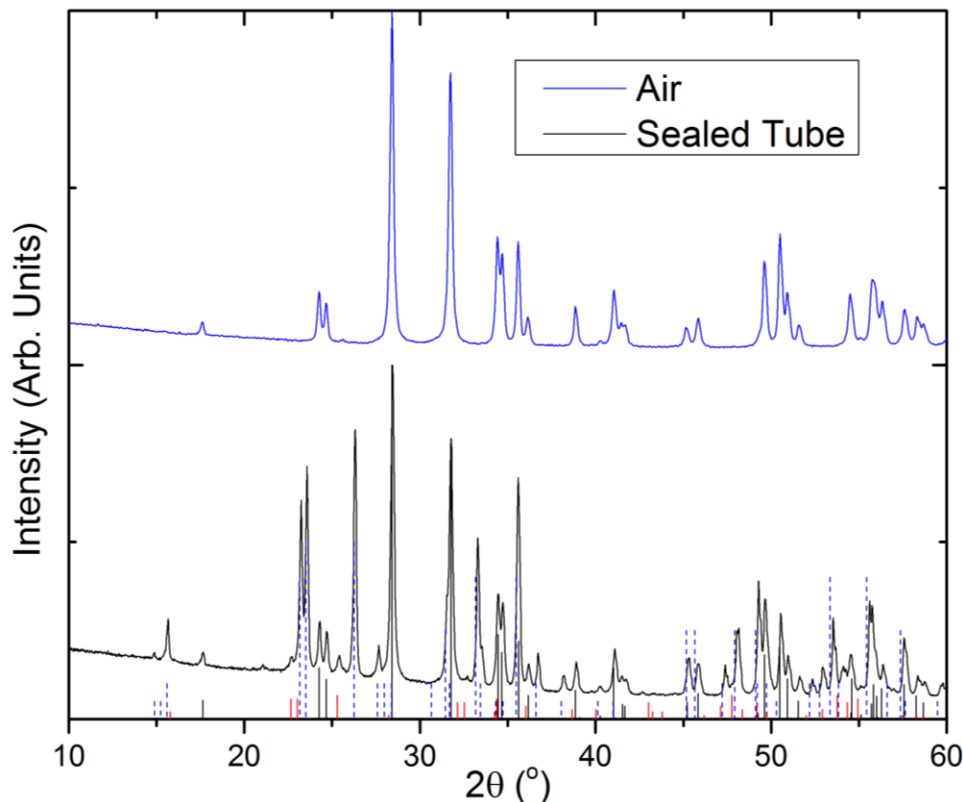


Figure 5.2. PXRD patterns of reaction products of HfO₂ and PTFE. Vertical lines are the predicted reflections for HfO₂ (black), α -HfF₄ (red), and Zr₂OF₆ (blue). Dashed lines indicate phases reported as a list of reflections without further structural information.

These results indicate similar but distinct behavior of the two fluoropolymer reagents. While both retain HfO₂, indicating incomplete reaction, as well as an apparent Hf-analogue of Zr₂OF₆, there are two phases exclusive to PVDF and one for PTFE. These differences are almost certainly connected to the compositions of the two polymers: the repeat unit of PVDF is (-CH₂CF₂-), while that of PTFE is (-CF₂-). While the processes of PVDF and PTFE breakdown are complex, with many reported intermediates and byproducts including hydrocarbons, aromatics, small molecules, each has characteristic/exclusive products that can distinguish it.^{17,23,24} For example, since only PVDF has H content in its chain, it can release HF as part of the polymer breakdown process whereas PTFE cannot. In fact, previous studies have identified HF loss as a major mechanism in this process.³⁹ Likewise, CF₄ has been reported as the primary product of PTFE

degradation in a vacuum but is not observed in pyrolysis of PVDF.^{17,39} While it is not clear that these are the only decomposition products responsible for fluorination of HfO₂ in the reactions studied here, they may provide insight into the exclusive products of these two reagents.

Previous studies have noted that HF rapidly attacks the SiO₂ tube generating gaseous SiF₄, allowing Si⁴⁺ to be incorporated into the products.³⁹ While Hirai et al. also detected SiF₄ as a result of the reaction between the silica container and CF₄ from PTFE breakdown, they found that intimate mixing could decrease the fraction of CF₄ that attacked the glass by causing CF₄ to react with the precursor first. However, since no silicate formation was observed in the PTFE reaction of this work, this was not a major side reaction in the current study. Furthermore, their experiments were carried out at higher temperatures (500-900 °C) than the ones here, which favors SiF₄ formation ($\Delta H = -168$ kJ/mol).¹⁷ Furthermore, Taken together, these findings suggest that at least at lower temperatures just above the decomposition point and when well-mixed with other reactants, PTFE is more resistant to side reactions with the container than PVDF, owing to apparently faster reaction by CF₄ than HF. This should make PTFE a more attractive option for sealed tube fluorinations.

As indicated above, each fluoropolymer produces two distinct fluoridated products, one of which is shared and one which is exclusive to either PVDF or PTFE. The identity of this second phase is another interesting contrast between these reactions. That the former results in an oxyfluoride whereas the latter produces HfF₄ suggests that PTFE may be a more effective fluorinating agent. However, rapid conversion of HF to SiF₄ in the PVDF reactions may lower its apparent reactivity, as suggested by Hirai and colleagues.¹⁷ Furthermore, in general, a weaker fluorinating agent that avoids passing through a pure fluoride intermediate to reach oxyfluoride

products may provide access to metastable heteroanionic phases. It is also worth noting that the tetragonal α -HfF₄ polymorph is produced in these reactions, in contrast to the monoclinic form β -HfF₄. For analogous ZrF₄ materials, the latter form is the stable phase at ambient conditions whereas the former is obtained by quenching from high temperatures and transforms to the monoclinic polymorph upon heating to moderate temperatures.⁴⁰ It is probable that HfF₄ shares the same behavior, meaning this work identifies a potential low-temperature synthetic route to the tetragonal phase. This may be facilitated by the pressure in the sealed tube generated by volatile products of the polymer decomposition. The solid solution Zr(O,F)_{4-x}, derived from the α -ZrF₄ structure is known and compositionally analogous Hf phases have been reported.^{12,41} Thus, an optimized version of this PTFE fluorination that produces phase pure α -HfF₄ may also unlock new pathways to heteroanionic phases.

Finally, the main fluorination product, the Hf analogue of “Zr₂OF₆”, also reveals a slight discrepancy between the two fluoropolymers. Specifically, the intensities of its peaks relative to those of HfO₂ are higher for PTFE, even though the side reaction with the tube would have consumed extra starting material in the PVDF sample, artificially increasing the relative intensity of the product peaks. While this may also be attributed to the lower fluorinating ability of SiF₄, it also suggests that the PTFE reaction is more selective for this unknown oxyfluoride. This reinforces the idea that PTFE is a more controlled reagent for general fluorination of oxides. It should be noted, however, that the fact that this phase is produced by both fluoropolymers suggests that there is at least one common fluorination mechanism between them, possibly mediated by a different decomposition product shared between PTFE and PVDF. Attempts to isolate this

potentially new heteroanionic Hf compound via adjustment of the fluorinating agent ratio, tube size, and reaction time were unsuccessful.

Precise identification of what processes occur during fluorination is difficult. Furthermore, while reducing HfO_2 is known to be significantly challenging (no reduced oxidation state hafnium oxide phases are known), chemical reduction is a viable reaction mechanism with fluoropolymers for many other materials in addition to the processes occurring in this study.⁴²⁻⁴⁵ Thus, how to generalize even the phenomenological results of these reactions to other systems is complicated. Nevertheless, the selective production of an unknown Zr_2OF_6 analogue and a possible low-temperature route to a high-temperature phase reveal the potential of fluoropolymers to have unique value as fluorinating agents.

5.3.2: Reaction with NH_4HF_2

The initial reactions with NH_4HF_2 were carried out at three fixed weight ratios of HfO_2 to NH_4HF_2 (2:1, 3:2, and 1:1). In contrast to the fluoropolymer results, the occurrence of a significant reaction is immediately evident in the PXRD pattern of the products. **Figure 5.3** shows that all three ratios primarily resulted in a mixture of $\beta\text{-HfF}_4$ and a set of unknown peaks without any match among known Hf-based oxides, fluorides, or oxyfluorides. Comparing the patterns of the three precursor mixtures reveals that the intensities of the unmatched peaks remain constant relative to each other, suggesting that they belong to a single, unknown phase. An expanded search showed that the peak positions matched those of $\text{Zr}_7\text{O}_9\text{F}_{10}$. Discrepancies in the predicted intensities, as well as the fact that no Zr was present in the precursors, indicated that the phase was likely an unknown Hf analogue of the Zr phase.

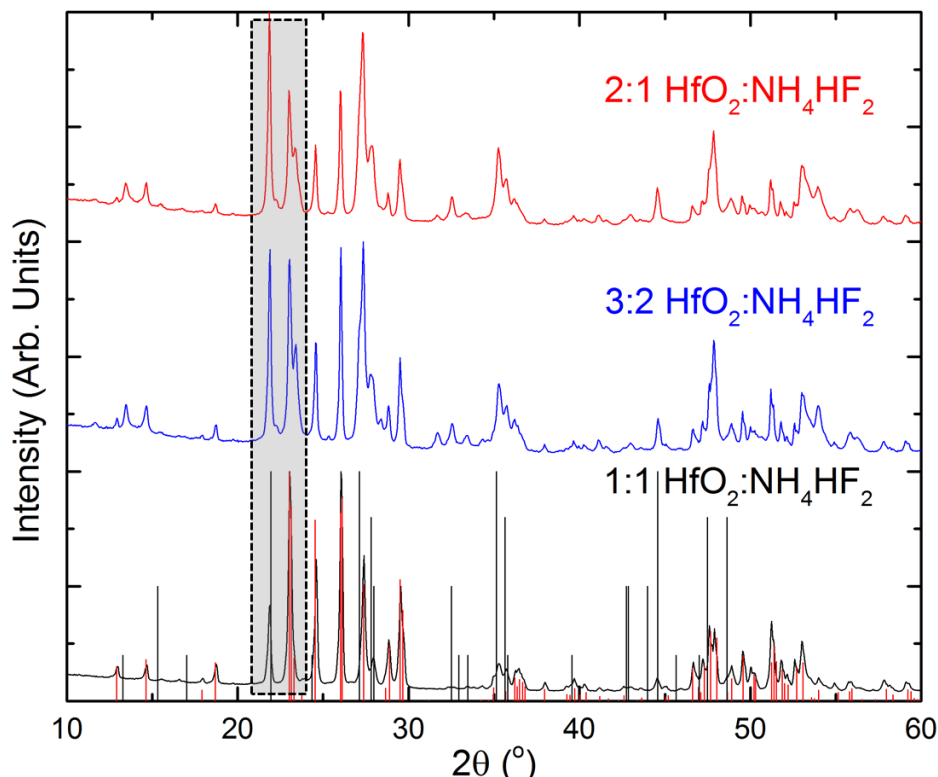


Figure 5.3. PXRD patterns of the reaction products of HfO_2 and NH_4HF_2 at three different weight ratios. Vertical lines indicate theoretical peak positions for $\beta\text{-HfF}_4$ (red) and $\text{Zr}_7\text{O}_9\text{F}_{10}$ (black). The shaded region indicates one easily-distinguished high intensity peak from each phase. The relative intensities of these peaks reverses as the reactant ratio is increased from 1:1 to 2:1 ($\text{HfO}_2:\text{NH}_4\text{HF}_2$).

Figure 5.3 also shows that increasing the proportion of HfO_2 in the initial reaction mixture results in less $\beta\text{-HfF}_4$ and more oxyfluoride in the product, as indicated by the decreasing intensity of its peaks relative to the others. However, a small amount of HfO_2 was present as a secondary phase in the 3:2 and 2:1 ratio samples, despite some $\beta\text{-HfF}_4$ remaining, suggesting that either some of the starting material had not reacted or that the decreased amount of fluorinating agent in the system favored hydrolysis of one or both of the fluoride-containing products at a rate comparable to their formation. As such, further reduction of NH_4HF_2 in the precursor mixture would have likely resulted in even more HfO_2 and failed to isolate the target phase even if all the $\beta\text{-HfF}_4$ was eliminated as desired. Instead, the product mixture was subjected to a second heating cycle, identical to the first, after grinding. **Figure 5.4** depicts the powder pattern of the 2:1 sample after

each heating cycle. The pattern of the reheated sample is nearly phase pure oxyfluoride, only minor HfO_2 and $\beta\text{-HfF}_4$ (< 5 wt %) was obtained. Later repetitions of this procedure required up to three additional heating steps were necessary to produce a similar level of phase purity of the target phase (see **Figure A.6**). As the original and repeat experiments were carried out in summer and winter, respectively, this was interpreted as a strong reaction rate dependence on the ambient humidity.

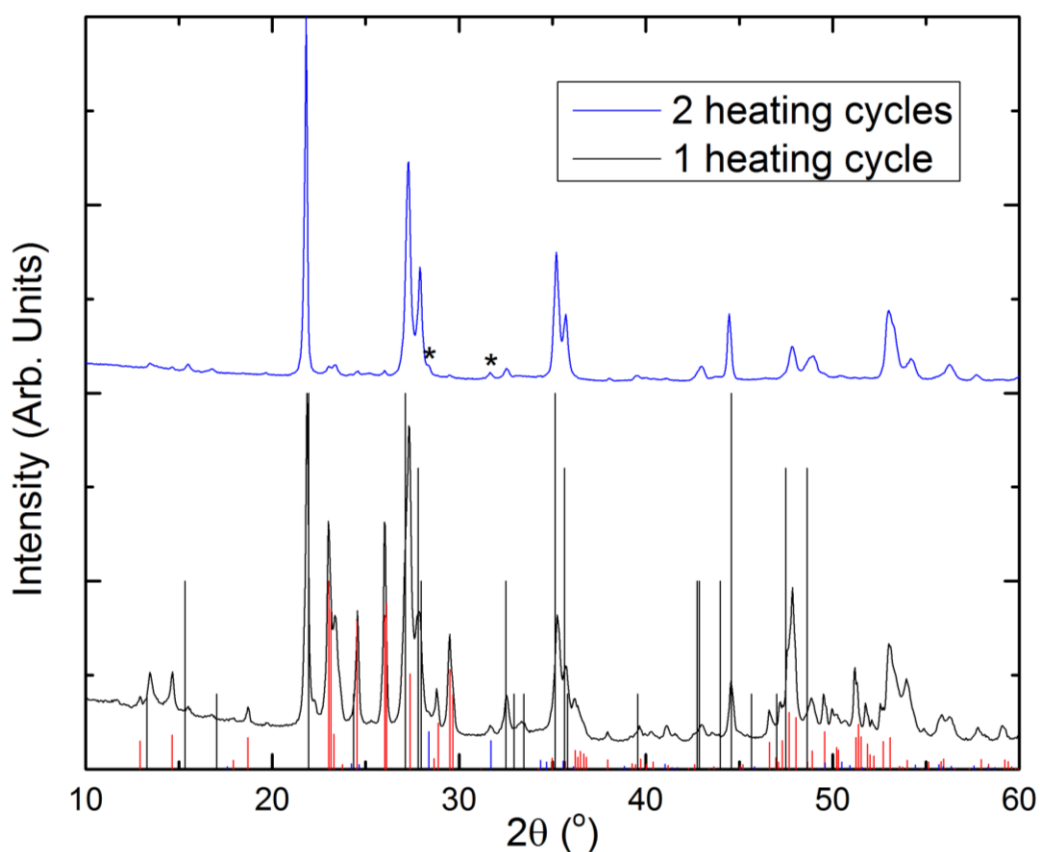


Figure 5.4. PXRD pattern of the reaction of HfO_2 with NH_4HF_2 in a 2:1 weight ratio after one and two heating steps at 420 °C. Vertical lines indicate theoretical peak positions for $\beta\text{-HfF}_4$ (red), $\text{Zr}_7\text{O}_9\text{F}_{10}$ (black), and HfO_2 (blue). Asterisks indicate the HfO_2 peaks in the top pattern for clarity.

Rietveld refinement was performed on the synchrotron diffraction pattern of the purest sample to examine the validity of the $\text{Zr}_7\text{O}_9\text{F}_{10}$ structure. A preliminary model for refinement was created using the published structure data for $\text{Zr}_7\text{O}_9\text{F}_{10}$ and replacing all Zr with Hf. Elemental

analysis carried out by Galbraith Laboratories determined that the bulk composition was 76.6% Hf and 12.16% F with 10% relative uncertainty, which is within error of the theoretical composition if the remainder is taken as O content. The results of this refinement, depicted in **Figure 5.5**, are unsatisfactory. Although the correspondence in peak number and arrangement with the pattern of the hypothetical $\text{Hf}_7\text{O}_9\text{F}_{10}$ is visually clear (as in the laboratory data), the insets show discrepancies in peak intensities and or some positions after many rounds of refinement. Furthermore, the quality of the sample results in broad peaks which are apparently difficult to model through particle size or strain effects, and result in negative anion isotropic thermal parameters. However, the presence of subtle structural complexities in the anion-deficient $\alpha\text{-UO}_3$ materials is a rule more than an exception.^{46,47} In fact, Withers et al. found that the $\text{Zr}_7\text{O}_9\text{F}_{10}$, originally reported as an anion-deficient $\alpha\text{-UO}_3$ with superstructure ordering like $\alpha\text{-U}_3\text{O}_8$ as depicted in **Figure 1.8c**, was better described as one member of the incommensurately modulated solid solution $\text{ZrO}_{2-x}\text{F}_{2x}$ ($0.698 \leq x \leq 0.714$) with a variable modulation vector.⁴⁶ In particular, they showed that changes in the modulation were primarily reflected in the PXRD pattern through shifting of the same minor, satellite reflections that are poorly fit in **Figure 5.5**. It should be noted that this entire, narrow composition range is within error of the elemental analysis results. As such, while the modulation approximated by the superstructure of $\text{Zr}_7\text{O}_9\text{F}_{10}$ appears incorrect, it remains possible that the new compound has an anion-deficient $\alpha\text{-UO}_3$ structure. ^{19}F NMR and TEM were employed to investigate this possibility.

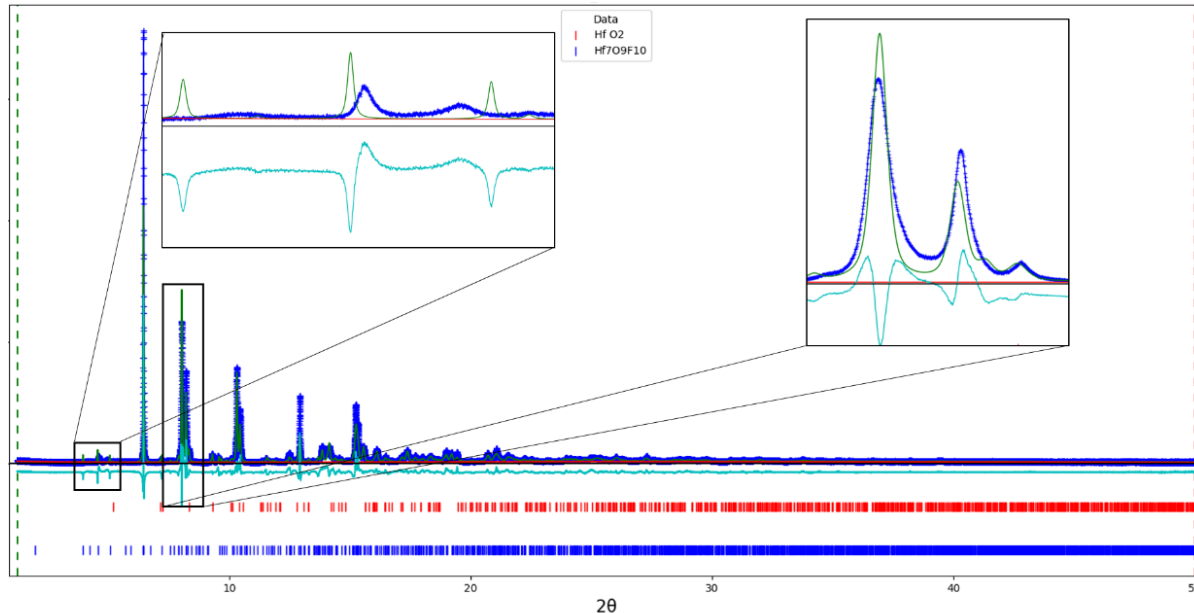


Figure 5.5. Rietveld refinement of synchrotron diffraction data of the new hafnium oxyfluoride phase, $wR = 26.409\%$. (Inset) Zoom-in views of areas of disagreement between refined model and experimental data.

As a local structure technique, ^{19}F solid-state NMR spectroscopy was used to determine whether the anion environments were consistent with the 2- and 3-coordinate environments expected of $\alpha\text{-UO}_3$ -related structures, which should be relatively independent long range effects such as modulation or superstructure. The ^{19}F isotropic chemical shift range of fluoride ions in diamagnetic transition metal compounds is strongly correlated with M–F bond distances. This relationship stems from the second-order “paramagnetic” contribution to chemical shielding, which is a function of distance between the nucleus and the valence p electrons.⁴⁷⁻⁴⁹ The relationships between local coordination and chemical shift have been established well enough to enable prediction in some chemical systems, particularly in alkali and main group fluorides.^{50,51} Such analysis requires model systems with known crystal structures and spectral assignments. From this basis, it is possible to estimate relative bond distances, *i.e.* ranges of bond distances, from measured chemical shifts in cases where the structure model is unknown or incomplete. As a first-

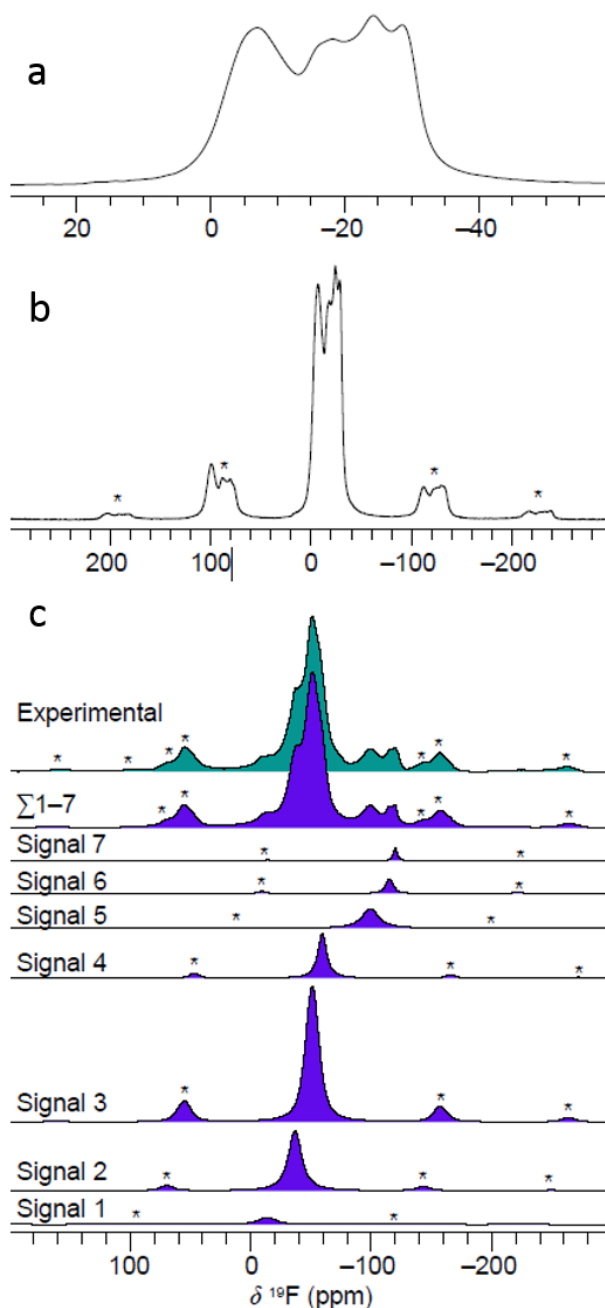


Figure 5.6. ^{19}F solid-state NMR spectroscopy of $\beta\text{-HfF}_4$ and the unknown Hf-O-F phase. (a) Isotropic resonances and (b) full spectrum of $\beta\text{-HfF}_4$. (c) Spectral fitting revealed that seven signals (bottom) were required to reproduce the experimental lineshape (top). The sum of the individual signals is shown just below the experimental spectrum. Details of the fitting parameters are given in **Table A.4**. Spectra were recorded at 40 kHz MAS; spinning sidebands are denoted with asterisks.

order approximation, we have observed a linear relationship among shift–bond length in covalent and ionic early transition metal fluorides such as TiF_4 , ZrF_4 , NbF_5 , TaF_5 , A_2ZrF_6 , A_3ZrF_7 ($\text{A} = \text{Li}^+$, Na^+ , K^+ , Rb^+ , Cs^+ , NH_4^+) and even $[\text{Mo}_3\text{O}_4\text{F}_9]^{5-}$ cluster compounds, where effects such as the nature of the alkali species or the presence of oxygen can be considered second-order offsets.^{51–56} Following this pattern for the aforementioned compounds, each transition metal has an apparent constant (in ppm/Å): $\text{Ti} \approx 1850 \text{ ppm}/\text{Å}$, $\text{Zr} \approx 270 \text{ ppm}/\text{Å}$, $\text{Nb} \approx 1250 \text{ ppm}/\text{Å}$, $\text{Ta} \approx 1050 \text{ ppm}/\text{Å}$. The sensitivity of shift to bond distance, combined with the high resolution of fast magic-angle spinning, mean that ^{19}F NMR can be a powerful probe of atomic structure in transition metal fluorides. While the precise values are preliminary and a systematic investigation is the subject of a separate study, the generality of this

phenomenon could be useful for the analysis of the new hafnium oxyfluoride phase found in this work. However, to our knowledge, no ^{19}F NMR studies of model hafnium (oxy)fluorides compounds have been published.

In the absence of reference data, $\beta\text{-HfF}_4$ was used as a model compound here to estimate a shift/bond distance correlation constant. $\beta\text{-HfF}_4$ has seven crystallographically distinct fluorine atoms, which have an average Hf–F bond length ranging from 2.051–2.115 Å and an observed chemical shift range of 24.5 ppm (**Figure 5.6a-b**). Under the assumption that the paramagnetic term and thus bond length dominates the shielding in $\beta\text{-HfF}_4$, this compound yields a ^{19}F constant of approximately 385 ppm/Å.

The new hafnium oxyfluoride contained multiple resonances with a total chemical shift range of about 106 ppm (**Figure 5.6c**). Deconvolution of the ^{19}F spectrum of Hf-O-F required seven signals (**Figure 5.6c**), which represents a lower limit on the number of distinct environments in the sample. Isotropic resonances were identified by comparison of the spectra at 36 and 40 kHz (see **Figure A.7**). The majority of the fluorine atoms are distributed in a narrow shift region at relatively high frequencies, indicative of short Hf-F bonds typical of bridging sites. The low frequency signals are assigned to intralayer fluorine atoms that typically have longer Hf–F bonds. The resonances in Hf-O-F are more broad than would be expected in an ordered oxyfluoride, which could be explained by anion disorder and/or a distribution of bond lengths that arises from an incommensurate structural modulation (*vide supra*).⁵⁶ If all the ^{19}F signals stem from a single phase, it would translate to an expected bond length range of about 0.28 Å. However, signals 6 and 7 have anomalously narrow peak widths and only comprise 4% of the ^{19}F signals, so these resonances likely belong to a secondary phase, which would lower the expected bond length range

to 0.22 Å. Overall, the ^{19}F solid-state NMR of Hf-O-F is consistent with the anion-deficient $\alpha\text{-UO}_3$ structure.

Complementary to NMR, TEM and STEM were performed in order to directly probe the symmetry and ordering, including possible modulation, of the new phase. **Figure 5.7** displays SAED of the Hf-O-F sample at the [017] (a), [027] (b), [215] (c) and [012] (d) zone axes. Surprisingly, the reflections match well with simulated patterns based on (**Figure A.8**) the hypothetical $\text{Hf}_7\text{O}_9\text{F}_{10}$ structure with the best fit lattice parameters produced by the refinement, despite its poor result. **Figures 5.7e** and **f** are simultaneously acquired HAADF- HRSTEM and ABF-HRSTEM images along the [010] zone axis from a region of interest where the sample crystallized perfectly. The SAED pattern of [010] zone axis inserted in **Figure 5.7e** also matches very well with the simulated diffraction pattern (**Figure A.8a**). Furthermore, the measured interplanar d-spacings of (200), (001) planes in HRTEM are 3.21, and 3.90 Å, respectively, which are in good agreement with the refinement results. HRSTEM imaging allows for direct observation of atomic columns in real space. However, since contrast in HAADF depends on the atomic number, only Hf atomic columns are observed clearly in **Figure 5.7e**. The image matches well with the inserted structure schematic with O and F hidden and only Hf atoms shown. To observe the lighter O and F atoms, ABF images were simultaneously acquired, as shown in **Figure 5.7f**. The weak dark spots in the center of the bright rows represent the atomic columns of oxygen and fluorine. However, clearly observing O and F remains challenging. Overall, the data strongly suggest that the phase has an anion-deficient $\alpha\text{-UO}_3$ structure with similar superstructure to $\text{Zr}_7\text{O}_9\text{F}_{10}$ or $\alpha\text{-U}_3\text{O}_8$. It should be noted, however, that apparent preferred orientation towards the b-axis hinders observation of extra intensity along the [010] zone axis, the expected direction of

modulation in these phases.^{46,57} As such, the discrepancies in the refinement may still arise from subtle structural differences unobserved here.

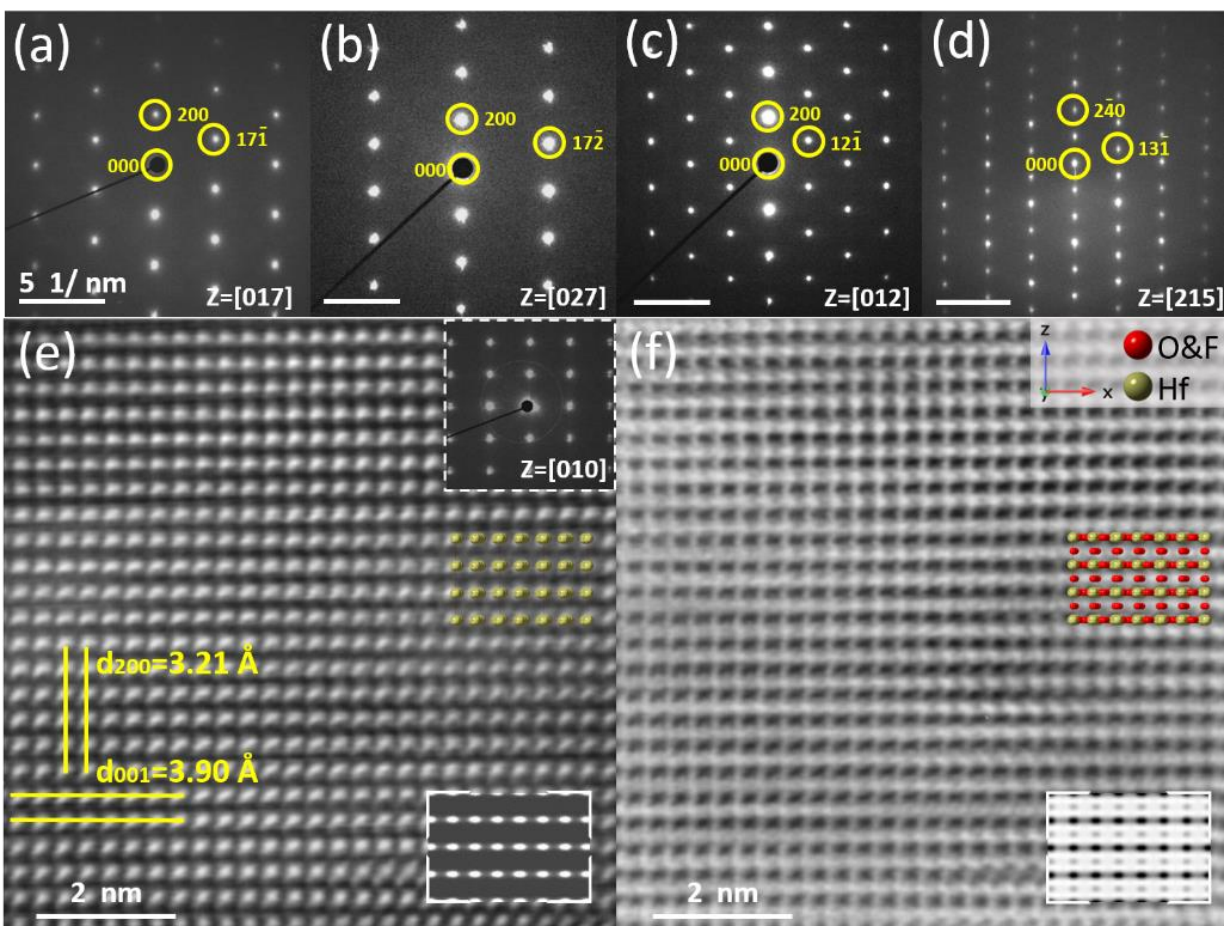


Figure 5.7. TEM of Hf-O-F compared with simulations based on hypothetical $\text{Hf}_7\text{O}_9\text{F}_{10}$ model with refined lattice parameters. SAED down the $[017]$ (a), $[027]$ (b), $[012]$ (c) and $[215]$ (d) zone axes. Simultaneously acquired HAADF-HRSTEM (e) and ABF-HRSTEM (f) images with SAED at the $[010]$ zone (upper), structure schematic (middle) and simulated image (lower) overlaid. The structure schematic inserted in (e) only shows the positions of Hf. Some lattice planes and their corresponding distances are marked.

Crystal quality and homogeneity may also play roles in the poor refinement results. Extra spots and characteristic diffuse intensity are present in some of the observed diffraction patterns of the new phase. **Figure 5.8a** and **b** both show SAED patterns at $[010]$ zone axis from the same particle but different regions. **Figure 5.8b** shows extra spots at the $\mathbf{G} \pm 0.5 \mathbf{c}^*$ reciprocal space positions. The extra spots correspond to imperfections in the crystallographic planes that stack

perpendicular to c-direction. **Figure 5.8e** displays HAADF- HRSTEM from a region of interest where many planar defects can be observed as marked with dashed boxes. Taking the area with the yellow dashed box as an example, **Figure 5.8f** shows a high-magnification HAADF image of this region. Additional sets of atomic planes perpendicular to c-direction are clearly observed (indicated by arrows). FFT of this image demonstrates that these features lead to extra spots as indicated by arrows. The width of the extra planes is around 3-5 nm. These stacking faults probably attributed to an agglomeration of interstitial point defects generated by the Hf atoms.

Another thing should be noted here is that the extra spots in the SAED pattern in **Figure 5.8b** diffuse along c^* -direction. The diffuse rods along the c^* direction are also present in the diffraction patterns along [210] zone axis in **Figure 5.8d**. **Figure 5.8c** and **d** were taken along [210] zone axis from the same particle but different regions. Compared to **Figure 5.8c** which can match well with the simulated pattern (**Figure A.8d**), the CBED pattern in **Figure 5.8d** shows diffuse intensity along the c^* direction, as indicated by arrows. The oriented intensity variation indicates compositional and displacive variation along the c-direction. This type of diffuse intensity was also observed in $Zr_7O_9F_{10}$ compound.⁴⁶ It is possible that this is due to anion ordering. In the current refined structure, O and F share all the anion sites. However, it is possible that O and F prefer different sites. Ordering of anions would likely have displacive effects on the Hf atoms.

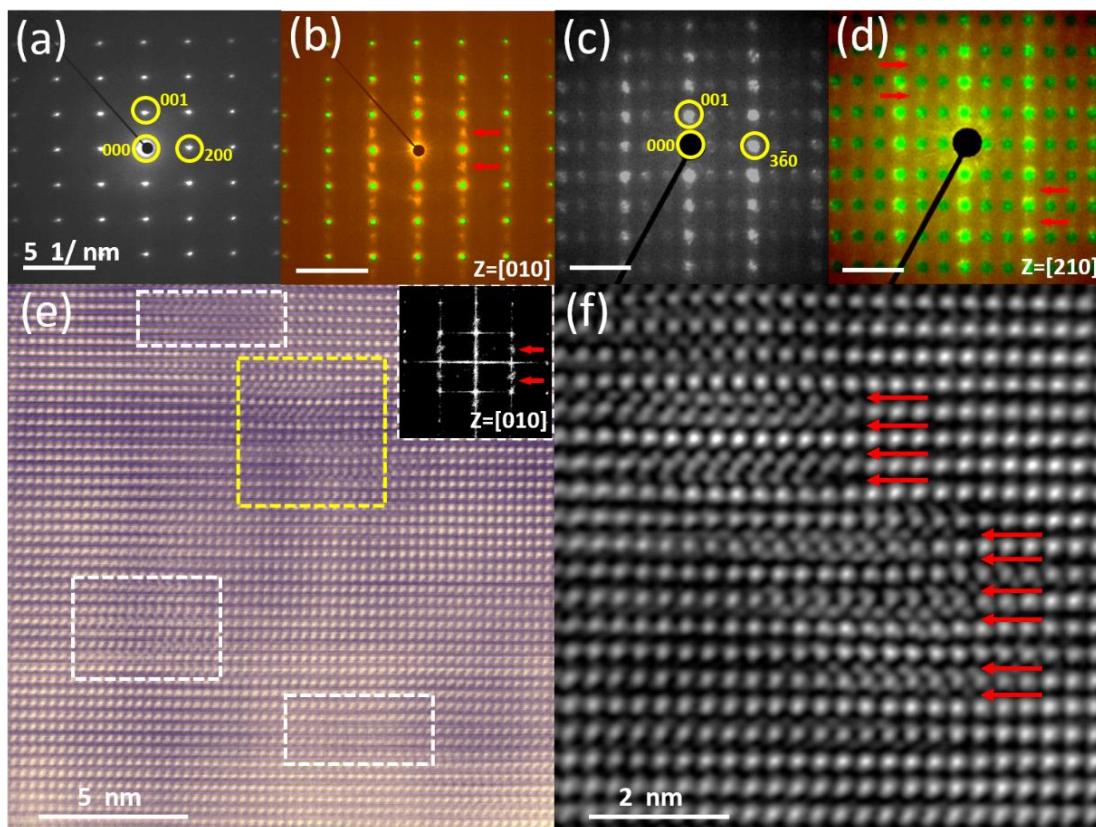


Figure 5.8. Defective regions in Hf-O-F particles. SAED patterns along [010] from the same particle without (a) and with (b) extra diffused spots. Convergent beam electron diffraction patterns along [210] without (c) and with (d) diffuse intensity. The patterns in (b) and (d) were colored to enhance the contrast. (e) HAADF-HRSTEM from a region of interest where some planar defects can be observed as marked with dashed boxes. (f) High-magnification image of the yellow-outlined region in (e) showing additional sets of atomic planes.

The observations from S/TEM identify two factors that may have contributed to the poor quality of the first Rietveld refinement. First, the crystallites were generally observed to be thin plates perpendicular to the b-axis. Second, the significant defects observed along the c-axis are expected to cause significant strain in that lattice direction. As such, the Rietveld refinement was reattempted using uniaxial models for both domain size and multistrain with a [010] and [001] unique axis, respectively. As shown in **Figure 5.9**, this substantially improves the model: wR decreases from 26.409% to 18.258% and the difference pattern shows less extra intensity on the main peaks. Full details for this refinement are reported in **Table A.5**. However, as shown in the insets, discrepancies still exist in the positions of the minor peaks.

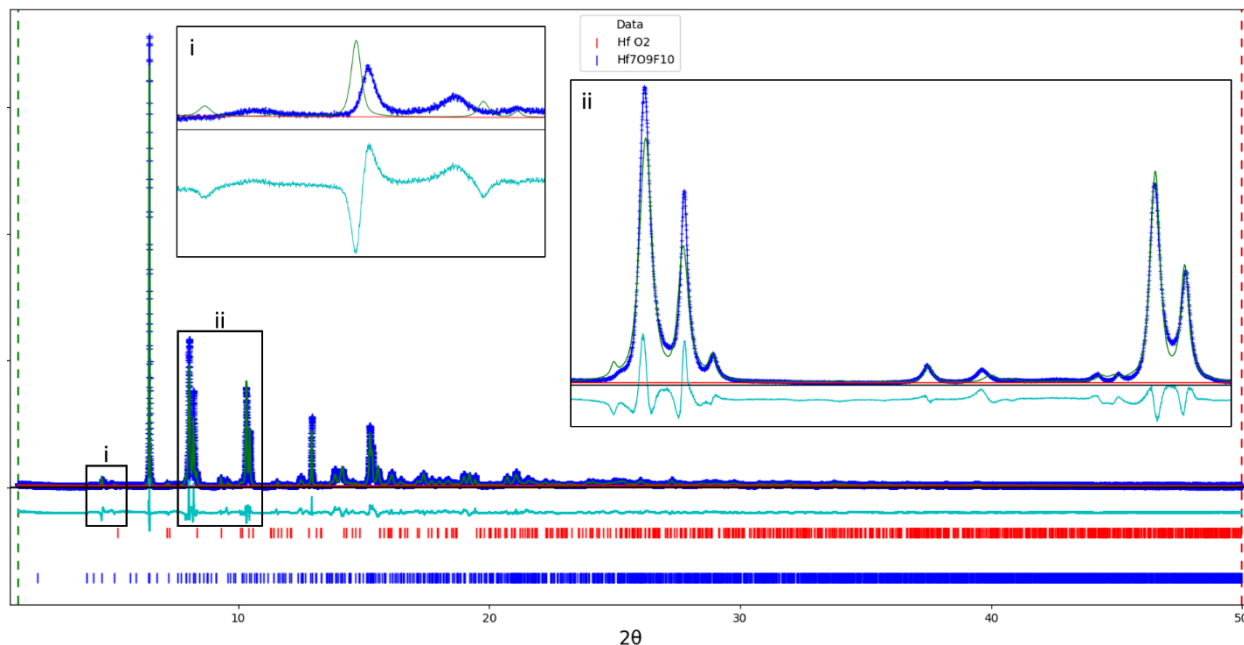


Figure 5.9. Improved Rietveld refinement using of synchrotron diffraction data of the new hafnium oxyfluoride phase using TEM results, $wR = 18.258\%$. (Insets) Zoom-in views of areas of disagreement between refined model and experimental data. (Blue) Observed powder pattern. (Green) Calculated powder pattern. (Light blue) Difference.

The thermal stability of the new hafnium oxyfluoride phase was characterized in inert atmosphere with thermogravimetric analysis (TGA), presented in **Figure 5.10** below. The signal is flat up until about $675\text{ }^{\circ}\text{C}$, at which point mass loss begins. The decrease in mass accelerates as the temperature is increased to $800\text{ }^{\circ}\text{C}$ and ends while dwelling at constant temperature, indicating the reactions has gone to completion with a total mass loss of $\sim 37\%$. PXRD of the remaining powder reveals phase pure HfO_2 (see **Figure A.9**). Given that both the atmosphere (He) and crucible (Au) were inert in this experiment, the product identity suggests that the decomposition reaction occurring is $\text{HfO}_{2-x}\text{F}_{2x(s)} \rightarrow (1-x/2)\text{HfO}_{2(s)} + x/2\text{HfF}_{4(g)}$ consistent with previous reports of high HfF_4 vapor pressures at $800\text{ }^{\circ}\text{C}$.^{58,59} The mass loss is also roughly consistent with 40%, the theoretical value when $x = 5/7$, corresponding to the overall stoichiometry $\text{Hf}_7\text{O}_9\text{F}_{10}$ identified by Holmberg in the Zr-O-F system.⁵ However, this composition is the F-rich endpoint of the solid solution identified by Withers et al. and the slight discrepancy may actually indicate a lower F-

content stoichiometry.⁴⁶ An expected value of 37% mass lost as HfF_4 is obtained when $x = 0.656$. Furthermore, given that a minor amount of $\beta\text{-HfF}_4$ (~5 %) was present in the sample, the true x -value should be even lower. Since this also means a lower anion to cation ratio, the structure is even more anion-deficient relative to $\alpha\text{-UO}_3$ which may explain why the superstructure attributed to the $x = 5/7$ Zr phase cannot match the minor details of the pattern well. It should be noted that although these x -values are outside the reported range for Zr, they are within error of the composition detected by elemental analysis and therefore may represent a distinguishing factor between Hf and Zr anion-deficient $\alpha\text{-UO}_3$ phases.

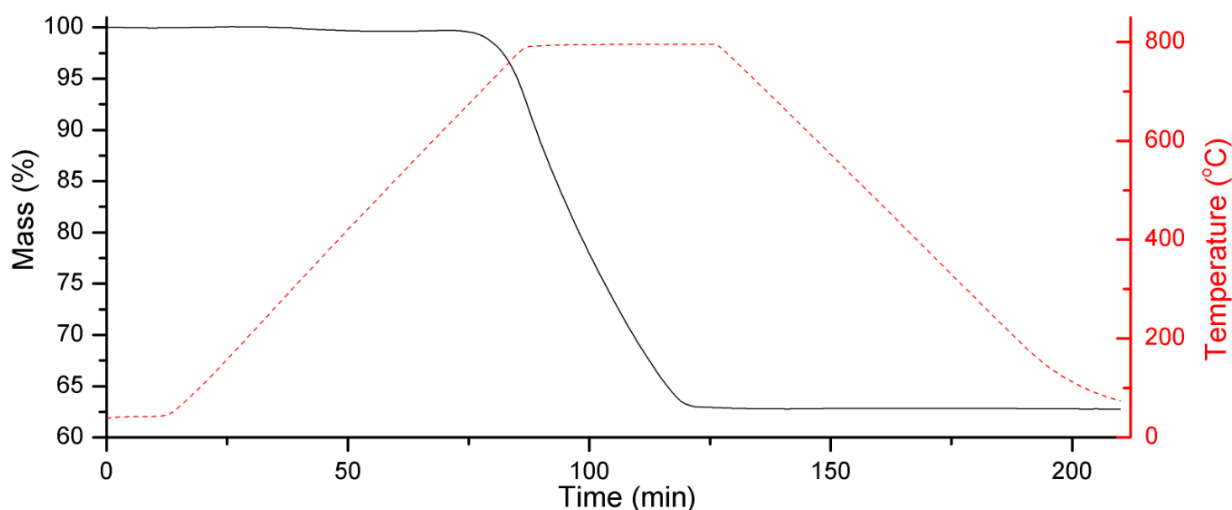
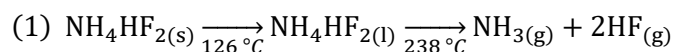


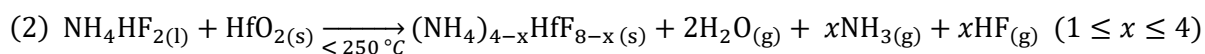
Figure 5.10. TGA in flowing He of the phase pure hafnium oxyfluoride obtained via reaction of HfO_2 and NH_4HF_2 .

5.3.3: Possible NH_4HF_2 Reaction Pathway

The thermal behavior of NH_4HF_2 is better established than that of PVDF and PTFE, allowing for more detailed insight into how its reaction with HfO_2 readily produces a new oxyfluoride. On its own, NH_4HF_2 undergoes the following reactions over the temperature range investigated in this study^{19,22}:



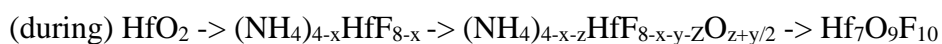
At first glance, this may lead one to expect that the reaction primarily proceeds through HfO₂ fluorination by HF. However the product differs markedly from the Hf₂OF₆ observed by Vilakazi et al. when they deliberately exposed HfO₂ to HF.¹² Ex-situ investigation of the reaction products at 250 °C explains this discrepancy. At that temperature, the PXRD pattern (**Figure A.10**) shows a nearly phase pure mixture of (NH₄)₂HfF₆ and (NH₄)₃HfF₇. As such, before NH₄HF₂ can decompose at 238 °C, it must react to form more stable ammonium hafnium fluorides according to the following reaction:



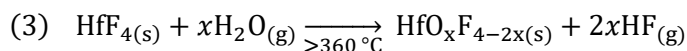
where the value of x is determined by the ratio of reactants and the reaction conditions (temperature, atmosphere). The evolution of gas in an open system is likely a significant driving force for this reaction despite the refractory nature of HfO₂. This is consistent with both previous observations of ammonium hafnium fluoride complexes formed when HfO₂ reacts with NH₄F, as well as the first step in the well-studied synthesis of anhydrous rare earth bromides beginning from the oxide and an ammonium bromide.^{9,19,23,60,61} That our results contain both the $x = 1, 2$ compositions is consistent with previous literature indicating that (NH₄)_{4-x}HfF_{8-x} decomposes with increasing temperature by sequential loss of NH₄F (as NH₃ and HF). Reports that the $x = 1$ to 2 transition starts at 245 °C explain why dwelling our samples at 250 °C for 12 hours before interruption produces only (NH₄)₂HfF₆ (see **Figure A.10**). The $x = 2$ to 3 and 3 to 4 transitions, reported to begin at 305 and 357 °C, also fit into the temperature range of our experiments.^{19,62}

Critically, the rapid formation of these ammonium hafnium fluoride intermediates means that there is no oxide left at the full reaction temperature (420 °C) to contribute to the formation of an oxyfluoride phase. As such, O must be reintroduced to the material to form the oxyfluoride.

Since the reaction was performed in an open system, hydrolysis is the most likely explanation, as even trace water present has been reported to convert metal fluorides and ammonium metal fluorides to oxyfluorides.⁶¹ Given our results this process must occur above 250 °C, either while heating at 5°C/minute or when dwelling at 420 °C. Depending on when the hydrolysis is most thermodynamically and kinetically favorable - during or after the stepwise loss of NH₃ and HF - two possible sequences of intermediates are hypothesized for the overall reaction over the course of multiple heating cycles of heating, dwelling at 420 °C for 12 hours, and cooling:



The first suggested sequence, in which hydrolysis only occurs **after** the stepwise loss is complete and only HfF₄ ($x = 4$ in equation 2) remains, is supported by thermal degradation studies for a large number of ammonium metal fluorides in inert atmosphere in which the final product is the pure fluoride.^{19,23} The presence of β -HfF₄ in our product mixture (**Figures 5.3 and 5.4**) after the first complete heating cycle (12 hours, 420 °C) suggests that at least some of the ammonium hafnium fluoride intermediate undergoes this process in air as well. The fluoride can then be converted to an oxyfluoride upon further heating in air:



The experimental results strongly suggest that this is the major process occurring during the second (identical) heating cycle, after which PXRD patterns show a transformation from a mixture of Hf₇O₉F₁₀ and β -HfF₄ to nearly phase pure oxyfluoride.

If this is true, then the same reaction should be possible simply through hydrolysis of β -HfF₄, without needing to react HfO₂ with NH₄HF₂. To investigate this commercial β -HfF₄ was

ground to a fine powder and then subjected to sequential cycles of the same reaction conditions as the $\text{HfO}_2 + \text{NH}_4\text{HF}_2$ mixture. Interestingly, no evidence of decomposition was observed by PXRD (see **Figure A.11**). However, raising the dwell temperature to 450 °C resulted in the appearance of very minor HfO_2 and $\text{Hf}_7\text{O}_9\text{F}_{10}$ peaks. Further increasing the temperature to 500 °C led to complete decomposition into a mixture of these two phases after 12 hours. Thermodynamic calculations for the complete hydrolysis of HfF_4 plotted in **Figure 5.11** suggest this reaction should only become favorable above 500 °C, consistent with experimental results. The presence of oxyfluoride in the decomposition product is notable since thermodynamics indicates that complete hydrolysis is favorable. This suggests that at these temperatures, the oxyfluoride presents a kinetic barrier to hydrolysis, possibly because of a reduced fraction of reactive anions in the structure, relative to the fluoride. Further heating at 500 °C decreases the relative fraction of the oxyfluoride phase, confirming that the mixture was not at equilibrium after the initial dwell at 500 °C. Thus, the selectivity of the $\text{NH}_4\text{HF}_2 + \text{HfO}_2$ reaction is not reproducible by simple hydrolysis of $\beta\text{-HfF}_4$. As such, the role of NH_4HF_2 as a fluorinating agent appears to be more complex than simply converting the oxide to the fluoride. It appears to activate the fluoride to hydrolysis, possibly through the production of nano- or poorly crystalline particles, such that it can occur at lower temperatures where the kinetic barrier to oxide formation provided by the oxyfluoride should be even more substantial.

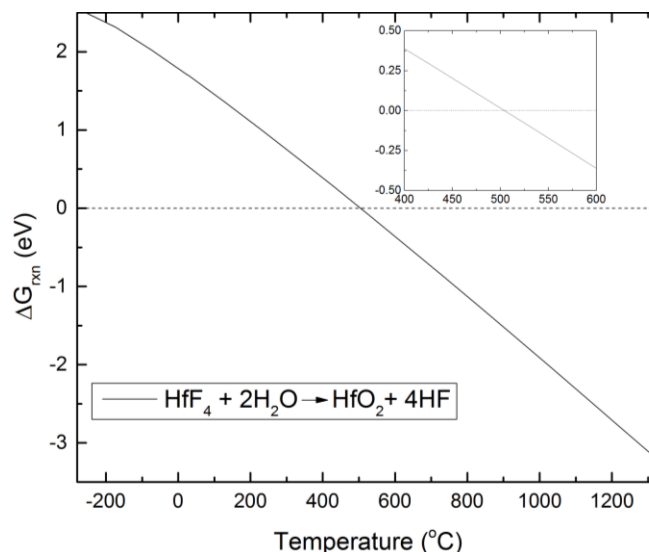
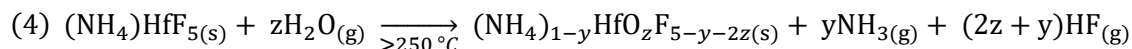


Figure 5.11. Calculated Gibbs reaction energy (ΔG) for the hydrolysis of β - HfF_4 as a function of temperature. (inset) Close-up on the temperatures at which ΔG becomes negative.

In the second, alternative sequence, hydrolysis of the ammonium hafnium fluoride material occurs **simultaneously** with loss of NH_3 and HF (at $x = 1, 2,$ or 3 in equation 2), necessarily resulting in one or more ammonium hafnium oxyfluoride intermediates. This is the reported progression of phases that occurred when $(\text{NH}_4)_2\text{ZrF}_6$ was heated in air at a relative humidity of 20-30%, as determined by Voit and colleagues via XRD and vibrational spectroscopy.²⁰ Assuming, as in the Zr case, that $(\text{NH}_4)_{4-x}\text{HfF}_{8-x}$ has decomposed to the $x = 3$ composition before hydrolysis occurs, the equation for this step is given by:



The results of the low temperature reaction depicted in **Figure A.10** show that $(\text{NH}_4)\text{HfF}_6$ is air stable (at least until 250 °C) and the loss of NH_4F from an ammonium hafnium fluoride phase is relatively rapid, making this assumption reasonable. Three successive intermediates were observed with increasing temperature for the analogous Zr reaction, $(\text{NH}_4)_2\text{Zr}_3\text{OF}_{12}$ ($y, z = 1/3$) at 310 °C, $(\text{NH}_4)\text{Zr}_3\text{O}_2\text{F}_9$ ($y, z = 2/3$) at 370 °C, and $\text{Zr}_7\text{O}_9\text{F}_{10}$ ($y = 1, z = 9/7$) at 500 °C. Since the reactions reported here were performed under air with the hydrolysis step occurring over a temperature range

(250 – 420 °C) consistent with the study by Voit et al., it is reasonable that an analogous Hf-mechanism may have occurred, especially since it is known to favor the formation of anion deficient α - UO_3 -related materials like the new phase.²⁰ Nevertheless, equation 4 does not predict the formation of any pure fluoride in the reaction, contradicting what was observed in the PXRD patterns in **Figures 5.3** and **5.4**. Furthermore, the conversion of $(\text{NH}_4)_{4-x}\text{HfF}_{8-x}$ to HfF_4 only requires loss of NH_3 and HF , whereas this process requires that along with hydrolysis. As such, it is improbable that the latter would happen independently of the former.

Instead, it is possible that the reaction occurs through both mechanisms simultaneously. Since the precursor is an intimate mixture of HfO_2 and NH_4HF_2 (melting point ~ 126 °C), the formation of $(\text{NH}_4)_{4-x}\text{HfF}_{8-x}$ at low temperatures also leads to a densification of the powder as the liquid is consumed.¹⁹ Reaction 4 may occur in portions of the sintered powder in good contact with the atmosphere, while reaction 3 dominates in the interior where hydrolysis could not occur as quickly as loss of NH_4F . Grinding the sample after the first heating step recreates a loose powder where most grains are in contact with the atmosphere, allowing equation 3 to convert the remaining β - HfF_4 to $\text{Hf}_7\text{O}_9\text{F}_{10}$. Another possibility is that only the first reaction mechanism occurs, with a faster rate of hydrolysis (reaction 4) on surface and exposed particles. However, it is unclear if this significant divergence in the behaviors of the Zr and Hf systems is reasonable, and mechanism one does not offer an explanation of why $\text{Hf}_7\text{O}_9\text{F}_{10}$ selectively forms rather than one of the other known Hf-O-F phases, which have been reported as products of the thermal decomposition of $\text{HfF}_4 \cdot x\text{H}_2\text{O}$ ($x = 1,3$).¹¹ In either case, an inhomogenous distribution of particle size or crystallinity could also explain why some oxyfluoride appears to form very fast, while a smaller fraction takes two to three times as long to react. Finally, reactions 3 and 4 may simply be favored at different temperatures,

with the latter being favored before decomposition of NH_4HfF_5 to HfF_4 begins, reported around $360\text{ }^\circ\text{C}$.¹⁹ In this case, the $5\text{ }^\circ\text{C}/\text{min}$ heating rate was likely too fast for meaningful reaction to be observed, given that only about 20 minutes would be spent in the temperature range in which equation 4 is favored.

Overall, the success of the reaction appears to be determined by how readily the precursor oxide reacts with NH_4HF_2 , which might be exploitable in high-throughput theoretical studies by searching for high-stability ammonium metal fluorides. Since this mechanism involves consumption of the precursor oxide to make the intermediate, NH_4HF_2 may not be ideal for carrying out topotactic fluorinations, as is often desired.^{11,21,26} Consistent with this, Slater found that conversion of Ca_2CuO_3 and Sr_2TiO_4 to $\text{Ca}_2\text{CuO}_2\text{F}_2$ and $\text{Sr}_2\text{TiO}_3\text{F}_2$ occurred readily with PVDF, but resulted in poorly crystalline products and significant fluoride side products with NH_4F .¹¹ It is worth noting that in cases where no ammonium metal fluoride intermediate is stable, NH_4HF_2 will decompose into NH_3 and 2HF at sufficiently high temperature, which may act as a more direct fluorinating agent without structural rearrangement. If further investigation of the mechanism of NH_4HF_2 fluorination confirms the role of ammonium metal oxyfluoride intermediates in controlling what oxyfluoride products may be obtained, these may also make a good new selection criterion for determining future synthetic targets with theory-based predictions.

5.4: Conclusions and Future Directions

The reactivity of HfO_2 with three fluorinating agents (PVDF, PTFE, and NH_4HF_2) was investigated. It appears to be limited with the fluoropolymer reagents, as there was no detectable reaction while open to the atmosphere as well as a significant fraction of unreacted HfO_2 in the

product mixture when encased in an evacuated, sealed tube. In the latter case, however, both fluoropolymers produced a complex mix of products which appears to include multiple hafnium oxyfluoride phases and/or metastable α -HfF₄. Comparison of these products with PXRD suggests that PTFE is a more effective reagent than PVDF for HfO₂ fluorination in silica as they exhibit a higher degree of fluorination and are not suggestive of significant side reactions with the container. Efforts to optimize both reactions by adjusting reaction time, temperature, and reagent ratios failed, but may be possible in alternative sealed setups such as a metal tube or in inert atmosphere rather than vacuum. In-situ PXRD may also help develop targeted heating profiles to isolate the new heteroanionic materials selectively produced via these reactions. In contrast to the fluoropolymers, reaction between HfO₂ and NH₄HF₂ in air was readily detected and a new hafnium oxyfluoride phase with an anion deficient α -UO₃ structure was discovered. Although the pattern could not be refined satisfactorily to the Zr₇O₉F₁₀ structure-type, a strong correspondence of peak position and number suggests the difference arises from subtle-features such as defects or modulation, well-known within the anion-deficient α -UO₃ structural family. ¹⁹F NMR confirms that the local environments of cations within the structure match those expected in the Zr₇O₉F₁₀, further supporting the structural relationship and indicating that the unknown material exhibits disorder between O and F. Comparison with hydrolysis of β -HfF₄ suggests that the speed and selectivity of this reaction are strongly facilitated by the existence and stability of the ammonium hafnium fluoride phases ((NH₄)_{4-x}HfF_{8-x}, 1 ≤ x ≤ 3). If so, these factors can be generalized to predict a priori which solid state fluorinating agent might work best for a given experiment. Finally, analysis of the mechanism of NH₄HF₂ fluorination in this work suggests that identifying stable ammonium metal oxyfluoride phases might be very useful in targeting unreported oxyfluorides.

CHAPTER 6: CONCLUSIONS AND FUTURE WORK

In this thesis, exploratory synthesis was performed within three general compositional systems: M-In-Ge-O (M = Zn, Cu, Co, Mn, Fe, Ni or some combination thereof), M-M'-Sb-O (M = Li, Ga, Cr, Fe, K; M' = In, Sc (M = Li), Fe (M = Li)), and Hf-O-F. In total, at least seven new materials were discovered across four structure-types, one of which was newly discovered here. Notably, in all of these cases the materials exhibit some feature that is poorly addressed by current computational methods: either occupational disorder in a large unit cell, or an unprecedented structure. Furthermore, these products all belong to one of three well-studied structural families: fluorite, rutile, and α -UO₃. However, beyond simply being new additions to old sets of materials that have been studied for decades, each of these discoveries reveals some new insights about their chemical or structural behavior. As such, the results of this thesis clearly demonstrate the unique value of exploratory approaches to materials design.

In **Chapter 3**, several new ADF phases were found to exhibit surprising occupancy disorder. In the ZIGO structure, a remarkable combination of order and disorder was identified in association with the newly observed CuZIGO solid solution, in which Cu preferentially occupies the 16f site along with three other cations. Additionally, high solubility limits for Co, Mn, Fe, and Ni were demonstrated in this structure with 100% substitution achieved in the former two cases. Furthermore, mixing any and all of these first row-transition metals into the structure below their solubility limits still appears to produce a very nearly phase pure material. This suggests that the ZIGO structure is a candidate for producing a high entropy oxide phase of unprecedented complexity. In the defect fluorite structure, three new cation-diverse compositions, M_{0.4}In₃SbO_{7.6} (M = Cr, Fe, Ga), were isolated. Since there is only one cation site in the resulting defect-fluorite structure, it is nominally triply occupied by ions with a wide range in size, another demonstration

of high entropy potential. The compositions of these phases suggest the addition of a minor amount of an M^{3+} cation to anion-ordered ADF In-Sb-O phases drives the anions to disorder, possibly owing to the decreased average cation size, increasing the symmetry. EDX indicates that despite synthetic sensitivity to the nominal composition, the actual product may be enriched in the $3+$ ion and deficient in Sb, at least in the $M = \text{Cr}$ case. However, for both structure types electron diffraction observes extra reflections (in post-quinary compositions for ZIGO), indicating that cation ordering which decreases the configurational entropy of the system may occur when enough different species are present.

In **Chapter 4** a profound addition to the rutile-related structural family was observed through the first single crystal structure solution of $\text{LiIn}_2\text{SbO}_6$. This new example has chains and tunnels that are not a constant size down their length, but rather oscillate between being one and two cation octahedra wide. This is the first example of an alternating-chain structure in the rutile-related materials, and demonstrates that others might be possible. If so, the frequency and magnitude of oscillations in the chain-width may become useful design parameters for rutile-related phases. Substitution of Sc and Fe in place of In resulted in compositional analogues that exhibit the same alternating-width structures at high temperatures. However, below transition temperatures of ~ 360 and 425 K in the Fe and Sc analogues respectively, the Li occupancy behavior appears to deviate from that observed in LIAO. For LSAO, it remains at the center of the channels but orders between adjacent tetrahedral sites, breaking the inversion symmetry of the structure. While both polarizations are present at least on a large enough scale to be recognized as twinned polar domains instead of static disorder. For LFAO, the low temperature structure remains inconclusive although possible evidence of octahedral Li coordination in the side channel sites has

been obtained. Finally, replacement of Li with K in reaction mixtures produces another new rutile-related material, likely $\text{K}_2\text{In}_5\text{Sb}_3\text{O}_{16}$, which crystallizes in the known hollandite structure. This suggests that large tunnel ions do not provide sufficient driving force to the framework cation-ordering which gives rise to the unique structure of $\text{LiIn}_2\text{SbO}_6$.

In **Chapter 5**, investigations into the fluorination of HfO_2 with common solid-state fluorinating agents revealed the first hafnium oxyfluoride member of the ADU family of materials. Rietveld refinement suggests that it is not a direct analogue of $\text{Zr}_7\text{O}_9\text{F}_{10}$, the only zirconium oxyfluoride ADU phase currently reported in the ICSD. However, ^{19}F NMR shows that the local F environments are consistent with F content on all the trigonal planar and linear anion sites of an ADU structure which is also consistent with disorder between O and F. Likewise, TEM data strongly demonstrate agreement between the observed reflections and those expected from an α - UO_3 type unit cell. In this thesis, it was discovered that the reaction between HfO_2 and NH_4HF_2 at 420 °C in air readily and selectively produces this ADU phase. However, TEM results also suggest that the mechanism of this reaction produces highly defective crystallite with inserted planes along the [001] direction. These defects might drive the selective decomposition pathway, as both thermodynamic calculations of the hydrolysis of β - HfF_4 , a likely intermediate step in this reaction pathway, only proceeds at or above 500 °C and is favored to produce HfO_2 . In contrast, reacting HfO_2 with PVDF and PTFE, two other commonly used fluorinating agents, did not produce the ADU product, but rather another apparently unreported hafnium oxyfluoride phase in a mixture of hafnium oxide, oxyfluoride, and fluoride products. Isolation of the second unknown hafnium oxyfluoride phase was unsuccessful. These results will be useful in the development of guidelines to predict a priori which solid state fluorinating agent might work best for a given experiment.

The discovery of new phases always raises more questions which deserve to be the subject of their own research projects. The fluorite related phases in **Chapter 3** are valuable candidates for high entropy oxides and should be investigated as such. Systematic synthetic investigations can be employed to identify more cations which may be mixed in the defect fluorite and ZIGO structures to increase configurational entropy. Local structure techniques such as EXAFS, XANES, and solid-state NMR should be used to probe substitution behavior of specific species to guide development of high entropy compositions and confirm their configurational entropy.¹⁻³ Finally, promising properties of interest in the identified defect fluorite phases (Cr/Fe/Ga-In-Sb-O) should be investigated. Oxygen ion conductivity can be measured in all three with AC impedance spectroscopy.⁴ Electronic conductivity and transparency in the potential TCO GIAO can be measured with a four-point probe and diffuse reflectance, respectively.^{5,6} The rutile-related phases in **Chapter 4** remain to be fully characterized. The relatively promising Li-conductivity of LFAO should be measured with AC impedance spectroscopy.⁴ LSAO can be similarly investigated to provide more datapoints for analysis of how the unique shared chain structure impacts ionic mobility in the channels. SHG should be performed on low temperature LSAO to further probe its true inversion symmetry. The ordering of In and Sb in hollandite-KIAO should be determined via either single crystals or combined neutron and X-ray powder diffraction. If possible, this information should be used to develop design principles for obtaining alternating width chains. **Chapter 5** identifies at least one new oxyfluoride phase that has not been isolated or characterized, and potential strategies for targeting others through reaction with NH_4HF_2 . The unknown phase observed in reactions between HfO_2 and the fluoropolymers should be investigated through a wider synthetic study using more specialized setups such as sealed metal tubes or reaction in inert gas

like Ar or N₂. Additionally, a systematic study of stable ammonium metal fluoride and oxyfluoride phases should be performed in order to identify oxides that may yield new oxyfluorides through reaction with NH₄HF₂ in air.

From a broader perspective, however, the results of this thesis taken together indicate possible strategies to optimize the field of materials discovery as a whole. It may seem contradictory to suggest guidelines for a process defined by its unrestricted pursuit of the unknown but, as mentioned earlier, exploratory synthesis works best in concert with theory-based materials design. Most likely, the latter is more appropriate for searching for new materials exhibiting with well-understood properties. As such, ensuring that exploratory efforts are probing different structural and compositional spaces than computational ones will maximize the efficiency of materials discovery initiatives. At high temperatures, the contribution of entropy to the free energy of a phase is increasingly large.^{7,8} As such, solid-state synthesis performed on a mixture of oxides with chemically similar cations, such as the first row transition metals, is fairly likely to produce highly disordered materials. An analogous approach may work for anion disordered phases as well. Finally, soft chemistry and low-temperature routes increase the chances of isolating metastable phases which might be looked over by high-throughput energy minimizing studies.⁹ In all cases, targeted compositions should be those with few or no known phases. With these strategies, exploratory synthesis can continue to probe the unknown materials landscape in a synergistic fashion with the ever-improving theory-based materials design.

APPENDIX 1. SUPPORTING INFORMATION

This appendix contains figures and tables which are part of the research detailed in the work above but are either tangential or partially redundant to the points being discussed in the text. They are included here for completeness and as a source of extra information for the more interested reader.

Chapter 4:

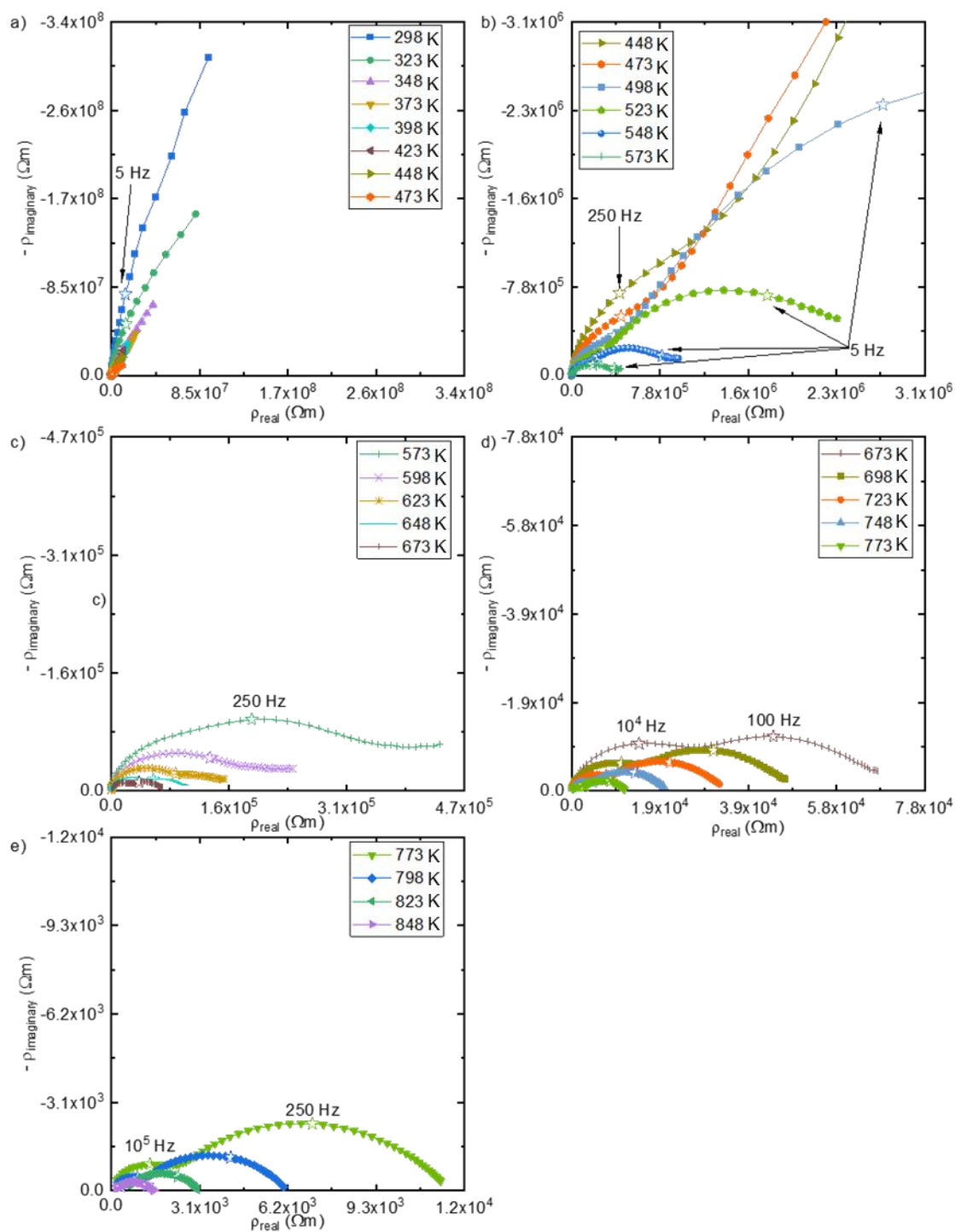


Figure A.1. Temperature-dependent impedance spectra of LIAO from: (a) 298 to 473 K, (b) 448 to 573 K, (c) 573 to 673 K, (d) 673 to 773 K, and (e) 773 to 848 K. Spectra are measured under synthetic air. Select frequencies are indicated by a star.

Table A.1. Crystallographic and collection parameters for LMAO (M = Sc, Fe).

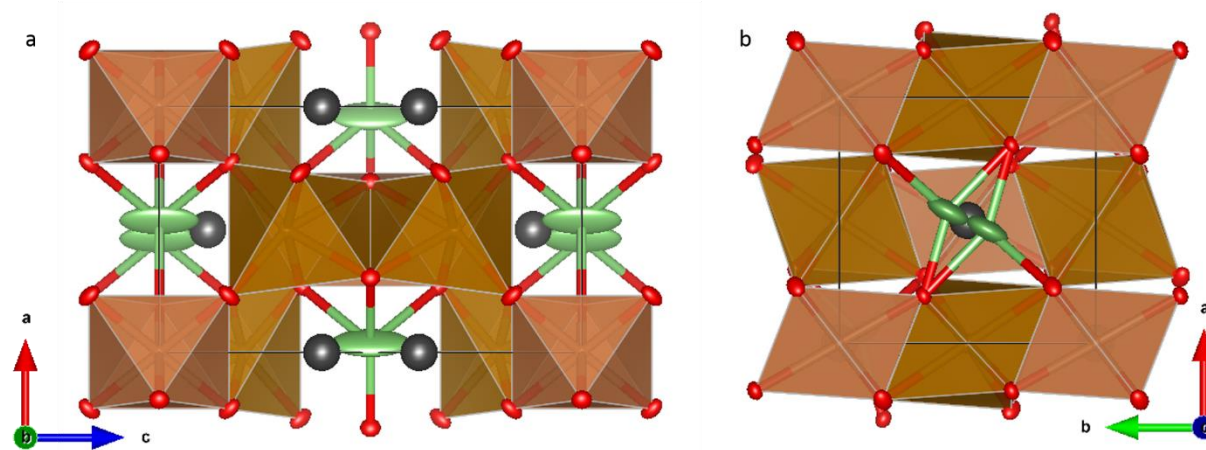
| Compound | LiSc ₂ SbO ₆ | | LiFe ₂ SbO ₆ |
|---|--|--------------------|------------------------------------|
| Temperature, K | 100.01 | 500.01 | 400.00 |
| λ , Å | 0.71073 | 0.71073 | 0.71073 |
| space group (No.) | <i>Pmn</i> 2 ₁ (31) | <i>Pnnm</i> (58) | <i>Pnnm</i> (58) |
| unit cell | | | |
| a, Å | 8.7108 (3) | 5.0440(2) | 4.9121(3) |
| b, Å | 5.06113 (19) | 5.2226(2) | 5.1359(3) |
| c, Å | 5.2466 (2) | 8.6533(4) | 8.46045(5) |
| V, Å ³ | 231.305(15) | 227.950(17) | 213.44(2) |
| Z | 2 | 2 | 2 |
| crystal color | Colorless | Colorless | Orange |
| crystal size, mm | 0.086 x 0.065 x 0.048 | 0.17 x 0.12 x 0.11 | 0.139 x 0.099 x 0.067 |
| ρ_{calc} , g cm ⁻³ | 4.517 | 4.584 | 5.234 |
| μ , mm ⁻¹ | 8.592 | 8.719 | 12.93 |
| Θ_{max} , deg | 37.595 | 29.155 | 29.107 |
| reflections collected | 2699 | 2220 | 2305 |
| R _{int} | 0.0202 | 0.0226 | 0.0164 |
| unique reflections | 1163 | 304 | 278 |
| parameters refined | 54 | 32 | 32 |
| R ₁ , wR ₂ [F _o > 4sig(F _o)] | 0.0193, 0.0497 | 0.0244, 0.0790 | 0.0138, 0.0414 |
| goodness-of-fit | 1.101 | 1.243 | 1.217 |
| diff. peak and hole, e Å ⁻³ | 0.86/-1.12 | 0.81,-1.27 | 0.71,-0.77 |
| Flack parameter | -0.04(5) | ----- | ----- |
| Twin Law [BASF] | (-1.0, 0.0, 0.0, 0.0, 1.0, 0.0, 0.0, 0.0, -1.0), [0.47(7)] | ----- | ----- |

Table A.2. Atomic coordinates and isotropic thermal parameters in LSAO at 100 and 500 K.

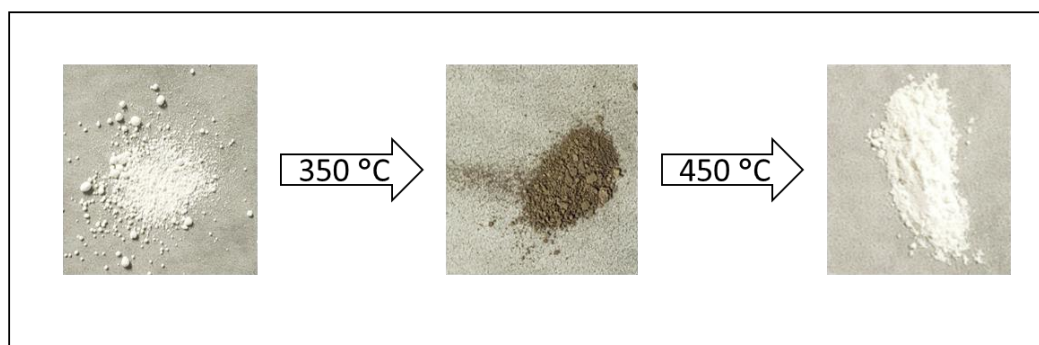
| Atom | Wyckoff Position | x | y | Z | U _{eq} |
|-------|------------------|-------------|-------------|-------------|-----------------|
| 100 K | | | | | |
| Sc | 4b | 0.19847(6) | 0.25557(9) | 0.5034(11) | 1.18(11) |
| Sb | 2a | 0.5 | 0.75676(5) | 0.5016(5) | 1.59(8) |
| Li | 2a | 0.5 | 0.2000(19) | 0.899(2) | 10.7(17) |
| O1 | 2a | 0.5 | 0.9471(6) | 0.1787(11) | 4.1(6) |
| O2 | 4b | 0.6558(2) | 0.9847(4) | 0.6778(9) | 4.0(4) |
| O3 | 4b | 0.3360(3) | 0.5388(4) | 0.3487(9) | 4.3(4) |
| O4 | 2a | 0.5 | 0.5580(6) | 0.8243(10) | 3.1(6) |
| 500 K | | | | | |
| Sc | 4f | 0 | 0.5 | 0.69947(12) | 2.5(3) |
| Sb | 2a | 0.5 | 0.5 | 0.5 | 4.6(3) |
| Li | 4g | 0.9575(18) | 0.095(3) | 0.5 | 28(3) |
| O1 | 8h | 0.27706(17) | 0.65529(11) | 0.66085(8) | 9.8(4) |
| O2 | 4g | 0.3061(3) | 0.17735(17) | 0.5 | 7.5(4) |

Table A.3. Atomic coordinates and isotropic thermal parameters in LFAO at 400 K.

| Atom | Wyckoff Position | x | y | z | U_{eq} |
|------|------------------|-------------|-------------|------------|----------|
| Fe | 4f | 0.5 | 0 | 0.6985(5) | 6.21(18) |
| Sb | 2a | 0.5 | 0.5 | 0.5 | 5.12(17) |
| Li | 4g | 0.962(2) | 0.077(2) | 0.5 | 63(5) |
| O1 | 8h | 0.73018(17) | 0.33032(18) | 0.66550(9) | 8.9(3) |
| O2 | 4g | 0.3069(3) | 0.1715(2) | 0.5 | 7.4(3) |

**Figure A.2.** Crystal structure of LFAO at 400 K with 4e off-center channel sites marked as black spheres, as viewed down the (a) b-axis and (b) c-axis. Overlap with Li thermal ellipsoid suggests there may be some transient Li content on the 4e site, which lies along the diffusion path between the adjacent Li sites.

Chapter 5:

**Figure A.3.** Color changes upon reaction of HfO_2 with PVDF. Fluoropolymer was added only to the initial reaction mixture.

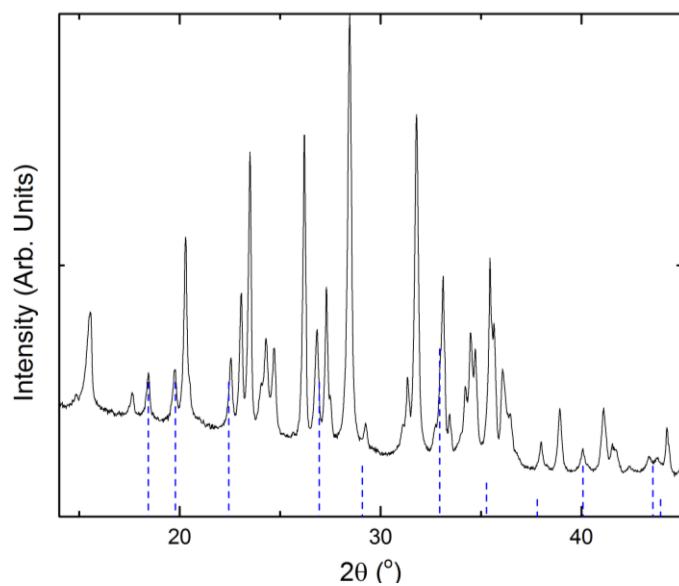


Figure A.4. PXRD patterns of reaction products of HfO_2 and PVDF in an evacuated sealed tube ($350\text{ }^\circ\text{C}$). Blue vertical lines are the reflections for $\text{Zr}_3(\text{OH})_2\text{F}_{10}$, which is reported as a list of reflections without further structural information.

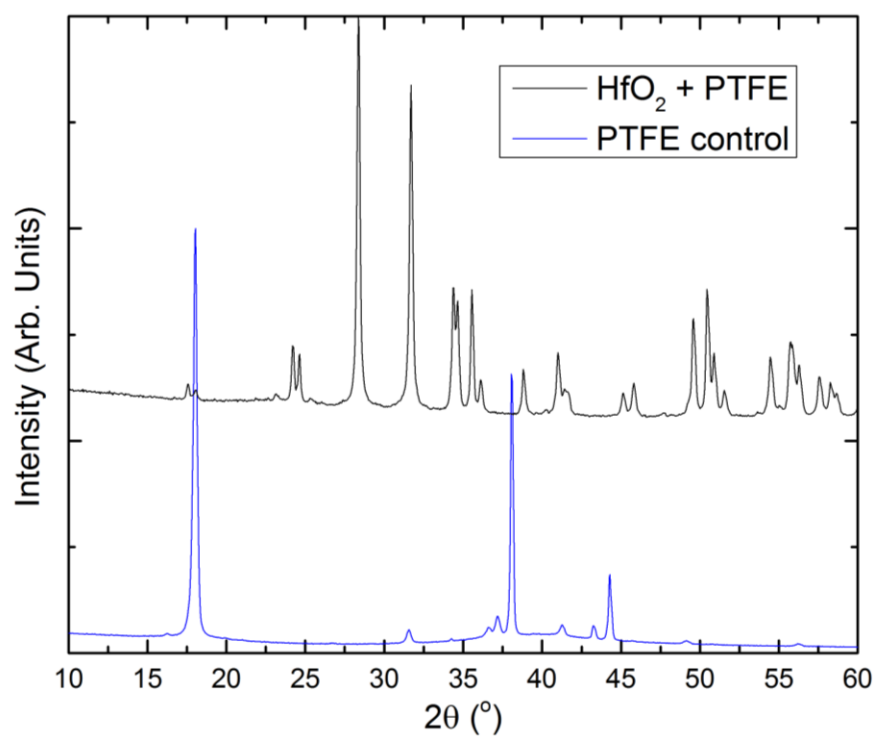


Figure A.5. Comparison of the products of heating a small amount of PTFE at $450\text{ }^\circ\text{C}$ in a sealed fused silica tube with (black) and without (blue) the presence of HfO_2 . The most intense peaks of the latter matches the position of the only unknown peak in the former (**Figure 2**, main text).

The data in **Figure A.5** appear to suggest that the phases indicated by the unknown peak at $\sim 18^\circ$ are not new oxyfluoride phases. The lowest angle non-HfO₂ peak corresponds well with a pattern produced when PTFE is heated to 450 °C in a sealed tube alone (PTFE control). This suggest that it belongs to some carbon residue or by product of reaction with the fused silica tube. The presence of C-based residue or secondary phases is consistent with the observed color change of the sample from white to light gray (**Figure A.3**). Although the other intense peaks of this pattern are not observed in the experimental pattern, it is highly likely that the control product is multi-phasic as a result of complex polymer degradation mechanisms, and that in the presence of additional material not all of them remain unreacted.

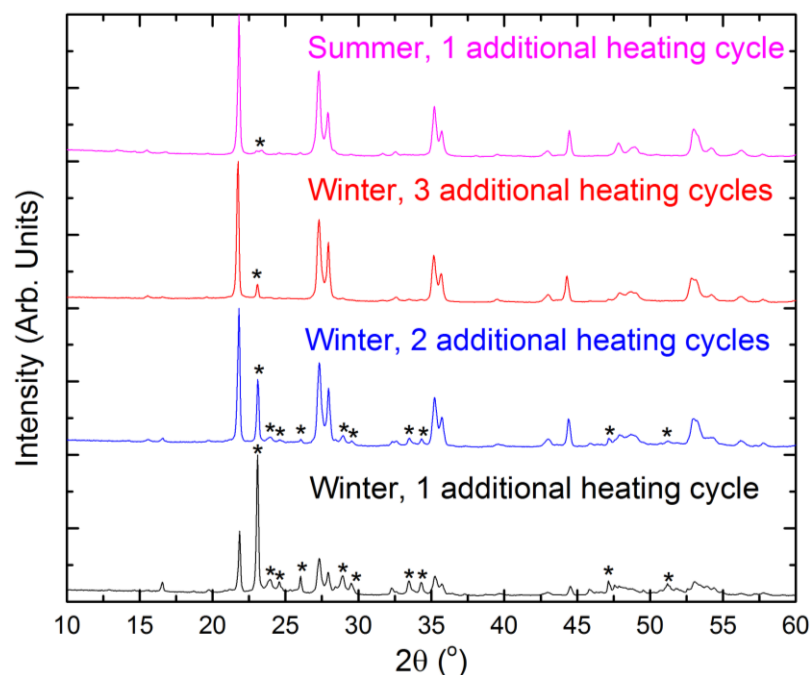


Figure A.6. PXRD patterns of the reaction products of HfO₂ and NH₄HF₂ after 1-3 additional heating cycles in different seasons (and therefore different ambient humidities). Asterisks mark prominent β -HfF₄ peaks.

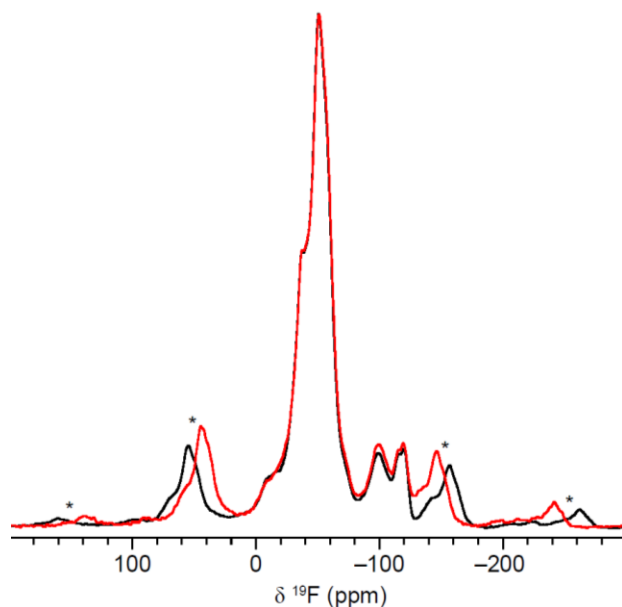


Figure A.7. Comparison of ^{19}F NMR of the unknown Hf-O-F phase at 40 (black) and 36 (red) kHz MAS. Peaks that do not shift represent isotropic resonances. Spinning sidebands are denoted with asterisks.

Table A.4. Spectral parameters used to fit the ^{19}F NMR spectrum of the hafnium oxyfluoride sample in **Figure 3** in the main text.^a

| | $\delta_{\text{iso}} [\pm 0.1]$ (ppm) | $\delta_{\text{CSA}} [\pm 10]$ (ppm) | $\eta_{\text{CSA}} [\pm 0.2]$ | Relative Intensity |
|---|---------------------------------------|--------------------------------------|-------------------------------|--------------------|
| 1 | -13.5 | -140 | 0.5 | 0.04 |
| 2 | -37.0 | -108 | 0.7 | 0.22 |
| 3 | -51.2 | -140 | 0.4 | 0.50 |
| 4 | -59.5 | -125 | 0.1 | 0.11 |
| 5 | -99.4 | -80 | 0.1 | 0.08 |
| 6 | -115.3 | -140 | 0.05 | 0.03 |
| 7 | -120.0 | -100 | 0.1 | 0.01 |

^aIn this work, the Haeberlen convention is adopted to describe the chemical shift tensor. In this convention, the isotropic shift δ_{iso} is given by $\delta_{\text{iso}} = \frac{\delta_{\text{XX}} + \delta_{\text{YY}} + \delta_{\text{ZZ}}}{3}$ with the chemical shift anisotropy δ_{CSA} defined as $\delta_{\text{CSA}} = \delta_{\text{ZZ}} - \delta_{\text{iso}}$ and the shift asymmetry η_{CSA} defined as $\eta_{\text{CSA}} = \frac{\delta_{\text{YY}} - \delta_{\text{XX}}}{\delta_{\text{ZZ}} - \delta_{\text{iso}}}$. Within these definitions, the principal components of the shift tensor are ordered such that $|\delta_{\text{ZZ}} - \delta_{\text{iso}}| \geq |\delta_{\text{XX}} - \delta_{\text{iso}}| \geq |\delta_{\text{YY}} - \delta_{\text{iso}}|$. *N.b.* This definition of δ_{CSA} is sometimes referred to as the reduced anisotropy, which is equal to 2/3 of the ‘full’ anisotropy $\Delta\delta = \delta_{\text{ZZ}} - \frac{\delta_{\text{XX}} + \delta_{\text{YY}}}{2}$ used by some authors and programs.

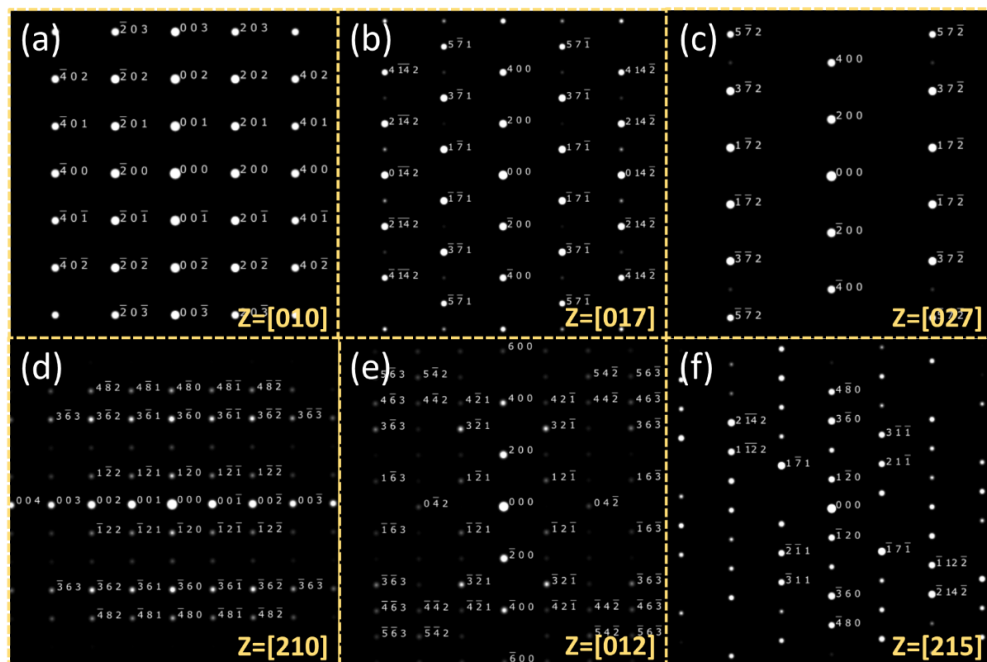


Figure A.8. Simulated SAED patterns of [010] (a), [017] (b), [027] (c), [210] (d), [012] (e) and [215] (f) zone axes of the Hf-O-F sample based on hypothetical model with lattice parameters from Rietveld refinement.

Table A.5. Rietveld refinement parameters for the hypothetical “Hf₇O₉F₁₀” structure.

| Source | Synchrotron |
|---------------------------------|--|
| Chemical Formula | Hf ₇ O ₉ F ₁₀ |
| Formula Weight | 1583.41 |
| Temperature (K) | 295 |
| Wavelength (Å) | 0.457927 |
| Crystal System | Orthorhombic |
| Space group (No.) | Pbam (55) |
| <i>a</i> (Å) | 6.3965(3) |
| <i>b</i> (Å) | 26.5759(11) |
| <i>c</i> (Å) | 4.06843(15) |
| $\alpha = \beta = \gamma$ (deg) | 90 |
| <i>V</i> (Å ³) | 691.61(8) |
| <i>Z</i> | 1 |
| Profile range | $0.5 \leq 2\theta \leq 50$ |
| GOF | 3.45 |
| R _p (%) | 13.82 |
| R _{wp} (%) | 18.26 |

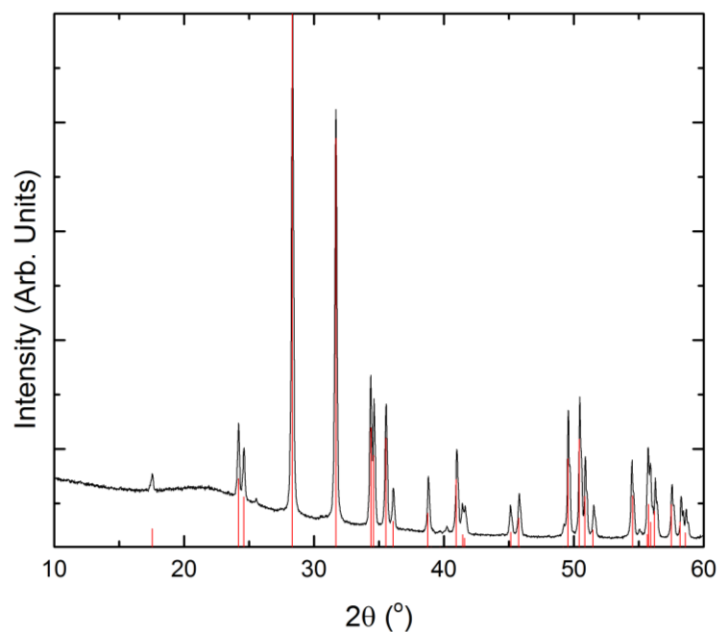


Figure A.9. PXRD of bulk hafnium oxyfluoride produced by reaction of HfO₂ with NH₄HF₂ after thermal analysis (TGA). Sample was heated at 10 °C/min to 800 °C in He atmosphere, held there for 30 minutes and cooled at the same rate. Red vertical lines indicate theoretical reflections for HfO₂. Low sample quantity (~30 mg) resulted in an incompletely covered glass PXRD slide, producing the observed amorphous background.

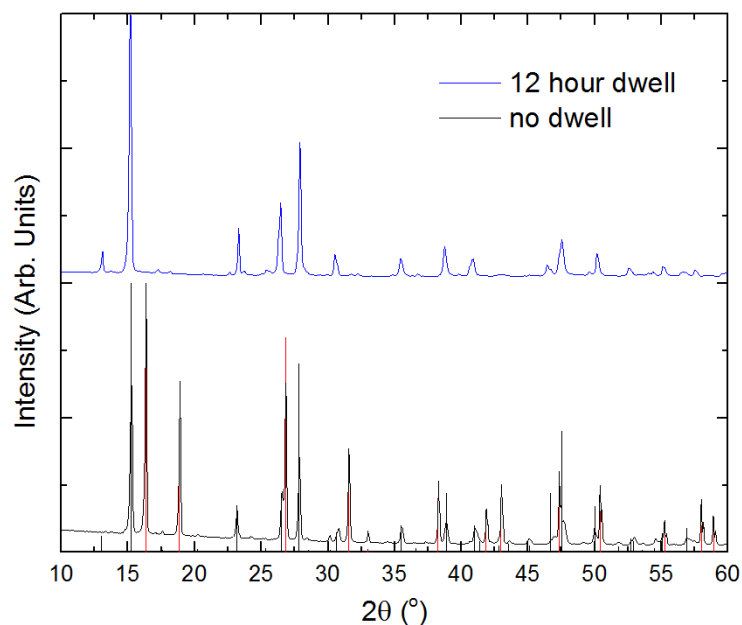


Figure A.10. PXRD of the product of a mixture of HfO₂ and NH₄HF₂ in 1:0.9486 weight (1:4 molar) ratio. After reaction at 250 °C in air for 12 hours. Vertical lines indicate the predicted peak positions for (NH₄)₂HfF₆ (black) and (NH₄)₃HfF₇ (red).

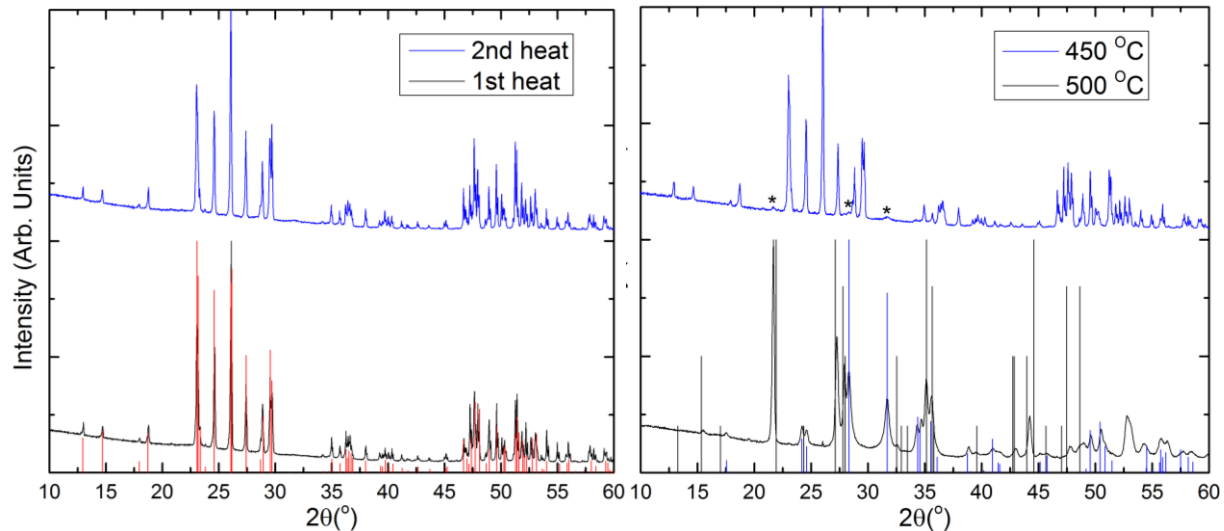


Figure A.11. PXR D of well-ground, commercial HfF_4 after heating in a covered Al_2O_3 crucible air. (left) successive cycles of heating to $420\text{ }^\circ\text{C}$ and dwelling for 12 hours. (right) High temperature heating cycles. Asterisks indicated positions of minor secondary phases. Vertical lines indicate predicted reflections for $\beta\text{-HfF}_4$ (red), HfO_2 (blue), and $\text{Zr}_7\text{O}_9\text{F}_{10}$ (black).

APPENDIX 2. REFERENCES

Chapter 1:

1. Bugaris, D. E.; zur Loye, H.-C. Materials Discovery by Flux Crystal Growth: Quaternary and Higher Order Oxides. *Angew. Chemie Int. Ed.* **2012**, *51* (16), 3780–3811.
2. Wood, J. The Top Ten Advances in Materials Science. *Mater. Today* **2008**, *11* (1), 40–45.
3. Teodorescu, R. NMR Magnets: A Historical Overview. In *Modern NMR Approaches to the Structure Elucidation of Natural Products*; Williams, A. J., Martin, G. E., Rovnyak, D., Eds.; The Royal Society of Chemistry: Cambridge, UK, **2015**; pp 26–37.
4. Bergerhoff, G.; Brown, I.D. in “Crystallographic Databases”, F.H. Allen et al. (Hrsg.) Chester, International Union of Crystallography, (1987).
5. Hulliger, J.; Aslam Awan, M. A “Single-Sample Concept” (SSC): A New Approach to the Combinatorial Chemistry of Inorganic Materials. *Chem. – A Eur. J.* **2004**, *10* (19), 4694–4702.
6. DiSalvo, F. J. Challenges and Opportunities in Solid-State Chemistry. *Pure Appl. Chem.* **2000**, *72* (10), 1799–1807.
7. DiSalvo, F. J. Solid-State Chemistry: A A Rediscovered Chemical Frontier. *Science* (80-.). **1990**, *247* (4943), 649 LP – 655.
8. Jansen, M. A Concept for Synthesis Planning in Solid-State Chemistry. *Angew. Chemie Int. Ed.* **2002**, *41* (20), 3746–3766.
9. Alberi, K.; Nardelli, M. B.; Zakutayev, A.; Mitas, L.; Curtarolo, S.; Jain, A.; Fornari, M.; Marzari, N.; Takeuchi, I.; Green, M. L.; et al. The 2019 Materials by Design Roadmap. *J. Phys. D. Appl. Phys.* **2018**, *52* (1), 13001.
10. Oganov, A. R., Pickard, C. J., Zhu, Q., & Needs, R. J. Structure prediction drives materials discovery. *Nature Reviews Materials.* **2019**, *4*(5), 331–348.
11. Hosono, H.; Paine, D. C.; Ginley, D. *Handbook of Transparent Conductors*; Springer Science & Business Media, 2010.
12. Fortunato, E.; Ginley, D.; Hosono, H.; Paine, D. C. Transparent Conducting Oxides for Photovoltaics. *MRS Bull.* **2007**, *32* (3), 242–247.
13. Calnan, S.; Tiwari, A. N. High Mobility Transparent Conducting Oxides for Thin Film Solar Cells. *Thin Solid Films* **2010**, *518* (7), 1839–1849.
14. Chopra, K. L.; Major, S.; Pandya, D. K. Transparent conductors—A Status Review. *Thin Solid Films* **1983**, *102* (1), 1–46.

15. He, Y.; Ma, E.; Xu, Z. Recycling Indium from Waste Liquid Crystal Display Panel by Vacuum Carbon-Reduction. *J. Hazard. Mater.* **2014**, *268*, 185–190.
16. Zhang, K.; Wu, Y.; Wang, W.; Li, B.; Zhang, Y.; Zuo, T. Recycling Indium from Waste LCDs: A Review. *Resour. Conserv. Recycl.* **2015**, *104*, 276–290.
17. A.C. Tolcin, *Mineral Commodity Summaries 2016*, U.S. Geological Survey, Reston, VA **2017**.
18. Coutts, T. J.; Young, D. L.; Li, X. Characterization of Transparent Conducting Oxides. *MRS Bull.* **2000**, *25* (8), 58–65.
19. Vostal, R.; Šingliar, U.; Fröhlich, P. Gewinnung von Indium Aus Extrem Verdünnten Lösungen. *Chemie Ing. Tech.* **2017**, *89* (1–2), 135–143.
20. Zhang, X.; Zhang, L.; Perkins, J. D.; Zunger, A. Intrinsic Transparent Conductors without Doping. *Phys. Rev. Lett.* **2015**, *115* (17), 176602.
21. Lany, S.; Zakutayev, A.; Mason, T. O.; Wager, J. F.; Poepelmeier, K. R.; Perkins, J. D.; Berry, J. J.; Ginley, D. S.; Zunger, A. Surface Origin of High Conductivities in Undoped In₂O₃ Thin Films. *Phys. Rev. Lett.* **2012**, *108* (1), 16802.
22. Swallow, J. E. N.; Williamson, B. A. D.; Sathasivam, S.; Birkett, M.; Featherstone, T. J.; Murgatroyd, P. A. E.; Edwards, H. J.; Lebens-Higgins, Z. W.; Duncan, D. A.; Farnworth, M.; et al. Resonant Doping for High Mobility Transparent Conductors: The Case of Mo-Doped In₂O₃. *Mater. Horizons* **2020**, *7* (1), 236–243.
23. Mizoguchi, H.; Kamiya, T.; Matsuishi, S.; Hosono, H. A Germanate Transparent Conductive Oxide. *Nat. Commun.* **2011**, *2*, 470.
24. Baek, J. H.; Seol, H.; Cho, K.; Yang, H.; Jeong, J. K. Comparative Study of Antimony Doping Effects on the Performance of Solution-Processed ZIO and ZTO Field-Effect Transistors. *ACS Appl. Mater. Interfaces* **2017**.
25. Zhang, Y. Electronegativities of Elements in Valence States and Their Applications. 2. A Scale for Strengths of Lewis Acids. *Inorg. Chem.* **1982**, *21* (11), 3889–3893.
26. Levy, M. R.; Stanek, C. R.; Chronos, A.; Grimes, R. W. Defect Chemistry of Doped Bixbyite Oxides. *Solid State Sci.* **2007**, *9* (7), 588–593.
27. Wen, S. J.; Campet, G.; Portier, J.; Couturier, G.; Goodenough, J. B. Correlations between the Electronic Properties of Doped Indium Oxide Ceramics and the Nature of the Doping Element. *Mater. Sci. Eng. B* **1992**, *14* (1), 115–119.
28. Campet, G.; Han, S. D.; Wen, S. J.; Manaud, J. P.; Portier, J.; Xu, Y.; Salardenne, J. The Electronic Effect of Ti⁴⁺, Zr⁴⁺ and Ge⁴⁺ Dopings upon the Physical Properties of In₂O₃

and Sn-Doped In₂O₃ Ceramics: Application to New Highly-Transparent Conductive Electrodes. *Mater. Sci. Eng. B* **1993**, *19* (3), 285–289.

29. Kang, S.-B.; Lim, J.-W.; Lee, S.; Kim, J.-J.; Kim, H.-K. Transparent Indium Oxide Films Doped with High Lewis Acid Strength Ge Dopant for Phosphorescent Organic Light-Emitting Diodes. *J. Phys. D. Appl. Phys.* **2012**, *45* (32), 325102.
30. Rickert, K.; Sedefoglu, N.; Malo, S.; Caignaert, V.; Kavak, H.; Poeppelmeier, K. R. Structural, Electrical, and Optical Properties of the Tetragonal, Fluorite-Related Zn_{0.456}In_{1.084}Ge_{0.460}O₃. *Chem. Mater.* **2015**, *27* (14), 5072–5079.
31. Hoel, C. A.; Gaillard, J.-F.; Poeppelmeier, K. R. Probing the Local Structure of Crystalline ZITO: In₂–2xSn_xZn_xO₃ (x≤0.4). *J. Solid State Chem.* **2010**, *183* (4), 761–768.
32. Kageyama, H.; Hayashi, K.; Maeda, K.; Atfield, J. P.; Hiroi, Z.; Rondinelli, J. M.; Poeppelmeier, K. R. Expanding Frontiers in Materials Chemistry and Physics with Multiple Anions. *Nat. Commun.* **2018**, *9* (1), 772.
33. Incorvati, J. T.; Wan, L. F.; Key, B.; Zhou, D.; Liao, C.; Fuoco, L.; Holland, M.; Wang, H.; Prendergast, D.; Poeppelmeier, K. R.; et al. Reversible Magnesium Intercalation into a Layered Oxyfluoride Cathode. *Chem. Mater.* **2016**, *28* (1), 17–20.
34. Wan, L. F., Incorvati, J. T., Poppelmeier, K. R. & Prendergast, D. Building a fast lane for Mg diffusion in α-MoO₃ by fluorine doping. *Chem. Mater.* **28**, 6900–6908 (2016).
35. Hancock, C. A.; Herranz, T.; Marco, J. F.; Berry, F. J.; Slater, P. R. Low Temperature Fluorination of Sr₃Fe₂O₇–x with Polyvinylidene Fluoride: An X-Ray Powder Diffraction and Mössbauer Spectroscopy Study. *J. Solid State Chem.* **2012**, *186*, 195–203.
36. Hirai, D.; Climent-Pascual, E.; Cava, R. J. Superconductivity in WO_{2.6}F_{0.4} Synthesized by Reaction of WO₃ with Teflon. *Phys. Rev. B* **2011**, *84* (17), 174519.
37. Donakowski, M. D.; Gautier, R.; Yeon, J.; Moore, D. T.; Nino, J. C.; Halasyamani, P. S.; Poeppelmeier, K. R. The Role of Polar, Lambda (Λ)-Shaped Building Units in Noncentrosymmetric Inorganic Structures. *J. Am. Chem. Soc.* **2012**, *134* (18), 7679–7689.
38. Hirai, D.; Sawai, O.; Nunoura, T.; Hiroi, Z. Facile Synthetic Route to Transition Metal Oxyfluorides via Reactions between Metal Oxides and PTFE. *J. Fluor. Chem.* **2018**, *209*, 43–48.
39. Tsujimoto, Y.; Yamaura, K.; Takayama-Muromachi, E. Oxyfluoride Chemistry of Layered Perovskite Compounds. *Applied Sciences* . **2012**.
40. Harada, J. K.; Charles, N.; Poeppelmeier, K. R.; Rondinelli, J. M. Heteroanionic Materials by Design: Progress Toward Targeted Properties. *Adv. Mater.* **2019**, *31* (19), 1805295.

41. Clément, R. J.; Lun, Z.; Ceder, G. Cation-Disordered Rocksalt Transition Metal Oxides and Oxyfluorides for High Energy Lithium-Ion Cathodes. *Energy Environ. Sci.* **2020**, *13* (2), 345–373.
42. Lee, J.; Papp, J. K.; Clément, R. J.; Sallis, S.; Kwon, D.-H.; Shi, T.; Yang, W.; McCloskey, B. D.; Ceder, G. Mitigating Oxygen Loss to Improve the Cycling Performance of High Capacity Cation-Disordered Cathode Materials. *Nat. Commun.* **2017**, *8* (1), 981.
43. Wells, A. F. *Structural Inorganic Chemistry*, 5th Edition.; Oxford university press, 2012.
44. Gardner, J. S.; Gingras, M. J. P.; Greedan, J. E. Magnetic Pyrochlore Oxides. *Rev. Mod. Phys.* **2010**, *82* (1), 53–107.
45. Bramwell, S. T.; Gingras, M. J. P. Spin Ice State in Frustrated Magnetic Pyrochlore Materials. *Science* (80-.). **2001**, *294* (5546), 1495 LP-1501.
46. Bel Hadj Tahar, R.; Ban, T.; Ohya, Y.; Takahashi, Y. Tin Doped Indium Oxide Thin Films: Electrical Properties. *J. Appl. Phys.* **1998**, *83* (5), 2631–2645.
47. Gómez, S. Y.; Hotza, D. Current Developments in Reversible Solid Oxide Fuel Cells. *Renew. Sustain. Energy Rev.* **2016**, *61*, 155–174.
48. Hull, S.; Norberg, S. T.; Ahmed, I.; Eriksson, S. G.; Marrocchelli, D.; Madden, P. A. Oxygen Vacancy Ordering within Anion-Deficient Ceria. *J. Solid State Chem.* **2009**, *182* (10), 2815–2821.
49. Baur, W. H. The Rutile Type and Its Derivatives. *Crystallogr. Rev.* **2007**, *13* (1), 65–113.
50. Bursill, L. Structural Relationships between β -Gallia, Rutile, Hollandite, Psilomelane, Ramsdellite and Gallium Titanate Type Structures. *Acta Crystallogr. Sect. B* **1979**, *35* (3), 530–538.
51. Post, J. E.; Heaney, P. J. Neutron and Synchrotron X-Ray Diffraction Study of the Structures and Dehydration Behaviors of Ramsdellite and “Groutellite.” *American Mineralogist*. 2004, pp 969–975.
52. Chabre, Y.; Pannetier, J. Structural and Electrochemical Properties of the Proton / γ -MnO₂ System. *Prog. Solid State Chem.* **1995**, *23* (1), 1–130.
53. Fujishima, A.; Honda, K. Electrochemical Photolysis of Water at a Semiconductor Electrode. *Nature* **1972**, *238* (5358), 37–38.
54. Over, H.; Seitsonen, A. P.; Lundgren, E.; Schmid, M.; Varga, P. Direct Imaging of Catalytically Important Processes in the Oxidation of CO over RuO₂(110). *J. Am. Chem. Soc.* **2001**, *123* (47), 11807–11808.

55. Soares, A.; Fraisse, B.; Morato, F.; Ionica-Bousquet, C. M.; Monconduit, L. On the Synthesis Conditions for Tailoring Lithium Composition in Ramsdellite Phases: Application for Li-Ion Batteries. *J. Power Sources* **2012**, *208*, 440–446.
56. Tsuyumoto, I.; Moriguchi, T. Synthesis and Lithium Insertion Properties of Ramsdellite Li_xTiO_2 Anode Materials. *Mater. Res. Bull.* **2015**, *70*, 748–752.
57. Pérez-Flores, J. C.; Hoelzel, M.; García-Alvarado, F.; Kuhn, A. Structural and Electrochemical Study of Vanadium-Doped TiO_2 Ramsdellite with Superior Lithium Storage Properties for Lithium-Ion Batteries. *ChemPhysChem* **2016**, *17* (7), 1062–1069.
58. Yoshikado, S.; Ohachi, T.; Taniguchi, I.; Onoda, Y.; Watanabe, M.; Fujiki, Y. Ac Ionic Conductivity of Hollandite Type Compounds from 100 Hz to 37.0 GHz. *Solid State Ionics* **1982**, *7* (4), 335–344.
59. Kerisit, S.; Rosso, K. M.; Yang, Z.; Liu, J. Computer Simulation of the Phase Stabilities of Lithiated TiO_2 Polymorphs. *J. Phys. Chem. C* **2010**, *114* (44), 19096–19107.
60. Grey, I. E.; Cranswick, L. M. D.; Li, C.; Bursill, L. A.; Peng, J. L. New Phases Formed in the Li–Ti–O System under Reducing Conditions. *J. Solid State Chem.* **1998**, *138* (1), 74–86.
61. Bystrom, A. M. The Crystal Structure of Ramsdellite, an Orthorhombic Modification of MnO_2 . *Acta Chem. Scand.* **1949**, *3*, 163–173.
62. Yamanaka, T.; Uchida, A.; Nakamoto, Y. Structural Transition of Post-Spinel Phases CaMn_2O_4 , CaFe_2O_4 , and CaTi_2O_4 under High Pressures up to 80 GPa. *Am. Mineral.* **2008**, *93* (11–12), 1874–1881.
63. Miura, H. The Crystal Structure of Hollandite. *Mineral. J.* **1986**, *13* (3), 119–129.
64. Schmid, S.; Thompson, J. G.; Rae, A. D.; Butler, B. D.; Withers, R. L.; Ishizawa, N.; Kishimoto, S. Structures of $\text{Ta}_{22}\text{W}_4\text{O}_{67}$ and $\text{Ta}_{74}\text{W}_6\text{O}_{203}$. I. Refined Structural Models Using Synchrotron Radiation. *Acta Crystallogr. Sect. B* **1995**, *51* (5), 698–708.
65. Loopstra, B. O. On the Crystal Structure of $\alpha\text{-U}_3\text{O}_8$. *J. Inorg. Nucl. Chem.* **1977**, *39* (9), 1713–1714.
66. Thompson, J. G.; Withers, R. L.; Kepert, C. J. Incommensurately Modulated $\text{ZrO}_{2-x}\text{F}_{2x}$: $0.698 \leq x \leq 0.714$. *J. Solid State Chem.* **1991**, *95* (1), 111–125.

Chapter 2:

1. Kanatzidis, M. G.; Poeppelmeier, K. R.; Bobev, S.; Guloy, A. M.; Hwu, S.-J.; Lachgar, A.; Lattner, S. E.; Raymond; Schaak, E.; Seo, D.-K.; et al. Report from the Third Workshop

on Future Directions of Solid-State Chemistry: The Status of Solid-State Chemistry and Its Impact in the Physical Sciences. *Prog. Solid State Chem.* **2008**, *36* (1), 1–133.

2. Vojisavljević, K.; Šćepanović, M.; Srećković, T.; Grujić-Brojčin, M.; Branković, Z.; Branković, G. Structural Characterization of Mechanically Milled ZnO: Influence of Zirconia Milling Media. *J. Phys. Condens. Matter* **2008**, *20* (47), 475202.
3. Kudaka, K.; Iizumi, K.; Sasaki, T.; Izumi, H. Effect of Milling Media on the Reaction Kinetics of the Mechanochemical Synthesis of Pentatitanium Trisilicide. *J. Am. Ceram. Soc.* **2000**, *83* (11), 2887–2889.
4. Schäfer, H. Preparative Solid State Chemistry: The Present Position. *Angew. Chemie Int. Ed. English* **1971**, *10* (1), 43–50.
5. Bugaris, D. E.; zur Loye, H.-C. Materials Discovery by Flux Crystal Growth: Quaternary and Higher Order Oxides. *Angew. Chemie Int. Ed.* **2012**, *51* (16), 3780–3811.
6. Kanatzidis, M. G. New Directions in Synthetic Solid State Chemistry: Chalcophosphate Salt Fluxes for Discovery of New Multinary Solids. *Curr. Opin. Solid State Mater. Sci.* **1997**, *2* (2), 139–149.
7. Cowley, J. M. *Diffraction Physics*; North-Holland Publication: Amsterdam, 1975.
8. Bragg, W. L. The Diffraction of Short Electromagnetic Waves by a Crystal. *Proc. Camb. Philol. Soc.* **1913**, *17*, 43–57.
9. Bragg, W. L. The Analysis of Crystals by the X-Ray Spectrometer. *Proc. R. Soc. London. Ser. A, Contain. Pap. a Math. Phys. Character* **1914**, *89* (613), 468–489.
10. Suryanarayana, C.; Norton, M. G. X-Rays and Diffraction BT - X-Ray Diffraction: A Practical Approach; Suryanarayana, C., Norton, M. G., Eds.; Springer US: Boston, MA, 1998; pp 3–19.
11. Bendersky, L. A.; Gayle, F. W. Electron Diffraction Using Transmission Electron Microscopy. *J. Res. Natl. Inst. Stand. Technol.* **2001**, *106* (6), 997–1012.
12. Young, R. A. *The Rietveld Method*; Oxford University Press: Oxford, 1993; Vol. 6.
13. Rietveld, H. A Profile Refinement Method for Nuclear and Magnetic Structures. *J. Appl. Crystallogr.* **1969**, *2* (2), 65–71.
14. Toby, B. H. R Factors in Rietveld Analysis: How Good Is Good Enough? *Powder Diffr.* **2006**, *21* (1), 67–70.
15. Brown, I. D. *The Chemical Bond in Inorganic Chemistry: The Bond Valence Model*; Oxford University Press, 2016; Vol. 27.

16. Adams, S. Relationship between Bond Valence and Bond Softness of Alkali Halides and Chalcogenides. *Acta Crystallogr. Sect. B* **2001**, 57 (3), 278–287.
17. Stebbins, J. F.; Xue, X. NMR Spectroscopy of Inorganic Earth Materials. *Rev. Mineral. Geochemistry* **2014**, 78 (1), 605–653.
18. MacKenzie, K. J. D.; Smith, M. E. *Multinuclear Solid-State Nuclear Magnetic Resonance of Inorganic Materials*; Pergamon: New York, 2002.
19. Abdi, F.; Aillerie, M.; Bourson, P.; Fontana, M. D.; Polgar, K. Electro-Optic Properties in Pure LiNbO₃ Crystals from the Congruent to the Stoichiometric Composition. *J. Appl. Phys.* **1998**, 84 (4), 2251–2254.
20. De Wit, J. H. W. Electrical Properties of In₂O₃. *J. Solid State Chem.* **1973**, 8 (2), 142–149.
21. Greener, E. H.; Whitmore, D. H.; Fine, M. E. Electrical Conductivity of Near-Stoichiometric A-Nb₂O₅. *J. Chem. Phys.* **1961**, 34 (3), 1017–1023.
22. Olesik, J. W. Elemental Analysis Using ICP-OES and ICP/MS. *Anal. Chem.* **1991**, 63 (1), 12A-21A.
23. Shindo, D.; Oikawa, T. Energy Dispersive X-Ray Spectroscopy BT - Analytical Electron Microscopy for Materials Science; Shindo, D., Oikawa, T., Eds.; Springer Japan: Tokyo, 2002; pp 81–102.
24. Kubelka, P.; Munk, F. An Article on Optics of Paint Layers. *Z. Tech. Phys* **1931**, 12 (593–601).
25. Huang, H.; Colabello, D. M.; Sklute, E. C.; Glotch, T. D.; Khalifah, P. G. Self-Referenced Method for Estimating Refractive Index and Absolute Absorption of Loose Semiconductor Powders. *Chem. Mater.* **2017**, 29 (11), 4632–4640.
26. Pankove, J. I. *Optical processes in semiconductors*. (Dover Publications, New York, 1975).
27. Valdes, L. B. Resistivity Measurements on Germanium for Transistors. *Proc. IRE* **1954**, 42 (2), 420–427.
28. Smits, F. M. Measurement of Sheet Resistivities with the Four-Point Probe. *Bell Syst. Tech. J.* **1958**, 37 (3), 711–718.
29. Irvine, J. T. S.; Sinclair, D. C.; West, A. R. Electroceramics: Characterization by Impedance Spectroscopy. *Adv. Mater.* **1990**, 2 (3), 132–138.
30. Coats, A. W.; Redfern, J. P. Thermogravimetric Analysis. A Review. *Analyst* **1963**, 88 (1053), 906–924.

Chapter 3:

1. Flynn, S.; Adekoya, A. J.; Saeed, S.; Zhang, C.; Dravid, V. P.; Gonzalez, G. B.; Poeppelmeier, K. R. $(\text{Cu}_x\text{Zn}_{1-x})_{0.456}\text{In}_{1.084}\text{Ge}_{0.46}\text{O}_3$ ($0 \leq x \leq 1$): A Complex, Ordered, Anion-Deficient Fluorite with Unusual Site-Specific Cation Mixing. *Inorg. Chem.* **2019**, *58* (22), 15610–15617.
2. Moore, P. B.; Araki, T. Braunitz; Its Structure and Relationship to Bixbyite, and Some Insights on the Genealogy of Fluorite Derivative Structures. *Am. Mineral.* **1976**, *61* (11–12), 1226–1240.
3. Ding, H.; Virkar, A. V.; Liu, F. Defect Configuration and Phase Stability of Cubic versus Tetragonal Yttria-Stabilized Zirconia. *Solid State Ionics* **2012**, *215*, 16–23.
4. Hoch, M.; Yoon, H. S.; Silberstein, A. NON-STOICHEIOMETRY IN TERNARY OXIDES WITH THE FLUORITE STRUCTURE. **1967**.
5. Chadda, D.; Ford, J. D.; Fahim, M. A. Chemical Energy Storage by the Reaction Cycle CuO/Cu₂O. *Int. J. Energy Res.* **1989**, *13* (1), 63–73.
6. Rickert, K.; Sedefoglu, N.; Malo, S.; Caignaert, V.; Kavak, H.; Poeppelmeier, K. R. Structural, Electrical, and Optical Properties of the Tetragonal, Fluorite-Related Zn_{0.456}In_{1.084}Ge_{0.46}O₃. *Chem. Mater.* **2015**, *27* (14), 5072–5079.
7. Mack, E.; Osterhof, G. G.; Kraner, H. M. VAPOR PRESSURE OF COPPER OXIDE AND OF COPPER. *J. Am. Chem. Soc.* **1923**, *45* (3), 617–623.
8. Choisnet, J.; Bizo, L.; Retoux, R.; Hébert, S.; Raveau, B. New Transparent Conductors with the M₇O₁₂ Ordered Oxygen-Deficient Fluorite Structure: From In₄Sn₃O₁₂ to In_{5.5}Sb_{1.5}O₁₂. *J. Solid State Chem.* **2004**, *177* (10), 3748–3751.
9. Toby, B. H.; Von Dreele, R. B. GSAS-II: The Genesis of a Modern Open-Source All Purpose Crystallography Software Package. *J. Appl. Crystallogr.* **2013**, *46* (2), 544–549.
10. Barthel J. Dr. Probe: A software for high-resolution STEM image simulation. *Ultramicroscopy.* **2018** Oct 1;193:1-1.
11. Kubelka, P.; Munk, F. An Article on Optics of Paint Layers. *Z. Tech. Phys* **1931**, *12* (593–601).
12. Bizo L., Choisnet J., Retoux R., Raveau B. The Great Potential of Coupled Substitutions in In₂O₃ for the Generation of Bixbyite-Type Transparent Conducting Oxides, In $2-x\text{M}_x\text{Sn}_x\text{O}_3$. *Solid State Commun.* **2005**, *136* (3), 163–168.

13. Lamoreaux, R. H.; Hildenbrand, D. L.; Brewer, L. High-Temperature Vaporization Behavior of Oxides II. Oxides of Be, Mg, Ca, Sr, Ba, B, Al, Ga, In, Tl, Si, Ge, Sn, Pb, Zn, Cd, and Hg. *J. Phys. Chem. Ref. Data* **1987**, *16* (3), 419–443.
14. Abs-Wurmbach, I.; Ohmann, S.; Westerholt, K.; Meier, T.; Mouron, P.; Choisnet, J. Magnetic Phase Diagrams of Mg-, Fe-, (Cu + Ti)- and Cu-Substituted Braunite $Mn_{2+}Mn_{63+}SiO_{12}$. *Phys. Chem. Miner.* **2002**, *29* (4), 280–290.
15. Zotov, N.; Miletich, R.; Boysen, H.; Tietze, H.; A. Kockelmann, W. Copper Substitution in (Cu,Mn) $7 O 12$ Braunite: A Combined Neutron and X-Ray Diffraction Study. *Mater. Sci. Forum - MATER SCI FORUM* **2000**, 321–324, 791–795.
16. Bizo L., Choisnet J., Raveau B. Coupled Substitutions in In_2O_3 : New Transparent Conductors $In_{2-x}M_{2x/3}Sb_{x/3}O_3$ (M = Cu, Zn). *Mater. Res. Bull.* **2006**, *41* (12), 2232–2237.
17. Mouron, P.; Odier, P.; Choisnet, J. Titanates de Cuivre Substitués À Structure Bixbyite: Les Composés $Cu_{1-x}Ti_{1-x}Fe_{2x}O_3$ ($0.15 \leq X \leq 0.33$). *J. Solid State Chem.* **1985**, *60* (1), 87–94.
18. Mouron, P.; Choisnet, J. A New Ordered Solid Solution with a Bixbyite Structure: The Compounds $Cu_{2+x}Ti_{2-x}Fe_{2-x}Sb_xO_9$ ($0 \leq X \leq 1.4$). *Mater. Res. Bull.* **1987**, *22* (10), 1355–1362.
19. Brown, I. D. *The Chemical Bond in Inorganic Chemistry: The Bond Valence Model*; Oxford University Press, 2016; Vol. 27.
20. Rost, C. M.; Sachet, E.; Borman, T.; Moballegh, A.; Dickey, E. C.; Hou, D.; Jones, J. L.; Curtarolo, S.; Maria, J.-P. Entropy-Stabilized Oxides. *Nat. Commun.* **2015**, *6*, 8485.
21. Chen, K.; Pei, X.; Tang, L.; Cheng, H.; Li, Z.; Li, C.; Zhang, X.; An, L. A Five-Component Entropy-Stabilized Fluorite Oxide. *J. Eur. Ceram. Soc.* **2018**, *38* (11), 4161–4164.
22. Anand, G.; Wynn, A. P.; Handley, C. M.; Freeman, C. L. Phase Stability and Distortion in High-Entropy Oxides. *Acta Mater.* **2018**, *146*, 119–125.
23. Shannon, R. D.; Prewitt, C. T. Effective Ionic Radii in Oxides and Fluorides. *Acta Crystallogr. Sect. B* **1969**, *25* (5), 925–946.
24. Attfield, J. P.; Cheetham, A. K.; Cox, D. E.; Sleight, A. W. Synchrotron X-Ray and Neutron Powder Diffraction Studies of the Structure of [Alpha]- $CrPO_4$. *J. Appl. Crystallogr.* **1988**, *21* (5), 452–457.
25. Denton, A. R.; Ashcroft, N. W. Vegard's Law. *Phys. Rev. A: At., Mol., Opt. Phys.* 1991, *43*, 3161– 3164

26. Cava, S. K. K. and Z. W. and T. K. and R. J. Magnetic and Electronic Properties of the Cu-Substituted Weyl Semimetal Candidate $ZrCo_2Sn$. *J. Phys. Condens. Matter* **2018**, *30* (7), 75701.
27. Palmer, G. B.; Poepelmeier, K. R.; Mason, T. O. Conductivity and Transparency of ZnO/SnO₂-Cosubstituted In₂O₃. *Chem. Mater.* **1997**, *9* (12), 3121–3126.
28. Bérardan, D.; Franger, S.; Dragoe, D.; Meena, A. K.; Dragoe, N. Colossal Dielectric Constant in High Entropy Oxides. *Phys. status solidi – Rapid Res. Lett.* **2016**, *10* (4), 328–333.
29. Berardan, D.; Meena, A. K.; Franger, S.; Herrero, C.; Dragoe, N. Controlled Jahn-Teller Distortion in (MgCoNiCuZn)O-Based High Entropy Oxides. *J. Alloys Compd.* **2017**, *704*, 693–700.
30. Freeman, J. J.; Friedman, R. M. Re-Examination of the Diffuse Reflectance Spectra of Cu/Al₂O₃ Catalysts. *J. Chem. Soc. Faraday Trans. 1 Phys. Chem. Condens. Phases* **1978**, *74* (0), 758–761.
31. Sharpe, P. K.; Vickerman, J. C. Solid State Properties of Copper Containing Spinel Solid Solutions (CuMg_{1-x}Al₂O₄). *J. Chem. Soc. Faraday Trans. 1 Phys. Chem. Condens. Phases* **1977**, *73* (0), 505–513.
32. Schoonheydt, R. A. Transition Metal Ions in Zeolites: Siting and Energetics of Cu²⁺. *Catal. Rev.* **1993**, *35* (1), 129–168.
33. Ferhat, M.; Zaoui, A.; Ahuja, R. Magnetism and Band Gap Narrowing in Cu-Doped ZnO. *Appl. Phys. Lett.* **2009**, *94* (14), 142502.
34. Tsuji, I.; Kato, H.; Kobayashi, H.; Kudo, A. Photocatalytic H₂ Evolution under Visible-Light Irradiation over Band-Structure-Controlled (CuIn)_xZn_{2(1-x)}S₂ Solid Solutions. *J. Phys. Chem. B* **2005**, *109* (15), 7323–7329.
35. Ferhat, M.; Zaoui, A.; Ahuja, R. Magnetism and Band Gap Narrowing in Cu-Doped ZnO. *Appl. Phys. Lett.* **2009**, *94* (14), 142502.
36. HIROTA, K.; INOUE, T.; MOCHIDA, N.; OHTSUKA, A. Study of Germanium Spinels (Part 3). *J. Ceram. Soc. Japan* **1990**, *98* (1141), 976–986.
37. Shimazaki, E.; Matsumoto, N.; Niwa, K. The Vapor Pressure of Germanium Dioxide. *Bull. Chem. Soc. Jpn.* **1957**, *30* (9), 969–971.
38. Miracle, D.B.; Miller, J.D.; Senkov, O.N.; Woodward, C.; Uchic, M.D.; Tiley, J. Exploration and Development of High Entropy Alloys for Structural Applications. *Entropy* **2014**, *16*, 494-525.

39. Sarkar, A.; Wang, Q.; Schiele, A.; Chellali, M. R.; Bhattacharya, S. S.; Wang, D.; Brezesinski, T.; Hahn, H.; Velasco, L.; Breitung, B. High-Entropy Oxides: Fundamental Aspects and Electrochemical Properties. *Adv. Mater.* **2019**, *31* (26), 1806236.
40. Shafi, S. P.; Lundgren, R. J.; Cranswick, L. M. D.; Bieringer, M. Formation, Structure and Magnetism of the Metastable Defect Fluorite Phases $AVO_{3.5+x}$ (A=In, Sc). *J. Solid State Chem.* **2007**, *180* (12), 3333–3340.
41. de los Reyes, M.; Whittle, K. R.; Zhang, Z.; Ashbrook, S. E.; Mitchell, M. R.; Jang, L.-Y.; Lumpkin, G. R. The Pyrochlore to Defect Fluorite Phase Transition in $Y_2Sn_2-XZr_xO_7$. *RSC Adv.* **2013**, *3* (15), 5090–5099.
42. Allpress, J. G.; Rossell, H. J. Fluorite-Related Phases Ln_3MO_7 , Ln = Rare Earth, Y, or Sc, M = Nb, Sb, or Ta. I. Crystal Chemistry. *J. Solid State Chem.* **1979**, *27* (1), 105–114.
43. Lan, Q. Q.; Shen, X.; Yang, H. W.; Zhang, H. R.; Zhang, J.; Guan, X. X.; Yao, Y.; Wang, Y. G.; Yu, R. C.; Peng, Y.; et al. Correlation between Magnetism and “Dark Stripes” in Strained $La_{1-x}Sr_xCoO_3$ Epitaxial Films ($0 \leq x \leq 0.1$). *Appl. Phys. Lett.* **2015**, *107* (24), 242404.
44. Liao, Y.; Cao, W.; Connell, J. W.; Chen, Z.; Lin, Y. Evolution of Moiré Profiles from van Der Waals Superstructures of Boron Nitride Nanosheets. *Sci. Rep.* **2016**, *6* (1), 26084.
45. Gludovatz, B.; Hohenwarter, A.; Catoor, D.; Chang, E. H.; George, E. P.; Ritchie, R. O. A Fracture-Resistant High-Entropy Alloy for Cryogenic Applications. *Science* (80-.). **2014**, *345* (6201), 1153 LP – 1158.
46. Wu, Y. D.; Cai, Y. H.; Wang, T.; Si, J. J.; Zhu, J.; Wang, Y. D.; Hui, X. D. A Refractory $Hf_{25}Nb_{25}Ti_{25}Zr_{25}$ High-Entropy Alloy with Excellent Structural Stability and Tensile Properties. *Mater. Lett.* **2014**, *130*, 277–280.
47. Dąbrowa, J.; Stygar, M.; Mikuła, A.; Knapik, A.; Mroczka, K.; Tejchman, W.; Danielewski, M.; Martin, M. Synthesis and Microstructure of the $(Co,Cr,Fe,Mn,Ni)_3O_4$ High Entropy Oxide Characterized by Spinel Structure. *Mater. Lett.* **2018**, *216*, 32–36.
48. Jiang, S.; Hu, T.; Gild, J.; Zhou, N.; Nie, J.; Qin, M.; Harrington, T.; Vecchio, K.; Luo, J. A New Class of High-Entropy Perovskite Oxides. *Scr. Mater.* **2018**, *142*, 116–120.
49. Rickert, K.; Boullay, P.; Malo, S.; Caignaert, V.; Poeppelmeier, K. R. A Rutile Chevron Modulation in Delafossite-Like $Ga_3-XIn_3Ti_xO_{9+x/2}$. *Inorg. Chem.* **2016**, *55* (9), 4403–4409.

Chapter 4:

1. Tsuyumoto, I.; Moriguchi, T. Synthesis and Lithium Insertion Properties of Ramsdellite Li_xTiO_2 Anode Materials. *Mater. Res. Bull.* **2015**, *70*, 748–752.

2. Koudriachova, M. V.; Harrison, N. M.; de Leeuw, S. W. Diffusion of Li-Ions in Rutile. An Ab Initio Study. *Solid State Ionics* **2003**, *157* (1), 35–38.
3. Post, J. E.; Heaney, P. J. Neutron and Synchrotron X-Ray Diffraction Study of the Structures and Dehydration Behaviors of Ramsdellite and “Groutellite.” *American Mineralogist*. 2004, pp 969–975.
4. Chabre, Y.; Pannetier, J. Structural and Electrochemical Properties of the Proton / γ -MnO₂ System. *Prog. Solid State Chem.* **1995**, *23* (1), 1–130.
5. Fujishima, A.; Honda, K. Electrochemical Photolysis of Water at a Semiconductor Electrode. *Nature* **1972**, *238* (5358), 37–38.
6. Over, H.; Seitsonen, A. P.; Lundgren, E.; Schmid, M.; Varga, P. Direct Imaging of Catalytically Important Processes in the Oxidation of CO over RuO₂(110). *J. Am. Chem. Soc.* **2001**, *123* (47), 11807–11808.
7. Soares, A.; Fraisse, B.; Morato, F.; Ionica-Bousquet, C. M.; Monconduit, L. On the Synthesis Conditions for Tailoring Lithium Composition in Ramsdellite Phases: Application for Li-Ion Batteries. *J. Power Sources* **2012**, *208*, 440–446.
8. Pérez-Flores, J. C.; Hoelzel, M.; García-Alvarado, F.; Kuhn, A. Structural and Electrochemical Study of Vanadium-Doped TiO₂ Ramsdellite with Superior Lithium Storage Properties for Lithium-Ion Batteries. *ChemPhysChem* **2016**, *17* (7), 1062–1069.
9. Kerisit, S.; Rosso, K. M.; Yang, Z.; Liu, J. Computer Simulation of the Phase Stabilities of Lithiated TiO₂ Polymorphs. *J. Phys. Chem. C* **2010**, *114* (44), 19096–19107.
10. Grey, I. E.; Cranswick, L. M. D.; Li, C.; Bursill, L. A.; Peng, J. L. New Phases Formed in the Li–Ti–O System under Reducing Conditions. *J. Solid State Chem.* **1998**, *138* (1), 74–86.
11. Murphy, D. W.; Di Salvo, F. J.; Carides, J. N.; Waszczak, J. V. Topochemical Reactions of Rutile Related Structures with Lithium. *Mater. Res. Bull.* **1978**, *13* (12), 1395–1402.
12. Kuhn, A.; Baehtz, C.; García-Alvarado, F. Structural Evolution of Ramsdellite-Type Li_xTi₂O₄ upon Electrochemical Lithium Insertion–deinsertion (0 ≤ x ≤ 2). *J. Power Sources* **2007**, *174* (2), 421–427.
13. Wiedemann, D.; Nakhal, S.; Franz, A.; Lerch, M. Lithium Diffusion Pathways in Metastable Ramsdellite-like Li₂Ti₃O₇ from High-Temperature Neutron Diffraction. *Solid State Ionics* **2016**, *293*, 37–43.
14. Koudriachova, M. V. Ramsdellite-Structured LiTiO₂: A New Phase Predicted from Ab Initio Calculations. *Chem. Phys. Lett.* **2008**, *458* (1), 108–112.

15. Abrahams, I.; Bruce, P. G.; David, W. I. F.; West, A. R. Refinement of the Lithium Distribution in $\text{Li}_2\text{Ti}_3\text{O}_7$ Using High-Resolution Powder Neutron Diffraction. *J. Solid State Chem.* **1989**, *78* (1), 170–177.
16. Tarte, P., & Gabelica-Robert, M. New Complex Antimonate and Tellurates Structurally Related to Lithium Antimonate LiSbO_3 . *Comptes Rendus de l'Académie Des Sciences*, **1983**, 296, 261.
17. Pospelov, A. A., Nalbandyan, V. B., Serikova, E. I., Medvedev, B. S., Evstigneeva, M. A., Ni, E. V., & Lukov, V. V. Crystal structure and properties of a new mixed-valence compound $\text{LiMn}_2\text{TeO}_6$ and the survey of the $\text{LiMM}'\text{XO}_6$ family (X = Sb or Te). *Solid State Sciences*, **2011**, *13*(11), 1931–1937.
18. Yuhasz, W. M. (2019). *Patent No. 10,202,510*. USA: Google Patents.
19. Baur, W. H. The Rutile Type and Its Derivatives. *Crystallogr. Rev.* **2007**, *13* (1), 65–113.
20. Bergerhoff, G.; Hundt, R.; Sievers, R.; Brown, I. D. The Inorganic Crystal Structure Data Base. *J. Chem. Inf. Comput. Sci.* **1983**, *23* (2), 66–69.
21. Belsky, A.; Hellenbrandt, M.; Karen, V. L.; Luksch, P. New Developments in the Inorganic Crystal Structure Database (ICSD): Accessibility in Support of Materials Research and Design. *Acta Crystallogr. Sect. B* **2002**, *58* (3), 364–369.
22. Kim, J.-W.; Lee, H.-G. Thermal and Carbothermic Decomposition of Na_2CO_3 and Li_2CO_3 . *Metall. Mater. Trans. B* **2001**, *32* (1), 17–24.
23. *SAINTE* V8.38A; Bruker Analytical X-ray Instruments: Madison, WI, USA, 2016.
24. Sheldrick, G. M. *SADABS*; University of Göttingen: Göttingen, Germany, 2002.
25. Sheldrick, G. M. Crystal Structure Refinement with SHELXL. *Acta Crystallogr. Sect. C Struct. Chem.* **2015**, *71* (1), 3–8.
26. Dolomanov, O. V.; Bourhis, L. J.; Gildea, R. J.; Howard, J. a. K.; Puschmann, H. OLEX2: A Complete Structure Solution, Refinement and Analysis Program. *J. Appl. Crystallogr.* **2009**, *42* (2), 339–341.
27. Spek, A. L. Single-Crystal Structure Validation with the Program PLATON. *J. Appl. Crystallogr.* **2003**, *36* (1), 7–13.
28. Toby, B. H.; Von Dreele, R. B. GSAS-II: The Genesis of a Modern Open-Source All Purpose Crystallography Software Package. *J. Appl. Crystallogr.* **2013**, *46* (2), 544–549.

29. Clark, S. J.; Segall, M. D.; Pickard, C. J.; Hasnip, P. J.; Probert, M. I. J.; Refson, K.; Payne, M. C. First Principles Methods Using CASTEP. *Z. Kristallogr. - Cryst. Mater.* **2005**, *220*, 567–570.
30. Vanderbilt, D. Soft Self-Consistent Pseudopotentials in a Generalized Eigenvalue Formalism. *Phys. Rev. B: Condens. Matter Mater. Phys.* **1990**, *41*, 7892–7895.
31. Perdew, J. P.; Burke, K.; Ernzerhof, M. Generalized Gradient Approximation Made Simple. *Phys. Rev. Lett.* **1996**, *77* (18), 3865–3868.
32. Monkhorst, H. J.; Pack, J. D. Special Points for Brillouin-Zone Integrations. *Phys. Rev. B* **1976**, *13*, 5188–5192.
33. Pickard, C. J. ; Mauri, F. All-electron magnetic response with pseudopotentials: NMR chemical shifts. *Physical Review B.* **2001**, *63*, 245101.
34. Yates, J. R.; Pickard, C. J. ; Mauri, F. Calculation of NMR Chemical Shifts for extended systems using Ultrasoft Pseudopotentials. *Physical Review B*, **2007**, *76*, 024401.
35. Profeta, M.; Mauri, F.; Pickard, C. J. Accurate First Principles Prediction of ¹⁷O NMR Parameters in SiO₂: Assignment of the Zeolite Ferrierite Spectrum. *J. Amer. Chem. Soc.* **2003**, *125*, 541.
36. Sturniolo, S.; Green, T. F. G.; Hanson, R. M.; Zilka, M.; Refson, K.; Hodgkinson, P.; Brown, S. P.; Yates, J. R. Visualization and Processing of Computed Solid-State NMR Parameters: MagresView and MagresPython. *Solid State Nucl. Magn. Reson.* **2016**, *78*, 64–70.
37. Pankove, J. I. *Optical processes in semiconductors*. (Dover Publications, New York, 1975).
38. Xu, X. Charge Transport across Single Grain Boundaries in Oxide Electrolytes. Northwestern University, ProQuest Dissertations Publishing, 2019. 22618334.
39. Fujihala, M.; Koorikawa, H.; Mitsuda, S.; Hagihala, M.; Morodomi, H.; Kawae, T.; Matsuo, A.; Kindo, K. Spin-Liquid Ground State in the Spin 1/2 Distorted Diamond Chain Compound K₃Cu₃AlO₂(SO₄)₄. *J. Phys. Soc. Japan.* **2015**, *84* (7), 73702.
40. Sorolla, M.; Wang, X.; Kubíčková, L.; Ksenofontov, V.; Möller, A.; Jacobson, A. J. A Mixed-Valent Iron (II/III) Diamond Chain with Single-Ion Anisotropy. *Inorg. Chem.* **2019**.
41. Hiroi, Z. Structural Instability of the Rutile Compounds and Its Relevance to the Metal–Insulator Transition of VO₂. *Prog. Solid State Chem.* **2015**, *43* (1), 47–69.
42. Schmidt, W.; Wilkening, M. Discriminating the Mobile Ions from the Immobile Ones in Li_{4+x}Ti₅O₁₂: ⁶Li NMR Reveals the Main Li⁺ Diffusion Pathway and Proposes a Refined Lithiation Mechanism. *J Phys Chem C.* **2016**, *120*, 11372–11381

43. Zhang, Z.-G.; Abe, T.; Moriyoshi, C.; Tanaka, H.; Kuroiwa, Y. Study of Materials Structure Physics of Isomorphic LiNbO_3 and LiTaO_3 Ferroelectrics by Synchrotron Radiation X-Ray Diffraction. *Jpn. J. Appl. Phys.* **2018**, *57* (11S), 11UB04.
44. Zhang, Z.-G.; Abe, T.; Moriyoshi, C.; Tanaka, H.; Kuroiwa, Y. Synchrotron-Radiation X-Ray Diffraction Evidence of the Emergence of Ferroelectricity in LiTaO_3 by Ordering of a Disordered Li Ion in the Polar Direction. *Appl. Phys. Express* **2018**, *11* (7), 71501.
45. Genkina, E. A. Accurate Definition of LiSbO_3 Crystal Structure. *Kristallografiya* **1992**, *37*, 356–358.
46. Bandis; Cramer, L.; Holt, T. E.; Langford, S. C.; Dickinson, J. T. On the White Light Luminescence Induced by Irradiation of Sodium Nitrate Single Crystals by 1064 Nm Laser Light. *Appl. Surf. Sci.* **2002**, *197–198*, 100–106.
47. de Wolff, P. M. Interpretation of Some Gamma- MnO_2 Diffraction Patterns. *Acta Crystallogr.* **1959**, *12* (4), 341.
48. Wells, A. F. *Structural Inorganic Chemistry*, 5th Edition; Oxford university press, 2012.
49. Bursill, L. Structural Relationships between β -Gallia, Rutile, Hollandite, Psilomelane, Ramsdellite and Gallium Titanate Type Structures. *Acta Crystallogr. Sect. B* **1979**, *35* (3), 530–538.
50. Bayer, G. InSbO_4 and ScSbO_4 , New Compounds with the Rutile Structure. *Zeitschrift fur Kristallographie - New Crystal Structures*. 1963, pp 158–160.
51. Choisnet, J.; Bizo, L.; Retoux, R.; Hébert, S.; Raveau, B. New Transparent Conductors with the M_7O_{12} Ordered Oxygen-Deficient Fluorite Structure: From $\text{In}_4\text{Sn}_3\text{O}_{12}$ to $\text{In}_{5.5}\text{Sb}_{1.5}\text{O}_{12}$. *J. Solid State Chem.* **2004**, *177* (10), 3748–3751.
52. Xu, K.; Xu, D.; Zhang, X.; Luo, Z.; Wang, Y.; Zhang, S. Visible-Light Activity of N-LiInO_2 : Band Structure Modifications through Interstitial Nitrogen Doping. *Appl. Surf. Sci.* **2017**, *391*, 645–653.
53. Goodenough, J. B. Ceramic Solid Electrolytes. *Solid State Ionics* **1997**, *94* (1), 17–25. *Ceramic materials for electronics: Processing, Properties, and Applications*. ed. Relva C. Buchanan. Marcel Dekker Inc.: New York City, p. 50. (1986).
54. Castellanos, M.; West, A. R. Order-Disorder Phenomena in Oxides with Rock Salt Structures: The System $\text{Li}_2\text{TiO}_3\text{-MgO}$. *J. Mater. Sci.* **1979**, *14* (2), 450–454.
55. David C. Apperley, Robin K. Harris, Paul Hodgkinson. *Solid-State NMR: Basic Principles and Practice*. Momentum Press, New York, **2012**.

56. Flack, H. D.; Bernardinelli, G. Centrosymmetric Crystal Structures Described as Non-Centrosymmetric: An Analysis of Reports in *Inorganica Chimica Acta*. *Inorganica Chim. Acta* **2006**, *359* (1), 383–387.
57. Shannon, R. D.; Prewitt, C. T. Effective Ionic Radii in Oxides and Fluorides. *Acta Crystallogr. Sect. B* **1969**, *25* (5), 925–946.
58. Das, B.; Reddy, M. V; Subba Rao, G. V; Chowdari, B. V. R. Nano-Phase Tin Hollandites, $K_2(M_2Sn_6)O_{16}$ ($M = Co, In$) as Anodes for Li-Ion Batteries. *J. Mater. Chem.* **2011**, *21* (4), 1171–1180.
59. Sharma, N.; Plévert, J.; Subba Rao, G. V; Chowdari, B. V. R.; White, T. J. Tin Oxides with Hollandite Structure as Anodes for Lithium Ion Batteries. *Chem. Mater.* **2005**, *17* (18), 4700–4710.
60. Fujimoto, K.; Ito, S.; Watanabe, M. Crystal Growth and Refinement of $K_{1.88}Ga_{1.88}Sn_{8.12}O_{16}$ Hollandite-Type Compound. *Solid State Ionics* **2006**, *177* (19), 1901–1904.
61. Needs, R. J.; Pickard, C. J. Perspective: Role of Structure Prediction in Materials Discovery and Design. *APL Mater.* **2016**, *4* (5), 53210.

Chapter 5:

1. Kolditz, L.; Feltz, A. Über Fluorhaltige Komplexe. III. Über Zirkontetrafluoridhydrate, Zirkonhydroxofluoride Und Ihre Kondensationsprodukte. *Zeitschrift für Anorg. und Allg. Chemie* **1961**, *310* (4-6), 217–224.
2. Gaudreau, B. Recherches sur le fluorure de zirconium et quelques-uns de ses dérivés. *Rev. Chim. Miner.*, **1965**, *2* (1), 1-52 .
3. Joubert, P. and Gaudreau, B. Sur quelques oxyfluorures de ZIRCONIUM tétravalent. *Rev. Chim. Miner.*, **1975**, *12*(4), 289-302.
4. Meyer, G. The Oxidation of Metals with Liebig Acids. *Zeitschrift für Anorg. und Allg. Chemie* **2008**, *634* (2), 201–222.
5. Holmberg, B. The Crystal Structure of $Zr_7O_9F_{10}$. *Acta Crystallogr. Sect. B* **1970**, *26* (6), 830–835.
6. Papiernik, R.; Frit, B. Structure Cristalline d'une Phase Cubique Desordonnée de Type ReO_3 Excedentaire En Anions : $ZrF_{2,67}O_{0,67}$. *Mater. Res. Bull.* **1984**, *19* (4), 509–516.
7. Lai, C. S.; Wu, W. C.; Wang, J. C.; Chao, T. sheng. Characterization of CF_4 -Plasma Fluorinated HfO_2 Gate Dielectrics with TaN Metal Gate. *Appl. Phys. Lett.* **2005**, *86* (22), 222905.

8. Wang, C.; Huo, Z.; Liu, Z.; Liu, Y.; Cui, Y.; Wang, Y.; Li, F.; Liu, M. Effects of Interfacial Fluorination on Performance Enhancement of High-k-Based Charge Trap Flash Memory. *Jpn. J. Appl. Phys.* **2013**, *52* (7R), 70201.
9. Hsieh, C.-R.; Chen, Y.-Y.; Lu, K.-W.; Lin, G.; Lou, J.-C. Effect of Interfacial Fluorination on the Electrical Properties of the Inter-Poly High-k Dielectrics. *Microelectron. Eng.* **2011**, *88* (6), 945–949.
10. Lu, T.-F.; Yang, C.-M.; Wang, J.-C.; Ho, K.-I.; Chin, C.-H.; Pijanowska, D. G.; Jaroszewicz, B.; Lai, C.-S. Characterization of K⁺ and Na⁺-Sensitive Membrane Fabricated by CF₄ Plasma Treatment on Hafnium Oxide Thin Films on ISFET. *J. Electrochem. Soc.* **2011**, *158* (4), J91.
11. Rickard, C. E. F.; Waters, T. N. The Hafnium Tetrafluoride-Water System. *J. Inorg. Nucl. Chem.* **1964**, *26* (6), 925–930.
12. Gaudreau, B. Comparaison des composés fluorés du hafnium et du zirconium. *C. R. Acad. Sci. Ser. C.* **1966**, *263*, 67–70.
13. Vilakazi, B. M.; Monnahela, O. S.; Wagener, J. B.; Carstens, P. A. B.; Ntsoane, T. A Thermogravimetric Study of the Fluorination of Zirconium and Hafnium Oxides with Anhydrous Hydrogen Fluoride Gas. *J. Fluor. Chem.* **2012**, *141*, 64–68.
14. Dey, C. C. Microcrystalline Phase Transformation from ZrF₄·HF·2H₂O to ZrO₂ through the Intermediate Phases ZrF₄·3H₂O, ZrF₄·H₂O, Zr₂O₇·H₂O and ZrF₄. *Chem. Phys. Lett.* **2014**, *612*, 8–13.
15. Monnahela, O. S.; Vilakazi, B. M.; Wagener, J. B.; Roodt, A.; Carstens, P. A. B.; Retief, W. L. A Thermogravimetric Study of the Fluorination of Zirconium and Hafnium Oxides with Fluorine Gas. *J. Fluor. Chem.* **2012**, *135*, 246–249.
16. Hirai, D.; Climent-Pascual, E.; Cava, R. J. Superconductivity in WO_{2.6}F_{0.4} Synthesized by Reaction of WO₃ with Teflon. *Phys. Rev. B* **2011**, *84* (17), 174519.
17. Hirai, D.; Sawai, O.; Nunoura, T.; Hiroi, Z. Facile Synthetic Route to Transition Metal Oxyfluorides via Reactions between Metal Oxides and PTFE. *J. Fluor. Chem.* **2018**, *209*, 43–48.
18. Slater, P. R. Poly(Vinylidene Fluoride) as a Reagent for the Synthesis of K₂NiF₄-Related Inorganic Oxide Fluorides. *J. Fluor. Chem.* **2002**, *117* (1), 43–45.
19. Rakov, E. G.; Mel'nichenko, E. I. The Properties and Reactions of Ammonium Fluorides. *Russ. Chem. Rev.* **1984**, *53* (9), 851–869.

20. Voit, E. I.; Didenko, N. A.; Gaivoronskaya, K. A. The Composition of Intermediate Products of the Thermal Decomposition of $(\text{NH}_4)_2\text{ZrF}_6$ to ZrO_2 from Vibrational-Spectroscopy Data. *Opt. Spectrosc.* **2018**, *124* (3), 328–336.
21. Kobayashi, Y.; Tian, M.; Eguchi, M.; Mallouk, T. E. Ion-Exchangeable, Electronically Conducting Layered Perovskite Oxyfluorides. *J. Am. Chem. Soc.* **2009**, *131* (28), 9849–9855.
22. Verkhoturova, V. L. S. and M. E. K. and Y. N. M. and V. I. S. and V. V. Study on the Process of Fe (III) Oxide Fluorination. *IOP Conf. Ser. Mater. Sci. Eng.* **2016**, *110* (1), 12069.
23. Baker, B. B.; Kasprzak, D. J. Thermal Degradation of Commercial Fluoropolymers in Air. *Polym. Degrad. Stab.* **1993**, *42* (2), 181–188.
24. Conesa, J. A.; Font, R. Polytetrafluoroethylene Decomposition in Air and Nitrogen. *Polym. Eng. Sci.* **2001**, *41* (12), 2137–2147.
25. Loginova, N. N.; Madorskaya, L. Y.; Podlesskaya, N. K. Relations between the Thermal Stability of Partially Fluorinated Polymers and Their Structure. *Polym. Sci. U.S.S.R.* **1983**, *25* (12), 2995–3000.
26. Hancock, C. A.; Herranz, T.; Marco, J. F.; Berry, F. J.; Slater, P. R. Low Temperature Fluorination of $\text{Sr}_3\text{Fe}_2\text{O}_{7-x}$ with Polyvinylidene Fluoride: An X-Ray Powder Diffraction and Mössbauer Spectroscopy Study. *J. Solid State Chem.* **2012**, *186*, 195–203.
27. Toby, B. H.; Von Dreele, R. B. GSAS-II: The Genesis of a Modern Open-Source All Purpose Crystallography Software Package. *J. Appl. Crystallogr.* **2013**, *46* (2), 544–549.
28. Bielecki, A.; Burum, D. P. Temperature Dependence of ^{207}Pb MAS Spectra of Solid Lead Nitrate. An Accurate, Sensitive Thermometer for Variable-Temperature MAS. *J. Magn. Reson. A* **1995**, *116* (2), 215–220. <https://doi.org/10.1006/jmra.1995.0010>.
29. Beckmann, P. A.; Dybowski, C. A Thermometer for Nonspinning Solid-State NMR Spectroscopy. *J. Magn. Reson.* **2000**, *146* (2), 379–380. <https://doi.org/10.1006/jmre.2000.2171>.
30. Barthel, J. Dr. Probe: A Software for High-Resolution STEM Image Simulation. *Ultramicroscopy* **2018**, *193*, 1–11. <https://doi.org/10.1016/j.ultramic.2018.06.003>.
31. Hohenberg, P. & Kohn, W. Inhomogeneous Electron Gas. *Phys. Rev.* **136**, B864–B871 (1964).
32. Kohn, W. & Sham, L. J. Self-Consistent Equations Including Exchange and Correlation Effects. *Phys. Rev.* **140**, A1133–A1138 (1965).

33. Kresse, G. & Furthmüller, J. Efficiency of ab-initio total energy calculations for metals and semiconductors using a plane-wave basis set. *Comput. Mater. Sci.* **6**, 15–50 (1996).
34. Kresse, G. & Furthmüller, J. Efficient iterative schemes for *ab initio* total-energy calculations using a plane-wave basis set. *Phys. Rev. B* **54**, 11169–11186 (1996).
35. Blöchl, P. E. Projector augmented-wave method. *Phys. Rev. B* **50**, 17953–17979 (1994).
36. Perdew, J. P., Burke, K. & Ernzerhof, M. Generalized Gradient Approximation Made Simple. *Phys. Rev. Lett.* **77**, 3865–3868 (1996).
37. Kresse, G. & Joubert, D. From ultrasoft pseudopotentials to the projector augmented-wave method. *Phys. Rev. B* **59**, 1758–1775 (1999).
38. M. W. Chase, Jr., C. A. Davies, J. R. Downey, Jr., D. J. Frurip, R. A. McDonald, and A. N. S. JANAF Thermochemical Tables, Third Edition. *J. Phys. Chem. Ref. Data* **14**, (1985).
39. Nguyen, T. Degradation of Poly[Vinyl Fluoride] and Poly[Vinylidene Fluoride]. *J. Macromol. Sci. Part C* **1985**, 25 (2), 227–275.
40. Laval, J.-P. Crystal Chemistry of Anion-Excess ReO₃-Related Phases. III. [Gamma]-ZrF₄, a High-Pressure Form of Zirconium Tetrafluoride and Comparison of MX₄ Structure Types. *Acta Crystallogr. Sect. C* **2014**, 70 (8), 742–748.
41. Papiernik, R.; Mercurio, D.; Frit, B. Structure Du Tetrafluorure de Zirconium, ZrF₄[Alpha]. *Acta Crystallogr. Sect. B* **1982**, 38 (9), 2347–2353.
42. Siegrist, T.; Cava, R. J.; Krajewski, J. J. REDUCED ALKALINE EARTH TANTALATES. *Mater. Res. Bull.* **1997**, 32 (7), 881–887.
43. McTaggart, F. K. Reduction of Zirconium and Hafnium Oxides. *Nature* **1961**, 191 (4794), 1192.
44. Reed, T. B. *Free Energy of Formation of Binary Compounds*; MIT press, **1971**.
45. Ellingham, H. J. T. Reducibility of Oxides and Sulfides in Metallurgical Processes. *J Soc Chem Ind* **1944**, 63, 125–133.
46. Thompson, J. G.; Withers, R. L.; Kepert, C. J. Incommensurately Modulated ZrO₂-xF_{2x}: 0.698 ≤ x ≤ 0.714. *J. Solid State Chem.* **1991**, 95 (1), 111–125.
47. Ramsey, N. F. Magnetic shielding of nuclei in molecules. *Phys. Rev.* **1950**, 78, 699.
48. Ramsey, N. F. Chemical effects in nuclear magnetic resonance and in diamagnetic susceptibility. *Phys. Rev.* **1952**, 86, 243.

49. Saika, A.; Slichter, C. A note on the fluorine resonance shifts. *J. Chem. Phys.* **1954**, *22*, 26–28.
50. Body, M.; Silly, G.; Legein, C.; Buzaré, J.-Y. Correlation between ^{19}F Environment and Isotropic Chemical Shift in Barium and Calcium Fluoroaluminates. *Inorg. Chem.* **2004**, *43* (8), 2474–2485.
51. Bureau, B.; Silly, G.; Buzaré, J. Y.; Emery, J. Superposition Model for ^{19}F Isotropic Chemical Shift in Ionic Fluorides: From Basic Metal Fluorides to Transition Metal Fluoride Glasses. *Chem. Phys.* **1999**, *249* (1), 89–104.
52. Murakami, M.; Noda, Y.; Takegoshi, K. Terminal and Bridging Fluorine Ligands in TiF_4 as Studied by ^{19}F NMR in Solids. *Solid State Nucl. Magn. Reson.* **2019**, *101*, 82–88.
53. Biswal, M.; Body, M.; Legein, C.; Sadoc, A.; Boucher, F. NbF_5 and TaF_5 : Assignment of ^{19}F NMR Resonances and Chemical Bond Analysis from GIPAW Calculations. *J. Solid State Chem.* **2013**, *207*, 208–217.
54. Legein, C.; Fayon, F.; Martineau, C.; Body, M.; Buzaré, J.-Y.; Massiot, D.; Durand, E.; Tressaud, A.; Demourgues, A.; Péron, O.; et al. ^{19}F High Magnetic Field NMR Study of $\beta\text{-ZrF}_4$ and CeF_4 : From Spectra Reconstruction to Correlation between Fluorine Sites and ^{19}F Isotropic Chemical Shifts. *Inorg. Chem.* **2006**, *45* (26), 10636–10641.
55. Rakhmatullin, A.; Boča, M.; Mlynáriková, J.; Hadzimová, E.; Vasková, Z.; Polovov, I. B.; Mičušík, M. Solid State NMR and XPS of Ternary Fluorido-Zirconates of Various Coordination Modes. *J. Fluor. Chem.* **2018**, *208*, 24–35.
56. Ding, F.; Griffith, K. J.; Koçer, C. P.; Saballos, R. J.; Wang, Y.; Zhang, C.; Nisbet, M. L.; Morris, A. J.; Rondinelli, J. M.; Poepelmeier, K. R. Multimodal Structure Solution with ^{19}F NMR Crystallography of Spin Singlet Molybdenum Oxyfluorides. *J. Am. Chem. Soc.* **2020**, *142* (28), 12288–12298.
57. Schmid, S.; Thompson, J. G.; Rae, A. D.; Butler, B. D.; Withers, R. L.; Ishizawa, N.; Kishimoto, S. Structures of $\text{Ta}_{22}\text{W}_{40}\text{O}_{67}$ and $\text{Ta}_{74}\text{W}_{60}\text{O}_{203}$. I. Refined Structural Models Using Synchrotron Radiation. *Acta Crystallogr. Sect. B* **1995**, *51* (5), 698–708.
58. Korenev, Y. M.; Sorokin, I. D.; Chirina, N. A.; Novoselova, A. V. Vapour Pressure of Hafnium Tetrafluoride. *Zhurnal Neorg. Khimii* **1972**, *17* (5), 1195–1198.
59. Postma, C. J.; Lubbe, S. J.; Crouse, P. L. Selective Sublimation/Desublimation Separation of ZrF_4 and HfF_4 . *Journal of the Southern African Institute of Mining and Metallurgy* . scieloza 2017, pp 939–946.
60. Meyer, G.; Dötsch, S.; Staffel, T. The Ammonium-Bromide Route to Anhydrous Rare Earth Bromides MBr_3 . *J. Less Common Met.* **1987**, *127*, 155–160.

61. G. Meyer, in: *Advances in the Synthesis and Reactivity of Solids, Volume 2* (T.E. Mallouk, editor), JAI.
62. Mikhailov, M. A.; Epov, D. G.; and Rakov, E. G. Thermodynamics of the Dissociation of Ammonium Fluorozirconates and Fluorohafnates. *Russ. J. Inorg. Chem.*, **1973**, *18*(1), 56–58.

Chapter 6:

1. Rost, C. M.; Sachet, E.; Borman, T.; Moballegh, A.; Dickey, E. C.; Hou, D.; Jones, J. L.; Curtarolo, S.; Maria, J.-P. Entropy-Stabilized Oxides. *Nat. Commun.* **2015**, *6*, 8485.
2. Stebbins, J. F.; Xue, X. NMR Spectroscopy of Inorganic Earth Materials. *Rev. Mineral. Geochemistry* **2014**, *78* (1), 605–653.
3. MacKenzie, K. J. D.; Smith, M. E. *Multinuclear Solid-State Nuclear Magnetic Resonance of Inorganic Materials*; Pergamon: New York, 2002.
4. Irvine, J. T. S.; Sinclair, D. C.; West, A. R. Electroceramics: Characterization by Impedance Spectroscopy. *Adv. Mater.* **1990**, *2* (3), 132–138.
5. Smits, F. M. Measurement of Sheet Resistivities with the Four-Point Probe. *Bell Syst. Tech. J.* **1958**, *37* (3), 711–718.
6. Kubelka, P.; Munk, F. An Article on Optics of Paint Layers. *Z. Tech. Phys* **1931**, *12* (593–601).
7. Oses, C.; Toher, C.; Curtarolo, S. High-Entropy Ceramics. *Nat. Rev. Mater.* **2020**, *5* (4), 295–309.
8. Sarkar, A.; Wang, Q.; Schiele, A.; Chellali, M. R.; Bhattacharya, S. S.; Wang, D.; Brezesinski, T.; Hahn, H.; Velasco, L.; Breitung, B. High-Entropy Oxides: Fundamental Aspects and Electrochemical Properties. *Adv. Mater.* **2019**, *31* (26), 1806236.
9. Alberi, K.; Nardelli, M. B.; Zakutayev, A.; Mitas, L.; Curtarolo, S.; Jain, A.; Fornari, M.; Marzari, N.; Takeuchi, I.; Green, M. L.; et al. The 2019 Materials by Design Roadmap. *J. Phys. D. Appl. Phys.* **2018**, *52* (1), 13001.